universität wien

DISSERTATION / DOCTORAL THESIS

Titel der Dissertation /Title of the Doctoral Thesis

„Studies on the Radical Generation and Dissolution Mechanisms of Chrysotile Asbestos – From the Laboratory to the Environment“

verfasst von / submitted by

Martin Walter BSc MSc

angestrebter akademischer Grad / in partial fulfilment of the requirements for the degree of

Doktor der Naturwissenschaften (Dr.rer.nat)

Wien, 2018 / Vienna 2018

Studienkennzahl lt. Studienblatt / degree programme code as it appears on the student record sheet:	A 796 605 299
Dissertationsgebiet lt. Studienblatt / field of study as it appears on the student record sheet:	Environmental Sciences
Betreut von / Supervisor:	Univ.-Prof. Dipl.-Geol. Dr. Stephan Krämer
Mitbetreut von / Co-Supervisor:	Dr. Walter Schenkeveld

Studies on the Radical Generation and Dissolution Mechanisms of Chrysotile Asbestos – From the Laboratory to the Environment

Foreword

The project “Studies on the Radical Generation and Dissolution Mechanisms of Chrysotile Asbestos – From the Laboratory to the Environment” was funded by an uni:docs scholarship of the University of Vienna and took place from October 2014 until September 2018. The main experimental work was carried out in the research group for environmental biogeochemistry and isotope geochemistry (Prof. Stephan Kraemer) at the Department for Environmental Geosciences of the Faculty of Earth Sciences, Geography and Astronomy, University of Vienna. An important part of the experimental work was furthermore carried out at the Institute of Pharmacology and Toxicology, University of Veterinary Medicine, Vienna (Prof. Lars Gille) as well as at the Institute of Solid State Physics, Technical University of Vienna (Prof. Michael Reissner). This doctoral thesis was printed and submitted for external evaluation at the beginning of September 2018.

The research carried out in the present doctoral thesis can be categorized into three basic endpoints (Figure 1):

- Proton- and ligand-promoted dissolution of chrysotile asbestos as a function of time and pH
- Hydroxyl radical ($HO^{\bullet}$) generation and degradation of hydrogen peroxide (H_2O_2) catalyzed by reactive sites on chrysotile asbestos surfaces
- Weathering of chrysotile asbestos in polluted soils

All hypotheses tested within this dissertation fall into one of these endpoints or are combinations of two of them. The experimental results presented in this thesis are subdivided into five chapters, each of them was written to be published separately in scientific journals. The first three chapters are based on mechanistic studies that were carried out in simplified batch dissolution experiments. Thereby, the first chapter focuses on the ligand- and proton-promoted dissolution of chrysotile asbestos as a function of pH and time and their influences on the $HO^{\bullet}$ generation by, and Fe speciation on, fiber surfaces. The second and third chapter primarily focus on active Fe-sites on chrysotile surfaces, which catalyze the generation of $HO^{\bullet}$ and the degradation of H_2O_2 in fiber-mediated Haber-Weiss cycles. Furthermore, the depletion and regeneration of these active Fe-sites during fiber dissolution were investigated in the second and third chapter. To conclude, the primary emphasis of the first three chapters was to elucidate the contributions of the different structural Fe species in chrysotile on fiber dissolution, $HO^{\bullet}$ generation and H_2O_2 degradation. The fourth and fifths chapter of this doctoral thesis focus on the weathering of chrysotile in complex soil systems and the capability of fibers that were sampled from polluted soils to generate $HO^{\bullet}$ radicals. In chapter four, dissolution of chrysotile and radical generation by chrysotile surfaces were examined in a simplified soil suspensions experiment, whereas in chapter five they were examined in a complex soil-microcosm setup. In both chapters, the influence of cement (e.g. in cement containing asbestos waste) on fiber weathering and the radical

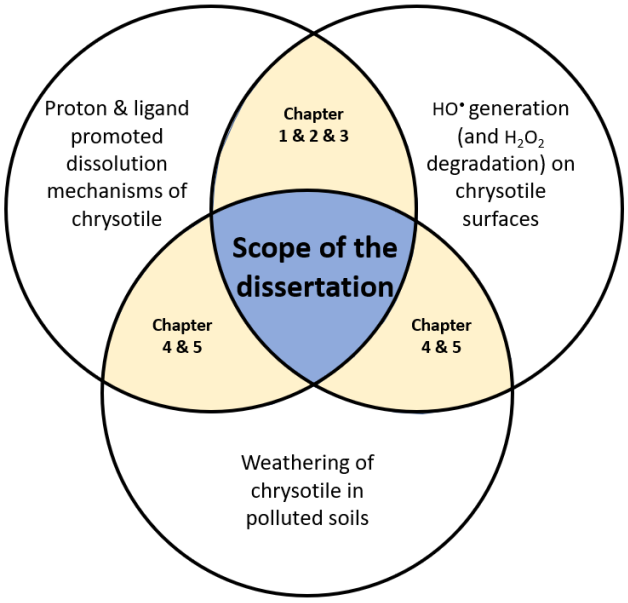

Figure 1: *The three basic endpoints investigated in this dissertation. The overlapping areas of two endpoints (in yellow) thereby define the research aims in the respective chapters, the overlapping area of all three endpoints (in blue) defines the whole scope of the dissertation.*

generation by fibers sampled from polluted soils was addressed. Finally, the effects of plants on the weathering of, and radical generation by, chrysotile in polluted soils was elucidated in chapter five.

All hypotheses of the dissertation were tested by in total four main analytical methods: Dissolution of metals and Si from fibers in batch experiments and in soils or soil suspensions were quantified by ICP-OES spectrometry (including preceding sample preparation steps, like e.g. fusion digestions), HO• generation on fiber surfaces by EPR spin trapping analyses, Fe bulk speciation of fibers by Mössbauer analyses and H_2O_2 degradation on fiber surfaces by UV/VIS-photospectrometry.

The results gained in this dissertation may be relevant for different scientific and non-scientific disciplines: Weathering studies of chrysotile in soils may especially be relevant for risk assessors and competent authorities dealing with asbestos polluted terrestrial sites and corresponding risk management decisions and strategies. HO• generation and H_2O_2 degradation studies may contribute to a broader understanding of the pathogenic mode of actions of asbestos fibers in asbestos associated diseases. Finally, mechanistic dissolution studies may be relevant for both environmental and toxicological research, as fiber dissolution is relevant in pathophysiology and in the environment.

A part of the data generated in this project was not used for this doctoral thesis, but for a separate master thesis which was written to graduate the toxicological master program at the Medical University of Vienna. The title of this master thesis is “The potential contribution of hexavalent chromium, nickel and pro-oxidants to the carcinogenicity of chrysotile asbestos”. This master thesis contains the data material for two further publications, which will be entitled “The potential

contribution of hexavalent chromium and nickel to the carcinogenicity of chrysotile asbestos" and "Mobilization of iron from chrysotile asbestos by the pro-oxidants citrate and ADP".

During this doctoral study, chrysotile fibers that were ordered from a commercial supplier in China experienced some unusual and bizarre conditions: They were regularly molten at 1050 °C, but also frozen in liquid nitrogen at -196 °C; they were made radioactive by irradiation with neutrons and were irradiated with gamma rays following decays of ^{57}Co-atoms; they were hardly bothered by alkaline solutions, but did not like acids, especially at elevated temperature; they were forced to produce numerous highly toxic $HO^{\bullet}$ radicals by degrading a lot of H_2O_2; they were irradiated by hard X-rays, but also cozy IR- and microwaves; constituents of them were excited in an argon plasma at almost 10000 Kelvin; they were bombarded with electrons just for some good snap-shots; they were fully coated with Fe and unintentionally with Al; they were powdered; they experienced strong magnetic fields; they were buried in soils sampled in Austria and in Spain; they had to bear anoxic atmospheres, high vacuum conditions and oxic air-bubbling treatments; and finally constituents of them were dissolved by an Italian line of plants that was originally cultivated in Argentine, by a herb that was ordered in Germany and by a grass that was ordered from a gardener supplier in Italy.

The possibilities of carrying out investigations in natural science are fascinating. I hope that the data of this thesis obtained by all these different methods will contribute to a broader understanding of this hazardous mineral.

General introduction

This part of the thesis contains a general introduction on asbestos fibers and its adverse properties in pathophysiology and in environmental pollution. It is subdivided into six parts (Figure 1): The mineralogy and geology of asbestos are introduced first (1), followed by the industrial applications (2) and historical and present use of asbestos (3), the adverse health effects associated with asbestos exposure (4), different exposure scenarios to asbestos (5) and the ecotoxicity, remediation and fate of asbestos or asbestos containing waste in the environment (6). At the end of this section, the main hypotheses that were formulated prior to the beginning of this project and the overall aims of this project are presented.

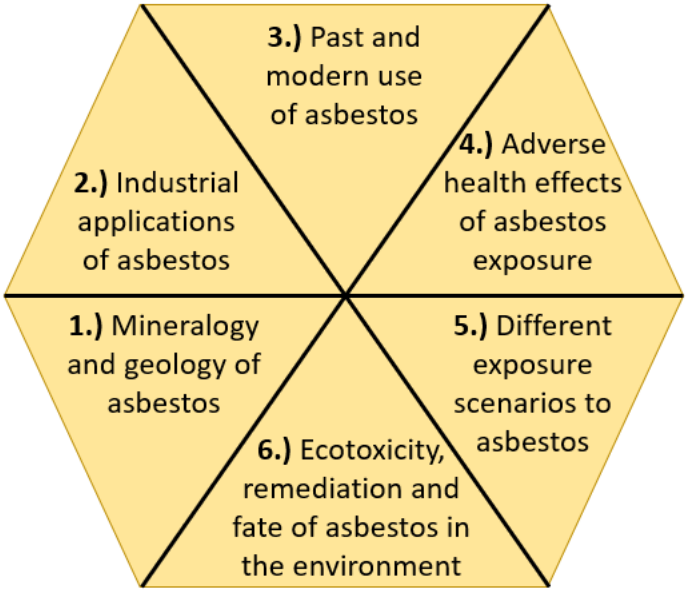

Figure 1: *Thematic structure of the general introduction.*

General introduction on the radical generation and dissolution mechanisms of asbestos: From the laboratory to the environment

1.) Mineralogy and geology of asbestos

Asbestos is a commercial term that has been introduced for six naturally occurring silicate minerals, which have a fibrous crystal habit [1, 2]. Two groups of asbestos minerals can be distinguished: sheet silicates of the serpentine group and chain silicates of the amphibole group [1, 3]. Chrysotile asbestos (also called white asbestos) is the only member of the serpentine group of asbestos, whereas the amphibole group contains five fibrous asbestos minerals: crocidolite (a fibrous polymorph of riebeckite, also called blue asbestos), amosite (a fibrous polymorph of the grunerite-cummingtonite mineral series, also called brown asbestos), tremolite, antophyllite and actinolite (which may be

accessory minerals in white asbestos) [1]. The ideal formula of the two commercially used forms of amphibole asbestos minerals are:

Amosite: $(Fe^{2+})_2(Fe^{2+},Mg)_5Si_8O_{22}(OH)_2$

Crocidolite: $Na_2(Fe^{2+},Mg)_3(Fe^{3+})_2Si_8O_{22}(OH)_2$

whereas the formula for serpentine asbestos is

Chrysotile: $(Mg_{3-x-y}R_x^{2+}R_y^{3+})(Si_{2-z}R_z^{3+})O_5(OH)_4$

where R_x^{2+} is Fe^{2+}, Mn^{2+} or Ni^{2+}, R_y^{3+} is Al^{3+}, Fe^{3+} and Cr^{3+} and R_z^{3+} is Al^{3+} and Fe^{3+} [1, 4, 5]. Chrysotile consists of octahedral magnesium hydroxide and tetrahedral silicon oxide layers which bundle together to a fiber with Mg hydroxide layers forming the external surface [6, 7]. Amphibole asbestos minerals are however double chain silicates, in which the crystalline properties are highly similar and generally may be distinguished only on the basis of chemical composition and the specific cation constituents [8]. Apart from the specific mineral formula which chemically distinguishes the six asbestos minerals, also the morphology of the mineral needs to meet certain fiber dimension criteria in order to be designated as asbestos. E.g. the WHO (World Health Organization) defines asbestos fibers as elongated minerals having an aspect ratio (defined as the length to width ratio) of at least 3:1, a length of more than 5 µm and a fiber diameter below 3 µm [2]. This morphologic definition implies that polymorphs of asbestos minerals with the same chemical formula, but non-fibrous crystal habit, are not designated as asbestos. Consequently, the non-asbestiform serpentine minerals lizardite and antigorite [7] as well as the non-fibrous polymorphs of crocidolite (riebeckite) and amosite (grunerite-cummingtonite) [1] are not considered as asbestos, even though they share the same chemical composition as their asbestiform analogues. Chrysotile and the non-commercially used amphiboles tremolite, antophyllite and actinolite are most commonly found in alpine-type ultramafic rocks (e.g. in serpentinites) in ophiolitic sequences, which were formed during the orogenesis and subsequent metamorphosis (and metasomatosis) of oceanic and mantle rocks [9, 10, 11]. The major deposits of the two commercial forms of amphibole asbestos (amosite and crocidolite) are however predominantly found in metamorphosed (and metasomatosed) banded ironstones, e.g. in Australia, South Africa and the US [11, 12].

The fibers of the two asbestos groups can be morphologically well distinguished by electron microscopy: In specimens of chrysotile asbestos, fibers of variable thicknesses and curvilinear "serpentine" morphology dominate, whereas long, straight and slender fiber morphologies with varying fiber thicknesses and lengths dominate in specimens of amphibole asbestos [8]. Figure 1 presents two electron microscope pictures of Shijiazhuang chrysotile, a commercially available serpentine asbestos that was ordered from a supplier in China. It has been used for all experiments

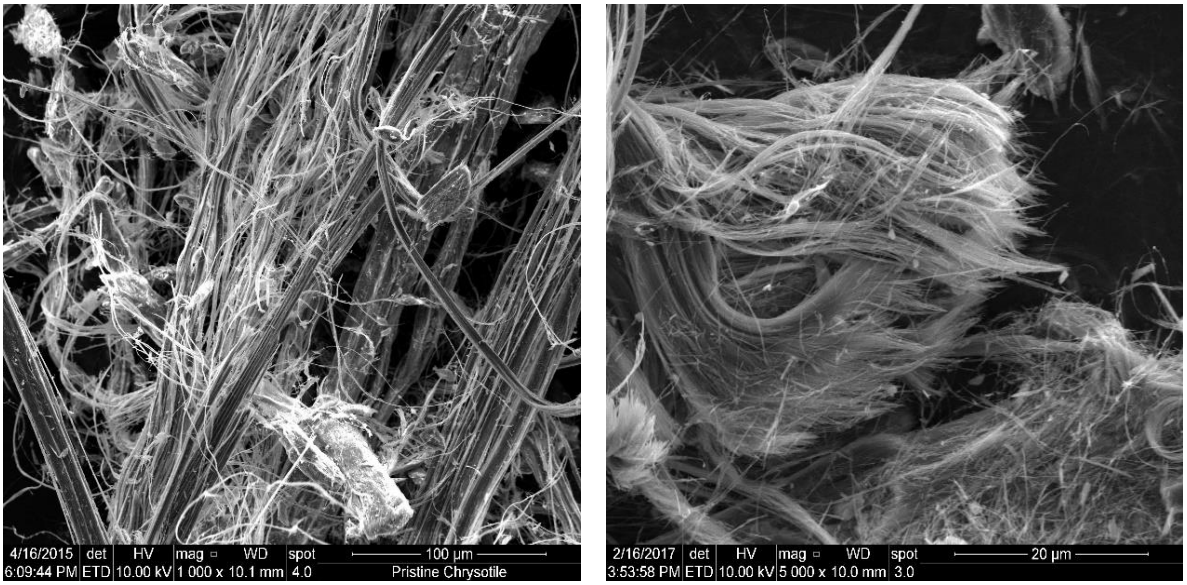

Figure 2: *SEM pictures of pristine Shijiazhuang chrysotile fibers. The fibers were investigated using a FEI Inspect S50 scanning electron microscope under high vacuum working conditions. Before the analyses, the fibers were mounted on Aluminum specimen stubs (Zeiss) equipped with PELCO carbon conductive tabs, on which the fibers were retained. The fibers on the specimen stubs were subsequently coated with carbon in a CC7650 SEM Carbon Coater and then stored in an evacuated desiccator until the SEM analysis*

carried out in this thesis. In the electron microscopic analysis of Shijiazhuang chrysotile, bigger polyfilamentous fiber bundles can be observed, from which small fibrils shed of, especially at the edges and ends of the fiber bundles (Figure 1). These fibrils, but also the fiber bundles, show a curvilinear morphology, which distinguishes them from the needle-like shape of amphibole asbestos. Additionally, bulk analyses of single fibers are frequently performed to identify and distinguish asbestos fibers. Especially selected area elemental composition analyses through energy dispersive X-ray spectrometry (EDS) are routinely applied by many investigators during electron microscopic examinations [8]. The Mg/Si ratio and the intensity of Fe are surrogate markers for the type of asbestos. Figure 2 presents a "chemical map" of Shijiazhuang chrysotile fibers generated by EDS, which indicates that Mg and Si are the dominating elements, whereas the intensity of Fe is only weakly elevated over the background. The Mg/Si ratio of ≈1.5 and the weak Fe intensity are the best markers to distinguish chrysotile from amphibole asbestos by EDS in the electron microscope.

2.) Industrial applications of asbestos

The name asbestos is derived from the Greek term for "unquenchable" or "indestructible" [8]. Within the group of six asbestos minerals, the most abundantly used commercial asbestos mineral was chrysotile asbestos, which accounted for more than 95% of the total usage of asbestos worldwide in

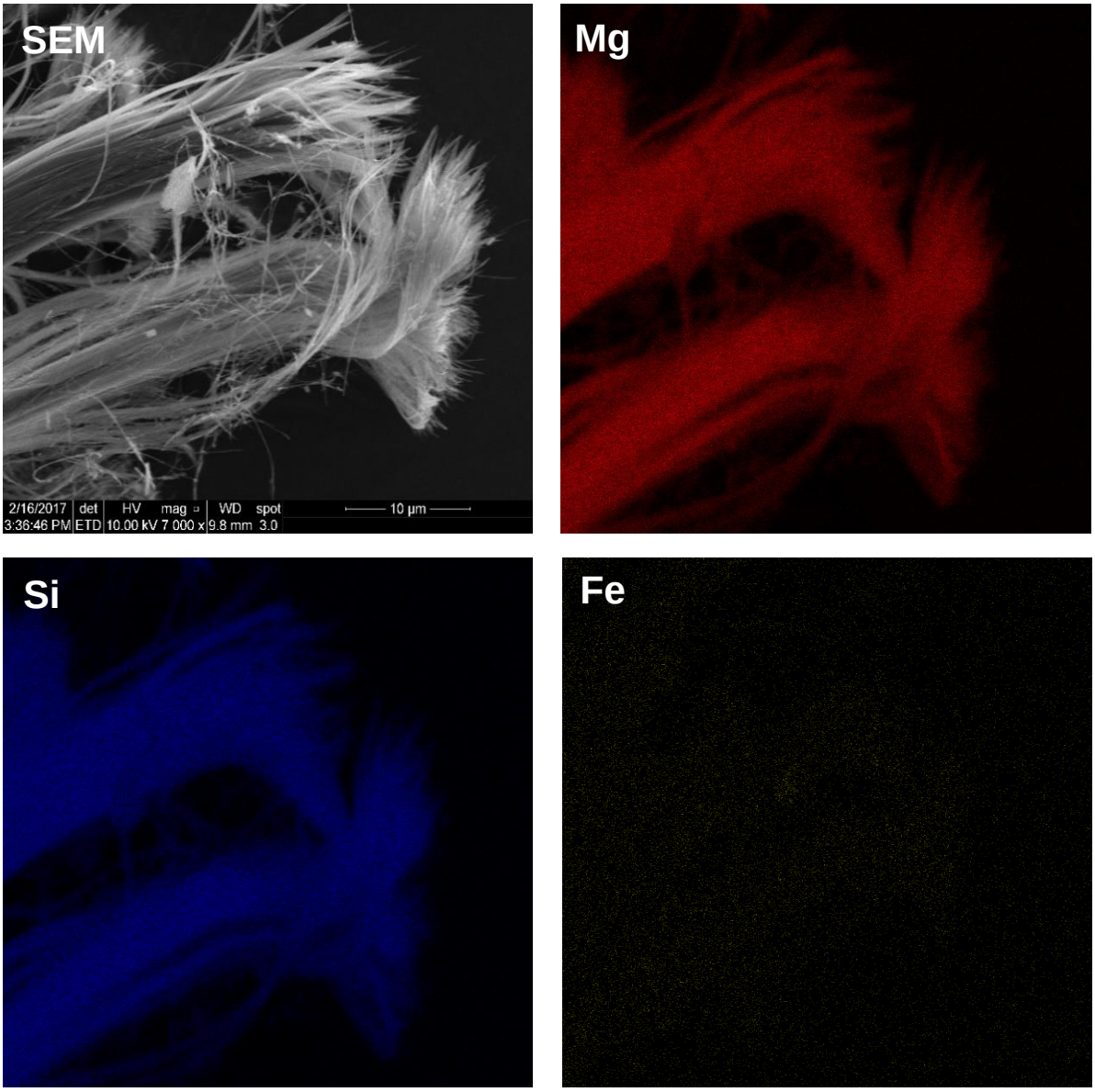

Figure 3: *SEM picture of Shijiazhuang chrysotile fibers (upper left panel) and the corresponding chemical maps of Mg, Si and Fe. The fibers were analogously investigated in a FEI Inspect S50 scanning electron microscope under high vacuum working conditions as described in figure caption 2. Additionally, a semi-quantitative micro-chemical Mg, Si and Fe analysis was performed by an energy dispersive X-ray unit (EDAX Apollo XV).*

1998 [13]. In the 21st century however, chrysotile accounts to virtually 100% of the global asbestos use [8]. Regarding the amphibole asbestos minerals, especially crocidolite and amosite were used for industrial applications, whereby crocidolite was mined worldwide, but amosite exclusively in South Africa (the origin of the name is Amosa, the acronym of the mining company Asbestos minerals of South Africa) [14]. Asbestos fibers were heavily used throughout the 20th century in a large number of industrial applications, because of their desirable physicochemical properties [8, 14]. Specifically favorable properties of asbestos are its high heat and fire resistance, electrical resistance, resistance

towards chemical and biological weathering, its large flexibility and the large tensile strength of the fibers [4, 8, 15]. Because of these properties, asbestos minerals have been abundantly used as additive materials in the construction industry (more than half of the total production of asbestos was used in this field), the shipping industry, and wherever there were needs for insulation [4, 16]. However, asbestos was also used in consumer applications, for example in textiles (especially chrysotile fibers may be spun and woven), in the inside of toasters or hair dryers, in arts and craft materials, pharmaceuticals and cosmetics, and even as a filter material which was used in the production of beer and wine [8, 14, 16]. Furthermore, the high friction and wear characteristics of chrysotile made this asbestos mineral a widely used material in such applications, as for example in friction clutches, brake linings and bearings [4]. The fiber characteristics influenced commercial exploitation: Long fibers were used as insulation materials and textiles, medium-long ones in asbestos cement and friction products, and short ones as reinforcing agents in floor tiles, joint compounds and roofing material [8].

3.) Past and modern use of asbestos:

Ancient usage of asbestos can be dated back to ca. 2500 B.C. in Finland, where the fibers were used to manufacture pottery and were believed to have magical properties [8]. Also, asbestos was used for the embalming of pharaohs in ancient Egypt [8]. Furthermore, Charles the Great reportedly astonished his guests at a feast by throwing table clothes made from asbestos into a fire from which the garments were remove clean and unharmed [8]. Significant commercial usage of asbestos did however not occur until the late nineteenth century, when the utilizations of asbestos in various industrial applications sharply increased in Northern America and Europe [8, 16, 17]. Regarding the latter, one of the hallmarks of industrial utilization of asbestos dates back to 1885, in which asbestos cement was started to be produced at large scales in the town of Vöcklabruck, Upper Austria [17]. Asbestos was mixed with cement in a ratio of approximately 1:10 [4] and was sold under the trademark Eternit. From 1907 onward, Eternit was produced at an even higher tonnage in northern Italy [18]. At the peak usage of asbestos in the US in 1972, approximately 775,000 metric tons of asbestos were processed [16]. In the countries of the European Union, Italy was the main producer and one of the main consumers of asbestos during the 20th century, owing to the fact that the largest European chrysotile quarry was located in the Piedmont region in northern Italy [18, 19]. The heavy use of the fibers during most of the twentieth century sharply declined after asbestos was banned in many countries because of the adverse health effects of asbestos fibers in humans, especially upon respiratory exposure [3, 20]. Within the member states of the European Union, asbestos has therefore been banned from the late 1980s onwards, but only on national levels [21]. The directive 1999/77/EC by the European Commission [22] then established a harmonized asbestos ban within the whole EU by 2005 in all of its then twenty-five member states [18]. In Northern American countries however, the use of asbestos

hasn't been banned yet [21], and in some (especially Asian) developing countries it even increases [23, 24]. Regarding the latter, China was the leading consuming nation in 2003 (using 492,000 metric tons), followed by decreasing order: Russia (133,000 tons), India (192,000 tons), Kazakhstan (174,000 tons), Ukraine (156,000 tons), Thailand (133,000 tons), Brazil (78,400 tons) and Iran (75,800 tons) [24]. When considering asbestos use on a global scale, the common idea in western European countries that the industrial usage of asbestos was exclusively a problem in the past can therefore clearly be negated.

4.) Adverse health effects of asbestos exposure

Adverse health effects following exposure to asbestos may affect various organs in the human body. The WHO-IARC (World Health Organization, International Agency for Research on Cancer) in its latest monograph on asbestos (2012) stated that there is sufficient evidence for the carcinogenicity of all forms of asbestos to humans (group 1) [2]. Asbestos causes mesothelioma in the pleura, peritoneum and pericardium and cancer of the lung, larynx and ovaries [2]. Positive associations have furthermore been observed between the exposure to all forms of asbestos and cancer of the pharynx, stomach and colorectum [2, 25]. Apart from these malignant diseases, respiratory asbestos exposure also causes non-malignant diseases as interstitial lung diseases (pneumoconiosis, which is in this case called asbestosis) and pleural thickening, plaques and effusions [26]. According to the WHO-IPCS (World Health Organization, International Program on Chemical Safety), each year at least 107,000 people die worldwide because of asbestos related lung cancer, mesothelioma and asbestosis resulting from occupational exposures [27]. Approximately half of all global deaths from occupational cancer are estimated to be caused by asbestos [27]. In developed countries, death because of occupational asbestos exposure is often the main work related cause of death by far, as for example in Germany, with 2121 confirmed cases in the year 2012 [28]. In general, exposure to asbestos is considered to be the second major cause for lung cancer (the first one being tobacco smoking), and the major cause of mesotheliomas [29].

Despite the clear evidence for the carcinogenicity of all asbestos fibers in humans [2], the scientific as well as the non-scientific perception on the carcinogenicity and toxicity of asbestos fibers was for decades biased by the "amphibole hypothesis", which was developed from the 1970s onwards and heavily discussed and disputed thereafter [30]. It states that adverse health effects caused by chrysotile exposure are mainly caused by amphibole phase contaminations (especially by tremolite) in the raw chrysotile material [30]. The amphibole hypothesis has thoroughly been reviewed with the result that mechanistic and lung burden studies do not provide convincing evidence for this hypothesis [29, 30, 31]. Another important aspect is that famous and influential researchers (especially pathologist) which advertised the amphibole hypothesis, received fees in the millions of dollars from the chrysotile asbestos processing industry, what indicates that this field of research may, similarly to

the research on adverse health effects caused by tobacco smoking, underly considerable conflicts of interests [29].

The pathogenic properties of asbestos fibers are complex and cannot be uniquely described by one variable. However, three key properties may be mentioned which are commonly regarded to determine the pathogenicity of the fibers: 1.) The fiber morphology (i.e. the crystal habit and aspect ratio of fibers); 2.) The biopersistence of the fibers in vivo; 3.) The reactivity of fiber surfaces to induce chemical stress to the cellular environment via the generation of reactive oxygen species (ROS) and reactive nitrogen species (RNS) at reactive surfaces sites [3, 32, 33]. These three pathogenic properties all contribute to the adverse outcome pathway in asbestos associated diseases, the weighted roles that these factors play in inducing pathologically irreversible responses are however still the subject of research [3].

Generally, long and thin fibers (fibers of a high aspect ratio) are considered to have higher potencies in inducing tumors than short thicker fibers of the same material type [3]. The study of Stanton et al. (1981) [34] has thereby been frequently cited as the basis for a concept in which fiber induced carcinogenicity is discussed to be mainly determined by the long and thin physical properties of fibers [3]. Elongated fibers in this concept are commonly referred to as “Stanton fibers”. Emplacement of asbestos fibers with a high aspect ratio in the lung or the pleura results in continuous, but unsuccessful attempts of alveolar macrophages and neutrophils to phagocytose fibers, a process called frustrated phagocytosis [32, 33, 35]. Because of the high aspect ratio of asbestos, the fibers cannot be removed from the lungs or the pleura by these phagocytic cells [3]. The unsuccessful phagocytosis of the fibers causes a permanent immune reaction and therefore a chronic inflammation in the affected parenchymal or pleural tissues, which may result both in tumor initiation and promotion [25]. During chronic inflammation, enzymatically formed ROS like hydrogen peroxide (H_2O_2) and superoxide ($O_2^{\bullet -}$) are released into the immediate extracellular environment [33]. Additionally, activated immune cells (alveolar macrophages and neutrophils) as well as endothelial and mesothelial cells produce elevated amounts of $^{\bullet}NO$ by iNOS (inducible NO-synthase) as a consequence of asbestos exposure [33]. The fact that non-asbestiform polymorphs of asbestos minerals with the exact identical chemical formula are nonpathogenic to humans underlines the important contribution of the fibrous crystal habit to the pathogenicity of asbestos minerals [8]. Even though the fiber length is commonly regarded as a key determinant of the fibrogenic and malignant capacity of asbestos in animal and in vitro models, human studies are less impressive, as reviewed by Kamp and Weitzman (1999) [33]. In the same review, an association between fiber size and the development of asbestosis in humans was reported to be unclear. Therefore, the fiber morphology alone cannot fully account for the pathogenic potency of asbestos fibers.

The biopersistency of asbestos fibers in vivo is furthermore a frequently discussed determinant in the pathology of asbestos associated diseases. The persistence of inhaled amphiboles is much greater than of chrysotile, and their clearance half-time is generally measured in decades whereas for chrysotile it is claimed to be measured in months [8, 33]. Because of the different biopersistency between chrysotile and amphiboles, the latter fibers are commonly regarded as more toxic and carcinogenic, but this is an area of considerable disagreement, as e.g. reviewed by [32, 33, 36]. Even though amphibole fibers seem to accumulate more readily in the distal lung parenchyma than chrysotile, and chrysotile induced asbestosis typically requires a threefold higher lung fiber concentration, parenchymal and pleural cells appear equally sensitive to chrysotile in terms of inducing asbestosis and mesothelioma in humans (as reviewed by Kamp and Weitzman (1999) [33]). Furthermore, even if, as frequently claimed, chrysotile is less potent in inducing mesothelioma than some amphiboles, there is little evidence to indicate a lower lung cancer risk [8, 31].

The last property of asbestos fibers which determines its pathogenicity, and which was considerably investigated over the last decades, is the chemical reactivity of the fiber surfaces. The surface charge of asbestos fibers may be an important property in this context as it causes electrostatic interactions of fibers with their cellular environment in vivo, e.g. negatively charged fibers bind proteins on their surface [3]. Freshly suspended chrysotile has a positively-charged surface below pH 8.9 [6]. The surface charge of asbestos fibers may however change during dissolution: e.g. charge reversal occurs when the outer Mg layer of chrysotile dissolves, exposing the negatively charged Si layer [6]. Obviously, also the specific surface area of the fibers is an important parameter as it determines the extent of potential chemical interactions of fibers in vivo (on an equal mass basis) [3]. The unit surface area of asbestos fibers may thereby vary considerably, as e.g. demonstrated in a study by Fubini et al. (1995), in which chrysotile asbestos had a more than a three times higher surface area than crocidolite at an equal mass basis [37]. Apart from the surface charge and area, a well investigate pathogenic mode of action of asbestos associated diseases is the fiber mediated generation of ROS and RNS by active sites on fiber surfaces [33]. The redox-reactivity of the fibers is largely related to iron at the mineral surface [25]: Fe is substituted into chrysotile asbestos during its petrogenesis (usually 2 - 3 wt%) [5], whereas the commercial amphiboles contain a high intrinsic Fe content in their mineral structure [1]. Regarding chrysotile, ferrous and ferric Fe are substituted in Mg-octahedra (Fe^{2+}[6] and Fe^{3+}[6] respectively), whereas only ferric Fe is substituted in Si-tetrahedra (Fe^{3+}[4]) [38, 39], even though the ionic radius of Fe^{3+}[4] (49 pm) is approximately twice as large as the ionic radius of Si^{4+}[4] (26 pm) [40]. Fe^{3+}[4], which substitutes Si^{4+}[4], is also found in amphibole asbestos [41]. Elevated concentrations of H_2O_2 and $O_2^{\bullet-}$, which are produced during chronic inflammatory processes (e.g. frustrated phagocytosis) by alveolar macrophages and neutrophils, may interact with Fe on the fiber surface [32]. Under homeostasis, both ROS exhibit a low potency for cellular damage [42] and can be enzymatically detoxified, e.g. by

superoxide dismutase (SOD; $O_2^{\bullet-}$) or catalase and glutathione peroxidase (H_2O_2) [33]. However, Fe on asbestos surfaces redox cycles in the presence of H_2O_2 and $O_2^{\bullet-}$ and degrades H_2O_2 to hydroxyl radicals ($HO^{\bullet}$), which cannot be enzymatically detoxified and hence have a high potency to damage DNA, proteins and lipids [25, 32, 42, 43, 44, 45]. In this Haber-Weiss cycle, Fe acts as a catalyst: Fe^{3+} is reduced by $O_2^{\bullet-}$ to Fe^{2+}, which is back-oxidized by H_2O_2 in the so-called Fenton reaction to yield Fe^{3+} and $HO^{\bullet}$ [25, 46]. The repeated oxidation and reduction of Fe has already been confirmed for structural Fe in amphibole asbestos [47]. The required reduction of ferric to ferrous Fe in asbestos to start the Fenton reaction may be governed by $O_2^{\bullet-}$, which is produced by activated immune cells in vivo [32], or by physiological compounds which are known to be able to reduce Fe, as e.g. ascorbate or cysteine [48]. Apart from that, also H_2O_2 may decompose in the presence of Fe^{3+} to hydroperoxyl ($HO_2^{\bullet}$), which can either directly reduce Fe^{3+} to Fe^{2+} or decompose to the even stronger reductant, $O_2^{\bullet-}$ [49]. Fe release from the asbestos lattice at circumneutral pH is coupled to the precipitation of secondary, low-soluble Fe(hydr)oxide minerals, which have a very low or even negligible hydroxyl radical forming potential (HRFP) [37, 50]. Hence, net Fe mobilization from fibers in this pH range only occurs in the presence of chelators like the bacterial siderophore desferrioxamine-B (DFOB), citrate and synthetic chelators like EDTA (ethylenediaminetetraacetic acid) [25, 48, 51]. The generation of $HO^{\bullet}$ decreases when Fe is removed from the fiber surface by ligand-promoted dissolution by siderophores, and when it precipitates as Fenton inactive Fe(hydr)oxide minerals during the dissolution of the fibers [50, 52]. Fe mobilization from fibers in vivo at pH 7.4 has been documented and was presumably caused by formation of soluble chelate complexes [25, 53]. The generation of $HO^{\bullet}$ radicals on fiber surfaces is not linked to the fiber bulk-Fe content [43]: For example, not all Fe surface species are equally Fenton-active or have an equal HRFP: Fubini et al. (1995) [37] demonstrated that Fe^{2+} in the Mg layers of chrysotile does no play a substantial role in $HO^{\bullet}$ generation. Furthermore, Fubini et al. (1995) demonstrated in a study on the generation of $HO^{\bullet}$ radicals by chrysotile and crocidolite (on an equal mass basis) that chrysotile was up to two times as effective as crocidolite in producing $HO^{\bullet}$ radicals, even though the latter contains much higher bulk-Fe contents [1, 35]. Hence, not the bulk-Fe, but the abundance of reactive Fe species on the fiber surfaces is relevant for the generation of highly reactive ROS [37]. However, the exact nature of these reactive Fe species on asbestos surfaces has not completely been elucidated yet. Because of the very small diffusion distance of $HO^{\bullet}$ radicals (6.9 nm), oxidative damage to DNA by Fe in asbestos was furthermore hypothesized to originate through the complexation of Fe from fiber surfaces by physiologically abundant pro-oxidant chelates like citrate and ADP, rather than by the redox cycling of reactive sites on asbestos surfaces [3, 25, 48].

The generation of another group of toxic radicals, the RNS, is also linked to asbestos exposure in vivo (as reviewed by Kamp and Weitzman (1999)) [33]. The most toxic RNS thereby is peroxynitrite ($^{\bullet}ONOO$), which is a reaction product of $O_2^{\bullet-}$ (e.g. as produced by macrophages and neutrophils) and

•NO (e.g. as produced via iNOS by inflammatory- and epithelial/mesothelial cells) in asbestos burdened tissues in vivo. Many biomolecules, as for examples DNA, unsaturated fatty-acid-containing phospholipids and molecules containing thiol groups, are oxidized and/or nitrated by •ONOO or •ONOO-derived radicals, [54]. Furthermore, •ONOO may be decomposed to HO• and •NO_2 radicals in vivo [54], indicating that HO• can also be generated by a Fe-independent mode during the exposure of asbestos [33].

The molecular responses to asbestos exposure were reviewed by Kamp and Weitzman (1999) [33]: Cell damage caused by asbestos exposure may induce signal transduction pathways (e.g. protein kinases, tyrosine kinases), which activate transcription factors (e.g. NFκB, inteleukine-6) for the expression of antioxidants (e.g. SOD, catalase and glutathione peroxidase), stress hormones and proteins (e.g. heat shock proteins, ferritin), cytokines and growth factors (e.g. TNFα, interleukins, TGFα and ß, PDGF and IGF-1). Furthermore, asbestos exposure may stimulate cellular signal transduction pathways which initiate apoptosis (e.g. via p53 and caspases) [33]. The production of growth factors and cytokines during these cellular response reactions favors the tumor promotion of initiated pre-malignant cells in chronically inflamed tissues and therefore the likeliness of the pathogenesis of asbestos associated malignant diseases [33]. Regarding tumor initiation by asbestos fibers, primary and secondary genotoxic modes of action have been discussed in asbestos burdened tissues [55]. As reviewed by Barlow et al. (2013), primary genotoxic effects are oxidative damage to DNA (as demonstrated by the formation of 8-OHdG DNA adducts), DNA damage (DNA single and double strand breaks) and/or chromosomal aberrations (clastogenicity and aneugenicity) in vitro and in vivo. Furthermore, lipid peroxidation products which are produced by the asbestos mediated radical generation are known to be able to bind as alkylating adducts to DNA and thereby induce genotoxicity [33]. The secondary genotoxic potential of asbestos is based on the excessive and persistent formation of ROS and RNS from inflammatory cells as a response to asbestos exposure, which either directly or indirectly attack DNA [55]. Secondary genotoxicity may also be derived by the oxidation of antioxidants like ascorbic acid and glutathione, which decreases the anti-oxidative capacity of asbestos burdened tissues towards inflammatory processes (as reviewed by the WHO-IARC [2]). Since inflammatory responses of tissues are known to persist only at sufficiently high doses of noxious substances, secondary genotoxicity is believed to only occur above a certain threshold dose [55]. Contrarily, the exposure to direct genotoxicants cannot be limited to a safe threshold dose, but only to a minimal risk dose.

The potency of asbestos to induce pleural, peritoneal and pericardial cancers indicates that the fibers, once inhaled, can penetrate the lung parenchyma and migrate to these serous membranes (as reviewed by the WHO-IARC [2]). The complex toxicokinetics of the inhaled fibers are even more remarkably demonstrated by the accumulation of asbestos in the ovaries of exposed females and the increased ovary cancer risk, as reviewed by Camargo et al. (2011) [56]. Similarly, the elevated risk for

colorectal cancer because of asbestos exposure was associated by the WHO-IARC with respiratory exposure to asbestos rather than oral exposure [2]. A consistent association between oral exposure to asbestos via the drinking water and cancer of the stomach or colorectum was not found in epidemiological studies (e.g. [57, 58]).

5.) Different exposure scenarios to asbestos

Asbestos associated diseases can be initiated by the respiratory exposure of sufficiently high amounts of asbestos. Exposure to asbestos may be distinguished into six exposure scenarios [8, 27, 59]:

a. Direct occupational exposure to asbestos
b. Para-occupational exposure to asbestos (household exposure)
c. Other non-occupational and non-environmental exposures (e.g. home-related domestic exposure)
d. Neighborhood environmental exposure to asbestos (e.g. near asbestos mines, demolition or processing sites)
e. Exposure to environmental pollution of asbestos containing products or wastes
f. Environmental exposure to geological occurrences of asbestos or asbestiform minerals.

As reviewed by the WHO-IARC [2], the background asbestos concentrations in the outdoor air of rural locations are typically 10^{-5} fibers cm^{-3}. In urban locations, they are tenfold higher [2]. Chrysotile is the predominant fiber type detected [2]. Worldwide, approximately 125 million people are exposed to elevated asbestos air concentrations on the workplace, making it by far the most important exposure route to asbestos [27]. Whereas the vast majority of people who die from asbestos associated diseases were exposed at the workplace (at least 107,000 per year worldwide), approximately 400 annual deaths have been attributed to non-occupational exposure to asbestos worldwide [27].

Regarding direct occupational exposure, mining of asbestos creates exposure levels that are rather low when compared to those of materials manufactured, averaging 0.9 fibers cm^{-3} [8]. In contrast, the subsequent mineral refining and milling (e.g. to “open” the fiber bundles into individual fibers) generates worker exposure levels of 6.0-12.1 fibers cm^{-3} [8]. As reviewed by the WHO-IPCS [27], the air fiber concentrations in different occupational settings had high variations; the asbestos textile industries generally constituted the workplaces with the highest exposures [8]. As an example for different occupational exposures, the geometric mean occupational exposures to asbestos fibers in the Republic of Korea were 0.40, 1.70 and 6.70 fibers cm^{-3} in the construction, asbestos friction and asbestos textile industries in 1984 [27]. In 1996, the corresponding exposures had decreased to 0.14, 0.55 and 1.87 fibers cm^{-3} respectively [27]. Also in Germany, occupational air fiber-concentrations decreased towards the end of the asbestos used: There was a steady decline in asbestos exposure between 1950 and 1990; the 90th percentile of the fiber count was between 0.5 and 1 fibers cm^{-3} in textile, paper/seals, cement, brake

pad and drilling/sawing activities in 1990 [27]. The most recent occupational exposure limits to asbestos have been set at 0.1 fibers cm^{-3} in the countries of the EU, in the US and in other countries [27].

Apart from occupational exposure, household exposure of wives and children of asbestos workers (termed "para-occupational exposure") has been demonstrated to increase the risk of asbestos associated diseases of these family members [60]: E.g. in a study carried out with wives of asbestos workers employed in the Eternit factory of Casale Monferrato in northern Italy, standardized mortality ratios of pleural cancers were significantly elevated [61]. A review on household asbestos exposure concluded a consistent elevated risk of mesothelioma in exposed populations, whereby a five-fold greater risk for mesotheliomas for persons with para-occupational exposure to asbestos was estimated [62]. Another important route of exposure is the non-occupational and non-environmental respiratory exposure to asbestos fibers during do-it-yourself home maintenance and renovation activities of asbestos containing cement products (e.g. fiber sheeting, water/drainage/flue pipes, roofing shingles, guttering etc.) [59]. The increased risk for asbestos associated diseases by handling asbestos material and the presence of asbestos material susceptible to damage (e.g. asbestos in roof shingles) was extensively reviewed by Magnani et al. (2000) [63].

Apart from the prevailing direct occupational exposure to asbestos, and reported cases of para-occupational household and domestic exposures, three non-occupational exposure pathways to asbestos may be summarize as environmental exposure to asbestos [15, 59]. At first, environmental neighborhood exposure, which results from outdoor air pollution, affects residents living close to asbestos mines and processing sites [64]. According to the WHO-IARC, outdoor air asbestos concentrations are 1000 times higher in close proximity to industrial sources of exposure (e.g. asbestos mines and processing sites, demolition sites etc.) than the general background air-concentration of asbestos in rural sites [2]. This results in a high amount of asbestos that is released into the immediate environment. Anthropogenic air emissions are not easily estimated, however, the total release of friable asbestos into the environment (includes air, water and soil) in the US was estimated to be 6.2 million kg in 1999 and 4.0 million kg in 2009 [2, 65]. As an example of neighborhood exposure, airborne asbestos fibers originating from a (today abandoned) asbestos mine in northern Greece polluted the air and soil in the proximity of this area, which is also inhabited [66]. As a result, the maximum air concentrations of fibers in villages near the former asbestos mine exceeded the occupational threshold in the EU of 0.1 fibers cm^{-3} [66]. Furthermore, in the city of Broni in Lombardy and in surrounding villages, 72 cases of malignant mesothelioma were attributed to neighborhood exposure to asbestos released by an asbestos cement plant [67]. The annual averages in the years of 2000 to 2003 were above or close the occupational threshold in the EU of 0.1 fibers cm^{-3} [67]. In the city of Bari in Italy, living within a range up to 500 m to an asbestos cement plant significantly increased the odds ratio for having malignant mesothelioma by 5.29 (95% CI: 1.18 - 23.74) [68]. In a further study, conducted in six

areas in Italy, Spain and Switzerland, the estimated odds ratio for the probability of obtaining pleural mesothelioma by living within 2000 meters from asbestos mines, asbestos cement plants or asbestos textile/shipyards/brakes factories was 11.5 (with a 95% CI of 3.5 - 38.4) [63]. In the meta-analysis of Bourdès et al. (2000), neighborhood exposure to asbestos generally increased risk ratios of pleural mesotheliomas between 5.1 and 9.3 [64]. In Amagasaki city (Japan), the regions with a significantly elevated standardized mortality ratio for mesothemioma reached 2200 meters away from a former large asbestos cement pipe plant in the direction in which the wind predominantly blew [69].

A second environmental exposure pathway to asbestos constitutes exposure to fibers via the anthropogenic pollution of the environment by asbestos containing products or wastes. As an example, near the city of Goor in the Netherlands, widespread pollution of friable and non-friable waste products from an asbestos cement plant was present, which was used to harden dirt tracks, yards, and driveways during 1935 - 1974 [70]. In this area, an expected 1.8 cases of malignant mesothelioma per year were estimated for 2.3 million person-years at risk, indicating that asbestos waste on the surface of roads and yards causes several cases of malignant mesothelioma each year in this densely populated polluted area (130,000 residents) [70]. Similarly, process waste (process sludge and dry waste, e.g. from pipe and sheet grinding) of an asbestos cement plant in a rural area of south-eastern Poland were made available to the workers of this plant. These wastes were exploited for the hardening of roads, paths, farmyards and sports fields and as construction material components [71]. In an epidemiologic study, four non-occupational cases of pleural mesothelioma were identified in this area, which were associated with the massive utilization of commonly available asbestos cement waste as road surface material [71]. Furthermore, the mean fiber air concentration in this area was significantly higher than levels recorded in other areas of Poland [72]. In Casale Monferrato in Northern Italy, the odds ratios of malignant pleural mesothelioma were 1.3 (95% CI: 0.7 - 2.3) for residents or workers using utensils of asbestos materials from an Eternit cement plant (that was active until 1986) and 3.4 (95% CI: 1.4 - 8.4) for those who were exposed to asbestos through having a garden or courtyard pavement with asbestos cement tailings [73]. Apart from the neighborhood exposure to an asbestos cement plant in the city of Bari in Italy, a second diseases cluster was associated to the “Torre Quetta” urban beach in Bari further away from the plant, where during 1950 - 1970 a not licensed waste disposal occurred [68]. The extent of pollution by asbestos containing waste may be considerably high, as for example demonstrated in Israel: In the vicinity of a former cement plant in the western Galilee, 72 public areas and an estimated 150,000 m^3 of soil were polluted with industrial asbestos waste, necessitating remediation at a total cost of 85 million dollars [74].

The last environmental exposure pathway constitutes exposure of residents to asbestos fibers that originate from geological occurrences of asbestos-rich bedrocks, or soils that derived from asbestos carrying bedrocks (e.g. serpentinite soils). As an example, a significantly higher proportion of malignant

mesothelioma in young individuals (<55 years) was identified in Clark and Nye counties of Nevada compared with the United States and other Nevada counties, which was associated with the geological occurrence of carcinogenic minerals (e.g. actinolite, erionite etc.) in this region [75]. The sources of these fibrous minerals are several plutons in southern Nevada and Arizona and alluvial fans emanating from asbestos-containing bedrocks, which potentially endanger the nearby cities of Henderson, Boulder City and Las Vegas [76]. Similarly, a study for mesothelioma cases in California demonstrated that the residential proximity to geologic sources of naturally occurring asbestos shows a dose-response association with mesothelioma risk [77]. In New Caledonia (France), the extensive use of a very friable tremolite containing rock, quarried from local outcroppings and used as a whitewash for indoor and outdoor walls of houses by residents, caused high incidence areas of malignant pleural mesothelioma [78]. Geogenic exposure to asbestos or asbestiform minerals is known to be a big issue in certain rural parts of Turkey: Emri et al. (2002) reviewed that in Turkey, the country with the highest prevalence of endemic asbestos-related pulmonary diseases worldwide, natural asbestos deposits have been locally used by the rural population to make whitewash or stucco for the walls, floors and roofs of houses, whereby tremolite was the most prominent asbestos mineral in deposits before chrysotile and anthophyllite [79]. This caused serious adverse health effects in the affected population. For example, asbestos-related benign and malignant diseases are endemic in some rural parts of the Eskişehir district in the central part of Anatolia, which makes asbestos one of the most serious chemical health hazards in this rural population after tobacco smoking [80]. Apart from asbestos, especially the asbestiform zeolite mineral erionite has been extensively investigated as a natural occurring hazardous fiber in Turkey. This fiber is present in volcanic tuff deposits in the Cappadocian region of Central Anatolia, which are used as building stone [79]. In these zeolite villages, malignant mesothelioma is responsible for more than 50% of the total deaths [79]. Apart from Turkey, geological erionite deposits can also be found in 12 US states, which causes reason for concern for an increased risk of malignant mesothelioma especially in North Dakota and Nevada [81]. Other natural occurrences of asbestos and related health problems of residents can be found in the review of Liu et al. (2017) [59].

6.) Ecotoxicity, remediation and fate of asbestos in the environment

The anthropogenic and environmental emissions of asbestos not only cause exposure of residents, but also contamination of the environment. Especially soil environments may become increasingly contaminated in this context. Asbestos in the environment may have ecotoxicology implications, which are far less well-studied than the human exposure to environmental asbestos pollution. Schreier and Timmenga (1986), for example, have demonstrated that earthworms (Lumbricus rebellus) not only accumulated nickel and manganese when introducing them into chrysotile rich sediments, most of them also perished within 21 - 31 days of exposure [82]. Bordeleau et al. (1977) demonstrated that

asbestos rich dust that had deposited on podzolic soils near an asbestos mine in Quebec decreased the fungal population and the abundance of obligate heterotrophic bacteria in that soil, but at the same time increased the abundance of facultative heterotrophic and autotrophic bacteria [83]. Furthermore, the same asbestos rich dust retarded the soil process of podzol formation by modifying the soil pH [84]. Another influence of asbestos pollution in soils is the leaching of heavy metals from fibers and subsequent accumulation in soils: Schreier (1987) demonstrated that because of a landslide of asbestos rich serpentinite material into Sumas River in Everson (Washington), heavy metals such as Ni, Cr, Co and Mn were released from the asbestos rich sediments and accumulated in the underlying organic rich soil horizons [85]. Not only soil organisms and soils may be affected by heavy environmental asbestos pollution: A storm in 1975 in Everson has deposited asbestos rich serpentinitic sediment on a grazing site used for beef cattle [86]. The cattle were consequently exposed to asbestos via inhalation and ingestion, which resulted in significantly elevated blood levels of Ni and Mn and an elevated fiber body burden [86].

Because of the health hazards that environmental asbestos contamination poses to exposed residents (as summarized before), and the ecotoxicity of the fibers, asbestos containing wastes need to be deposited in specially designated landfills for hazardous wastes [87]. The deposition of asbestos containing waste is regulated by the EU Regulation No. 1357/2014 [88]: As asbestos is a group 1 carcinogen according to the WHO-IARC [2], all wastes that contain asbestos concentrations of ≥ 0.1 wt% are classified as hazardous waste which induces cancer or increases its incidence. The European waste catalogue classifies eight types of asbestos containing wastes (e.g. wastes from asbestos processing and asbestos cement manufacture or brake pads, insulation materials and construction materials containing asbestos) which are all classified as hazardous waste throughout the EU [89]. Landfills that are used for the disposal of these wastes need to fulfill certain safety criteria in the countries of the European Union, which are regulated by the Council Directive 1999/31/EC [90]. These landfills e.g. need to contain a leachate collection and sealing system as well as an artificial sealing liner, impermeable mineral layer, a drainage layer with > 0.5 m and a top soil cover of > 1 m [90].

In the case of uncontrolled asbestos disposal into the environment, remediation programs of polluted sites may be necessary. There is no harmonized policy in the EU regarding the remediation of asbestos polluted soils. However, because of widespread environmental pollution with asbestos in the Netherlands (e.g. [70]), local competent authorities developed some pioneer guidelines for risk assessments on asbestos pollution in the environment. The intervention level for asbestos polluted soils in the Netherlands is 100 mg kg^{-1} [91]. Once a polluted site exceeds this value, a site-specific tiered approach for the assessment of the human health risk is performed, in which the probability for emission of fibers to air (tier 1), the respirable fraction in the soil and in house dust of residents (tier 2) and the concentration of asbestos fibers in outdoor and/or indoor air (tier 3) are assessed [91]. The

location specific risks of an asbestos contaminated site are then divided into two categories: “no unacceptable risks” and “unacceptable risks” [92]. The polluted site is classified in the “no unacceptable risks” category if, given the sites present us, there is no likelihood of emission because exposure to asbestos-containing soil contamination is impossible (e.g. due to permanent vegetation coverage) [92]. However, the competent authority may prescribe control measures and a register of limitations for the site. The location is classified in the “unacceptable risks” category if measurements in indoor or outdoor air show that the negligible risk level is being exceeded, which requires urgent remediation measures (i.e. start remediation within 4 years) [92]. In the countries of the European Union, the most common remediation technique of contaminated soils has up to now been the excavation of the soil and its disposal in landfills [93]. Regarding asbestos polluted soils, the most commonly performed remediation strategy is the manual removal of contaminants (i.e. bigger pieces of asbestos containing waste) from soil and the subsequent excavation of the contaminated soil layer (with > 0.5 m) and disposal in landfills for hazardous wastes [92].

For cases in which asbestos polluted environments are not remediated (e.g. the “no unacceptable risk” scenarios in the Dutch asbestos soil remediation strategy), or in which remediation is impossible because of a widespread and disperse pollution with fibers, studies on the weathering kinetics of asbestos in different polluted environments are crucial to estimate the persistence of asbestos fibers in polluted soils in the frame of risk assessments. The weathering kinetics of asbestos in soils can thereby be assessed in fiber dissolution studies. Considering that chrysotile accounted for more than 95% of the total usage of asbestos worldwide [13], it is consequently the most prevalent asbestos mineral in environmental pollution. The dissolution of chrysotile is commonly described as a step-by-step dissolution of alternating Mg and Si layers, which is governed by the fast dissolution of Mg layers and the slow dissolution of Si layers [94, 95, 96, 97]. Exposed Mg layers at the surface of pristine fibers dissolve within hours over a broad pH range, whereas exposed Si layers dissolve much slower and therefore determine overall dissolution rates [94, 97]. Dissolution rates are inversely related to pH [94, 96, 97, 98, 99], e.g. from pH 7 to 10 the Mg dissolution rate was reported to scale with $[H^+]^{0.24}$ [97]. Over a broader pH range (pH 2 to 8), dissolution rates of Mg and Si scaled exponentially with decreasing pH [96]. Mg dissolution rates of chrysotile in simplified laboratory flow through and batch experiments were in the tens of pmol m^{-2} s^{-1} at low pH values and at single digit pmol m^{-2} s^{-1} values at circumneutral and mildly alkaline pH, whereas Si dissolution rates at acidic and circumneutral pH were lower than predicted by stoichiometry [96, 97]. The stoichiometric dissolution of chrysotile has a narrow pH window: The fibers dissolved incongruently at circumneutral and acidic pH values (starting somewhere around pH 3), whereas they dissolved congruently at mildly acidic pH values (pH 3 to 6) [96, 97, 99]. In acids (e.g. nitric, hydrochloric and sulfuric acid), the bulk-Mg content of chrysotile dissolves rapidly within hours to days, depending on the acid concentration and on the type of the acid [95, 100, 101].

The Si-bulk however does not sufficiently dissolve in acids [100], not even at elevated temperature [102], since the Si content of the dissolving fibers transforms into an acid-insoluble amorphous siliceous material [100, 101]. At alkaline pH, the fibers are practically insoluble because of the low solubility of the outermost brucite-like Mg hydroxide layers [99]. Considering the highly alkaline pH of solutions in equilibrium with cement [103], chrysotile asbestos contained in cement waste in the environment may be particularly resistant towards weathering. Cement may thereby inhibit the weathering of chrysotile by two different mechanisms: First the cement matrix may completely embed the fibers and thereby prevent fiber weathering by the soil-solution, and second the cement matrix may cause a local alkalization of the soil-solution and thereby inhibit or slow down the dissolution of the fibers [99]. The dissolution of amphibole asbestos minerals was not as thoroughly investigated as the dissolution of chrysotile. In a comparative dissolution study of chrysotile and crocidolite at pH 7 by Gronow (1987) [94], Mg surface normalized dissolution rates of Mg were approximately one order of magnitude slower for crocidolite. However, Si dissolution rates at the same pH were identical in both asbestos minerals in the same study [94].

Apart from the proton promoted dissolution of asbestos fibers, the ligand promoted dissolution of the fibers, e.g. by oxalate, citrate and natural or synthetic siderophores, was extensively investigated in batch dissolution experiments [3, 37, 48, 51, 99]. The main focus of these studies was the ligand promoted dissolution of Fe from asbestos (as summarized before in the context of the Fe related health hazards of the fibers). An enhancement of metal dissolution by the release of chelating ligands was however also observed for asbestos fibers in the presence of various biota, either in laboratory studies or in the environment [50, 104, 105, 106, 107, 108]. Very different groups of organisms (lichens, fungi, bacteria and plants) were demonstrated to colonize and/or dissolve constituents of asbestos or asbestos bearing rocks and soils. One of the first studies on the interaction of lichens with asbestos by Christensen (2004) described the growth of twenty-two epilithic and calciphilic lichen species and six mosses on corrugated asbestos-cement tiles from a single roof in the city of Copenhagen [109]. The effect of lichens on asbestos weathering was then intensively studied by Favero-Longo and coworkers in Torino, Italy. Lichens were demonstrated to attack chrysotile on serpentinite rocks where lichen selectively grew on the fibers and secreted metabolites (like oxalic acid), which in the long run turned the fibers into a non-toxic amorphous material [108]. Epilithic lichen species like Spoastatia testudinea, Lecidea atrobrunnea and Rhizocarpon geographicum were found to facilitate physical (by hyphal penetration up to 2 mm in depth) and biogeochemical weathering (e.g. oxalate exudation) of serpentine minerals in serpentinite soils and hence influence pedogenetic processes in these soils [110]. Furthermore, pioneer lichens rapidly colonized asbestos veins in serpentinite blocks and walls of the 1990 abandoned Balangero asbestos mine, the largest asbestos mine of Western Europe [111]. Interaction of lichens with chrysotile was demonstrated by Favero-Longo et al. (2007) in sterile

cultured isolates of lichen-forming ascomycetes [104]. In this study, tight adhesion of hyphae to chrysotile fibers was observed in all tested species, whereby this interaction depleted the surface of the investigated asbestos fibers of Mg, e.g. by the exudation of lichen derived metabolites such as oxalic acid, pulvinic acid and norstictic acid [50, 104]. An in detail investigation of lichens on asbestos-cement roofs furthermore demonstrated that lichens modified the physical and chemical properties of asbestos cement sheets and induced incongruent dissolution of chrysotile and crocidolite, which promoted the bioattenuation of these products [112]. Lichen cultivation as a bioattenuation strategy in the Balangero asbestos mine in Italy (by the transplantation of whole thalli of Xanthoparmelia tinctina) seemed feasible on asbestos rich walls that were not exposed to strong erosion processes [113]. Finally, a decreased $HO^{\bullet}$ generation by asbestos fiber surfaces in lichen cultures was detected, which indicates that metal chelates released by lichens can remove Fenton-active metals from asbestos surfaces [105].

Apart from lichens, fungi were demonstrated to facilitate weathering reactions of asbestos in the field and in the laboratory. In one of the first studies, Martino et al. (2003) demonstrated that fungi bind asbestos fibrils with their hyphae and thereby limit their dispersal in suspensions. Furthermore, fungi exuded potent siderophores, which deprived the fiber surface of free radical generating sites [114]. Regarding these processes, Fusarium oxysporum was most effective in a study among different fungi species [115]. Fursarium oxysporum removed Fe from three different asbestos minerals in the order chrysotile > crocidolite > amosite by the exudation of fungal siderophores [107]. This removal of Fe fully blunted $HO^{\bullet}$ generation by chrysotile and crocidolite fibers, but only partially by amosite fibers [107]. In another study, chrysotile and crocidolite fibers that were Fe-depleted on the fiber surface by the fungal species Verticillium sp. and Paecilomyces sp. had a decreased $HO^{\bullet}$ generation [116]. Subsequently, these fibers also had a decreased potential to damage DNA in vitro (measured by the generation of 8-oxo-7,8-dihydro-2'-deoxyguanosine), indicating a decreased hazard potential of fibers weathered by fungi [116]. A fungal species isolated from serpentinitic rocks in the alps (Verticillium leptobactrum) was especially effective in solubilizing Mg and Si from chrysotile fibers and was proposed as a bioweathering species for soils that are heavily polluted with asbestos [60]. A detailed review on the bioattenuation processes of fungi on asbestos fibers was written by Daghino et al. (2010) [117].

The effect of bacteria on asbestos weathering was not as extensively studied as asbestos weathering by lichen and fungi: However, in a study by Bhattacharya et al. (2016), a decrease in the iron content of asbestos was observed following incubations with bacterial isolates, most likely because of the release of bacterial siderophores [106]. Similarly, the potential effect of plants on mobilization of metals from asbestos fibers in the environment has hardly been investigated, even though plants are known to mobilize Fe and other heavy metals from soils by the exudation of phytosiderophores [118,

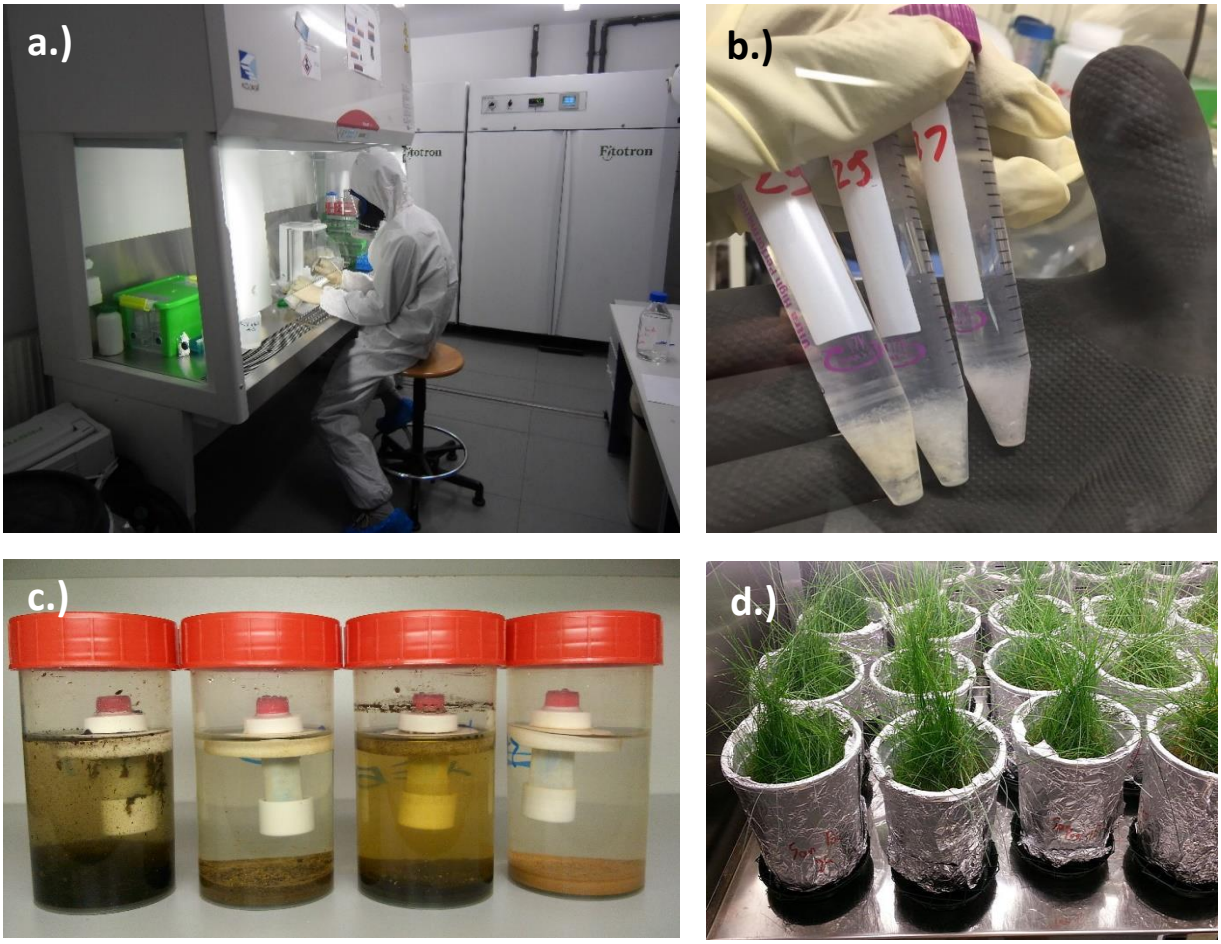

Figure 4: *Laboratory pictures of various experimental setups and procedures. Panel a.) Working with asbestos in a safety bench in a specially suited working gear; Panel b.) anoxic dissolution experiments with different coloring of fibers originating from different Fe-surface states (from left: blank altered fibers, DFOB altered fibers and blank-altered fibers plus ascorbate); Panel c.) Fiber dissolution experiments in soil suspensions of a podzolic soil (left), an agricultural soil, a calcareous soil high in SOC and a calcareous soil low in SOC (right); Panel d.) Long term microcosm experiments with fibers buried in (planted) soils (in this picture poa pratensis cv Baron).*

119]. Deposits from the abandoned Balangero asbestos mine in Italy were colonized by low-covering hyperaccumulators such as Thlaspi sylvium and Minuartia lacrifolia. Only decades later mature plant communities completely covered the asbestos-rich debris, thereby limiting the dispersion of fibers [111]. In a column experiment, a Ni-hyperaccumulator (Leptoplax emarginata) increased Mg-dissolution from chrysotile by more than 2-fold and mobilized 1.65% of total Ni from chrysotile, whereas in unplanted treatments only 0.03% of Ni were mobilized [120]. Since an acidification of the rhizosphere was not observed in the treatments, the increased Ni mobilization in the presence of the Ni-hyperaccumulator either indicated a ligand-promoted mobilization of Ni by plant-borne chelating agents, or an increased Ni mobilization induced by the plant-associated bacterial microflora. However, metal mobilization from asbestos by non-serpentinite endemic plants has not been studied yet.

Apart from the chemical properties of soils (e.g. soil solution pH) and biota that influence weathering of asbestos in the environment, also meteorological and hydrological characteristics were demonstrated to influence the weathering kinetics of fibers. For example, Favero-Longo et al. (2009) demonstrated that physical weathering by freezing-thawing and wetting-drying cycles (mimicked in the laboratory) stimulated fiber dissolution and decreased $HO^{\bullet}$ generation on asbestos fiber surfaces [121]. In the same study, chrysotile was more influenced by physical weathering as tremolite asbestos [121].

All the studies summarized in this section of the introduction indicate that asbestos fibers may undergo complex chemical, biological and physical weathering mechanisms in polluted environments. However, many potentially important parameters of asbestos weathering in the environment, as for example the influence of soil properties like soil solution pH and the plant cover of non-serpentinitic soils, haven not been assessed in that context yet.

Main hypotheses and overall aims of this project:

Because of the dominance of chrysotile asbestos in the historical use of asbestos (more than 95% of all asbestos minerals used were chrysotile) [13], and the fact that it is de facto the only asbestos mineral that is still in use today [8], the research of this thesis exclusively focusses on chrysotile asbestos.

Based on the state-of-the-art knowledge on the radical generation and dissolution mechanisms of asbestos, as introduced before, this section provides a small overview on the main six hypotheses that were formulated prior to the beginning of the project as well as on the overall aim of this project. These six hypotheses were the starting point of all investigations described in this thesis. Many new hypotheses were formulated after obtaining new experimental data. All hypotheses of this thesis were tested in batch fiber dissolution experiments, fiber dissolution experiments in soil suspensions and in complex soil microcosms (Figure 4). The corresponding analytical analyses of the experiments comprised ICP-OES (and sometimes ICP-MS) analyses to quantify metal and Si mobilization from fibers or soils, EPR spin trapping techniques to analyze $HO^{\bullet}$ generation by pristine and altered fibers, Mössbauer spectroscopy to analyze the valance and coordination of bulk-Fe in pristine and altered fibers as well as the valance and coordination of ^{57}Fe atoms that were precipitated on altered fiber surfaces, and UV-VIS photospectrometry to analyze H_2O_2 degradation by pristine and altered fibers.

The six hypotheses, as summarized in Table 1, can be subdivided into two groups: Hypothesis one deals with the molecular mechanisms of $HO^{\bullet}$ generation on fiber surfaces by structural Fe in chrysotile,

Table 1: *The main hypotheses formulated prior to the beginning of the project.*

Hypothesis Nr.	Hypothesis concerns:	Hypothesis:	Hypothesis addressed in chapter:
1	Radical generation in general	We hypothesize that the effective generation of $HO^{\bullet}$ radicals by the low bulk-Fe exposed on chrysotile surfaces is based on a different coordination environment of Fe^{3+} in chrysotile as compared to the more abundant Fe^{3+} in Fe-(hydr)oxides.	1, 2, 3
2	Weathering in soils	We hypothesize that the dissolution of chrysotile fibers in polluted soils is inversely related to the respective soil solution pH.	1, 4, 5
3	Weathering in soils	We hypothesize that the dissolution of chrysotile in asbestos cement waste in polluted soils is inhibited by cement because of its high alkalinity.	1, 4, 5
4	Weathering in soils	We hypothesize that plants not endemic to serpentinite soils may increase the dissolution of metals from chrysotile surfaces by the exudation of metal chelating ligands into asbestos polluted soils.	1, 5
5	Radical generation by fibers sampled from soils	We hypothesize that plants decrease the generation of $HO^{\bullet}$ radicals of soil-sampled chrysotile fibers. This may be facilitated by the exudation of plant-borne metal chelating ligands into asbestos polluted soils, which complex Fenton active metals from the fiber surfaces.	1, 5
6	Radical generation by fibers sampled from soils	We hypothesize that cement in chrysotile containing cement waste inhibits the dissolution of Fenton active metals from fiber surfaces in polluted soils. Therefore, we hypothesize that fibers from polluted soils have a higher potency to generate $HO^{\bullet}$ radicals when they were located in the vicinity of cement.	1, 4, 5

hypothesis two to six deal with the radical generation and dissolution mechanisms of chrysotile asbestos in the environment.

At first, we hypothesize that the effective generation of $HO^{\bullet}$ radicals by the comparatively low Fe contents on chrysotile surfaces relative to Fe-(hydr)oxides surfaces (on an equal surface area basis) [5, 122] is based on a specific coordination environment of Fe in chrysotile, which increases the Fenton-reactivity of this Fe species (Hypothesis 1). The absence of these reactive Fe species may consequently be the rationale of the low or negligible HRFP of Fe-(hydr)oxides [35, 37]. Since the only ferrous bulk-Fe species in chrysotile (Fe^{2+}[6]) was demonstrated to be non-Fenton reactive [37], we further hypothesize that the Fenton-reactive Fe species in chrysotile is ferric Fe that is able to be reduced to an ultimate Fenton-active ferrous Fe species. In order to be Fenton-reactive for more than one redox cycle, we further hypothesize that the Haber-Weiss redox cycling of this reactive Fe species in

chrysotile does not destroy the crystal lattice of the asbestos fibers. Hypothesis 1 was investigated in great detail in chapter 1, 2 and 3 of the thesis. The results gained in these chapters were important to understand experimental results from chapter 4 and 5.

The other five hypotheses focus on the radical generation and dissolution mechanisms of chrysotile fibers in polluted soil environments, whereby the corresponding results are discussed in chapter 1, 4 and 5. Considering the inverse relationship between chrysotile dissolution and pH (as discussed in the context of simplified laboratory dissolution experiments) [94, 96, 97, 98, 99], we hypothesize that the dissolution of chrysotile fibers in polluted soils is inversely related to the respective soil solution pH (Hypothesis 2). Accordingly, since solutions in equilibrium with cement have a high alkaline pH [103], we hypothesize that the dissolution of chrysotile in the vicinity of cement (e.g. as in asbestos cement waste) in polluted soils gets inhibited (Hypothesis 3). Considering the stimulating effects of lichens and fungi on asbestos dissolution by the release of metal chelating agents (as summarized before), we hypothesize that plants may increase the dissolution of metals from chrysotile surfaces by the exudation of metal chelating ligands into asbestos polluted soils. Since this has only been questioned for a serpentinite-endemic Ni-hyperaccumulator, we thereby hypothesize that also non-serpentinite endemic plants can accelerate chrysotile dissolution in contaminated soils (Hypothesis 4). Accordingly, we hypothesize that plants that are not endemic to serpentinite soils decrease the generation of $HO^{\bullet}$ radicals by chrysotile fibers sampled from soils by exuding metal chelating ligands into asbestos polluted soils, which complex Fenton active metals from the fiber surfaces (Hypothesis 5). This has analogously been described for lichens and fungi (as summarized before). Finally, accordingly to hypothesis 3, we hypothesize that cement in chrysotile containing cement waste inhibits the dissolution of Fenton active metals from fiber surfaces in polluted soils. This both affects the dissolution of Fenton-active metals as mediated by the soil characteristics (e.g. soil solution pH) and by plants (by the exudation of metal chelating agents).

All hypotheses that were tested in this work aim to contribute to the scientific investigation of the three basic endpoints that define the scope of this thesis (as already mentioned in the foreword): 1.) Proton- and ligand-promoted dissolution of chrysotile asbestos as a function of time and pH; 2.) $HO^{\bullet}$ generation out of the degradation of H_2O_2 as catalyzed by reactive sites on chrysotile asbestos surfaces; 3.) Weathering of chrysotile asbestos in polluted soils. Knowing the proton- and ligand-promoted dissolution mechanisms and rates of chrysotile as a function of pH, is crucial for estimating the biopersistency of the fibers in vivo, but also the persistency of chrysotile in polluted soil environments. Furthermore, the high efficacy of the $HO^{\bullet}$ generation by chrysotile surfaces is decreased by the proton- and ligand-promoted dissolution of Fenton-reactive sites on the fiber surfaces. The experiments of mainly the first chapter of this thesis address these issues. Regarding the generation of $HO^{\bullet}$ radicals in fiber-mediated Haber-Weiss cycles, the experiments of this thesis aim to ultimately identify the

Fenton-reactive Fe species on chrysotile surfaces. Fenton-reactive Fe on asbestos surfaces has been investigated since the 1980s, the exact nature of the "reactive Fe species" on asbestos surfaces is however still not known today. Hence, chapter 1 and especially chapter 2 and 3 are dedicated to identifying this reactive Fe species, which catalyzes the pathologically highly important generation of $HO^{\bullet}$ radicals. The results of these chapters may contribute to the better understanding of the toxicity and carcinogenicity of chrysotile asbestos, which may be important in developing effective therapies against early stages of asbestos associated diseases. Finally, the experiments carried out at the end of this thesis (chapter 4 and 5) aim to contribute to the investigation of the dissolution mechanisms and dissolution rates of chrysotile, as well as to the Fenton-reactivity of chrysotile fibers, in geochemically different polluted soil environments. Since widespread disperse asbestos pollution and non-remediated asbestos polluted soils are abundant in many countries worldwide, the experiments carried out for this thesis strive to provide a scientific reference for risk assessors and competent authorities dealing with environmental asbestos pollution. Each year, still more than 100,000 people die worldwide because of occupational exposure to asbestos, and an additional 400 people die worldwide because of environmental asbestos exposure [27]. As asbestos associated diseases are almost exclusively an avoidable health risk, the overall aim of this thesis is to contribute to the scientific investigation of this hazardous mineral, which will help health professionals, competent authorities and risk assessors in their efforts to minimize the number of people that develop asbestos associated diseases.

First Chapter

"The effect of pH and biogenic ligands on the weathering of chrysotile asbestos; the pivotal role of tetrahedral Fe in dissolution kinetics and radical formation"

Authors: Martin Walter[a], Walter D.C. Schenkeveld*[a]†, Michael Reissner[b], Lars Gille[c], Stephan M. Kraemer[a]

Publication intended in: "Chemistry – A European Journal"

[a] Department of Environmental Geosciences, University of Vienna
Althanstraße 14 (UZA II), 1090 Vienna, Austria
*Email: w.d.c.schenkeveld@uu.nl

[b] Institute of Solid State Physics, TU Wien
Wiedner Hauptstraße 8-10, 1040 Vienna, Austria

[c] Institute of Pharmacology and Toxicology, University of Veterinary Medicine, Vienna
Veterinärplatz 1, 1210 Vienna, Austria

† current address:
Copernicus Institute of Sustainable Development, Faculty of Geosciences, Utrecht University Princetonlaan 8A, 3584 CB Utrecht, The Netherlands

Abstract

Chrysotile asbestos is a soil pollutant in many countries. It is a carcinogenic mineral, partly due to its surface chemistry. In chrysotile, Fe^{2+} and Fe^{3+} substitute Mg octahedra (Fe[6]), whereas Fe^{3+} substitutes Si tetrahedra (Fe^{3+}[4]). Fe on fiber surfaces can generate hydroxyl radicals ($HO^{\bullet}$) in Fenton reactions, which damage biomolecules. To better understand chrysotile weathering in soils, we determined net Mg and Si dissolution rates over the pH range 3.0 - 11.5, in the presence and absence of biogenic ligands. Also, we examined $HO^{\bullet}$ generation and Fe bulk speciation of pristine and weathered fibers by EPR and Mössbauer spectroscopy. Dissolution rates were increased by ligands and inversely related to pH with complete inhibition at cement pH (11.5). Surficial Mg layers readily dissolved at low pH, but only within days at neutral pH. On longer timescales, the slow dissolution of Si layers became rate-determining. In absence of ligands, Fe[6] precipitated as Fenton-inactive Fe phases, whereas Fe[4] (7% of bulk-Fe) remained redox active throughout 2-week experiments and at pH 7.5 generated 50 ± 10% of the $HO^{\bullet}$ yield of Fe[6] at pristine fiber surfaces. Ligand-promoted dissolution of Fe[4] (and potentially tetrahedral Al) labilized exposed Si layers. This increased Si and Mg dissolution rates and lowered $HO^{\bullet}$ generation to near-background level. We conclude that Fe[4] surface species control long-term $HO^{\bullet}$ generation and dissolution rates of chrysotile at natural soil pH.

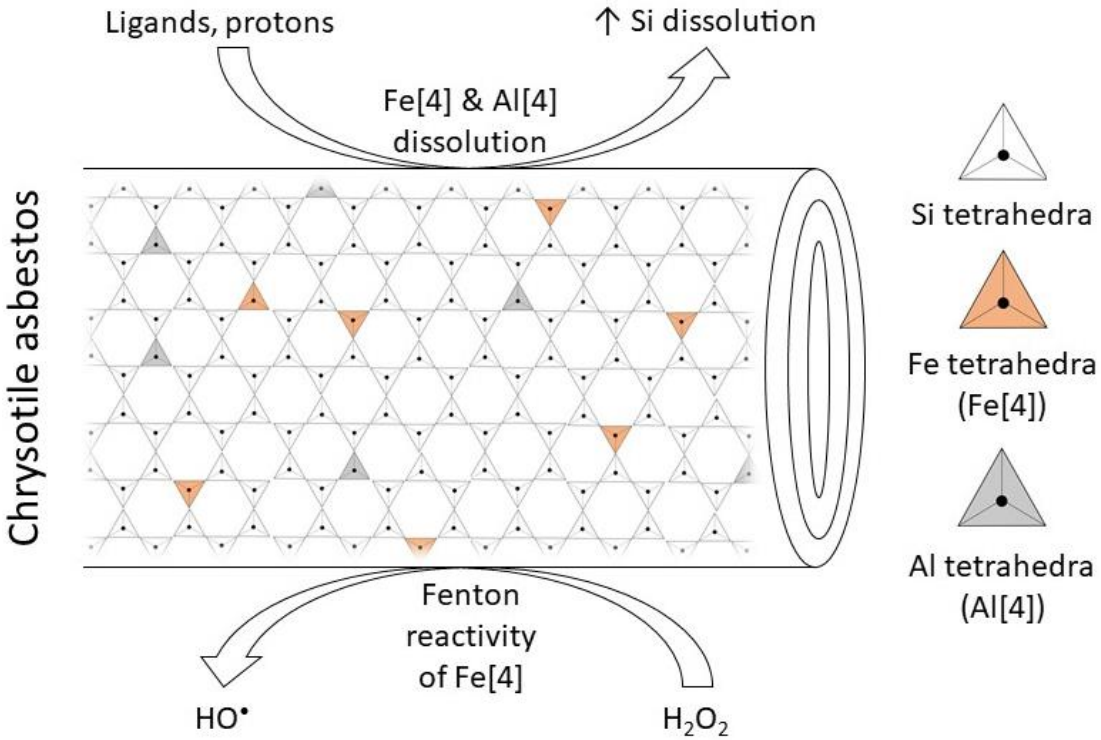

Introduction

Asbestos is a generic term for silicate minerals with a fibrous crystal habit used in technical applications, including five amphiboles and one serpentine mineral (chrysotile) [1, 25]. Due to its favorable properties in terms of heat resistance, non-combustibility and exceptional tensile strength [15], asbestos has been used, for example, in roofing, thermal and electrical insulation, cement pipes and sheets, flooring and coatings [59]. The use of asbestos has largely been banned in EU countries since the late 1980s because of adverse health effects upon fiber inhalation [21]. In northern America its use hasn't been banned yet [21] and in some Asian countries it even increases [23]. Asbestos can cause diseases like pulmonary fibrosis and asbestosis, carcinoma in the lung and mesothelioma in the pleura [25, 29, 33, 59]. The health risks of asbestos are primarily related to the persistence, fibrous morphology and redox reactivity of the fibers upon inhalation. The persistence results from slow chemical dissolution and low excretion rates of fibers due to their size and shape [33, 36, 123]. The redox reactivity of the fibers is largely related to iron at the mineral surface which can participate in Fenton-like redox reactions generating reactive oxygen species (especially the hydroxyl radical $HO^{\bullet}$) and reactive nitrogen species [33]. These radicals may damage DNA, proteins and lipids [32, 43, 44, 45]. Each year, more than 100,000 people die from asbestos-related diseases [27]. Furthermore asbestos is involved in the pathology of 8 - 15% of lung carcinomas and nearly all pleural mesotheliomas [29]. The WHO-IARC defines all asbestos minerals as carcinogenic to humans (group 1) [2].

Asbestos contamination in buildings and engineered environments has received most attention, but natural environments may also be contaminated either geogenically [75, 76, 77, 78, 79] or anthropogenically with loose asbestos (e.g. in the vicinity of former asbestos mines or processing sites) [59, 63, 64, 66, 67, 69] or asbestos containing waste [59, 68, 70, 71, 73]. Thereby, environmental exposure to asbestos increases the incidence of asbestos associated diseases in exposed residents and causes approximately 400 casualties each year worldwide [27]. Many countries struggle with environmental asbestos pollution: according to the US-EPA, the release of friable asbestos into air, water and soil was 6.2 million kg in 1999 (from 86 facilities) and 4.0 million kg in 2009 [2, 65]. In the vicinity of a former cement plant in the western Galilee (Israel), 72 public areas and an estimated 150,000 m^3 of soil were polluted with industrial asbestos waste, necessitating remediation at a total cost of 85 million dollars [74]. Near the city of Goor in the Netherlands, widespread pollution of friable and non-friable waste products from an asbestos cement plant was present, which was used to harden dirt tracks, yards, and driveways during 1935 – 1974 [70]. This was expected to cause several cases of excess malignant mesothelioma each year. A similar use of asbestos waste products and related increases of asbestos associated diseases was reported for Italy[68, 73] and in Poland[71].

In industrial applications, mainly chrysotile asbestos has been used (<95%) [13], and, as a consequence, this mineral is also most commonly encountered in soils contaminated with asbestos. For this reason, we focus on chrysotile asbestos in this study. Chrysotile [$Mg_3Si_2O_5(OH)_4$] consists of octahedral magnesium-hydroxide and tetrahedral silicon oxide layers which bundle together to a fiber with Mg-hydroxide layers forming the external surface [6, 7]. The dissolution of chrysotile has been extensively studied. Freshly suspended chrysotile has a positively charged surface below pH 8.9, but charge reversal occurs when the outer Mg layer dissolves, exposing the negatively charged Si layer [6]. Dissolution rates are inversely related to pH [94, 96, 97, 98, 99], e.g. from pH 7 to 10 the Mg dissolution rate was reported to scale with $[H^+]^{0.24}$ [97]. Over a broader pH range (pH 2 to 8), dissolution rates of Mg and Si were reported to scale exponentially with pH[96]. Organic chelators like oxalate, which are commonly observed in soils [124] and were found to be exuded by lichens and fungi in contact with asbestos [50, 107, 112], enhance Mg dissolution rates of asbestos [99] at acidic and mildly acidic pHs [97, 99]. In soil environments, rates of mineral weathering processes depend on specific soil chemical conditions. The presence of cement in asbestos cement waste locally buffers soil pH in the highly alkaline pH range and is also expected to affect weathering rates.

Because of the risk associated with Fe, its dissolution behavior from chrysotile deserves specific attention. Fe is substituted into chrysotile during petrogenesis (usually ≈ 2 - 3 wt%) [5]: Ferrous and ferric Fe are substituted in Mg octahedra (Fe^{2+}[6] and Fe^{3+}[6]), whereas only ferric Fe is substituted in Si tetrahedra [38, 125] (Fe^{3+}[4]), even though the ionic radius of Fe^{3+}[4] (49 pm) is approximately twice as large as the ionic radius of Si^{4+}[4] (26 pm) [40]. In the circumneutral pH range and in the presence of oxygen, Fe release from the chrysotile lattice is coupled to the precipitation of secondary Fe(hydr)oxide minerals with very low solubility. Therefore, net Fe mobilization only occurs in the presence of chelators like the bacterial siderophore desferrioxamine B (DFOB), citrate and synthetic chelators like EDTA [25, 48, 51]. Fe mobilization from fibers in vivo at pH 7.4 has been documented and was presumably caused by formation of soluble chelate complexes [126].

The surface Fe content of fibers can be correlated with the fibers' hydroxyl radical forming potential (HRFP) assuming that Fe at the surface can be repeatedly oxidized and reduced in a Haber Weiss (as demonstrated for amphibole asbestos) [25, 37, 47]:

$$Fe^{2+} + H_2O_2 \rightarrow Fe^{3+} + HO^{\bullet} + OH^- \quad (1a)$$

$$Fe^{3+} + H_2O_2 \rightarrow Fe^{2+} + HOO^{\bullet} + H^+ \quad (1b)$$

The HRFP decreases when Fe is removed from the fiber surface by ligand-promoted dissolution [50, 52], and when it precipitates as Fenton-inactive Fe(hydr)oxide minerals during the dissolution of the fibers[50]. Both processes have only been observed at selected pH values (especially at the physiologic pH 7.4) or in unbuffered solutions [50]. Al is the second most abundantly substituted metal in chrysotile (the Al_2O_3 content of UICC chrysotile is in between 0.5 and 1%) [5]. Alike Fe, Al is substituted into

octahedral and tetrahedral positions in chrysotile; octahedrally coordinated Al is usually more abundant than tetrahedrally coordinated Al (Al^{3+}[4]) [127]. The dissolution of Al from mineral surfaces is also enhanced by ligands such as oxalate and DFOB [128, 129].

Many reported chrysotile dissolution studies have provided valuable insight into asbestos geochemistry, but it is difficult to translate their findings to environmental systems such as soils. These studies include acid leaching studies [95, 100, 130], but also dissolution studies in which the pH was not [50, 98] or insufficiently buffered [99]. In some studies very high ligand concentrations were used [99] or pH-buffering was done with metal chelators [94] (e.g. TRIS (2-amino-2-(hydroxymethyl)propane-1,3-diol) or citrate) [48, 131] without taking into account the effect of these ligands on chrysotile dissolution. Overall, the effect of biogenic ligands on chrysotile dissolution rates and fiber reactivity have not been investigated in a comprehensive way over the environmentally and physiologically relevant pH range yet. Particularly the role of Fe and Al have only been marginally addressed in this context.

The aim of the present study was to explore how biogenic ligands affect the weathering rates and radical generation over an environmentally and physiologically relevant pH range, and to identify the role of Fe and Al in fiber dissolution kinetics and redox reactivity. Substitution of foreign metals into crystal lattices is known to increase dissolution rates of minerals, e.g. in case of Al substitution in Fe(hydr)oxide minerals [128, 132]. In this context we hypothesize that substituted metals in the Si layers like Fe and potentially Al may play an important role in long-term dissolution of chrysotile. After fast initial dissolution of the octahedral Mg hydroxide layer (except at alkaline pH), dissolution of Si is considered the rate determining step in overall dissolution [94, 95, 96, 97, 99]. We hypothesize that the complexation or hydrolysis of tetrahedrally substituted metals may labilize the Si layer surface, e.g. through formation of surface-defects, and thereby accelerate overall chrysotile dissolution rates. A similar labilization of Si-lattices by proton and ligand-promoted Al dissolution has been observed in feldspars [129]. Furthermore, we hypothesize that Fe[6] contributes little to the long-term Fenton activity on dissolving fiber surfaces due to rapid precipitation as secondary Fenton-inactive Fe minerals during fast Mg dissolution. Since Si dissolution is comparatively slow we hypothesize that Fe^{3+}[4] is the only relevant long-term Fenton-active radical forming Fe species in chrysotile. These hypotheses were tested in batch dissolution experiments with subsequent analysis of metal concentrations in solution (ICP-OES), HRFP (EPR) and Fe speciation in the fibers (^{57}Fe Mössbauer analysis).

Table 1.) *Bulk analysis of pristine and weathered Shijiazhuang chrysotile asbestos. a.) Mean bulk Mg, Si, Fe and Al content of Shijiazhuang chrysotile asbestos determined by fusion digestion (n = 15) and neutron activation analysis (NAA, n = 2). Values in brackets indicate standard deviations. b.) Results from Mössbauer analysis of pristine fibers and fibers weathered for 2 weeks at pH 3.0, either in a 1 mmol L^{-1} DFOB or a blank treatment. S1 to S3 correspond to the sub-spectra assigned to chrysotile (Figure 4), values in square brackets indicate the Fe coordination. S4 and S5 correspond to the magnetite sub-spectra (Figure 4); defining parameters for these spectra are presented in SI-Table 6. A ferrihydrite sub-spectrum (S6; based on data from Murad and Schwertmann, 1980) [156] was added for interpreting the spectrum of the blank treatment ("+ FH" compared to "original species" without the addition of S6). eQVzz/4 refers to the quadrupole splitting, CS to the center shift relative to ^{57}Co**Rh**, and Γ to the line widths. FH indicates ferrihydrite.*

a.) Elemental contents of pristine chrysotile asbestos

	Mg	**Si**	**Fe**	**Al**
	g kg^{-1}	g kg^{-1}	g kg^{-1}	g kg^{-1}
Fusion digestion	249 (6.8)	188 (3.3)	19.0 (1.4)	8.0 (0.5)
NAA			21.5 (0.4)	

b.) Mössbauer analysis of pristine and weathered fibers

		eQVzz/4	**CS**	**Γ/2**	**Fraction in chrysotile**	
Pristine		mm s^{-1}	mm s^{-1}	mm s^{-1}	%	
S1	Fe^{2+} [6]	1.29	1.05	0.22	38	
S2	Fe^{3+} [6]	0.33	0.19	0.38	55	
S3	Fe^{3+} [4]	0.22	0.09	0.3	7	
			Total bulk-Fe in chrysotile:		68	
DFOB altered						
S1	Fe^{2+} [6]	1.29	1.05	0.22	38	
S2	Fe^{3+} [6]	0.33	0.19	0.38	55	
S3	Fe^{3+} [4]	0.22	0.09	0.3	7	
			Total bulk-Fe in chrysotile:		68	
Blank altered					*Original species*	*+ FH*
S1	Fe^{2+} [6]	1.29	1.05	0.22	29	30
S2	Fe^{3+} [6]	0.33	0.19	0.38	65	56
S3	Fe^{3+} [4]	0.22	0.09	0.3	6	5
S6	FH	0.355	0.23	0.228	-	8
			Total bulk-Fe in chrysotile:		73	67

Results and discussion

Magnetite and chlorite contamination in *Shijiazhuang chrysotile asbestos*

This study addresses the role of Fe in the dissolution and redox reactivity of chrysotile. Therefore, Fe from impurities in the chrysotile asbestos could potentially compromise the interpretations of the results from the experiments. For this reason we first assessed these Fe containing impurities. Magnetite (Fe_3O_4) is a common impurity in chrysotile asbestos [38]; for example, approximately 60% of the bulk Fe in Canadian UICC-chrysotile is in magnetite [39]. After selective removal of visible magnetite particles, analysis of the Mössbauer spectra of pristine Shijiazhuang chrysotile fibers revealed that still 32% of bulk Fe was in magnetite (Table 1). The potential contribution of magnetite to radical generation and Fe dissolution has been assessed previously. Fubini and Mollo (1995) [35] measured free radical generation by 45 mg of magnetite (135 arbitrary units (a.u.)) and chrysotile (223 a.u.) with the same specific surface area (27 $m^2\ g^{-1}$). Furthermore, Fubini et al. (1995) [37] reported that a 100 mmol L^{-1} DFOB solution buffered at pH 7.4 mobilized 50 µmol L^{-1} Fe from both 1 g L^{-1} chrysotile (27 $m^2\ g^{-1}$) and 1 g L^{-1} magnetite (21 $m^2\ g^{-1}$) over three days of incubation. Because, normalized to mass, radical formation by and Fe dissolution from magnetite and chrysotile are similar, but the magnetite content of the Shijiazhuang chrysotile asbestos is small (1.5 ± 0.2%) compared to the chrysotile content (86.4 ± 4.6%) (XRD-Rietveld content), the contribution of magnetite to the HRFP and to Fe dissolution were assumed negligible. This assumption was tested in preliminary experiments. The EPR DMPO/$HO^{\bullet}$ signal of ≈ 1 mg of extracted magnetite (≈six times as much as the content expected in the chrysotile samples analyzed by EPR) was only slightly above the background level and mobilized Fe concentrations from ≈2 mg of extracted magnetite in a 100 ml 1 mmol L^{-1} DFOB solution (corresponding with the magnetite suspension density in the chrysotile dissolution experiments) buffered at pH 3.0 for up to 336 h was below the limit of quantification (LOQ). However, magnetite contamination will affect total bulk Fe measurements by fusion digestions and NAAs.

Shijiazhuang chrysotile asbestos further contained larger grains of chlorite, an Al- and Fe-bearing mineral ($(Mg,Fe)_5Al_2Si_3O_{10}(OH)_8$). The Rietveld-fraction of chlorite (2.4 ± 2.9%) corresponded to 2.3 ± 2.8 g kg^{-1} Al. Since 8 g kg^{-1} of Al were detected by fusion digestions in chrysotile, over 25% were possibly located in chlorite. Furthermore, Fe in chlorite may interfere with dissolution experiments and Mössbauer analyses. The worst-case amount of Fe possibly located in chlorite, assuming that all chlorite in the fibers was chamosite (the Fe endmember of the chlorite group), was calculated to be 9.4 ± 11.3 g kg^{-1}. However, Albino (1995) [19] found a similar Fe content in chlorites as in associated serpentinite minerals. Considering the low chlorite content in our sample, this would point towards a minor contribution of chlorite-associated Fe to the total Fe content. However, the Fe partitioning between chlorite and chrysotile may be influenced by the specific conditions during serpentinization.

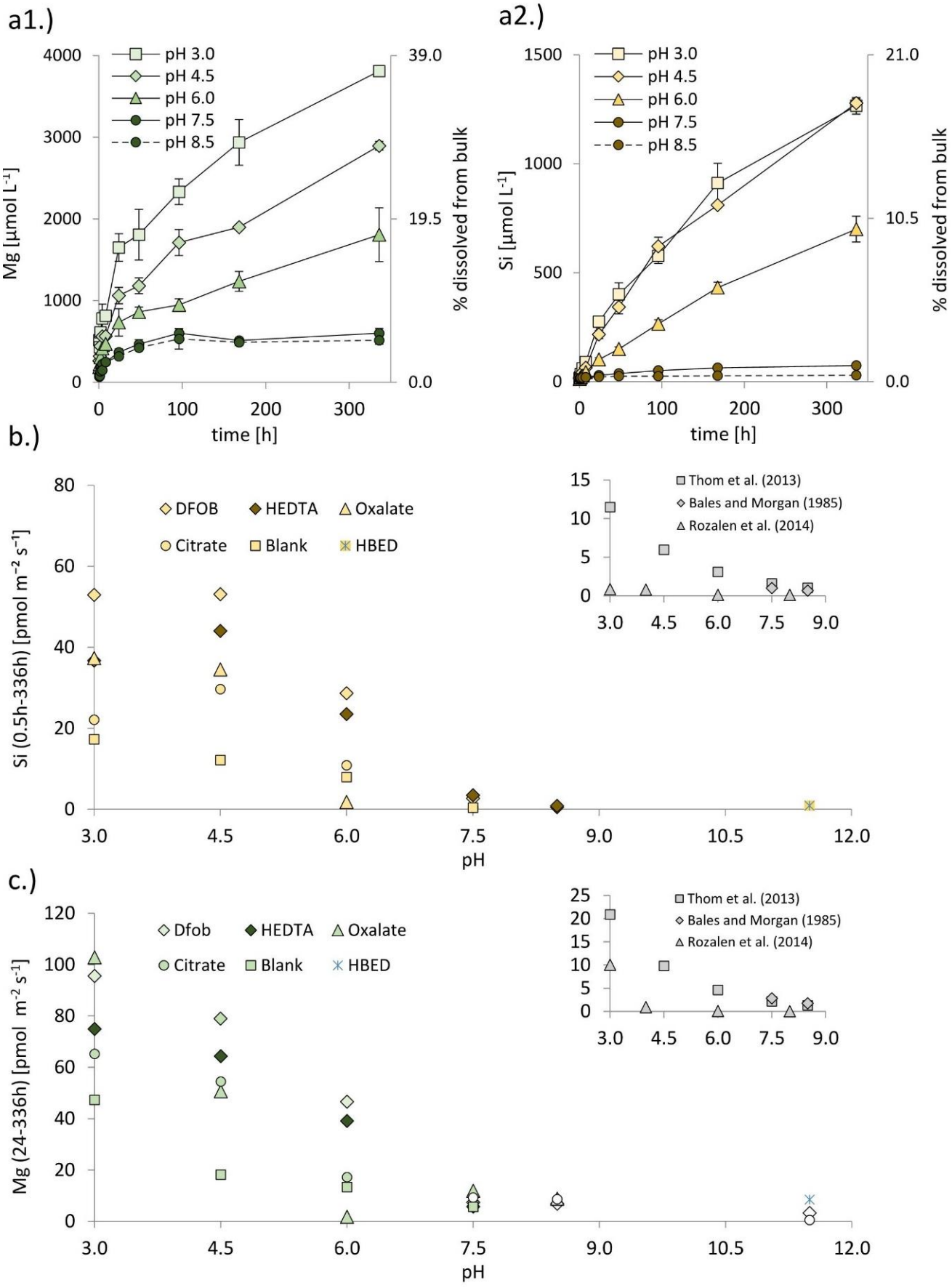
a1.)
pH 3.0
pH 4.5
pH 6.0
pH 7.5
pH 8.5
Mg [µmol L-1]
% dissolved from bulk
time [h]
a2.)
Si [µmol L-1]
b.)
DFOB
HEDTA
Oxalate
Citrate
Blank
HBED
Si (0.5h-336h) [pmol m-2 s-1]
pH
Thom et al. (2013)
Bales and Morgan (1985)
Rozalen et al. (2014)
c.)
Dfob
Mg (24-336h) [pmol m-2 s-1]

↑ ***Figure 1:*** *Mg and Si dissolution from 1 g L^{-1} chrysotile asbestos in blank and 1 mmol L^{-1} ligand treatments buffered at pH 3.0, 4.5, 6.0, 7.5, 8.5 and 11.5. Panel a1.) Mobilized Mg concentrations as a function of time in the presence of 1 mmol L^{-1} DFOB. Slopes of the first stage Mg dissolution (0.5 – 8h) can be well distinguished from slopes of the second stage (24 - 336h); Panel a2.) Mobilized Si concentrations from fibers as a function of time in the presence of 1 mmol L^{-1} DFOB. No dissolution stages were distinguished. In both panel a1 and a2, the percentage of total bulk dissolution is indicated on the secondary y-axis. Error bars indicate standard deviations (n = 2). Mobilized Mg and Si concentrations as a function time for all other treatments can be found in SI-Figure 2; Panel b.) Si dissolution rates (regression from 0.5 to 336 h); Panel c.) Mg dissolution rates calculated for the second stage (regression from 24 to 336 h). Symbols without color filling indicate rates for treatments in which the outermost Mg layer had not completely dissolved after 24 h. Rates of treatments with $R^2 < 0.5$ are not reported. Data included in panel b and c is presented in SI-Table 1. Dissolution rates for blank treatments reported in Bales and Morgan (1985)[19a], Rozalen et al (2014)[19d] and Thom et al. (2013)[19e] have been included for comparison in panel b and c. Since the pH in Rozalen et al (2014) drifted during incubation, the calculated rates were plotted on the initial pH value of the incubation solutions.*

Net dissolution rates of Si and Mg

Consistent with previous observations [94, 97, 99], net Mg dissolution rates changed systematically over time with a first stage of rapid dissolution (0.5 - 8 h), transitioning to a second stage (24 - 336 h) with slower dissolution (Figure 1a1). The fast Mg dissolution in the first stage (SI-Figure 1) was observed at all pH values except for pH 11.5 (see all rates in SI-Table 1).

The Si mobilization rates decreased much less with incubation time. Hence, only little Si was mobilized during the short first stage of Mg dissolution (Figure 1a2), which was dominated by Mg dissolution from the outermost layer during this stage. Si dissolution rates calculated from blank treatments were well comparable to previously published values [96, 97] (Figure 1b). However, calculated rates from this study, from Bales and Morgan (1985) [97] and from Thom et al. (2013) [96] were considerably higher than those reported by Rozalen et al. (2014) [99]. This may be explained by a pH drift towards more alkaline conditions in some incubations in the latter study. Overall, net Si dissolution rates calculated in this study increased with decreasing pH. In the blank and the oxalate treatment, this increase continued down to pH 3.0. In all other treatments, rates only increased down to pH 4.5. Upon further decreasing the pH to 3.0, the rates remained approximately constant (DFOB) or even declined (citrate and HEDTA (hydroxyethylenediaminetriacetic-acid)).

Net Si dissolution rates were generally higher in the presence of ligands than in the corresponding blank treatment over the entire pH-range (Figure 1b). The difference was largest for treatments

Table 2: *Mobilized Mg, Fe and Si concentrations after 336 h of incubation at pH 3, 7.5 and 8.5. Mobilized Mg concentrations ranged from ≈400-850 µmol L^{-1}, which is within a factor 1-2 compared to the calculated mobilized Mg concentration for complete dissolution of the outermost Mg layer (406 µmol L^{-1}). Dissolution of Fe from the outer Mg layer corresponded with Fe concentrations of ≈30 µmol L^{-1}. This concentration was mobilized after 336 h by DFOB and HEDTA at pH 7.5 and 8.5 and 0.5 h at pH 3. After removal of the first Mg layer at pH 7.5 and 8.5, Si mobilization was elevated due to Fe^{3+}[4] and potentially Al^{3+}[4] complexation by DFOB and HEDTA, which caused a labilization of the Si layer and facilitated Si dissolution. Values in round brackets indicate standard deviations (n = 2).*

	pH 3.0; 0.5 h µmol L^{-1}	**pH 7.5; 336 h** µmol L^{-1}	**pH 8.5; 336 h** µmol L^{-1}
First layer Mg:			
Blank	552 (144)	585 (105)	448 (22)
DFOB	516 (48)	601 (59)	516 (50)
Oxalate	896 (103)	836 (330)	425 (14)
Citrate	453 (5)	563 (22)	386 (71)
HEDTA	468 (43)	638 (33)	578 (79)
First layer Fe:			
Blank	15.5 (2.4)	0.9 (0.0)	0.1 (0.1)
DFOB	26.1 (1.7)	29.3 (0.2)	30.5 (3.2)
Oxalate	36.8 (3.9)	0.1 (0.1)	0.1 (0.0)
Citrate	16.4 (0.4)	9.3 (0.5)	4.4 (0.6)
HEDTA	27.4 (2.7)	32.4 (0.5)	33.3 (4.2)
Si dissolution:			
Blank	11.6 (0.7)	15.4 (0.7)	8.5 (0.2)
DFOB	16.1 (0.5)	73.9 (7.7)	29.5 (1.8)
Oxalate	20.7 (1.9)	12.1 (1.3)	11.5 (0.7)
Citrate	15.4 (0.1)	22.7 (0.6)	21.6 (0.2)
HEDTA	23.0 (0.0)	101 (3.1)	49.2 (3.9)

involving chelating ligands with a high affinity for Fe and Al (DFOB, HEDTA and HBED (N,N'-di(2-hydroxybenzyl)ethylenediamine-N,N'-diacetic-acid)), even though Si in general forms only weak complexes with low stability constants with metal-chelates [133]. From pH 3.0 - 6.0, net Si dissolution rates were highest in DFOB treatments and from pH 7.5 - 8.5, rates were highest in the HEDTA treatments. Mobilized Si concentrations after 336 h in the HEDTA and DFOB-treatments at pH 7.5 and 8.5 were evidently higher than in all other treatments (Table 2). At pH 11.5, Si was only mobilized in the HBED treatment (Figure 1b; SI-Table 2).

During the slow second stage of Mg dissolution, calculated net Mg dissolution rates were considerably lower than corresponding rates from the first stage (Figure 1c). Calculated rates from blank treatments in this stage were well comparable to previously published values [96, 97]. However, the rates calculated in Rozalen et al. (2014) [99] at pH 4.0 were considerably lower. We observed that net Mg

dissolution rates during the second stage generally decreased with increasing pH from acidic (3.0) to neutral (7.5) in all treatments (Figure 1c). In the oxalate treatments, the net Mg dissolution rate strongly decreased from pH 3 to pH 6, and then mildly increased again to pH 7.5. Within the pH range of 3.0 to 7.5, Mg dissolution rates were consistently higher in the presence of hexadentate chelating ligands like DFOB and HEDTA than in the blank treatment. In the presence of oxalate, Mg dissolution rate by oxalate increased at low pH, but were inhibited at pH ≥ 6.0. Equilibrium modelling indicated under-saturation of Mg oxalate precipitates under all experimental conditions suggesting that net-dissolution was not affected by precipitation of Mg-oxalate. At pH 7.5 and 8.5 absolute and relative differences in net Mg dissolution rates were small. Under very alkaline conditions (pH 11.5), no Mg was mobilized from the outermost layer, except in the presence of HEDTA, citrate and HBED (Figure 1c; SI-Table 2). Brucite solubility is very low under such conditions [97, 99, 101]; it was predicted to be oversaturated at concentrations mobilized by HBED (Table 3). In fact, equilibrium modelling suggests that the Mg complexes of ligands like HEDTA, citrate and HBED dominate Mg solution speciation at such high pH values (data not shown).

Relationship between net dissolution rates and mineral structure

Weathering of chrysotile is commonly thought of as a layer-by-layer dissolution of alternating Mg- and Si sheets [94, 97]. These sheets are bended onto themselves to form needles composed of Mg- and Si layer spirals with the octahedral Mg layer on the convex outer side [134]. Therefore, the first layer dissolving from pristine fibers is the outermost Mg hydroxide layer. We interpret the rapid first stage of Mg dissolution to correspond to the fast dissolution of the outer octahedral Mg layer until it is completely removed. Because the first stage Mg dissolution was fast compared to potential residence times of chrysotile in the environment or in vivo, even at circumneutral pH, its duration can be regarded as negligible. The second stage is characterized by slow, rate-determining dissolution of the tetrahedral Si layer, which then constitutes the mineral surface. The underlying Mg layer can only dissolve as fast as the removal of the Si layer allows. This is consistent with our observation of more constant Si dissolution rates over time with no distinguishable stages (Figure 1a2). Equilibrium modelling (Table 3) suggests that 1 g L^{-1} chrysotile remained under-saturated in all treatments at pH 3.0 - 8.5 throughout the 336 h incubation. This is consistent with literature on even higher solid to solution (SSR) values [97, 99].

The amount of Mg in the first layer can be estimated from the Mg surface site density of chrysotile (2 nmol cm^{-2}) [97] and the measured specific surface area of pristine fibers (20.3 m^2 g^{-1}) to be 406 µmol g^{-1}. However, additional Mg may have dissolved from brucite (4.5 ± 2.1% or 771 ± 360 µmol g^{-1} by XRD-Rietveld refinement). Due to this uncertainty, it can only be noted that dissolved Mg concentrations

Table 3: *Saturation indices (log(IAP/K_{sol})) for chrysotile asbestos and secondary minerals that might form during the fibers' dissolution. Saturation indices were calculated using PHREEQC and the SIT database for pH 3-11.5. Mg, Si, Fe and Al concentrations mobilized after 336 h of incubation in blank ("BL") or 1 mmol L^{-1} DFOB ("DFOB") treatments at pH 3.0-8.5 and 1 mmol L^{-1} HBED treatments at pH 11.5 were used as input data. The pe was set to equilibrium with air, and temperature at 20°C. "Am. ferr." indicates amorphous ferrihydrite, "Am. SiO_2" amorphous SiO_2.*

Phase	**Formula**	**pH 3.0**	**pH 4.5**	**pH 6.0**	**pH 7.5**	**pH 8.5**	**pH 11.5**	**pH 11.5**
							+ HBED	- HBED
Chrysotile (Bl)	$Mg_3Si_2O_5(OH)_4$	-32.5	-24.5	-16.2	-10.1	-4.9	-5.4	8.9
Brucite (Bl)	$Mg(OH)_2$	-14.7	-12.0	-9.1	-6.3	-4.3	-3.2	1.5
Am. SiO_2 (DFOB)	SiO_2	-0.1	-0.1	-0.4	-1.4	-1.9	-4.3	-4.3
Am. ferr. (BL)	$Fe(OH)_3$	-0.1	1.6					
Am. ferr (DFOB)	$Fe(OH)_3$	-8.1	-8.2	-8.3	-8.6	-8.2	-6.6	3.3
Diaspore (BL)	AlO(OH)	-4.5	0.6	2.9	2.5	1.6	-0.7	-0.7

after the fast initial phase of dissolution were approximately within a factor of 2 compared to the calculated Mg surface layer in all treatments (Figure 1a1; SI-Figure 2; SI-Table 2). Since in blank treatments hardly any Si dissolved from the fibers up to the first sampling time at pH 3 and during the whole incubation time at pH 7.5 - 8.5 (SI-Table 2), it may be assumed that only the outermost Mg layer of fibers had dissolved (Table 2).

After dissolution of this outermost Mg layer, the first Si layer covers the surface and its dissolution becomes rate-limiting. At pH 3.0 - 6.0 however, relatively quick dissolution of the Si layer enabled faster dissolution of Mg from deeper layers (Figure 1a). Comparison of the net dissolution rates of Si and Mg during the second stage demonstrates that chrysotile dissolved congruently (Si : Mg = 2 : 3) at pH 4.5 and 6.0 in all treatments (except in the oxalate treatment at pH 6.0 and citrate treatment at pH 4.5), but incongruently in most treatments at pH 3.0 and pH 7.5 & 8.5 (Figure 1, SI-Table 1). Incongruent dissolution of chrysotile was previously observed in the acidic pH range (below pH 3.0) by Rozalen et al. (2014) [99] and in the neutral to alkaline pH range by Bales and Morgan (1985) [97]. To examine whether incongruent dissolution at pH 3.0 was caused by precipitation of Si-phases, an additional incubation experiment was performed at a lower SSR of 0.25 g L^{-1} including blank and 1 mmol L^{-1} DFOB, oxalate and citrate-treatments. Even though dissolution of chrysotile in the blank treatments was closer to congruency than at a higher SSR, rates in the ligand-treatments were still far away from it (SI-Table 3). Furthermore, already during the first incubation day at the regular SSR of 1 g L^{-1}, the dissolved Si concentrations (below 200 µmol L^{-1}) were similar or even lower at pH 3.0 compared to pH 4.5. Both observations suggest that precipitation of secondary Si phases is presumably not the cause for

incongruent dissolution of chrysotile at pH 3.0. Furthermore, equilibrium modelling predicts (slightly) negative saturation indices for amorphous SiO_2 at pH 3.0 - 11.5 for Si concentrations mobilized after 336 h by 1 mmol L^{-1} DFOB or HBED (Table 3), the treatment with the largest mobilized Si concentrations, which supports this argument.

Dissolution of substituted trivalent metals (Fe and Al) and labilization of the Si layer

In Figure 2, the Fe concentration mobilized from fibers at an acidic (3.0), mildly acidic (6.0), mildly alkaline (8.5) and highly alkaline (11.5) pH are presented as a function of time. Fe concentrations mobilized at pH 4.5 and 7.5 are listed in SI-Table 4. In Figure 3, Al mobilization from fibers is shown at pH 3.0, 4.5, 6.0 and 7.5 (Al-mobilization was negligible at alkaline pH (SI-Table 3)). High mobilized Fe and Al concentrations are well correlated with high Mg and Si dissolution rates.

At pH 3.0 (Figure 2a), transiently mobilized Fe concentrations in the blank treatment decreased after an initial mobilization from 16 µmol L^{-1} (0.5 h) to 8 µmol L^{-1} (336 h), presumably because of precipitation of secondary Fe minerals on the fiber surface, as e.g. observed by Turci et al. (2007) [50]. The residual Fe concentration of 8 µmol L^{-1} after 336 h of incubation corresponds with the Fe^{3+} solution concentrations in equilibrium with ferrihydrite at pH 3.0 [135]. Also our equilibrium model suggests potential precipitation of amorphous ferrihydrite, with a saturation index close to zero (Table 3). At all pH values > 3.0, the equilibrium models suggest that the mobilized Fe concentrations exclusively resulted from formation of soluble Fe-ligand complexes (data not shown). Unlike the blank treatment, mobilized Fe concentrations at pH 3.0 increased with increasing incubation time in the presence of ligands. By the end of the experiment (336 h), citrate, DFOB, oxalate and HEDTA had mobilized 41, 86, 80 and 74 µmol L^{-1} Fe, respectively. At pH 4.5 (SI-Table 4), only sub-micromolar Fe concentrations were mobilized in the blank-treatment. In all other treatments Fe concentrations similarly increased with incubation time, but to a lesser extent than at pH 3.0: DFOB and HEDTA again mobilized the largest Fe concentrations. At pH 6.0 (Figure 2b), Fe concentrations in the blank-treatment were below the LOQ. In the oxalate treatment they decreased from 12 (0.5 h) to 3 µmol L^{-1} (336 h), implying a depletion of Fe from solution. In the DFOB and HEDTA treatments, mobilized Fe concentrations gradually increased. In the citrate-treatment the Fe concentration reached a plateau of around 15 µmol L^{-1} after 4h. Mobilized Fe concentrations at pH 7.5 (SI-Table 4) and 8.5 (Figure 1c) were below the LOQ in the blank- and oxalate treatments. In the citrate treatment also at pH 7.5 and 8.5 an Fe mobilization plateau was observed, yet after 48 h and at lower concentration levels. Mobilized Fe concentrations by DFOB and HEDTA increased until 96 h and remained at a plateau of approximately ≈30 µmol L^{-1} until 336 h at both pH values. Presumably, Fe mobilization by these ligands was limited by the slow dissolution kinetics of the first Si layer at pH 7.5 and 8.5, preventing them from dissolving Fe from deeper layers.

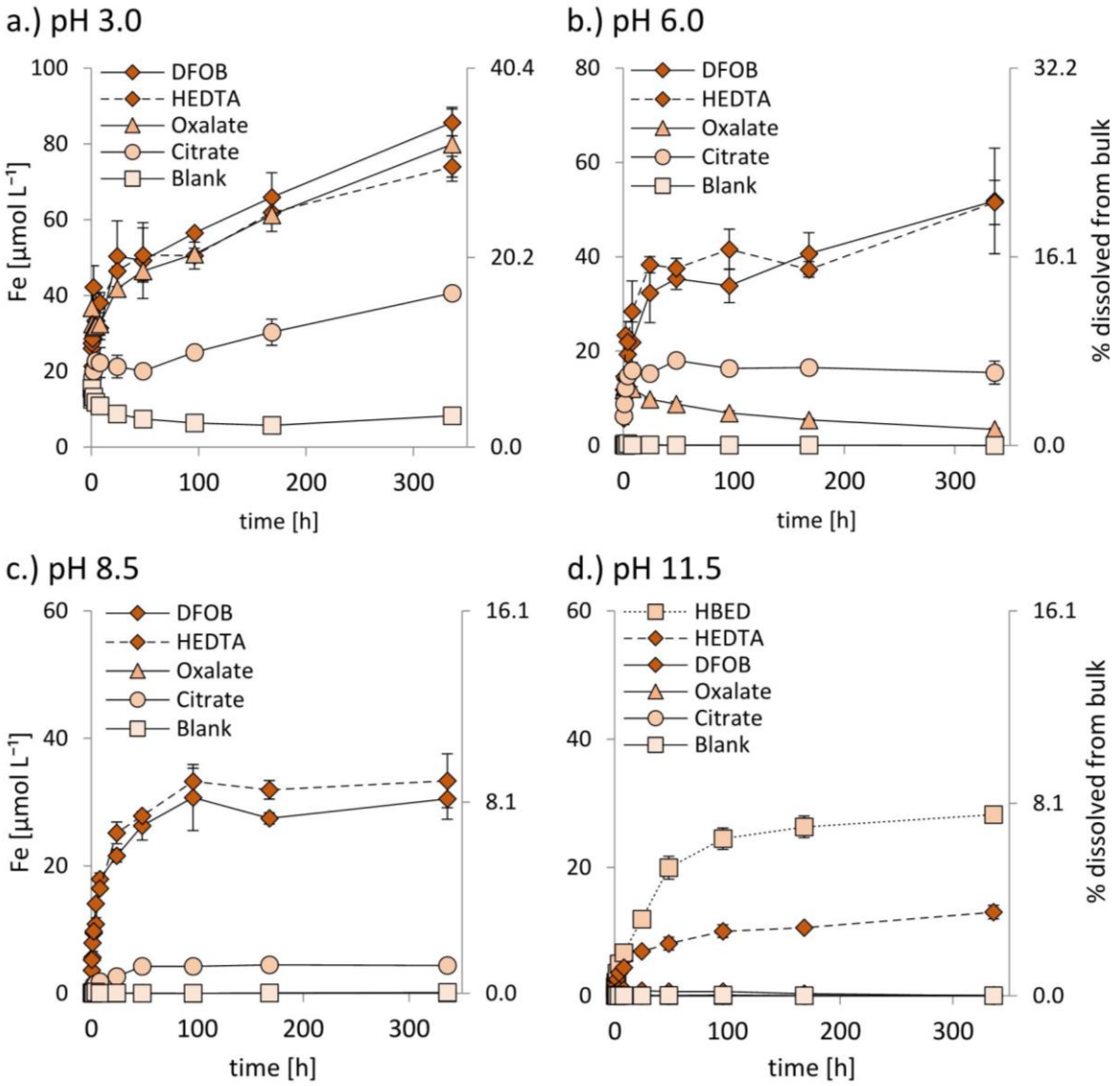

Figure 2: *Mobilized Fe concentrations from 1 g L^{-1} chrysotile material in blank and 1 mmol L^{-1} DFOB, oxalate, citrate or HEDTA solutions, buffered at pH 3.0; 6.0; 8.5 and 11.5, and in a 1 mmol L^{-1} HBED solution buffered at pH 11.5. Error bars indicate standard deviations (n = 2). On the secondary y-axis, Fe mobilization is expressed as a percentage of the initial chrysotile bulk Fe content (the mean of the bulk Fe content determined in fusion digestions and the NAA analysis minus the Fe in magnetite). Data to this figure is presented in SI-Table 4.*

A similar amount of Fe was mobilized at pH 3 by DFOB, HEDTA and oxalate within the first 0.5 h, before Si dissolution became substantial (Table 2). We conclude that the 30 µmol L^{-1} Fe mobilized by DFOB and HEDTA mainly represents the Fe content of the outermost Mg layer (Table 2) that was mobilized during the first dissolution stage, with a contribution from the underlying Si layer. This is supported by the relatively high Si concentrations mobilized in the HEDTA and DFOB treatments at pH 7.5 and 8.5 after 336 h (Table 2) compared to the corresponding blank and oxalate treatments. HEDTA and DFOB

have a low affinity for Si, but presumably mobilized Fe^{3+}[4] from the first exposed Si layer leading to labilization of the Si layer structure by creating crystal defects and corresponding high energy Si sites. These labile Si sites consequently enhanced Si dissolution rates. The accelerating effect of defect site generation by removal of Fe from the Si layer on Si layer dissolution may also operate in the absence of ligands. In this pH range it is more difficult to observe hydrolytic Fe removal from the Si layer, because Fe may re-precipitate at the mineral surface precluding observations of net-mobilization from the silica sheet. However, evidence for changes in speciation of Fe in the solid phase, and therefore support for this mechanism, was gained from measurements of HRFP (vide infra). At any rate, it is striking that we observed increasing net Si dissolution rates with decreasing pH from 6.0 to 3.0, which could be related to increasing Fe release from the sheet. However, Saldi et al. (2007) [136] also observed increasing dissolution rates of talc (a magnesium silicate) with decreasing pH in the acidic pH range. They attributed this to a labilization of partially liberated silica tetrahedra formed at talc edge surfaces from the exchange of Mg^{2+} for two protons. Therefore, the pH dependence of net Si dissolution rates cannot unambiguously be attributed to the effect of Fe mobilization from the Si sheet.
A mass balance analysis for the treatments at pH 3.0 after 336 h demonstrates that addition of 1.0 mmol L^{-1} chelating ligands can result in an increase in mobilized Mg concentration relative to the blank treatment (2.0 mmol L^{-1}) that exceeds the added ligand concentration. This was the case for the DFOB treatment (3.8 mmol L^{-1}) and the oxalate treatment (4.2 mmol L^{-1}) (SI-Table 2). Because Si dissolution is rate limiting for overall dissolution in the low pH range, the enhanced Mg dissolution resulted from enhanced Si dissolution, due to labilization of the Si layer by ligand-controlled Fe^{3+}[4] dissolution.
At pH 11.5 (Figure 2d), mobilized Fe-concentrations in most treatments were below the LOQ, however, in the HEDTA- and HBED-treatments they increased from ≈1 µmol L^{-1} (0.5 h) to 13 and 28 µmol L^{-1} (336 h), respectively. HBED mobilized an amount of Fe corresponding to the estimated Fe content (≈30 µmol L^{-1}) of the first Mg and Si layer.
Mobilized Al concentrations at pH 3.0 (Figure 3a) in the blank- and citrate treatments increased similarly throughout incubation from 5 µmol L^{-1} after 0.5 h to 18 µmol L^{-1} after 336 h. In the presence of other ligands, mobilized Al concentrations were higher. The highest mobilized Al concentrations were measured in DFOB and oxalate treatments after 336 h. At pH 4.5 (Figure 3b), Al concentrations in the blank treatment increased until 48 h and subsequently decreased, suggesting precipitation of an Al containing phase. Results from equilibrium modelling suggest that secondary Al-containing precipitates like diaspore (α-AlO(OH)) may form in the blank treatments from pH 4.5 upward (Table 3). In the presence of ligands, however, measured Al concentrations at pH 4.5 - 7.5 increased over time (except for oxalate at pH 7.5), but to a lesser extent than observed at pH 3.0 (Figure 3b-d). Above pH 7.5, a clear increase in mobilized Al concentrations was only observed for DFOB at pH 8.5 and for HBED at pH 11.5 (SI-Table 4).

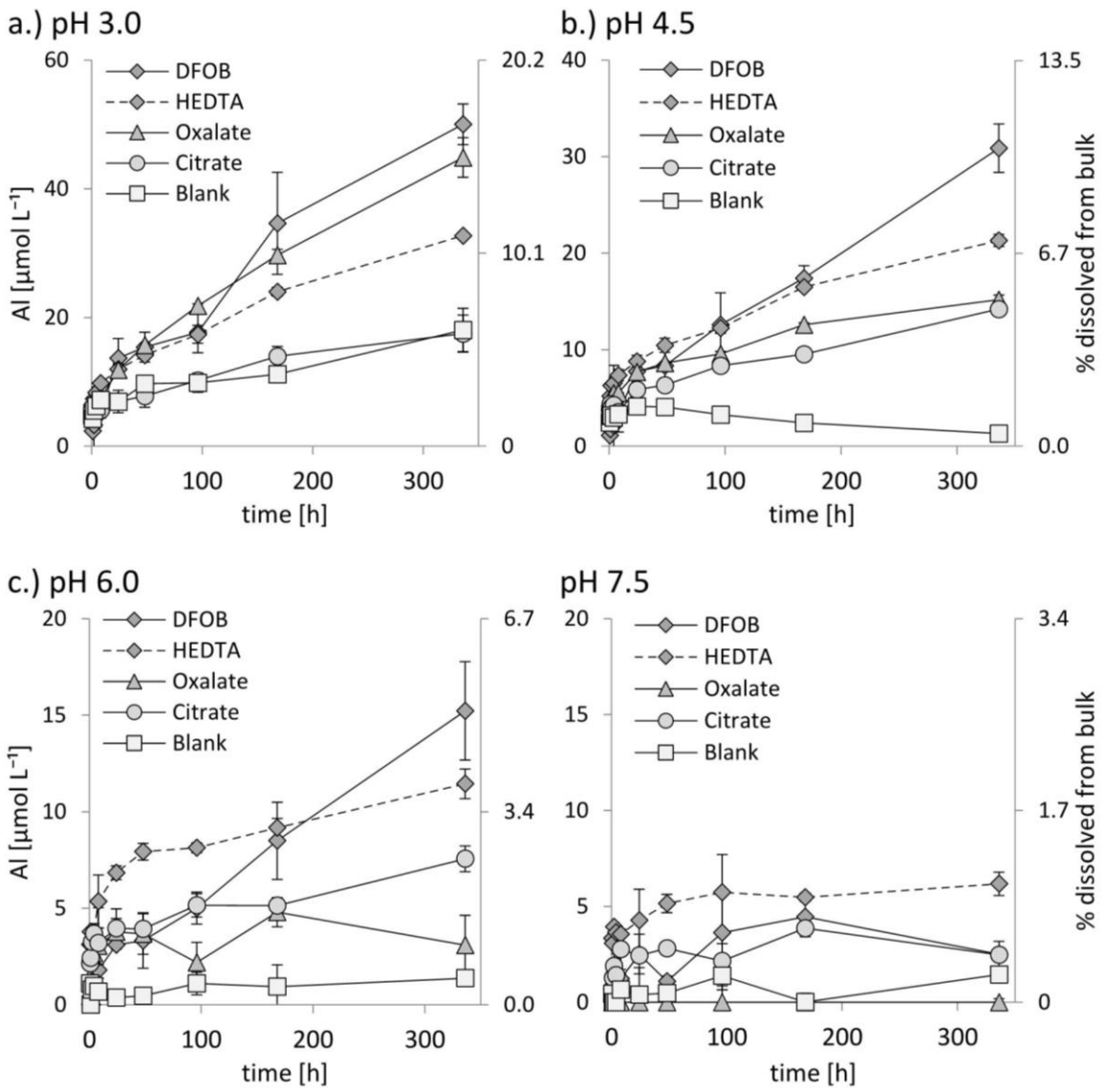

Figure 3: *Mobilized Al concentrations from 1 g L^{-1} chrysotile material in blank and 1 mmol L^{-1} DFOB, oxalate, citrate or HEDTA solutions buffered at pH 3.0, 4.5, 6.0 and 7.5. Error bars indicate standard deviations (n = 2). On the secondary y-axis, Al mobilization is expressed as a percentage of the initial chrysotile bulk Al content. Apart from chrysotile, also amounts of Al are located in chlorite impurities (discussion in the main text). Data included in this figure is presented in SI-Table 5.*

Since Al can be substituted into the Si layers of chrysotile, ligand- and proton-promoted dissolution of Al^{3+}[4] may, similarly as the dissolution of Fe^{3+}[4], contribute to Si labilization in chrysotile. Enhanced Si dissolution rates by the removal of Al^{3+}[4] have been reported for feldspars [129]. Hence, proton-promoted dissolution of Al^{3+}[4] may have increased Si dissolution from chrysotile at low pH values (Figure 3a and 3b), whereas ligand-promoted dissolution of Al^{3+}[4] may have increased Si dissolution over a wider pH range (Figure 3).

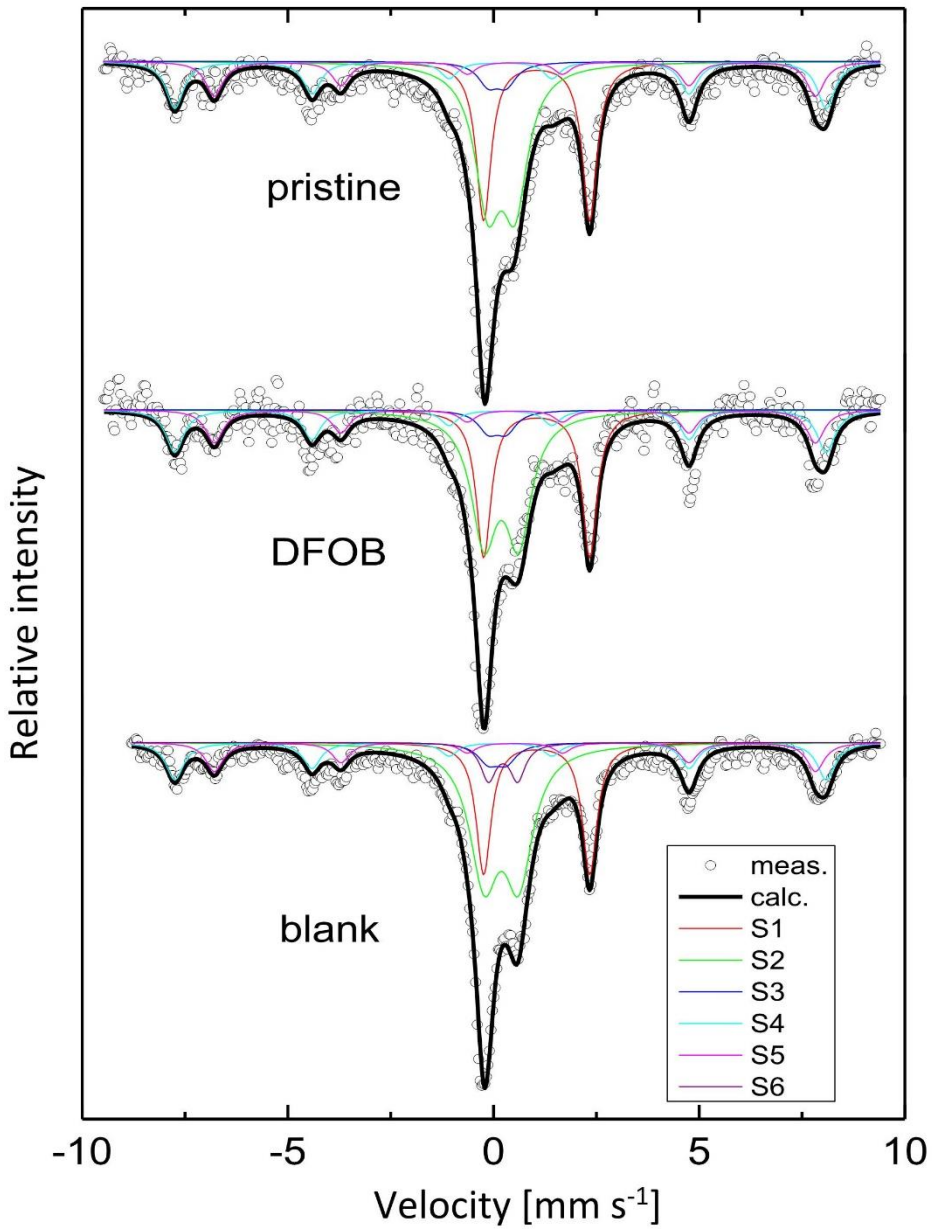

Figure 4: *Mössbauer spectra of pristine fibers and fibers weathered for 336 h at pH 3.0 in a blank and 1 mmol L^{-1} DFOB solution. S1-S3 are sub-spectra of chrysotile: S1 represents Fe^{II}[6], S2 and S3 represent Fe^{3+}[6] and Fe^{3+}[4], respectively. The S4 and S5 sub-spectra represent Fe in magnetite. In the spectrum of fibers weathered in the blank-treatment, a ferrihydrite sub-spectrum (S6) was added. Center shift data of S1-3 and S6 are presented in Table 1, for S4-5 they are listed in SI-Table 6.*

Analysis of Mössbauer spectra of weathered fibers

Assuming that hyperfine parameters of chrysotile do not change by weathering, parameters for quadrupole splitting, center shift and line width were obtained, which fit well to those reported in literature [38] (Figure 4/Table 1). The relative abundancies of Fe^{3+}[6], Fe^{3+}[4] and Fe^{2+}[6] and the fraction of Fe in chrysotile fibers after the DFOB treatment corresponded with pristine fibers. This suggests that during weathering by DFOB, no secondary Fe-bearing phases were created. This was not

the case for fibers weathered in the blank treatment: the relative abundancies of the three crystallographic Fe sites differed from those in the pristine fibers (Table 1). The increase in Fe^{3+}[6] at the expense of Fe^{2+}[6] in the blank treatment is in agreement with the proposed accumulation of Fe as Fe^{3+}(hydr)oxide minerals on the fiber surface where Fe^{2+}[6] and Fe^{3+}[4] were oxidized and/or changed coordination environment and precipitated as Fe^{3+}[6]. By including ferrihydrite in the interpretation of the Mössbauer spectrum obtained for the fibers weathered in the blank treatment, circa 6% of the bulk Fe was attributed to ferrihydrite (Table 1/SI-Table 6). This fraction of ferrihydrite approximately corresponds to the theoretical amount of Fe available for precipitation by dissolving Mg and Si layers during alteration (SI-Table 7).

The effect of chrysotile weathering on its HRFP

Weathering chrysotile at different pH values in the presence or absence of Fe chelating ligands altered the redox reactivity of fiber surfaces to different extents, as quantified by EPR spin trapping (Figure 5). As Fe at the chrysotile surface is largely responsible for the HRFP [25], EPR measurements can assist in linking surface Fe redox reactivity to surface Fe speciation.

Fibers weathered at pH 11.5 in blank, oxalate, citrate and DFOB treatments had HRFPs that differed less than 15% from the HRFP of pristine fibers (100%). This is consistent with the marginal Mg and Fe mobilization and suggests an (almost) unaltered Fe surface speciation. Among the ligands included in this experiment, only HBED strongly decreased the HRFP of chrysotile fibers at pH 11.5 to 22%; it was also the only ligand at this pH that mobilized Fe in concentrations to a substantial degree (28 µmol L^{-1}). Both at pH 8.5 (75 - 80%) and at pH 7.5 (60%) the HRFP of fibers weathered in the blank and oxalate treatment were comparable. In both treatments, no Fe was mobilized, but the outermost Mg layer substantially dissolved. Consequently, Fe dissolving from the first Mg layer (≈ 30 µmol L^{-1}) precipitated as secondary Fe phases on the fiber surface, as supported by dissolution experiments at pH 3.0 and discussed in the context of our Mössbauer spectroscopy observations. Since hardly any Si was mobilized, the coordination of Fe in the first Si layer presumably remained unaltered. Given that the HRFP of Fe(hydr)oxides is negligible [35, 50], the measured HRFPs of weathered fibers from the blank- and oxalate treatments at pH 7.5 and pH 8.5 were probably largely caused by Fe^{3+}[4] in the exposed Si layer. This demonstrates that the Fe^{3+}[4] content of exposed Si layers (which only represented 7.0% of the bulk-Fe in chrysotile) generated a HRFP corresponding to ≈60% of the HRFP generated from the whole exposed Fe[6] pool (HRFP = 100%) in pristine fibers, suggesting that at the chrysotile surface on average a single Fe[4] is approximately an order of magnitude more potent than a single Fe[6] in generating hydroxyl radicals. The HRFP of fibers weathered in the citrate treatments were at both pH values 15 to 20 percent point higher than in the corresponding blank treatment. This was surprising,

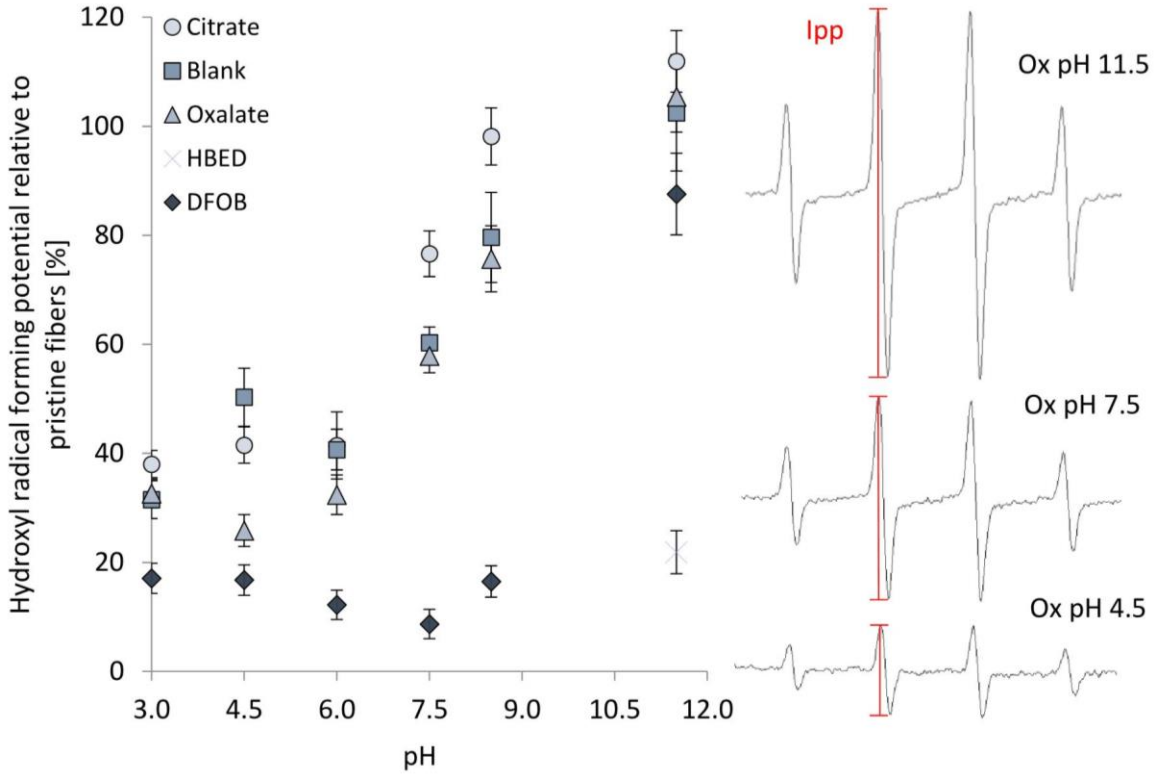

Figure 5: *EPR spin trapping DMPO/HO• peak-to-peak intensity (Ipp) of fibers weathered in blank and 1 mmol L^{-1} ligand treatments at various pH values (pH 3.0, 4.5, 6, 7.5, 8.5 and 11.5) relative to the Ipp of pristine reference fibers (100%). The incubation time was 336 h. Error bars indicate standard deviations (n = 4). For visualization, 3 DMPO/HO• spectra of fibers weathered in 1 mmol L^{-1} oxalate-treatments at pH 4.5, 7.5 and 11.5 are shown. The Ipp of the second peak from the left (indicated by red bars) was used for determining the peak-to-peak intensity. Data to this figure is presented in SI-Table 9.*

since in the citrate treatments, some Fe was mobilized (16 µmol L^{-1} at pH 7.5 and 8 µmol L^{-1} at pH 8.5). Because in citrate treatments at neutral pH no substantial mobilized Si concentrations were measured (Figure 2c and SI-Table 2), this suggests that citrate complexed Fe[6] from the fiber surface, but not Fe^{3+}[4]. The DFOB treatment strongly decreased the HRFP to 17% at pH 8.5 and to 9% at pH 7.5. This can be related to the ability of DFOB to complex most Fe from both the Mg and the Si layer (Table 2), rendering an Fe depleted surface. The lowest HRFPs in the blank treatments were observed at pH 3.0 - 6.0: ≈40 ± 10%. At these pH values, elevated Si concentrations were measured, implying dissolution and alteration of the Si layer structure (but not at pH ≥ 7.5). Assuming that the Fe^{3+}[4] content in Si layers at pH 3.0 - 6.0 hydrolytically dissolved from the Si lattices and only thereafter triggered Si labilization, a Si layer partially depleted in Fe^{3+}[4] would consequently form. Partial Fe depletion may explain the lower HRFPs of blank fibers incubated at pH ≤ 6.0 relative to the ones at pH 7.5 & 8.5. The nearly two times larger ionic radius of Fe^{3+}[4] relative to Si^{4+}[4] could facilitate the hydrolysis of Fe^{3+}[4]

from Si layers. After dissolving from the Si lattice, Fe^{3+}[4] would presumably change its coordination to Fe^{3+}[6] in Fe precipitates. This change in coordination was already suggested based on the results from Mössbauer spectroscopy on blank altered fibers at pH 3.0. Fibers weathered in oxalate and citrate treatments at pH 3.0 - 6.0 had similar HRFPs as measured in the corresponding blank treatments (≈40 ± 10%, except for the oxalate treatment at pH 4.5), even though oxalate and citrate mobilized Fe from the fibers in this pH range. Given that only little or no Fe was mobilized in the corresponding blank treatments, the similar HRFPs were independent of whether 1) Fe was removed from the fiber surface (oxalate, citrate), or 2) precipitated on the fiber surface (blank). From pH 3.0 - 6.0, mobilized Si concentrations (SI-Table 8) and net Si dissolution rates (Figure 1b) were consistently highest in the DFOB treatments suggesting that the kinetics of Fe^{3+}[4] dissolution from the Si layers by DFOB were faster than in citrate, oxalate and blank treatments. The faster Fe^{3+}[4] dissolution kinetics in DFOB treatments may cause a relatively fast depletion of Fe^{3+}[4] from Si-layers. This may explain the consistently lower HRFPs of fibers measured in the DFOB treatment at pH 3.0 - 6.0 (≈ 12 - 17%). The similar HRFP in the citrate, oxalate and blank treatment at pH=3.0 suggest that the Fe^{3+}[4] dissolution rates were equal in these treatments and that proton-promoted dissolution governed the overall Fe[4] dissolution rate. The larger Si dissolution rates in the oxalate and citrate treatment compared to the blank treatment (Figure 1b) might be related to enhanced Al^{3+}[4] dissolution by the ligands.

HRFP in relation to fiber weathering kinetics at pH 7.5

The two different modes of decreasing the HRFP of fibers (ligand-promoted Fe dissolution and proton-promoted Fe hydrolysis with subsequent precipitation of Fe(hydr)oxide minerals on fiber surfaces) have different kinetics and a different steady state as illustrated by the decrease in HRFP over time at pH 7.5 in the blank- and DFOB treatment (Figure 6). Within 0.5 h, the HRFP of fibers in the blank treatment at pH 7.5 had decreased to 77%. After 8 h, it had further decreased to 57% after which it remained approximately constant (≈50 ± 10%) until 336 h. This indicates that already after 8 h, there was no Fe3+[6] contributing to the generation of radicals anymore. This supports our hypothesis that Fe[6] at the surface becomes Fenton-inactive quickly (due to precipitation as hydroxide minerals within hours), while Fe^{3+}[4] (generating the HRFP of ≈50 ± 10%), remained Fenton-active for the entire incubation time. This implies that Fe^{3+}[4] is the only relevant long-term Fenton-active Fe surface species in weathered fibers. However, this does not apply to fibers weathering in very alkaline conditions (e.g. fibers embedded in cement) since the Mg layer, and consequently the Fe[6] content it bears, do not dissolve under these conditions. The initial decrease in HRFP of the fibers weathered at pH 7.5 in the DFOB treatment was faster than in the blank treatment. Furthermore, the HRFP did not reach a plateau value during the incubation. After 0.5 h, the HRFP had already decreased to 54%, after which it then further decreased gradually to 9% after 336 h. This implies that even in the presence of

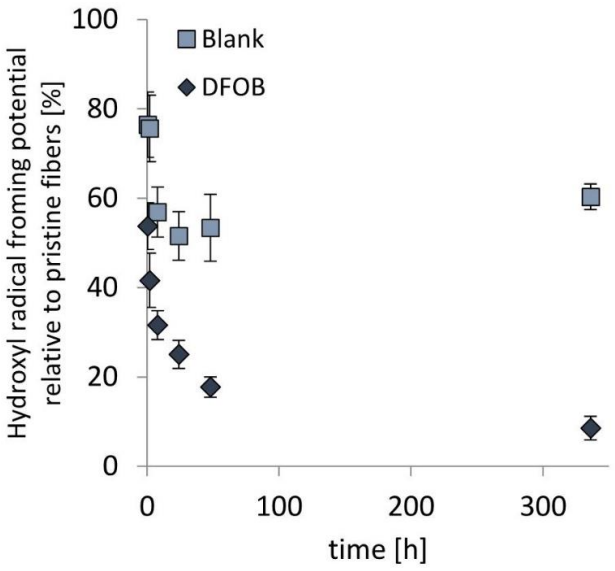

Figure 6: *EPR spin trapping DMPO/HO• peak-to-peak intensity (Ipp) of fibers weathered in blank and 1 mmol L^{-1} DFOB-treatments at pH 7.5 for 0.5, 2, 8, 24, 48 or 336 h, relative to the Ipp of pristine reference fibers (100%). Error bars indicate standard deviations (n = 4). Data to this figure is presented in SI-Table 10.*

a strongly Fe-binding ligand like DFOB, the depletion of Fe^{3+}[4] from Si layers, at neutral pH values, only occurs in the order of days.

Implications

Our results show that on the long term, Si dissolution is rate determining for chrysotile weathering in the environmentally relevant pH range (3 - 8.5); at the pH of cement Mg dissolution is inhibited. Fe^{3+}[4] (and potentially Al^{3+}[4]) in the Si layers of chrysotile proved to play an important role in the dissolution kinetics of the fibers, even though its abundancy was comparably low (7.0% of Fe-bulk in the fibers). The labilization of Si layers by dissolution of Fe^{3+}[4] (and potentially Al^{3+}[4]) can strongly enhance Si dissolution rates. Fe^{3+}[4] dissolution from Si layers was accelerated by chelating ligands. However, only ligands that can dissolve Fe^{3+}[4] may accelerate dissolution rates at circumneutral pH in the environment. In asbestos-contaminated soils with circumneutral pH (e.g. carbonaceous soils), hard Lewis-base, hexadentate ligands like siderophores (e.g. DFOB) and phytosiderophores could potentially increase long-term dissolution rates of chrysotile. However, weaker biogenic ligands like oxalate, which is e.g. exuded by fungi in contact with chrysotile [107], did not induce Si labilization at neutral pH, and are therefore unlikely to affect overall dissolution rates in such environments. With respect to the radical formation of fibers, our results demonstrate that Fe[6] from the Mg layers loses its ability to generate HO• radicals quickly (within hours) over a wide pH range due to precipitation of low Fenton-active secondary Fe phases (as reported in this study and e.g. observed by Turci et al.

(2007) [50]). Given this quick precipitation of Fe[6] during fiber dissolution, complexation of Fe[6] by ligands in soils will in the long run not decrease the HRFP of fibers markedly, as shown for instance in citrate treatments at neutral pH. In the long run, Fe^{3+}[4] proved to be the only Fenton-active Fe surface species in chrysotile in the natural soil pH range (3 - 9). At the alkaline pH of cement, Fe[6] did contribute to the HRFP as the outermost Mg layer does not dissolve under these conditions. In spite of its low abundancy, Fe^{3+}[4] in the Si layer exhibited ≈50±10% of the HRFP of the over ten times more abundant Fe[6] in pristine fibers. Turci et al. (2012) showed that the HRFP of synthetic, Fe doted nano-chrysotile-crystals [137] first increased with increasing Fe content (until 0.67 wt% Fe), but with further increasing Fe content decreased again [138]. The authors concluded that isolated Fe in chrysotile is most potent in radical formation. This, on the one hand, may explain the almost negligible HRFPs of precipitated Fe(hydr)oxide minerals, and on the other hand supports that even low concentrations of an Fenton-active Fe species may dominate the redox reactivity of the whole fiber, as demonstrated in this study for Fe^{3+}[4] in natural fibers. The pivotal role of Fe^{3+}[4] in dissolution kinetics and long-term radical generation described here may also apply for other silicates and their associated pathologies (e.g. amphiboles, silica, zeolites or asbestiform talcum).

Experimental section

Materials and characterization of chrysotile asbestos

All chemical reagents were bought in pro analysis quality from VWR (unless specifically mentioned). Chrysotile asbestos was purchased from Shijiazhuang Mining IMP&EXP Trade Co. LTD, China. XRD-Rietveld analysis of ≈ 1 g of ground material (3 min in a WC ball-mill at 30 strokes per minute) identified chrysotile (86.4 ± 4.6%), brucite (4.5 ± 2.1%), talc (3.4 ± 2.0%), chlorite (2.4 ± 2.9%), magnetite (1.5 ± 0.2%), quartz (1.0 ± 0.2%) and calcite (0.8 ± 0.2%) (SI-Figure 3). Additionally, single fibers were analyzed by Raman spectroscopy and identified as chrysotile (SI-Figure 4). The mean BET surface area of 5 replicates, determined with 7 adsorption points, was 20.3 $m^2\ g^{-1}$ (with a standard deviation (SD) of 0.9 $m^2\ g^{-1}$). The bulk elemental composition of the chrysotile asbestos (Table 1) was determined by fusion digestion: fibers were mixed with $Li_2B_4O_7$ in a ratio of 1:9 and molten in Pt crucibles at 1050 °C for 9 minutes in a Linn high-therm oven. Afterwards the borate melt was dissolved in 1.25 mol L^{-1} trace metal grade HNO_3 using a magnetic stirrer at 1100 rpm for approximately one hour. Metal concentrations were analyzed by ICP-OES. For comparison, serpentinite reference samples (LGC standards (Laboratory of the Government Chemist)) were also analyzed. Measured oxide contents (and the reported loss on ignition) of 20 replicates added up to 99.6% (±1.8 SD) of the mass. The bulk

Fe content was additionally analyzed by a neutron activation analysis for duplicate samples of 100 mg (NAA; Table 1). The bulk Fe content determined by fusion digestion (19.0 ± 1.4 µmol L^{-1} SD) was comparable to the bulk Fe content determined by the NAA (21.5 ± 0.4 µmol L^{-1} SD). For reasons of comparison, mobilized metal concentrations in dissolution experiments were also expressed as a percentage of the total Mg, Si, Fe (mean values of fusion digestions and NAA) and Al (fusion digestion) content (Figure 1 (panel a), 2, 3; SI-Figure 2). Fe bulk speciation and magnetite contamination were determined by ^{57}Fe Mössbauer spectroscopy.

Dissolution experiments

Chrysotile dissolution studies and fiber alteration for EPR and Mössbauer analysis were carried out in a SSR of 1 g L^{-1}. Fibers were incubated at six pH values (3, 4.5, 6, 7.5, 8.5 and 11.5) in solutions containing 50 mmol L^{-1} buffer. pH 3 - 8.5 represented the soil pH range, whereas pH 11.5 represented the alkaline pH of cement (e.g. in asbestos cement waste) [103]. The non-metal-complexing tertiary amine ("Better") buffers [139] PIPPS (1,4-piperazinedipropanesulfonic-acid, at pH 3.0; 4.5 and 8.5,), MES (2-(*N*-morpholino)ethanesulfonic-acid, at pH 6.0) and MOPS (3-(*N*-morpholino)propanesulfonic-acid, at pH 7.5) were used to accommodate that. The buffers maintained the pH within 0.3 pH units from the target value throughout the experiment. At pH 11.5 no buffer was required for this. To avoid differences in ionic strength (IS) between treatments, the IS of all pH treatments was adjusted to 300 mmol L^{-1} by variable NaCl addition depending on the calculated protonation of the buffers. "Blank"-dissolution experiments (only buffer and electrolyte) were compared with dissolution experiments including 1 mmol L^{-1} citrate, oxalate, DFOB (Novartis), HEDTA (Sigma Alrdich) or HBED (Sigma Aldrich). HEDTA is a synthetic chelating agent that was used as a proxy for phytosiderophores, because it has identical functional groups and comparable affinity for metals. Phytosiderophores are exuded by grasses for Fe acquisition and can mobilize Fe and a range of other metals from soil [118, 119]. HBED is a synthetic ligand with a very high affinity for Fe that is used in Fe fertilizers [140]. Dissolution studies were carried out in duplicates. Pristine fibers were incubated in 15 ml PP-tubes (VWR) for 10 incubation times (0.5; 1; 2; 4; 8; 24; 48; 96; 168 and 336 h) in pH adjusted IS-buffer containing 1 mmol L^{-1} citrate, oxalate, DFOB, HEDTA, HBED or no ligand (blank). Experiments with HBED were done exclusively at pH 11.5. Samples were kept in an end-over-end shaker at 15 RPM at 20 ± 2°C in the dark.

Solution and fiber sampling was done destructively. Suspensions were filtered over 0.45 µm Sartorius cellulose-acetate syringe filters. Aliquots of the filtrate were acidified with trace metal grade HNO_3 to 0.14 mol L^{-1}. Fibers were sampled by vacuum filtration in Büchner funnels equipped with 0.47 µm Nylon membranes (Magna) and washed with ultra-pure water to remove adsorbed free ligands and metal complexes. Afterwards, fibers were dried and stored in an evacuated desiccator until analysis. Metal and Si concentrations in the solution samples were analyzed by ICP-OES spectrometry (Optima 5300-

DV, Perkin Elmer). The calibration standards were matrix-matched with the samples. All mobilized Si & Mg, Fe and Al concentrations can be found in SI-Table 2, 4 and 5 respectively.

Net dissolution rates of Mg and Si were calculated by dividing the slopes of linear regression lines of mobilized concentrations as a function of time by the BET surface area of the pristine fibers. Almost all R^2 values of linear regressions for determining the rates at pH 3.0 - 6.0 were larger than 0.9, whereas R^2 values of rates calculated at circumneutral pHs were lower. Rates were not reported for experiments with R^2 values <0.5. For Si, all dissolution data were used to accomplish this (Figure 1b). For Mg dissolution rates, two stages were distinguished (Figure 1c). The first stage net dissolution rates were calculated using data for the first 5 time points (0.5 to 8 h). The second stage net dissolution rates were calculated using data for t > 8 h, if the concentration in all datapoints was higher than 406 µmol L^{-1} (the rationale for this criterion was discussed before).

Equilibrium modelling

The chemical equilibrium modelling program PHREEQC [141] and the SIT database were used to assess the solution saturation state of secondary minerals that could potentially precipitate during dissolution experiments. The Mg, Si, Fe and Al concentrations mobilized after 336 h of incubation, the pH, the electrolyte concentrations and the ligand concentration (1 mmol L^{-1}) were used as input data. The pH was varied from 3 to 11.5. The temperature was set to 20 °C and the pe value was adjusted to be in equilibrium with atmospheric oxygen at the respective pH values. Modeling results are presented in Table 3.

Mössbauer measurements

Pristine and altered fibers were analyzed by ^{57}Fe Mössbauer spectroscopy at room temperature in standard constant acceleration mode with a ^{57}Co**Rh** source, relative to which all center shift data are given. Altered fibers had been exposed to a pH 3.0 buffered solution without (blank) or with addition of 1 mmol L^{-1} DFOB in 500 ml LDPE containers for 336 h (mobilized metal concentrations are reported in SI-Table 8). Fibers were vacuum dried and ground in a tungsten carbide ball mill for 30 sec (a time which was shown not to affect Fe^{2+}/Fe^{3+} ratios in minerals) [142] at 30 strokes per minute to avoid spatial anisotropy of fibers in specimens. 500 mg were then pressed between Teflon foils (Zuma) and analyzed. The spectra were analyzed by solving the full Hamiltonian. Thickness of the samples was taken into account after Mørup and Both (1975) [143]. All defining parameters for the Mössbauer spectra are presented in SI-Table 6.

EPR spin trapping measurements

Pristine fibers were incubated for 0.5, 2, 8, 24, 48 or 336 h in 50 ml PP tubes (Greiner bio one) at pH 3.0 - 11.5, in absence (blank) or presence of 1 mmol L^{-1} ligands (DFOB, oxalate, citrate and HBED), as

described under *dissolution experiment*. The $HO^{\bullet}$ generation by pristine and altered fibers via Fenton-like redox reactions in the presence of H_2O_2 and 5-5'-dimethyl-1-pirroline-N-oxide (DMPO) as spin trap was determined using an X-band EPR-spectrometer (Bruker EMX) and a split ring resonator (Bruker MD5). This technique has frequently been used in this context [35, 37, 43, 50, 121]. 11 mg of fibers were incubated for 0.5 h in 0.5 ml of a 125 mmol L^{-1} H_2O_2 and 12.5 mmol L^{-1} DMPO solution buffered at pH 7.4 with a 250 mmol L^{-1} chelex-treated phosphate buffer. After incubation and centrifugation (5 min with 14000 RPM at room temperature) 50 µl of the supernatant were aspirated into a glass capillary (intraMark Blaubrand) and subsequently sealed with Critoseal. Then the capillary was transferred into the resonator and the EPR measurements were started with the following parameters: microwave frequency 9.6856 GHz; microwave power 20 mW, modulation frequency 100 kHz; modulation amplitude 2 G; time constant 0.327 s; center field 3449 G; scan rate 36 G min^{-1}; sweep width 100 G; scan time 168 s; attenuation 3.17×10^{5}; scans 1. EPR measurements were done in quadruplicates. To quantify the change in HRFP, the signal intensity (Ipp, peak-to-peak intensity) of altered fibers was expressed as a percentage of Ipp of pristine fibers, which was measured as a reference in each measurement session. Intensities of DMPO-$HO^{\bullet}$ spectra were quantified by the height of the second peak from the left in the quadruplet (Figure 5). Mobilized metal concentrations during fiber alteration for EPR measurements are reported in SI-Table 8.

Second Chapter

"Identifying the reactive sites of hydrogen peroxide decomposition and hydroxyl radical formation on chrysotile asbestos surfaces"

Authors: Martin Walter[a], Walter D.C. Schenkeveld*[a]†, Gerald Geroldinger[b], Lars Gille[b], Michael Reissner[c], Stephan M. Kraemer[a]

Publication intended in: "Particle and Fibre Toxicology"

[a] Department of Environmental Geosciences, University of Vienna
Althanstraße 14 (UZA II), 1090 Vienna, Austria
*Email: w.d.c.schenkeveld@uu.nl

[b] Institute of Pharmacology and Toxicology, University of Veterinary Medicine, Vienna
Veterinärplatz 1, 1210 Vienna, Austria

[c] Institute of Solid State Physics, TU Wien
Wiedner Hauptstraße 8-10, 1040 Vienna, Austria

† current address:
Copernicus Institute of Sustainable Development, Faculty of Geosciences, Utrecht University Princetonlaan 8A, 3584 CB Utrecht, The Netherlands

Abstract

Chrysotile was by far the most abundantly used asbestos mineral and is toxic and carcinogenic upon inhalation. A major contribution to the adverse health effects by chrysotile is the chemical reactivity of the fiber surfaces, which catalyze the formation of highly reactive hydroxyl radicals ($HO^{\bullet}$) from H_2O_2. In this Haber Weiss cycle, Fe on the surface of chrysotile fibers is known to act as a catalyst. Specifically, H_2O_2 can be decomposed by Fe^{3+} into reductants, which reduce Fe^{3+} on chrysotile surfaces to Fe^{2+}, which is than back-oxidized by H_2O_2 (Fenton-oxidation) to yield $HO^{\bullet}$. Chrysotile contains three structural Fe species: ferric and ferrous octahedral Fe and ferric tetrahedral Fe (Fe^{3+}[4]). Also, external Fe may adsorb to or precipitate on the fiber surface. The goal of this research was to identify the catalytic Fe species on chrysotile surfaces responsible for H_2O_2 decomposition and $HO^{\bullet}$ generation. We demonstrate that Fe^{3+}[4] is the only structural Fe species responsible for $HO^{\bullet}$ generation and the preferred Fe species in H_2O_2 decomposition on chrysotile surfaces at the physiologic pH 7.4. After depleting Fe from fiber surfaces, a remanent fiber-related H_2O_2 decomposition mode was identified, which may have been catalyzed by functional groups in the Si layer and/or by magnetite impurities. Fe(hydr)oxide-precipitates on chrysotile surfaces contributed to H_2O_2 decomposition, but were, on an atom basis, substantially less efficient than H_2O_2 decomposition by Fe^{3+}[4]. External Fe on fiber surfaces increased $HO^{\bullet}$ generation only when it became incorporated and tetrahedrally coordinated into vacant sites in the Si layer. In general, our results indicate that at the physiologic pH 7.4 Fe^{3+}[4] on chrysotile surfaces is largely responsible for inducing oxidative stress via the Haber-Weiss cycle. This may be relevant for other pathogenic silicates in which Fe^{3+}[4] has been detected, e.g. quartz, asbestiform talcum, amphiboles and synthetic and natural zeolites. However, even if no structural Fe^{3+}[4], or no Fe at all, is present in a pathogenic mineral, our results suggest that the presence of vacancy sites in a Si lattice alone can pose a risk, for incorporation of external Fe into a tetrahedral coordination environment suffices for $HO^{\bullet}$ generation.

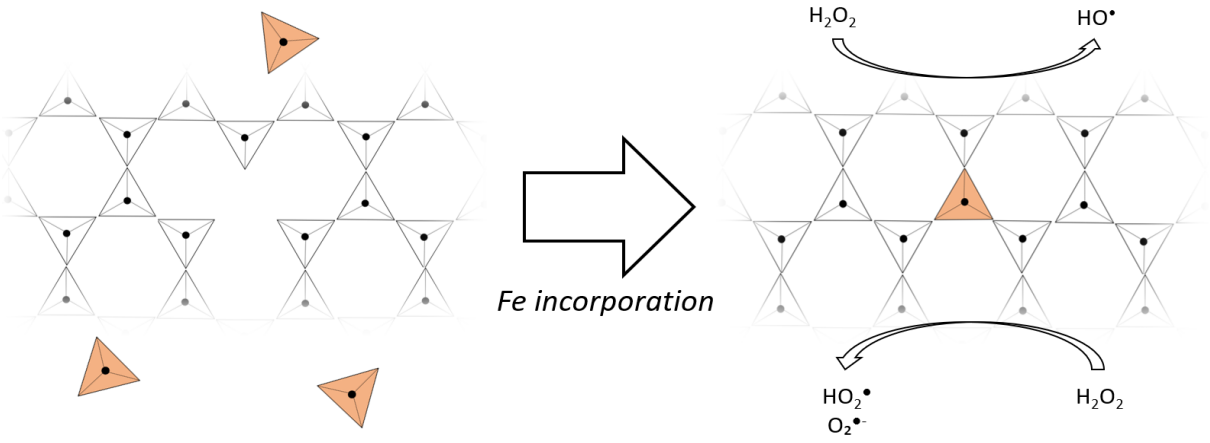

Introduction

The term asbestos refers to a heterogeneous group of five fibrous amphiboles and one fibrous serpentine mineral (chrysotile) [1, 25]. Due to favorable properties such as a large tensile strength, heat resistance and non-combustibility, asbestos has been used in a vast variety of industrial applications [14], e.g. in thermal and electrical insulation, roofing, cement pipes and sheets, flooring and coatings [144, 145]. However, respiratory exposure to asbestos minerals causes adverse health effects like pneumoconiosis, fibrosis of the lung, pleural plaques and effusions, carcinomas in the lung and mesotheliomas in the pleura [25, 29, 33, 144]. Given the carcinogenic potential of asbestos, the WHO-IARC classified all asbestos minerals as group 1 carcinogens [2]. More than 100,000 people die each year because of asbestos, mostly following occupational exposure [27]. Because of the intrinsic health hazard of asbestos, its use has been banned in EU-countries since the late 1980s [21]. In northern American countries its use has not yet been banned [21] and in some Asian countries it even increases [20, 23].

Chrysotile [$Mg_3Si_2O_5(OH)_4$] makes up more than 95% of all historically used asbestos [13]. As a result, exposure to asbestos predominantly concerns chrysotile. Therefore, we focused on this mineral in this study. Chrysotile asbestos consists of octahedral Mg hydroxide- and tetrahedral Si layers which bundle together to a fiber with Mg-hydroxide layers at the surface [6, 7]. During petrogenesis, Fe is substituted into the crystal lattice (usually up to 2 - 4 wt%) [5]. Ferrous and ferric Fe are found in the Mg layers (Fe^{3+}[6] and Fe^{2+}[6], respectively), whereas in the Si layers, exclusively ferric Fe is found (Fe^{3+}[4]) [38, 39, 146]. Fe is by far the most abundant redox-active metal in chrysotile [5].

Weathering of chrysotile at circumneutral pH is commonly described as a step-by-step dissolution of alternating Mg and Si layers. Mg layers at the fiber surface dissolve within hours, whereas exposed Si layers dissolve much slower and therefore determine overall dissolution rates [94, 97, 146]. However, enhanced dissolution of Fe^{3+}[4] from Si layers by ligands like the siderophore desferrioxamine-B (DFOB) causes the formation of vacancy sites, which increase the dissolution rate of the Si layer, even at circumneutral pH [146].

Apart from its high persistency in vivo [33, 36, 123], asbestos-induced pathologies can be linked to its fibrous morphology and the surface chemistry of the fibers [25, 33]. Emplacement of asbestos fibers in the lung or the pleura results in continuous, but unsuccessful attempts of macrophages and neutrophils to phagocytose fibers, a process called frustrated phagocytosis. During this process enzymatically formed reactive oxygen species (ROS) like hydrogen peroxide (H_2O_2) and superoxide ($O_2^{\bullet -}$) are released into the immediate extracellular environment [33]. Both exhibit a low potency for

cellular damage under homeostasis [42] and can be enzymatically detoxified. At elevated concentrations, H_2O_2 and $O_2^{\bullet-}$ may, however, interact with Fe on the fiber surface. This interaction induces cyclical redox reactions generating hydroxyl radicals ($HO^{\bullet}$), which have a high potency to damage DNA, proteins and lipids [25, 32, 42, 43, 44, 45]. In this Haber-Weiss cycle, Fe acts as a catalyst: Fe^{3+} is reduced by $O_2^{\bullet-}$ to Fe^{2+}, which is back-oxidized by H_2O_2 in the so-called Fenton reaction, yielding Fe^{3+} and $HO^{\bullet}$ [25, 46]. Furthermore, in the presence of Fe^{3+}, H_2O_2 may decompose to hydroperoxyl ($HO_2^{\bullet}$), which can either directly reduce Fe^{3+} to Fe^{2+} or decompose to the even stronger reductant, $O_2^{\bullet-}$ [49].

Considering the role of H_2O_2 and its degradation products in Fe redox cycling at the chrysotile fiber surface, the H_2O_2-decomposition potential of chrysotile may be regarded as an important indicator for the redox reactivity of the fibers. H_2O_2 decomposition by asbestos has, however, only been assessed in a limited number of studies [37, 147, 148]. An involvement of the Fenton and Haber-Weiss pathway in H_2O_2 decomposition by asbestos was demonstrated by Eberhardt et al. (1985) [147]. Furthermore, Fubini et al. (1995) [37] assessed H_2O_2 decomposition for various Fe-containing minerals. They found that rates of decomposition by chrysotile and crocidolite were comparable, but smaller than by magnetite and larger than by hematite.

A part of the decomposition of H_2O_2 by chrysotile occurs through Fenton reactions mainly involving Fe surface species [25, 32, 52]. However, not all Fe surface species are equally Fenton-active or have an equal hydroxyl radical forming potential (HRFP). Fubini et al. (1995) [37] demonstrated that Fe^{2+}[6] on chrysotile surfaces does not play a substantial role in $HO^{\bullet}$ generation. Later, Walter et al. (2018a) suggested that the HRFP of the surface exposed Fe^{3+}[4] in chrysotile amounted to 50 ± 10% the HRFP of octahedral Fe, despite its low abundancy (7% of the bulk-Fe in Shijiazhuang-chrysotile) [146]. In other words, this corresponds to almost an order of magnitude larger HRFP per Fe^{3+}[4] site compared to octahedral Fe. Fe^{3+}[4] is the only Fe species in chrysotile which remains Fenton-active during long term dissolution (weeks) at circumneutral pH, because the Si layer in which it is incorporated dissolves slowly, whereas octahedral Fe in the readily dissolving Mg layers rapidly oxidizes and/or precipitates into Fenton-inactive Fe(hydr)oxide minerals [146]. Depletion of all three Fe species (including Fe^{3+}[4]) from chrysotile surfaces by ligands like DFOB decreased the HRFP of the fibers, almost to background values [52, 146]. Not only structural Fe in asbestos may generate ROS, also external Fe that associates with surface of asbestos (or other silicates) can increase oxidative stress in vivo and in vitro [25, 35, 149, 150, 151].

To our knowledge, the relation between Fe speciation at the fiber surface and H_2O_2 decomposition rate has not been established yet. Also, the relation between the speciation of external Fe after associating with the chrysotile fiber surface and the change in HRFP of, and H_2O_2 decomposition by,

the fibers has not yet been explored. Hence, the understanding of which Fe species at the chrysotile surface are responsible for catalyzing the prerequisite for the first step (H_2O_2 decomposition to reductants), and the second step (Fenton oxidation) of the Haber-Weiss cycle is incomplete. Investigating the reactive sites of H_2O_2 decomposition and $HO^{\bullet}$ generation on chrysotile surfaces is important in assessing the overall redox reactivity of chrysotile asbestos, which is a major determinant in the pathogenicity of the fibers [3, 32]. In this study we addressed this knowledge gap.

Thereby we hypothesize that H_2O_2 is decomposed by either structural $Fe^{3+}[4]$ within exposed Si layers of the dissolving fibers, or by secondary Fe minerals precipitated on the fiber surface. The precipitated Fe may originate from external sources or from fiber dissolution during which structural Fe is released [146]. Furthermore, we hypothesize that external Fe only substantially contributes to the HRFP of chrysotile fibers when it becomes tetrahedrally coordinated by incorporation into a Si layer. The rationale for this hypothesis is the high HRFP of $Fe^{3+}[4]$ in chrysotile [146] relative to the very low HRFP of Fe(hydr)oxides [35] precipitated on chrysotile surfaces. Finally, we hypothesize that chrysotile fibers with surfaces depleted in Fe (e.g. due to a ligand pre-treatment) may still possess a potential health hazard of generating $HO^{\bullet}$ when external Fe is incorporated into vacant surface sites in the Si layer.

The hypotheses were tested in batch incubation experiments and subsequent ICP-OES, UV-VIS-photospectrometry, Mössbauer spectroscopy, and EPR spectroscopy analyses.

Methods

Chemical reagents and asbestos characterization

All chemical reagents used in this study were at least pro analysis quality and were ordered from VWR (unless otherwise mentioned). Chrysotile asbestos was purchased from Shijiazhuang Mining IMP&EXP Trade Co, China. The material was characterized by XRD-Rietveld phase analysis, Raman spectroscopy, BET specific surface area measurement, Mössbauer spectroscopy, fusion digestion and neutron activation analysis (Walter et al. (2018a) [146]). Key results are presented in Table 1: Shijiazhuang chrysotile asbestos contains ≈249 g kg^{-1} Mg and ≈188 g kg^{-1} Si; i.e. the stoichiometric Mg/Si ratio is close to 1.5. Fe (≈20 g kg^{-1}) and Al (≈8 g kg^{-1}) are the major substituents [146]. Mössbauer analyses demonstrated that in pristine Shijiazhuang chrysotile asbestos (Table 1), almost all Fe is substituted into the octahedral Mg layer (≈55% $Fe^{3+}[6]$ and ≈38% $Fe^{2+}[6]$), whereas only 7% is substituted into the

Table 1.) *Bulk characteristics of pristine Shijiazhuang chrysotile asbestos (previously reported in Walter et al. (2018a) [146]). Values in round brackets represent standard deviations.*

Bulk characteristics of chrysotile asbestos			
Bulk composition:		*Fusion digestion (n = 15):*	*NAA[1] (n = 2):*
Mg	[g kg^{-1}]	249 (7)	
Si	[g kg^{-1}]	188 (3)	
Fe	[g kg^{-1}]	19.0 (1.4)	21.4 (0.3)
bulk Fe speciation:		*Mössbauer:*	
Fe^{2+}[6]	[%]	38.4	
Fe^{3+}[6]	[%]	54.6	
Fe^{3+}[4]	[%]	7.0	
Total Fe in chrysotile[2]	[%]	68.2	

[1] neutron activation analysis
[2] Remaining Fe (31.8%) is in magnetite impurities

tetrahedral Si layer. Phase impurities were established by XRD-Rietveld analysis, and include magnetite (1.5 ± 0.2%) [146], hosting ≈ 32% of the total bulk Fe (Table 1).

General experimental procedure

All experiments were carried out using fiber suspensions with a solid to solution ratio (SSR) of 1 g L^{-1}. The non-metal-complexing tertiary amine ("Better") buffer [139] MOPS (3-(*N*-morpholino)propanesulfonic-acid) was used at a concentration of 50 mmol L^{-1} to maintain the pH of experimental solutions at 7.4 ± 0.3. The ionic strength of the buffer solutions was adjusted to 300 mmol L^{-1} by addition of NaCl. Solutions in blank treatments contained only pH-buffer and electrolyte, while DFOB (Novartis) treatments additionally contained ligand concentrations of 1 mmol L^{-1}. In H_2O_2 decomposition experiments DFOB was used to quench the redox-activity of Fe. This method has been used previously (e.g. [152], [153]).

Preconditioning of chrysotile fibers

Fibers were preconditioned to obtain fiber types with different specific surface chemistry. The preconditioning involved suspension for 336 h in buffered pH 7.4 blank solutions ("blank-altered fibers") or in pH 7.4 buffered 1 mmol L^{-1} DFOB solutions ("DFOB-altered fibers"). In blank-altered fibers, the outermost Mg layer had dissolved during preconditioning, and the Fe content of the dissolved Mg layer had precipitated on the fiber surface as low-Fenton active secondary Fe phases [35, 146]. In DFOB-altered fibers the Fe content of the dissolved outermost Mg layer as well as the Fe content of

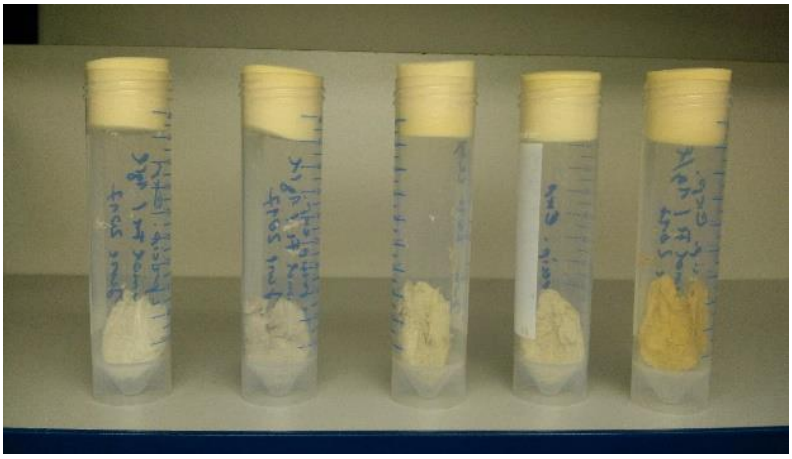

Figure 1.) *Preconditioning of fibers and the resulting change in colors. From left to right: DFOB-altered fibers with 0, 3 and 30 µmol g^{-1} Fe, respectively, blank-altered fibers with 0 µmol g^{-1} Fe and DFOB-altered fibers with 300 µmol g^{-1} Fe.*

the slowly dissolving Si layer was complexed and mobilized by DFOB. Fe mobilization from the Si layer causes the formation of vacancy sites, which promote Si dissolution [146].

To test whether external Fe can be incorporated into vacancy sites in the Si layer and whether this incorporated Fe participates in H_2O_2 decomposition and $HO^{\bullet}$ generation, DFOB-altered fibers were suspended in pH 7.4 buffered solutions containing 0, 3, 30 and 300 µmol L^{-1} of Fe^{2+} under anoxic conditions in a N_2-filled anoxic chamber (Brown box). The suspensions were then immediately oxygenated outside the anoxic chamber by air bubbling for 24 h, while magnetically stirring it at 500 rotations min^{-1}. The Fe^{2+} rapidly oxidized and Fe not incorporated into vacancy sites precipitated onto the fiber surface as Fe(hydr)oxide minerals, coloring the fibers beige to yellow (see Figure 1). As a negative control, the same concentrations of Fe were precipitated onto blank-altered fibers (which lack vacancy sites in the Si layer) following the same procedure. The obtained altered fiber types are referred to as "DFOB-altered fibers + 0, 3, 30 or 300 µmol g^{-1} Fe" and "Blank-altered fibers + 0, 3, 30 or 300 µmol g^{-1} Fe". Preconditioned fibers were collected in Büchner funnels on 0.47 µm Nylon membranes (Magna) and dried by vacuum filtration. To remove potentially adsorbing free DFOB or DFOB metal complexes, fibers were washed with ultra-pure water and then vacuum dried and stored in an evacuated desiccator until they were used in follow-up experiments.

Metal and Si concentrations mobilized during the fiber preparations are presented in SI-Table 1.

^{57}Fe addition and Mössbauer analyses

^{57}Fe Mössbauer spectroscopy analyses were done at room temperature in standard constant acceleration mode with a ^{57}Co**Rh** source, relative to which all center shift data are given. The analyzed

fiber types were DFOB and blank altered fibers + 0 µmol g^{-1} Fe, and DFOB- and blank-altered fibers + 3 µmol g^{-1} Fe. These fiber types were prepared following the procedure described above, except that isotopically enriched ^{57}Fe (Sigma Aldrich, > 95 atom % isotopic purity) was used. The isotopically enriched metallic ^{57}Fe-powder was dissolved over night at 70 °C in a 2 mol L^{-1} HCl solution, according to Arrigo et al. (2017) [154]. This procedure yielded a $^{57}Fe^{2+}$ solution, which was purged with N_2 for 2 h and then put into the anoxic glove box. The isotopic composition of Fe in the stock solution was verified by ICP-MS (^{57}Fe was 99.2 % relative to total Fe), and the Fe^{2+} concentration was verified spectrophotometrically by a ferrozine assay [155]. Aliquots of the $^{57}Fe^{2+}$ stock solution were added to DFOB- and blank-altered fiber suspensions to obtain a 3 µmol g^{-1} $^{57}Fe^{2+}$ concentration.

After vacuum filtration and drying of the fibers, 700 mg of each fiber type were ground in a WC ball mill (Resch Schwingmühle MM 400) for 30 sec (a duration which does not affect Fe^{2+}/Fe^{3+} ratios in minerals [142]) at 30 strokes per minute in order to avoid spatial anisotropy of fibers in specimens. 500 mg of the milled fibers were pressed between Teflon foils (Zuma) and were analyzed by solving the full Hamiltonian. Thickness of the samples was taken into account after Mørup and Both (1975) [143]. A ferrihydrite sub-spectrum (based on data from Murad and Schwertmann, 1980, [156]) was used to account for Fe-precipitation on blank altered fibers + 0 µmol g^{-1} ^{57}Fe (precipitated Fe-content of the Mg layer that had dissolved) and DFOB and blank altered fibers + 3 µmol g^{-1} ^{57}Fe (precipitation of the added ^{57}Fe). No ferrihydrite sub-spectrum was used to fit DFOB altered fibers + 0 µmol g^{-1} ^{57}Fe because of the presence of DFOB during the fibers' preconditioning. Each sample was measured two times: first in a wider velocity range to cover the full magnetically split-spectrum of magnetite impurities, which allowed to obtain the amount of magnetite in the samples, and second in a narrow velocity range to better resolve the chrysotile and ferrihydrite spectra. The spectra reported in this publication were analyzed in the wider velocity range, the obtained data of the two different velocity ranges can be found in SI-Table 2.

Experimental procedure for H_2O_2 decomposition experiments

In H_2O_2 decomposition experiments, metal mobilization from, and decomposition of H_2O_2 by differently preconditioned fibers was assessed. Fiber types included were: pristine fibers, blank-altered fibers, DFOB-altered fibers and both blank- and DFOB- altered fibers + 0, 3, 30 or 300 µmol g^{-1} Fe. The initial experimental H_2O_2 concentration was 3.3 g L^{-1} (≈ 0.3%), which was prepared by diluting a 30% stock solution (Sigma Aldrich, for trace analysis) a hundred times. The H_2O_2 concentration of the stock was determined by redox titration with $KMnO_4$: 334 ± 2 g L^{-1} H_2O_2. Experiments were carried out in duplicates in 15 ml PP tubes (VWR) that were shaken in an end-over-end shaker at 15 round per minutes (RPM) at 20 ± 2 °C in the dark. Samples were taken destructively after 0.5, 1, 4, 8, 24, 48, 96, 168 and 336 h. Suspensions were filtered over 0.45 µm Sartorius cellulose acetate syringe filters. An

aliquot of each filtrate was acidified to 0.14 mol L^{-1} HNO_3 (trace metal grade) for metal (Mg and Fe) and Si concentration analysis by ICP-OES (Perkin Elmer Optima 5300-DV). Another aliquot of each filtrate was diluted for H_2O_2 concentration measurement. Calibration standards for ICP-OES analysis were matrix-matched with the samples. The decomposition of H_2O_2 was assessed by measuring the H_2O_2 concentration in diluted filtrates spectrophotometrically by the titanium sulfate method [157] immediately after each sampling round. One ml of a 1.9 - 2.1 % titanium(IV) oxysulfate solution (Sigma Aldrich) was added to 0.5 ml of the diluted filtrate and light absorption by the resulting peroxytitanyl-ion was measured at 410 nm by a Varian Cary 50 UV/VIS spectrophotometer. H_2O_2 concentrations in the samples were quantified by an external linear calibration method (7 to 42 mg L^{-1} H_2O_2); filtrates were diluted down to fit the calibration range. Because H_2O_2 also reacts with MOPS buffer [158], a control treatment to determine the H_2O_2 decomposition rate in absence of fibers was also included. In an additional experiment, H_2O_2 decomposition by pristine, blank- and DFOB-altered fibers was examined in the presence of 1 mmol L^{-1} DFOB using the same experimental procedure. The absorption maximum of the FeDFOB complex (425 nm; ε = 2460 mol^{-1} cm^{-1}) [159] and the peroxytitanyl-ion (410 nm; ε = 689 mol^{-1} cm^{-1}) [157, 160] are in close proximity. However, FeDFOB concentrations were orders of magnitude smaller and the molar attenuation coefficients of the complexes are only less than one order of magnitude different. Therefore the contribution of FeDFOB to overall light absorption at 410 nm could be neglected.

EPR spin trapping analyses of hydroxyl radicals generated by Fe on altered fibers surfaces

The HRFP of fiber specimen in the presence of H_2O_2 was quantified with 5-5'-dimethyl-1-pirroline-N-oxide (DMPO) as spin trapping agent using a X-band EPR-spectrometer (Bruker EMX) and a split ring resonator (Bruker MD5). This spin trapping technique has frequently been used for this purpose before [35, 37, 43, 50, 121, 146]. 11 mg fibers were incubated for 0.5 h in 0.5 ml of a 125 mmol L^{-1} H_2O_2 and 12.5 mmol L^{-1} DMPO solution buffered at pH 7.3 with a 250 mmol L^{-1} chelex-treated phosphate buffer. After 25 min of incubation and 5 min of centrifugation (with 14000 RPM at room temperature), 50 µl of the supernatant were aspirated into a glass capillary (intraMark Blaubrand) and subsequently sealed with Critoseal. The capillary was then transferred into the resonator. The parameters for the EPR measurements are presented in Walter et al. (2018a) [146]. EPR measurements were performed on four aliquots of the respective preconditioned fiber stocks. To quantify the change in HRFP, the signal intensity (Ipp, Intensity peak-to-peak) of the second peak from the left in the DMPO/$HO^{\bullet}$ quadruplet of altered fibers was expressed as a percentage of Ipp of four replicates of pristine fibers, which were measured as a reference each measurement session. For comparison, the HRFP of a poorly crystalline Fe(oxy)hydroxide (3 ± 0.2 mg of 2-line ferrihydrite, synthesized according to Schwertmann and Cornell

(2000) [122]) was measured following the same procedure. An amorphous Fe(hydr)oxide like 2-line ferrihydrite may first precipitate upon Fe addition to the fibers and subsequent oxygenation [122, 161].

Statistical analysis and supplementary data

For statistical evaluation of EPR spin trapping results, a F-test was used to determine equal or unequal variance between samples. If samples had an equal variance, a one-way ANOVA (alpha 0.05) test was used to determine if there was a significant difference in the data. If a significant difference was found between more than three samples, a Tukey HSD post-hoc test (alpha 0.05) was subsequently used to confirm and identify differences between samples. If samples had unequal variance, a non-parametric Kruskal-Wallis (alpha 0.05) test was used to test significance between samples. If a significant difference was found between more than three samples, a Dunn post-hoc test with a Bonferroni correction (alpha 0.0167) was subsequently used to confirm and identify differences between samples. All statistical tests with the exception of the Dunn post-hoc test were performed using the StatPlus:mac Pro software (Build 6.3.05/Core v6.2.30, AnalystSoft Inc). The Dunn post-hoc test was performed using XLSTAT Base (v2018, Addinsoft).

All data in Figure 2 to 5 are also reported in SI-Table 2 to 5, respectively.

Results

Color changes related to Fe at chrysotile surfaces

Complexation and mobilization of Fe from the brownish pristine chrysotile fibers by DFOB resulted in the whitish color of DFOB-altered fibers. Interaction of DFOB-altered fibers with 3 µmol g^{-1} Fe changed the whitish color to greyish after exposure to oxygen; interaction with 30 µmol g^{-1} Fe reversed the color to brownish, comparable to the color of pristine (not shown) and blank-altered fibers, and interaction with 300 µmol g^{-1} Fe changed the color to rusty-orange (Figure 1). Interaction of pristine fibers with 0, 3 and 30 µmol g^{-1} Fe did not lead to a clear deviation from the brownish fiber color of blank altered fibers, whereas precipitation of 300 µmol g^{-1} Fe again changed the color of the fibers to rusty-orange (SI-Figure 1).

Coordination environment of ^{57}Fe after interaction with chrysotile surfaces

Precipitating 3 µmol of ^{57}Fe on one gram of blank altered fibers decreased the fraction of total Fe in chrysotile by 13.1% and only marginally increased the fraction of Fe^{3+}[4] in chrysotile by 4.2% (Figure

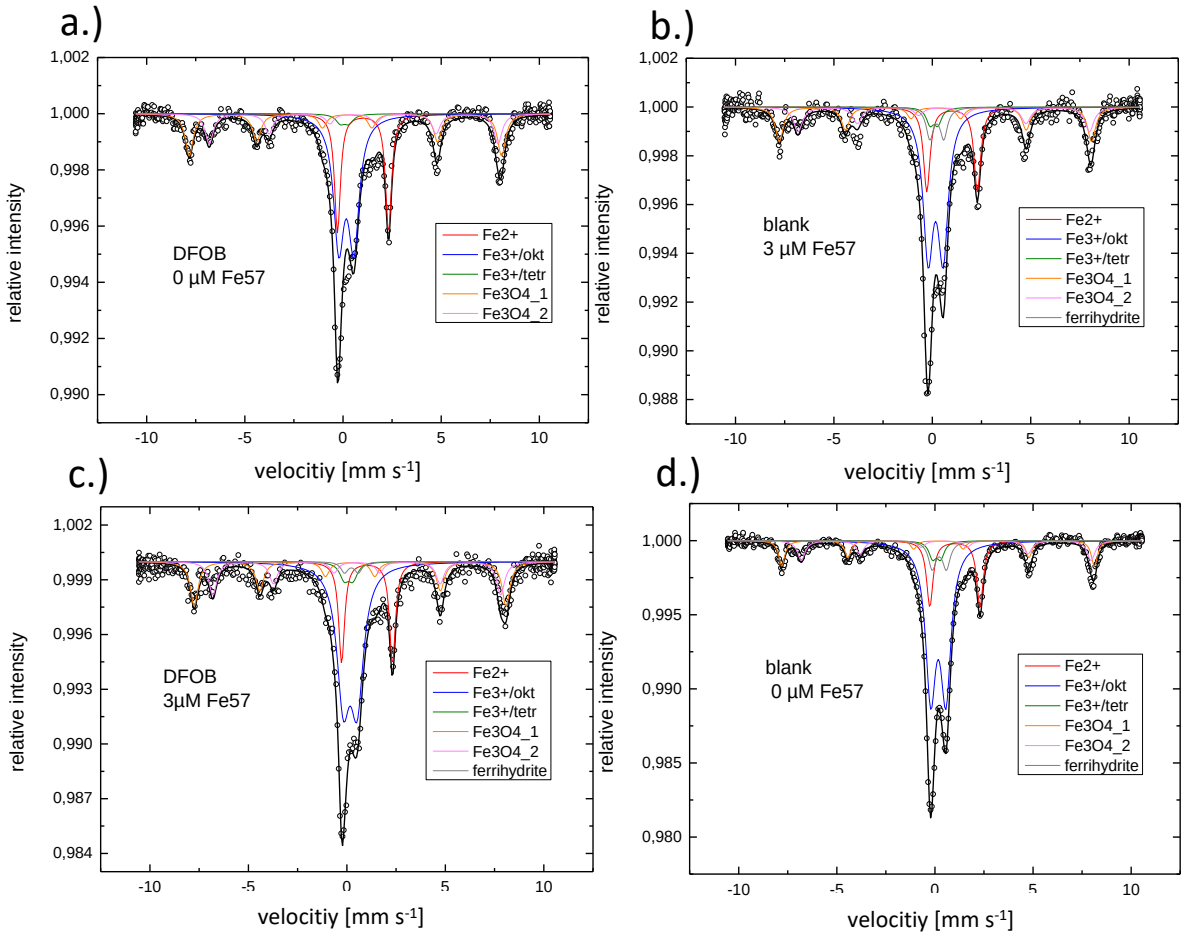

Figure 2.) *Mössbauer spectra of DFOB (Panel a and c) and blank (Panel b and d) altered fibers with 0 or 3 µmol g^{-1} of ^{57}Fe precipitated on the fiber surface. All blank altered fibers and DFOB altered fibers + 3 µmol g^{-1} ^{57}Fe were fitted with a ferrihydrite sub-spectrum to account for Fe-precipitation on the fiber surface (Table 2).*

2, Table 2). However, the fraction of total Fe in ferrihydrite increased by 59.6% as a consequence of the precipitation of ^{57}Fe on the fiber surface, whereas the fraction of Fe in octahedral positions in blank altered fibers approximately remained constant (Table 2). Precipitating 3 µmol ^{57}Fe on one gram of DFOB altered fibers decreased the fraction of total Fe in chrysotile less clearly than observed in blank altered fiber treatments (only by 3.4%), but substantially increased the fraction of Fe^{3+}[4] in chrysotile by 45.5% (Figure 2, Table 2). The fraction of octahedral Fe in chrysotile decreased by ≈2.6% after addition of 3 µmol ^{57}Fe, a fraction of the added ^{57}Fe could however be accounted to ferrihydrite precipitates (3.1 % of the total Fe).

Table 2.) *Mössbauer analyses of the fraction of total octahedral Fe and Fe^{3+}[4] in chrysotile in DFOB and blank altered fibers with 0 or 3 µmol g^{-1} ^{57}Fe precipitated on the fiber surface. Blank altered fiber spectra were either fitted with or without ferrihydrite. Fe-spectra of chrysotile and ferrihydrite were recorded in a narrower velocity range to obtain a higher resolution.*

	Fe precipitation on fiber surfaces		**Relative Δ after precipitation**
	0 µmol g^{-1} ^{57}Fe	**3 µmol g^{-1} ^{57}Fe**	
Blank altered fibers:			
Total Fe in chrysotile	67.9 %[1]	59.0 %[1]	-13.1 %
Fe[6] total	92.9 %	92.6 %	-0.3%
Fe^{3+}[4]	7.1 %	7.4 %	+4.2 %
Ferrihydrite	5.2 %	8.3 %	+59.6 %
DFOB altered fibers:			
Total Fe in chrysotile	58.8 %[2]	56.8 %[1]	-3.4 %
Fe[6] total	94.5 %	92.0 %	-2.6 %
Fe^{3+}[4]	5.5 %	8.0 %	+45.5 %
Ferrihydrite	-	3.1 %	-

[1] Remaining Fe is in magnetite impurities and secondary Fe-precipitates like ferrihydrite
[2] Remaining Fe is in magnetite impurities

Dissolution of metals and Si from pristine and altered chrysotile fibers in the presence of H_2O_2

In Figure 3, Mg and Si concentrations mobilized from pristine and altered chrysotile fibers in the presence of H_2O_2 (initial concentration: 3.34 g L^{-1}) are reported as a function of time. Only sub-micromolar Fe concentrations were measured during all experiments (data not shown).

For Mg mobilization from pristine fibers, two stages can be distinguished (Figure 3, Panel a1): a first rapid stage during the first hours of the experiment, and a second stage in which mobilized Mg concentrations reached a plateau of approximately 500 to 600 µmol L^{-1} between 96 and 336 h. The first stage can be interpreted to represent the rapid dissolution of the outermost Mg layer of chrysotile, whereas in the second stage, the outermost Mg layer had already been completely dissolved [146]. Mg mobilization from DFOB- and blank-altered fibers cannot be divided into two dissolution stages, but increased linearly throughout the experiment. Si concentrations mobilized from all three fiber types increased linearly throughout the experiment (Figure 3, Panel a2). Mobilized Si concentrations were consistently higher for DFOB-altered fibers than for blank-altered and pristine fibers. Adsorption and/or precipitation of added Fe onto DFOB-altered fiber surfaces considerably decreased the rate of Mg (Figure 3, Panel b1) and Si (Figure 3, Panel b2) mobilization throughout the experiment. The decrease was however not proportional to the amount of Fe applied. Addition of 3 µmol g^{-1} Fe to DFOB-altered fibers decreased mobilized Mg and Si concentrations by approximately 25% after 336 h,

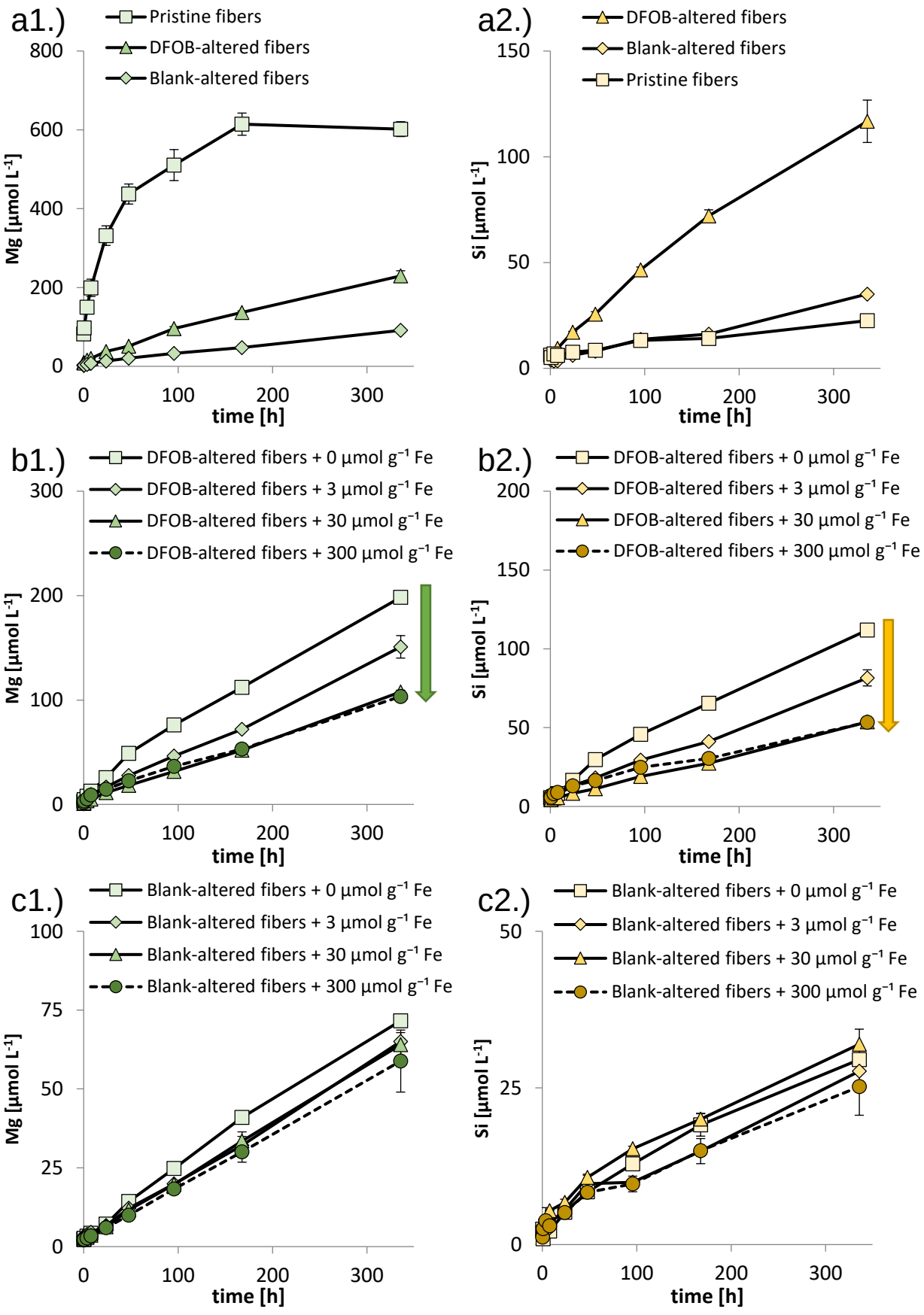
a1.)
Pristine fibers
DFOB-altered fibers
Blank-altered fibers
Mg [µmol L-1]
time [h]
a2.)
DFOB-altered fibers
Blank-altered fibers
Pristine fibers
Si [µmol L-1]
time [h]
b1.)
DFOB-altered fibers + 0 µmol g-1 Fe
DFOB-altered fibers + 3 µmol g-1 Fe
DFOB-altered fibers + 30 µmol g-1 Fe
DFOB-altered fibers + 300 µmol g-1 Fe
Mg [µmol L-1]
time [h]
b2.)
DFOB-altered fibers + 0 µmol g-1 Fe
DFOB-altered fibers + 3 µmol g-1 Fe
DFOB-altered fibers + 30 µmol g-1 Fe
DFOB-altered fibers + 300 µmol g-1 Fe
Si [µmol L-1]
time [h]
c1.)
Blank-altered fibers + 0 µmol g-1 Fe
Blank-altered fibers + 3 µmol g-1 Fe
Blank-altered fibers + 30 µmol g-1 Fe
Blank-altered fibers + 300 µmol g-1 Fe
Mg [µmol L-1]
time [h]
c2.)
Blank-altered fibers + 0 µmol g-1 Fe
Blank-altered fibers + 3 µmol g-1 Fe
Blank-altered fibers + 30 µmol g-1 Fe
Blank-altered fibers + 300 µmol g-1 Fe
Si [µmol L-1]
time [h]

↑ ***Figure 3.)*** *Mg and Si mobilization from 1 g L^{-1} pristine and altered fibers incubated at pH=7.4 (50 mmol L^{-1} MOPS) with addition of 3.34 g L^{-1} H_2O_2. Panel a.) Mobilized Mg (a1) and Si (a2) concentrations from pristine fibers and blank- and DFOB-altered fibers; Panel b.) Mobilized Mg (b1) and Si (b2) concentrations from DFOB-altered fibers + 0, 3, 30 and 300 µmol g^{-1} Fe. The arrows indicate a decrease in mobilized Mg and Si concentration with increasing Fe addition; Panel c.) Mobilized Mg (c1) and Si (c2) concentrations from blank-altered fibers + 0, 3, 30 and 300 µmol g^{-1} Fe. Error bars indicate standard deviations.*

addition of 30 µmol g^{-1} Fe decreased mobilized Mg and Si concentrations by approximately 50%, and addition of 300 µmol g^{-1} Fe did not result in a further decrease in mobilized Mg and Si concentrations. Adsorption and/or precipitation of added Fe onto blank-altered fiber surfaces did, however, not decrease Mg and Si mobilization as strongly as observed in DFOB-altered fiber treatments (Figure 3, Panel c1 and c2, respectively): addition of 300 µmol g^{-1} Fe only decreased mobilized Mg concentrations by 18% and mobilized Si concentrations by 20% after 336 h.

H_2O_2 decomposition by pristine and differently altered chrysotile fibers

H_2O_2 decomposition kinetics in the presence of chrysotile and MOPS buffer was first order with respect to H_2O_2 concentration, following the differential rate law

(1) $$Rate_{(H_2O_2)} = -\frac{d[H_2O_2]}{dt} = k_{tot}[H_2O_2],$$

in which k_{tot} represents the overall decomposition constant of the measured H_2O_2 decomposition. Chrysotile fibers accelerated H_2O_2 decomposition relative to the MOPS-buffered blank treatment (Figure 4, Table 3). For the MOPS-buffered blank treatment, k_{tot} was $1.2*10^{-3}$ h^{-1}. For treatments with chrysotile, k_{tot} values varied and were a factor 2 to 5 higher depending on the pretreatment: $2.5*10^{-3}$ h^{-1} for DFOB-altered fibers, $4.2*10^{-3}$ h^{-1} blank-altered fibers, and $6.2*10^{-3}$ h^{-1} for pristine fibers (Figure 4a, Table 3). The addition of DFOB as a redox quencher for Fe largely inhibited differences in the H_2O_2 decomposition between these three fiber types (Figure 4b). In the treatment with DFOB-altered fibers, the application of DFOB as redox quencher had no effect on H_2O_2 decomposition; for the treatments with pristine and blank-altered fibers, H_2O_2 decomposition decreased as a result of DFOB addition (Figure 4a, 4b). Fe addition to DFOB-altered fibers increased k_{tot} values, but not proportionally (Figure 4c, Table 3). For the treatments with DFOB-altered fibers and DFOB-altered fibers + 0 µmol g^{-1} Fe k_{tot} values did not differ ($2.5*10^{-3}$ h^{-1}), demonstrating that the fiber preparation procedure without Fe addition did not affect the H_2O_2 decomposition rate. Addition of 3, 30 and 300 µmol g^{-1} Fe increased k_{tot} values to $2.7*10^{-3}$ h^{-1}, $3.5*10^{-3}$ h^{-1} and $5.3*10^{-3}$ h^{-1}, respectively. A non-proportional increase of k_{tot}

Table 3.) *First order reaction law with the k_{tot} values of 1 g L^{-1} pristine and altered chrysotile fiber treatments, which represents the overall decomposition constant of the measured H_2O_2 decomposition. Furthermore, the corresponding half-lives ($t_{1/2}$) of hydrogen peroxide decomposition and the R^2 value of the exponential fits are presented (data from Figure 3). [H_2O_2] represents the hydrogen peroxide starting concentration.*

Exp. Nr.	Treatment	First order reaction k_{tot} values according to $Rate_{(H_2O_2)} = -\frac{d[H_2O_2]}{dt} = k_{tot}[H_2O_2]$	R^2	$t_{1/2}$ [h]
1	MOPS pristine fibers	$6.2*10^{-3}$	0.998	112
2	MOPS blank-altered fibers	$4.2*10^{-3}$	0.996	165
3	MOPS DFOB-altered fibers	$2.5*10^{-3}$	0.956	277
4	MOPS DFOB-altered fibers + 0 µmol g^{-1} Fe	$2.5*10^{-3}$	0.944	277
5	MOPS DFOB-altered fibers + 3 µmol g^{-1} Fe	$2.7*10^{-3}$	0.992	257
6	MOPS DFOB-altered fibers + 30 µmol g^{-1} Fe	$3.5*10^{-3}$	0.982	198
7	MOPS DFOB-altered fibers + 300 µmol g^{-1} Fe	$5.3*10^{-3}$	0.986	131
8	MOPS buffer panel a & c of Figure 3	$1.2*10^{-3}$	0.931	578
9	MOPS blank-altered fibers + 0 µmol g^{-1} Fe	$4.2*10^{-3}$	0.979	165
10	MOPS blank-altered fibers + 3 µmol g^{-1} Fe	$4.2*10^{-3}$	0.983	165
11	MOPS blank-altered fibers + 30 µmol g^{-1} Fe	$4.9*10^{-3}$	0.988	142
12	MOPS blank-altered fibers + 300 µmol g^{-1} Fe	$6.0*10^{-3}$	0.995	116
13	MOPS buffer panel d of Figure 3	$1.4*10^{-3}$	0.995	495
14	NaOH pristine fibers	$46.7*10^{-3}$	0.936	14.8
15	NaOH blank-altered fibers	$41.5*10^{-3}$	0.995	16.7
16	NaOH buffer	$1.0*10^{-3}$	0.772	693

values was also found for treatments in which Fe had been added to blank-altered fibers (Figure 4d, Table 3). Addition of 0 or 3 µmol g^{-1} Fe did not change the k_{tot} values relative to blank-altered fibers ($4.2*10^{-3}$ h^{-1}), but addition of 30 and 300 µmol g^{-1} Fe increased them to $4.9*10^{-3}$ h^{-1} and $6.0*10^{-3}$ h^{-1}, respectively.

The contributions of different reactive sites on chrysotile surfaces to overall H_2O_2 decomposition were determined in a tiered approach (Table 4). In addition to contributions from tetrahedral Fe and Fe(hydr)oxide precipitates, the difference in decomposition rate between the MOPS buffer control and the DFOB-altered fiber treatment suggests a contribution from a remanent H_2O_2 decomposition pathway (Figure 4b). It was assumed that the degradation mechanisms were independent, so that the decomposition constants for the different mechanisms are additive to the k_{tot} of the reaction. The

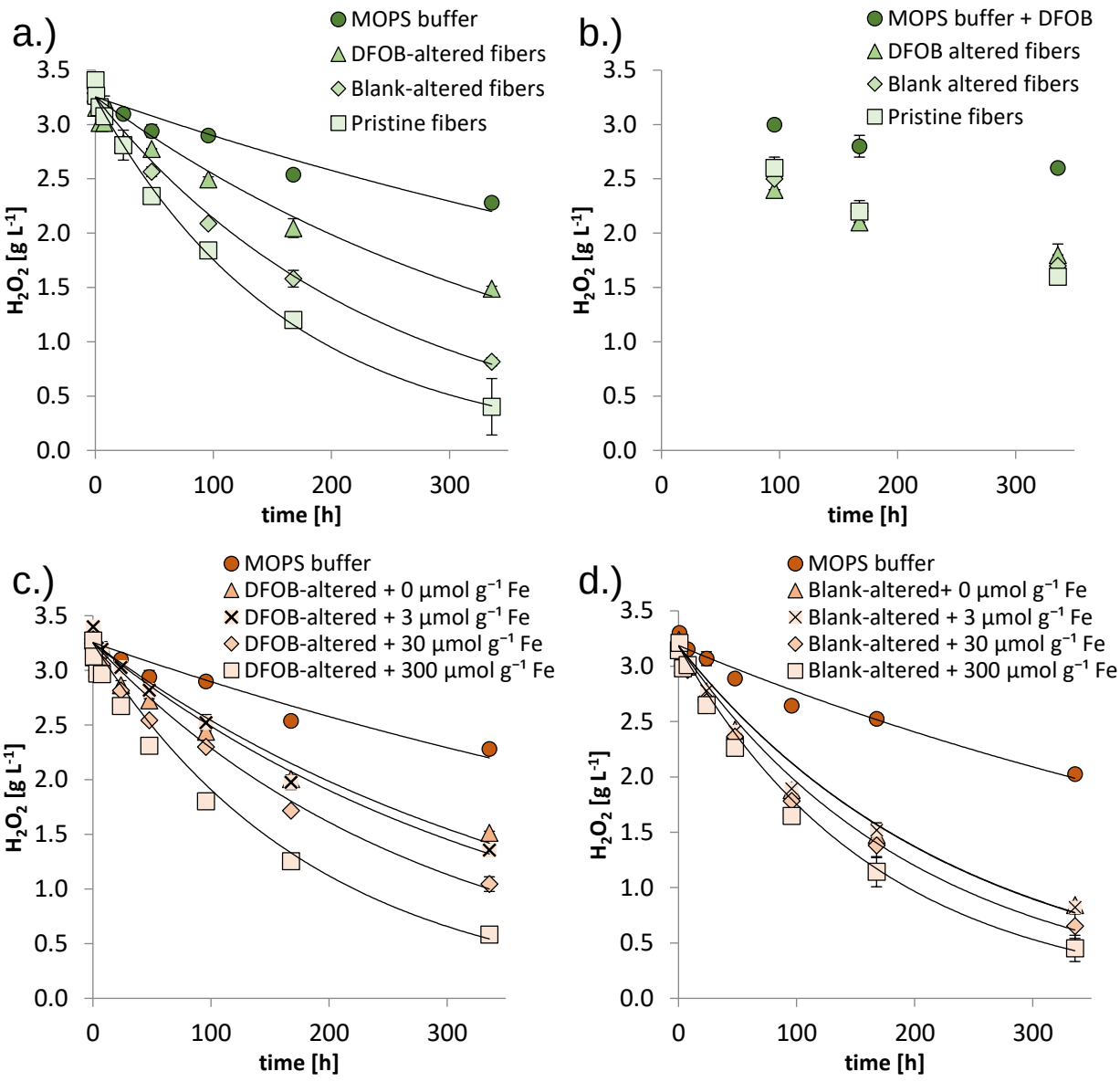

Figure 4.) *Decomposition of H_2O_2 (initial concentration 3.34 g L^{-1}) by 1 g L^{-1} pristine or altered chrysotile fibers at pH=7.4 (30 mM MOPS). Equations describing the exponential fits of the data are presented in Table 3. Panel a.) Decomposition of H_2O_2 in the presence of pristine fibers and blank- and DFOB-altered fibers; Panel b.) H_2O_2 decomposition in the presence of MOPS buffer + 1 mmol L^{-1} DFOB, in absence of fibers, and in presence of pristine fibers, DFOB-altered fibers and blank-altered fibers; Panel c-d.) Decomposition of H_2O_2 in absence of fibers and in presence of DFOB-altered fibers + 0, 3, 30 and 300 µmol g^{-1} Fe (Panel C) and blank-altered fibers + 0, 3, 30 and 300 µmol g^{-1} Fe (Panel d). Error bars indicate standard deviations.*

control experiment with only MOPS buffer provided the contribution from the MOPS buffer. The contribution from the remanent decomposition was calculated by subtracting the contribution from the MOPS buffer from the k_{tot} value of the DFOB-altered fibers treatment, under the assumption that DFOB had removed most iron from the fiber surface. For the contribution of Fe precipitates it was assumed that the outer Mg and Si layer contain approximately 30 µmol g^{-1} of Fe (SI-Table 1, Walter et

Table 4.) *Breaking down the overall H_2O_2 decomposition rate constant for the blank-altered fiber treatment to the contributions of different reactive surface sites and the MOPS buffer, assuming linear additivity and using the fitted constants (k(Exp.X)) for the treatments reported in Table 3.*

Decomposition mode	Exp Nr.	Calculation of contributions to H_2O_2 decomposition by blank altered fibers	Value
1.) MOPS buffer	8	k(Exp.8)	k1 = $1.2*10^{-3}$
2.) Remanent H_2O_2 decomposition	3	k(Exp.3) – k1 = k2	k2 = $1.3*10^{-3}$
3.) Secondary Fe precipitates	11, 9	k(Exp.11) – k(Exp.9) = k3	k3 = $0.7*10^{-3}$
4.) Tetrahedral Fe	2	k1 + k2 + k3 + k4 = k(Exp.2) => k(Exp.2) – k1 – k2 – k3 = k4	k4 = $1.0*10^{-3}$

al. (2018a) [146]), and that the large part of this amount precipitates in the blank treatment (as only a minor fraction of the Fe is located in the slowly dissolving Si layer), and that precipitation of an additional 30 µmol g^{-1} Fe has the same effect size on the k_{tot} value as the Fe that precipitated from the outer layer. The contribution of Fe precipitates to the k_{tot} value can then be calculated by subtracting the k_{tot} value of the blank-altered treatment from the blank altered + 30 µmol g^{-1} Fe treatment. Finally, the contribution of tetrahedral Fe can be calculated by taking k_{tot} values and subtracting the other three contributions (Table 4).

Using the assumed linear additivity and the k_{tot} values of treatments presented in Table 3, the k_{tot} value of the blank-altered fiber treatment ($4.2*10^{-3}$ h^{-1}; Table 3, treatment 2) can be broken down by modifying equation one with the contributions of the three types of active surface sites and the contribution of the MOPS buffer:

$$(2) \qquad Rate_{(H_2O_2)} = -\frac{d[H_2O_2]}{dt} = (k_1 + k_2 + k_3 + k_4)[H_2O_2]$$

Thereby, k_1 = $1.2*10^{-3}$ h^{-1} stands for the contribution of the MOPS buffer, k_2 = $1.3*10^{-3}$ h^{-1} for the remanent decomposition, k_3 = $0.7*10^{-3}$ h^{-1} for Fe precipitate sites and k_4 = $1.0*10^{-3}$ h^{-1} for tetrahedral Fe sites (Table 4). Hence, the contribution of the different surface sites on blank altered fiber surfaces to H_2O_2 decomposition is comparable, varying within a factor 2.

pH had a strong effect on H_2O_2 decomposition rate: in 0.1 mol L^{-1} NaOH (pH 12 - 13) the decomposition rate by pristine and altered fibers was approximately an order of magnitude faster than at pH 7.4 (Table 3).

Effect of Fe addition to pretreated chrysotile fibers on $HO^{\bullet}$ generation

Pretreatment of Shijiazhuang chrysotile asbestos decreased the HRFP relative to pristine fibers to 50 ± 10% and to 9% for blank-altered fibers and DFOB-altered fibers, respectively [146]. The HRFP of DFOB- and blank-altered fibers + 0 μmol g^{-1} Fe reported here (Figure 5) correspond with these published values. Addition of 3, 30 and 300 μmol g^{-1} Fe to DFOB-altered fibers progressively increased the HRFP from 7% (0 μmol g^{-1} Fe) to 17%, 24% and 36%, respectively (Figure 5a). For all treatments with Fe addition, the HRFP was significantly larger than in the + 0 μmol g^{-1} Fe treatment. Also, among two consecutive Fe addition treatments, the HRFP was always significantly larger in the treatment receiving more Fe. For the blank-altered fibers, addition of 3, 30 and 300 μmol g^{-1} did not significantly change the HRFP relative to the blank-altered fibers + 0 μmol g^{-1} Fe (Figure 5b). Furthermore, the HRFP of 3 mg of 2-line ferrihydrite was 11% (relative to the HRFP of 11 mg pristine chrysotile fibers). The total amount of Fe in 3 mg of 2-line ferrihydrite ($\triangleq 1.8$ mg Fe) is a thousand times larger than the 1.8 μg on the fiber surface of the aliquots of DFOB-altered fibers + 3 μmol g^{-1} Fe. Despite this large difference in amount, the gain in HRFP (an increase from 7% to 17%) due to addition of 3 μmol g^{-1} Fe to DFOB-altered fibers was comparable with the overall HRFP of 3 mg of ferrihydrite (11%).

Discussion

Contribution of impurities in Shijiazhuang chrysotile asbestos to H_2O_2 decomposition

Because H_2O_2 is more rapidly decomposed by magnetite then by asbestos per mass unit [37], it could potentially affect the H_2O_2 decomposition rate in our experiments. However, since magnetite is only a phase contaminant (1.5 ± 0.2%) in Shijiazhuang chrysotile asbestos, whereas chrysotile is the predominant phase (86.4 ± 4.6%) [146], we assume that the contribution of magnetite in Shijiazhuang chrysotile to H_2O_2 decomposition rates is little. Nevertheless, it may contribute to the remanent mode of H_2O_2 decomposition that was identified before.

Speciation of added Fe and implications for fiber dissolution

Unlike our observation, Ghio et al. (1998) reported Fe mobilization from chrysotile by H_2O_2 [148]. However, Ghio et al (1998) used HEPES (4-(2-hydroxyethyl)-1-piperazineethanesulfonic acid) as a buffering agent, a tertiary amine buffer which was due to its metal-complexing capacity not included by Kandegedara and Rorabacher (1999) [139] in their list of non-complexing group of “Better” buffers.

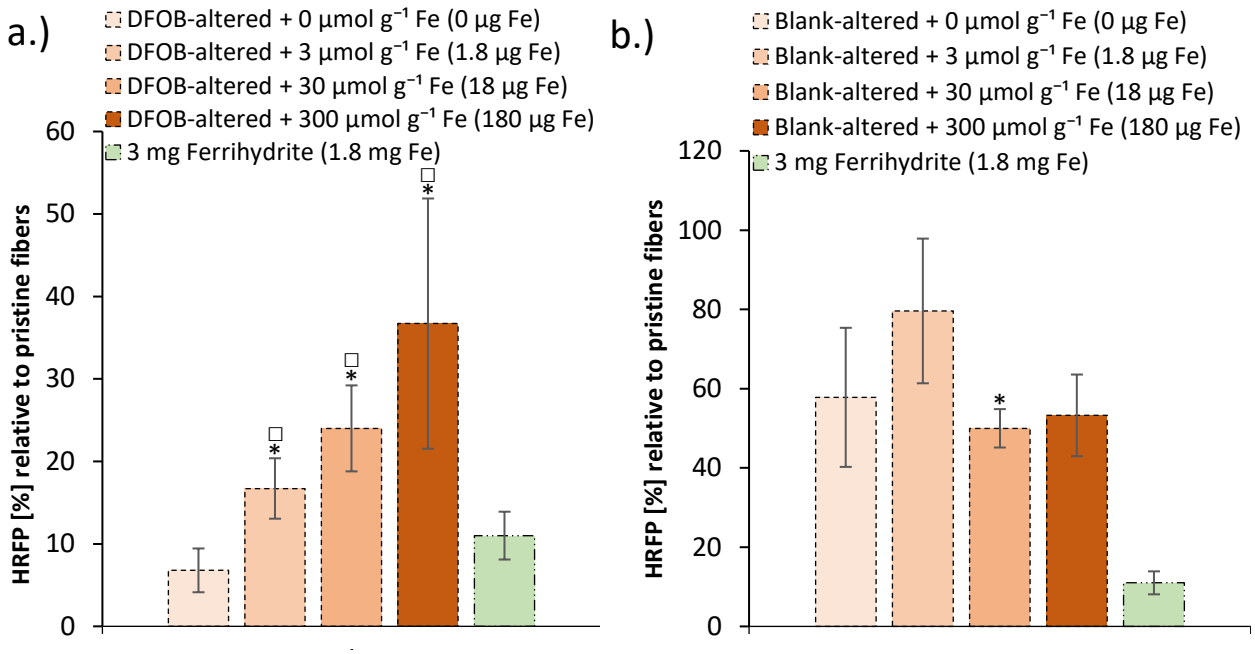

Figure 5.) *HRFP measured by the DMPO/* HO•*-EPR intensity in % relative to pristine fibers (≙100%). Panel a.) HRFP of DFOB-altered fibers + 0, 3, 30 and 300 µmol g^{-1} Fe, and 3 mg ferrihydrite (containing approximately ten times more Fe than added in the + 300 µmol g^{-1} Fe treatment); Panel b.) HRFP of blank-altered fibers + 0, 3, 30 and 300 µmol g^{-1} Fe. Error bars indicate standard deviations.* □ *indicates a significant increase in HRFP relative to the corresponding + 0 µmol g^{-1} Fe treatment, * indicates a significant difference in HRFP relative to the directly preceding treatment with smaller Fe addition.*

Therefore, the results obtained by Ghio et al. (1998) may have been altered by HEPES, which would be consistent with the solely sub-micromolar mobilized Fe concentrations by H_2O_2 reported in this study.

Si dissolution was considerably larger from DFOB-altered fibers than from pristine fibers, whereas Si dissolution from blank-altered and pristine fibers were comparable (Figure 3, Panel a2). The faster Si mobilization from DFOB-altered fibers is a consequence of the complexation of Fe^{3+}[4] by DFOB during the pretreatment, which caused formation of vacancy sites in the Si layer resulting in Si labilization as discussed in Walter et al. (2018a) [146]. Si mobilization from blank-altered fibers was considerably slower, because no Fe^{3+}[4] had been removed from the Si layers during the pretreatment [146]. The linear increase in Mg concentration from DFOB- and blank-altered fibers indicates that the rapidly (at pH 7.4) dissolving outer Mg layer had entirely dissolved during the pretreatment and that Mg dissolution kinetics were controlled by the slower linear dissolution kinetics of the overlying Si layer. The considerably higher Mg mobilization rate from DFOB-altered fibers presumably resulted from the correspondingly higher rate-controlling Si mobilization rate, allowing segments of deeper Mg layers to dissolve more rapidly.

Mössbauer spectroscopy analyses of DFOB and blank altered fibers + 3 µmol g^{-1} ^{57}Fe demonstrated that ^{57}Fe only became tetrahedrally coordinated when added to DFOB altered fibers (increased fraction of Fe^{3+}[4] in chrysotile by 45.5%, Figure and Table 2). This implies that the added ^{57}Fe had been incorporated in tetrahedral vacancy sites in the Si layer of the DFOB altered fibers. However, not all of the added ^{57}Fe coordinated tetrahedrally, a fraction of it precipitated as ferrihydrite on the fiber surface. For blank-altered fibers + 3 µmol g^{-1} ^{57}Fe, the Fe^{3+}[4]-fraction remained approximately constant as no vacancy sites in the Si layer were present (Figure 2, Table 2). The stronger decrease of the fraction of total-Fe in blank altered fibers relative to DFOB altered fibers after ^{57}Fe-addition indicates that external Fe preferably gets incorporated in DFOB altered fibers, but not in blank altered ones (Figure and Table 2). The visible color change from whitish to greyish by addition of 3 µmol g^{-1} Fe to DFOB-altered fibers may thereby be a consequence of tetrahedral incorporation, considering that the color of Fe precipitates on fiber surfaces was determined to cause a rather brownish color.

The incorporation of Fe into vacancy sites re-stabilized the labilized Si layer of DFOB-altered fibers and reduced the Si dissolution rate, and, consequently, also the Mg dissolution rate, considerably (Figure 3, panel b1 and b2). The considerable reduction in mobilized Si and Mg concentration by addition of only 3 µmol g^{-1} Fe (by 30 and 47 µmol L^{-1} after 336h, respectively – i.e. a reduction by 25% relative to corresponding treatment without Fe addition) and the fact that an increase in Fe addition from 30 to 300 µmol g^{-1} did not lead to a further decrease in mobilized Mg and Si concentrations, support that the effect of Fe addition is from stabilization of the Si layer rather than from surface coverage by precipitated Fe(hydr)oxide minerals that prevent dissolution. The latter observation also suggests that between addition of 3 and 30 µmol g^{-1} Fe, all vacancy sites became occupied with tetrahedrally coordinated Fe. For treatments in which saturation of the vacancy sites was reached (DFOB altered + 30 and 300 µmol g^{-1} Fe) Mg and Si dissolution rates were similar as in the blank-altered fiber treatment (Figure 3, Panel a1 and a2). The absence of similar trends in mobilized Si and Mg concentration for Fe addition to blank-altered fibers further supports that external Fe only becomes tetrahedrally coordinated if there are vacancy sites in the surface Si layer (Figure 3, Panel c1 and c2).

Active sites of H_2O_2 decomposition on chrysotile surfaces

H_2O_2 decomposition rates (Figure 4a) and HRFPs (Figure 5) were highest in treatments with pristine fibers. This is presumably related to a (transient) contribution from Fe in the outermost Mg layer. At pH 7.4 this layer dissolves within the timespan of a few days, in the treatment with NaOH the Mg layer did not dissolve at all (SI-Table 6) and the contribution from Fe in this layer is lasting longer.

Apart from the two hypothesized Fe-related modes of H_2O_2 decomposition, a remanent mode of H_2O_2 decomposition was identified (Figure 4a and 4b). To our knowledge this mode of H_2O_2 decomposition had not yet been described for chrysotile, or asbestos in general. Since it made the largest contribution to the k_{tot} of blank-altered fibers (Table 4), it may also be relevant in vivo. The exposed Si surface of blank-altered chrysotile fibers has a polar character and contains surface silanol groups which can form hydrogen bonds; both these features are known to facilitate heterolytic decomposition of peroxides [162] like H_2O_2. Apart from the possible contribution of magnetite impurities to H_2O_2 decomposition (as discussed before), the exposed Si surface may hence considerably contribute to fiber-mediated H_2O_2 decomposition.

In spite of the more than ten times smaller surface concentration of $Fe^{3+}[4]$ in blank-altered fibers relative to octahedral Fe which had precipitated as Fe(hydr)oxide minerals, their contributions to H_2O_2 decomposition were comparable (Table 4). For blank-altered fibers + 300 µmol g^{-1} Fe (containing 100 times more octahedral Fe) octahedral Fe increased H_2O_2 decomposition rates only by a factor of 2.5. Several aspects may contribute to the relatively large contribution of tetrahedral Fe. First, only a fraction of the Fe in Fe precipitates resides at the mineral surface and is able to react with H_2O_2, whereas all tetrahedral Fe substituted into the exposed Si layer can contribute to H_2O_2 decomposition. Second, in other silicate minerals like nontronites, it has been shown that $Fe^{3+}[4]$ is preferentially reduced over octahedral Fe [163, 164, 165] suggesting a lower redox potential of $Fe^{3+}[4]$ in silicate minerals. This lower redox potential may contribute to a higher reactivity of $Fe^{3+}[4]$ with regard to H_2O_2 decomposition. With respect to HRFP, also a much higher reactivity was observed for tetrahedral Fe than for octahedral Fe precipitates. The rationale for the high redox reactivity of $Fe^{3+}[4]$ in silicates has, to our knowledge, not been discussed in literature yet. However, since coordination proved to be the key determinant for the redox reactivity of Fe on chrysotile surfaces, and since $Fe^{3+}[4]$ is incorporated in a crystalline tetrahedral environment, we postulate that the intrinsic properties of Fe in its tetrahedral coordination environment may be the molecular reason for the high redox reactivity of $Fe^{3+}[4]$: However, this is hypothetical and needs to be evaluated in follow up studies.

Active sites of $HO^{\bullet}$ generation by structural and external Fe on chrysotile surfaces

Only Fe added to DFOB-altered fibers significantly increased $HO^{\bullet}$ generation by chrysotile (Figure 5a). This is the result of incorporation of Fe into vacancy sites in the Si layer of DFOB-altered fiber surfaces, where Fe becomes tetrahedrally coordinated. This Fe[4] is particularly active in $HO^{\bullet}$ generation. Blank-altered fibers do not have such vacancy sites, and therefore addition of Fe did not lead to an increase in HRFP.

$HO^{\bullet}$ generation appears more strongly biased towards Fe^{3+}[4] over octahedral Fe compared to H_2O_2 decomposition. The EPR spin trapping analyses demonstrated that the HRFP of 3 mg of ferrihydrite and 11 mg DFOB-altered fibers + 3 µmol g^{-1} Fe were comparable, despite the thousand times larger total Fe concentration in the former. The difference between the HRFP of chrysotile and Fe-(hydr)oxides may be explained by the occurrence of Fe^{3+}[4] in these minerals: The HRFP of hematite for example, which contains no Fe^{3+}[4] [161], was below the LOD in a study by Fubini et al. (1995) [35]. However, the HRFP of magnetite, which contains structural Fe^{3+}[4] [161], was per mass unit more than half as high as the HRFP of chrysotile asbestos in the same study [35]. This may also apply to H_2O_2 decomposition, which was high in magnetite (even higher than chrysotile), but low in hematite at equal masses [37]. Addition of 300 µmol g^{-1} Fe to blank-altered fibers, which corresponds with more than two times the bulk Fe content of Shijiazhuang-chrysotile (Table 1), did not increase the HRFP of chrysotile. Therefore, we conclude that Fe precipitates on asbestos do not contribute to the HRFP.

The high Fenton-reactivity of Fe^{3+}[4] in chrysotile may, analogously to H_2O_2 decomposition, be explained by the lower redox potential of Fe^{3+}[4] compared to octahedral Fe, as observed in nontronites [163, 164, 165] and a potentially rapid back-oxidation of the potential ultimate Fenton-active Fe-species Fe^{2+}[4] to Fe^{3+}[4] by H_2O_2, yielding $HO^{\bullet}$. The rational for the low redox potential and therefore the high HRFP of Fe^{3+}[4] may thereby be similarly postulated by the intrinsic properties of the d-orbitals of Fe in its tetrahedral coordination environment. In contrast to Mg and Si mobilization and H_2O_2 decomposition, addition of 30 µmol g^{-1} Fe to DFOB-altered fibers did not recover the HRFP to the level of blank-altered fibers. However, for DFOB-altered fibers + 300 µmol g^{-1} Fe the HRFP was not significantly different from blank-altered fibers (50 ± 10%, [146]), indicating a complete recovery of the Fenton reactivity (Figure 5a).

Conclusions

The results from this study demonstrate that both Fe^{3+}[4] and Fe^{3+}[6] in Fe(hydr)oxide precipitates contribute to H_2O_2 decomposition by chrysotile asbestos; in the case of asbestos fibers incubated at pH 7.4 in absence of a ligand (blank-altered) the contributions of both Fe species were, despite the concentration difference of a factor 10, in the same order. $HO^{\bullet}$ generation by chrysotile asbestos is governed by Fe^{3+}[4]; the contribution from Fe precipitates is negligible. A remanent mode of H_2O_2 decomposition by chrysotile was identified, which may be related to silanol functional groups at the surface-exposed Si layer and/or to magnetite impurities. H_2O_2 decomposition per se does not exhibit a high toxic potential in vivo, since its decomposition products can be detoxified enzymatically, but the

reductants obtained by H_2O_2 decomposition can reduce surface Fe^{3+}[4] and thereby enable the Fenton-oxidation of this highly redox reactive Fe species.

The occurrence of Fe^{3+}[4] in Fe-(hydr)oxides may, as well as in chrysotile, be correlated with their HRFP and their H_2O_2 decomposition capacity. However, whereas Fe(hydr)oxide minerals are not pathogenic [166], many different silicates other than chrysotile are, and in many of them Fe^{3+}[4] has been detected, e.g. in quartz, in a variety of sheet silicates including talcum, in amphiboles and in synthetic and natural zeolites [41, 167, 168, 169, 170, 171, 172, 173]. But even if no structural Fe^{3+}[4], or no Fe at all, is present in a pathogenic mineral, our results demonstrate that the presence of vacancy sites in a Si lattice can pose a risk, for incorporation of external Fe into the tetrahedral coordination environment suffices for $HO^{\bullet}$ generation. This may be particularly relevant in zeolites (e.g. erionite), which often have non-detectable bulk-Fe contents, but a higher potential to induce mesothelioma than asbestos [25]. Thereby, the dissolution of tetrahedral Al (which is a stoichiometric constituent of framework silicates) may create abundant vacancy sites in the Si-lattice of zeolite-fibers, which may be available for the incorporation of Fenton-active tetrahedrally coordinated Fe. In general, our data indicate that at circumneutral pH the generation of highly toxic $HO^{\bullet}$ does neither depend on the total bulk Fe content nor on the valence of Fe in chrysotile. The Fenton reactivity of chrysotile fibers depends on the amount of tetrahedrally coordinated Fe that is exposed on the surface of the fiber.

Third Chapter

"Presence, loss and recovery of redox cycling tetrahedral iron on chrysotile asbestos surfaces during dissolution"

Authors: Martin Walter[a], Walter D.C. Schenkeveld*[a]†, Gerald Geroldinger[b], Lars Gille[b], Stephan M. Kraemer[a]

Publication intended in: "Particle and Fibre Toxicology"

[a] Department of Environmental Geosciences, University of Vienna
Althanstraße 14 (UZA II), 1090 Vienna, Austria
*Email: w.d.c.schenkeveld@uu.nl

[b] Institute of Pharmacology and Toxicology, University of Veterinary Medicine, Vienna
Veterinärplatz 1, 1210 Vienna, Austria

† current address:
Copernicus Institute of Sustainable Development, Faculty of Geosciences, Utrecht University Princetonlaan 8A, 3584 CB Utrecht, The Netherlands

Abstract

Chrysotile asbestos is a toxic and carcinogenic mineral that has been used in western countries in a variety of industrial applications. It is still in use in other parts of the world today. The pathogenicity of asbestos is partly governed by the capability of Fe on the fiber surface to redox-cycle and catalyze the generation of highly toxic hydroxyl-radicals ($HO^{\bullet}$) out of H_2O_2, which is produced in inflammatory processes. Recently, tetrahedrally coordinated Fe (Fe^{3+}[4]) in the fibers' Si layers was identified to be the only Fe species that catalyzes this process. In this publication we investigated the presence, loss and recovery of redox cycling Fe^{3+}[4] on chrysotile surfaces during dissolution at pH 7.4. We demonstrate that structural Fe^{3+}[4] can fully redox cycle in exposed Si layers of chrysotile, either by H_2O_2 or by a combination of ascorbate and O_2. This redox cycling hardly promoted Si dissolution. Reduced tetrahedral Fe was stable (under anoxic conditions) and was the only ultimate Fenton-active Fe species on chrysotile surfaces. Fe that was not incorporated in the fibers' Si layers redox cycled outside the chrysotile structure and adsorbed as Fe^{2+} to chrysotile surfaces or precipitated as Fe^{3+} on the fiber surface in secondary Fe phases. We further demonstrate that redox-cycling of Fe^{3+}[4] synergistically increased its ligand promoted dissolution. The depletion of redox-cycling Fe^{3+}[4] from chrysotile surfaces was to a certain extent transient since Fe^{3+}[4] surface sites were recovered by the incorporation of catalytically active Fe in vacancies of the fibers' Si layer and by the surface-exposure of Fe^{3+}[4] from deeper Si layers after the dissolution of Fe^{3+}[4]-depleted layers. Our results suggest that the high catalytic activity and weathering resistance of Fe^{3+}[4] on fiber surfaces largely contribute to the redox-reactivity of asbestos fibers. Hence, Fe^{3+}[4] may clearly contribute to asbestos associated diseases.

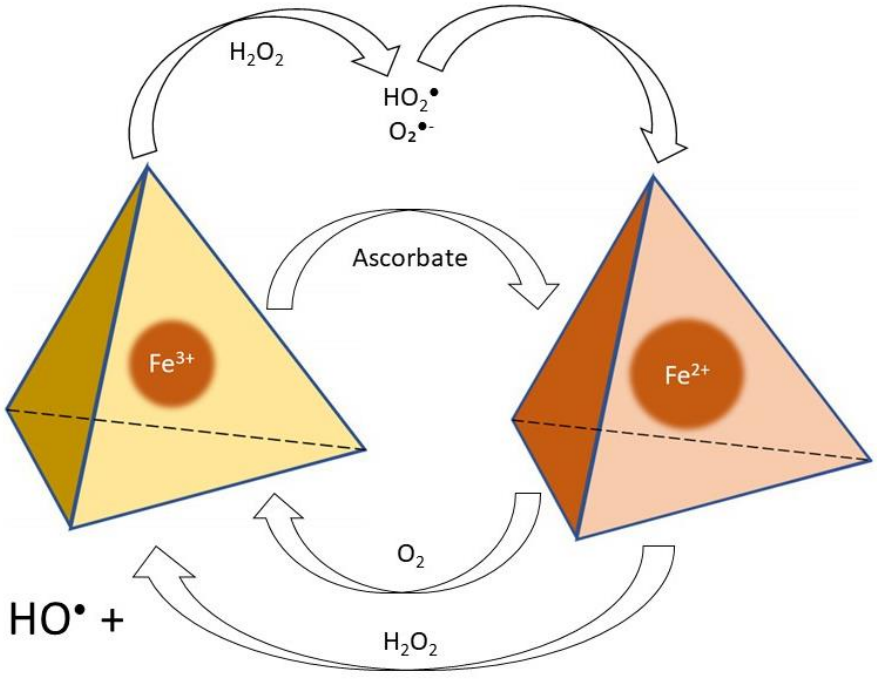

Background

Asbestos is a commercial term that was introduced for one serpentine mineral (chrysotile) and five amphiboles, all having a fibrous crystal habit [1]. The fibers were used in thermal and electrical insulation, roofing, cement pipes and sheets, flooring and coatings [16, 59] because they share favorable properties like unusual tensile strength, heat resistance and non-combustibility [14, 16]. However, the use of asbestos has been banned in EU-countries from the late 1980s onwards [21] since the minerals may, upon inhalation, induce pulmonary fibrosis and subsequently asbestosis, pleural effusion and plaques, but also malignant neoplasms like lung-carcinomas and pleural mesotheliomas [25, 29, 33, 59]. The WHO-IARC classifies all asbestos minerals as carcinogenic to humans (group 1) [144]. More than 100,000 people die because of asbestos each year, mostly because of occupational exposure [27]. Despite the severe adverse health effects that asbestos may induce, the use of the fibers has not been prohibited in northern American countries yet [21], whereas it even increases in some Asian countries [20, 23].

The historical use of asbestos was dominated by chrysotile (>95%) [13]. We consequently focus on chrysotile in this publication. Chrysotile asbestos [$Mg_3Si_2O_5(OH)_4$] consists of octahedral Mg and tetrahedral Si layers bundling together to a fiber with the external surface being Mg hydroxide [6, 7]. At pH 7.4, the positively charged outermost Mg layer dissolves within hours to days and renders a negatively charged exposed Si layer, which due to low dissolution kinetics controls the dissolution of deeper Mg layers [6, 97, 146]. Fe is substituted into the fibers' crystal structure during their petrogenesis (usually 2 – 4 wt%) and is the most abundant redox active metal in chrysotile [5]. Ferrous and ferric Fe enter Mg octahedra (Fe^{2+}[6] and Fe^{3+}[6] respectively), whereas exclusively ferric Fe enters Si tetrahedra (Fe^{3+}[4]) [38, 39, 146, 174]. Chelators like the siderophore desferrioxamine-B (DFOB) mobilize Fe from all three crystal sites at pH 7.4 [25, 146, 174]. The proton- or ligand-promoted dissolution of Fe^{3+}[4] causes the formation of vacant Si sites, which labilize the Si layer of chrysotile and therefore increase Si dissolution and, accordingly, Mg dissolution from deeper layers [146, 174].

Asbestos fibers are characterized by a high biopersistency in vivo [33, 36, 123]. Due to their fibrous crystal habit, alveolar macrophages furthermore fail to phagocytose and remove the fibers from exposed parenchymal lung or pleural tissues [3]. During this process (which is called frustrated phagocytosis), enzymatically formed reactive oxygen species (ROS) like hydrogen peroxide (H_2O_2) and superoxide ($O_2^{\bullet-}$) are released into the extracellular environment [33]. Fe on the fiber surface may interact with both ROS in redox reactions and catalyze the generation of highly reactive hydroxyl radicals ($HO^{\bullet}$), which cannot be enzymatically detoxified and have a high potency to damage DNA,

proteins and lipids [25, 32, 42, 43, 44, 45]. The catalytic property of Fe in this Haber-Weiss reaction is governed by redox cycles of Fe^{3+}, which is reduced by $O_2^{\bullet-}$ to Fe^{2+} and then back-oxidized by H_2O_2 in the so-called Fenton reaction to yield Fe^{3+} and $HO^{\bullet}$ [25, 46]. Fe^{2+} was demonstrated to be absent on the surface of pristine chrysotile fibers [48]. H_2O_2 may however decompose in the presence of Fe^{3+} to hydroperoxyl ($HO_2^{\bullet}$), which can either directly reduce Fe^{3+} to Fe^{2+}, or decompose into $O_2^{\bullet-}$, an even stronger reductant [49]. Apart from high $O_2^{\bullet-}$ and H_2O_2 levels caused by frustrated phagocytosis, physiologically abundant reductants such as ascorbate [175] are additionally known to reduce Fe^{3+} to Fe^{2+}. The concentration of ascorbate in bronchoalveolar lavages was demonstrated to increase during pulmonary redox-stress [176].

Among all three Fe species, Fe^{3+}[4] was demonstrated to be, despite its low abundancy (usually in the low % range), the dominating species in H_2O_2 decomposition and the only causal Fe species for $HO^{\bullet}$ generation on dissolving chrysotile surfaces [146, 174]. During dissolution at circumneutral pH, it remained Fenton-active for weeks in situ in exposed Si layers of chrysotile [146]. External Fe that was added to chrysotile surfaces was identified to exclusively catalyze fiber-mediated Haber-Weiss cycles when it incorporated tetrahedrally in vacancies of the fibers' Si layers [174]. The ionic radius of Fe^{3+}[4] is 49 pm, whereas the respective ionic radius of ferrous tetrahedral Fe (Fe^{2+}[4]) is 63 pm [177]. Because of the smaller ionic radius of Si^{4+} (26 pm), only Fe^{3+}[4] may substitute into tetrahedra, but not Fe^{2+}[4], resulting that Fe^{2+} does not substitute Si during the petrogenesis of natural silicates [161, 177]. Consequently, it has never been detected in chrysotile so far [38, 39, 146, 161, 174]. However, Fe^{3+}[4] has been found to be preferentially reduced over octahedral Fe in nontronites [163, 164, 165] to Fe^{2+}[4]. Additionally, Walter et al. (2018b) postulated that Fe^{2+}[4] is the ultimate Fenton-active Fe species for $HO^{\bullet}$ generation on chrysotile surfaces [174].

So far, the presence of Fe^{2+}[4] as the ultimate Fenton-active Fe species on chrysotile surfaces has never been verified. The high observed generation of $HO^{\bullet}$ radicals by tetrahedral Fe (Fe[4]) in the presence of H_2O_2 [146, 174] requires Fe[4] to redox cycle between Fe^{3+}[4] and Fe^{2+}[4] inside the Si layer of chrysotile, which has never been experimentally assessed yet. Furthermore, a contribution of the redox cycling of Fe[4] to the labilization of the fibers' Si layers and therefore overall Si dissolution has never been examined. Because of the layered structure of chrysotile [94], the formation of vacancies in Si layers by the depletion of Fe^{3+}[4] and the consequent dissolution of deeper Mg layers [146] may again expose Fe^{3+}[4] from underlying Si layers. Additionally, Fe dissolving from Mg layers may become incorporated in vacancies of Fe^{3+}[4]-depleted Si layers and become catalytically active, as demonstrated for external Fe [174]. This recovery of Fe^{3+}[4] during the dissolution of Fe^{3+}[4]-depleted fiber surfaces has to our knowledge never been assessed so far.

By addressing these research questions, we hypothesize that Fe[4] can fully redox cycle inside the crystal lattice of chrysotile asbestos by hardly promoting the dissolution of the respective Si layer. In this context we additionally hypothesize that Fe[4] undergoes cyclical redox reactions in the presence of H_2O_2 (which decomposes into reductants or directly oxidizes Fe^{2+}[4]), or by ascorbate as reductant and O_2 as oxidant. Contrarily to the redox cycling of Fe[4], we hypothesize that Fe not incorporated as Fe^{3+}[4] in the fibers' Si layers redox cycles outside the chrysotile structure, either by adsorbing as Fe^{2+} to chrysotile surfaces, or by precipitating as Fe^{3+}[6] in secondary Fe phases on the fiber surface. Regarding the ligand-promoted dissolution of Fe^{3+}[4], as observed by Walter et al. (2018a) and (2018b) [146, 174], we hypothesize that redox cycling of Fe^{3+}[4] promotes Si dissolution in the presence of Fe^{3+}[4]-complexing ligands. The rationale for this hypothesis is that redox cycling increases the ionic radius of Fe[4] by the reduction to Fe^{2+}[4], which may locally expand the Si lattice and thereby sterically favor the complexation of Fe[4] by ligands. Finally, we hypothesize that the depletion of redox active Fe^{3+}[4] sites from fiber surfaces, e.g. by Fe^{3+}[4]-complexing ligands, may be recovered during further fiber dissolution by the surface-exposure of Fe^{3+}[4] from deeper Si layers and by the incorporation of Fe from dissolving Mg layers into vacancies of exposed Si layers.

Assessing the redox-cycling of structural Fe[4] in on fiber surfaces contributes to the understanding of the high redox reactivity of this Fe species in chrysotile and may, apart from chrysotile, also be relevant for understanding the redox properties of other pathogenic silicate minerals.

All hypotheses were mostly tested at the physiologic lung pH of 7.4 in batch dissolution experiments and subsequent ICP-OES and EPR spin trapping analyses.

Methods

Material

Commercial chrysotile was purchased from Shijiazhuang Mining IMP&EXP Trade Co from China. Raman-identification of single fibers, XRD-Rietveld phase analyses, BET surface area measurement, Mössbauer bulk-Fe analysis, fusion digestion and a neutron activation analysis of the same batch of Shijiazhuang chrysotile were already carried out by Walter et al. (2018a) [146]. Selected bulk characteristics of Shijiazhuang chrysotile are summarized in Table 1. All chemical reagents were bought at least in p.a. quality from VWR (unless specifically mentioned).

Table 1.) *Bulk characteristics of pristine Shijiazhuang chrysotile fibers (as previously reported by Walter et al. (2018a) [146]). Values in round brackets represent standard deviations.*

Bulk characteristics of chrysotile asbestos			
Bulk composition:		*Fusion digestion (n = 15):*	*NAA[1] (n = 2):*
Mg	[g kg^{-1}]	249 (7)	
Si	[g kg^{-1}]	188 (3)	
Fe	[g kg^{-1}]	19.0 (1.4)	21.4 (0.3)
bulk Fe speciation:		*Mössbauer:*	
Fe^{2+}[6]	[%]	38.4	
Fe^{3+}[6]	[%]	54.6	
Fe^{3+}[4]	[%]	7.0	
Total Fe in chrysotile[2]	[%]	68.2	

[1] neutron activation analysis
[2] Remaining Fe (31.8%) is in magnetite impurities

General experimental procedure of anoxic and oxic experiments

All dissolution experiments and all corresponding fiber alterations were done in a solid to solution ratio of 1 g L^{-1}. 50 mmol L^{-1} of the non-metal-complexing tertiary amine ("Better") buffer [139] MOPS (3-(*N*-morpholino)propanesulfonic-acid) and PIPPS (1,4-Piperazinedipropanesulfonic-acid) were used to maintain the pH of samples at 7.4 ± 0.3 and 3.0 ± 0.3 respectively. To compare the results of this study with two previously published studies on Shijiazhuang chrysotile [146, 174], ionic strength levels of all samples were adjusted to 300 mmol L^{-1} by addition of NaCl. Apart from the buffered-only "blank"-treatments, treatments were carried out in the presence of DFOB (Novartis), an Fe^{2+}-specific ligand (ferrozine, Sigma Adrich) and the reductant ascorbate at a default concentration of 1 mmol L^{-1}.
Duplicates of fiber dissolution experiments were incubated for 0.5, 1, 4, 8, 24, 48, 96 and 336 h in 15 ml PP-tubes (VWR) in an end-over-end shaker at 15 round per minute (RPM) at 20 ± 2°C in the dark.
Both solution and fiber sampling were done destructively: Fiber-suspensions were filtered over 0.45 µm Sartorius cellulose acetate syringe filters (VWR). Aliquots of the filtrate were acidified with trace metal grade HNO_3 to 0.14 mol L^{-1}. Fibers were sampled by vacuum filtration and retained by 0.47 µm Nylon membranes (Magna) in Büchner funnels and washed with ultra-pure water to remove potentially adsorbed free ligands or metal complexes. Then, the fibers were vacuum dried and kept in an evacuated desiccator for follow-up experiments or EPR analyses.
Metal (Mg and Fe) and Si contents of the experimental solutions and of all fiber-sampling solutions were analyzed by ICP-OES spectrometry (Optima 5300-DV, Perking Elmer). The calibration standards

were matrix-matched with the samples. Mobilized metal and Si concentrations from fiber-sampling solutions can be found in SI-Table 1.

Fiber preparation prior to oxic and anoxic dissolution experiments

To identify redox cycling Fe^{3+}[4] and its loss and recovery on chrysotile surfaces, fibers were differently altered prior to the respective experiments to obtain four different fiber types with a characteristic surface chemistry. Pristine fibers were incubated under oxic conditions for 336 h in buffered pH 7.4 blank solutions ("blank altered fibers") and in pH 7.4 buffered 1 mmol L^{-1} DFOB solutions ("DFOB altered fibers"). Both treatments were already described by Walter et al. (2018a), and experimentally used by Walter et al. (2018b) [146, 174]. During the fibers' preconditioning, the outermost Mg layer of both fiber types dissolved. The Fe content of the dissolving Mg layer however either precipitated on the fiber surface as non-Fenton-active secondary Fe-phases (blank altered fibers) [146], or was complexed and removed from the fiber surface by DFOB (DFOB altered fibers). The preconditioning with DFOB removed the Fe^{3+}[4]-content of the exposed non-dissolving Si layer, causing the formation of vacant sites in the Si layer, which promote Si dissolution [146, 174].

Furthermore, anoxic fiber preconditioning was carried out in a glove box (coy chamber) filled with forming gas (with ≤ 3% of H_2 and O_2 contents below 1 ppm throughout the experiments). Pristine fibers were altered for 336 h in pH 7.4 buffered anoxic ascorbate solutions ("ascorbate altered fibers"). The respective vacuum filtration and vacuum drying of ascorbate altered fibers was exclusively carried out inside the anoxic glove box. Ascorbate altered fibers were then re-oxidized in a pH 7.4 buffered solution under air bubbling and magnetic stirring (500 RPM) for 24 h outside the glovebox. The respective fibers were then again vacuum filtrated and vacuum dried (under oxic conditions) and are called "re-oxidized ascorbate altered fibers".

Anoxic dissolution experiments

Anoxic dissolution experiments were carried out in the same glove box under the same conditions as described above. Pristine, blank and DFOB altered fibers and re-oxidized ascorbate altered fibers were incubated in buffered pH 7.4 blank, ascorbate, ferrozine and ferrozine + ascorbate solutions. Data of pristine fibers, blank and DFOB altered fibers incubated in pH 7.4 blank and ferrozine treatments can exclusively be found in SI-Figure 1.

Oxic dissolution experiments

Blank and DFOB altered fibers were incubated in buffered pH 7.4 blank or DFOB solutions. Additionally, an experiment was carried out in which pristine fibers, blank and DFOB altered fibers were incubated for 96 and 336 h in pH 7.4 buffered DFOB or ferrozine solutions containing a 100x diluted H_2O_2 of a 30

% H_2O_2 stock (Sigma, for trace analysis) at the beginning of the experiment. Prior to the experiment, the concentration of the H_2O_2 stock was determined in three $KMnO_4$ titrations and was calculated to be 334 g L^{-1}, with a standard deviation of 2 g L^{-1}. Data reported in this publication are compared to already published dissolution data of pristine Shijiazhuang fibers incubated in pH 7.4 blank and 1 mmol L^{-1} DFOB solutions [146] and of pristine, blank and DFOB altered Shijiazhuang fibers incubated in pH 7.4 buffered 3.34 g L^{-1} H_2O_2 solutions [174]. The corresponding H_2O_2 decomposition kinetics of the latter dissolution experiments can be found in the publication of Walter et al. (2018b) [174].

Measurement of the HRFP of fibers by EPR spin trapping

The generation of $HO^{\bullet}$ by pristine and altered fibers due to Fenton-like redox reactions in the presence of H_2O_2 was quantified with 5-5'-dimethyl-1-pirroline-N-oxide (DMPO) as spin trap using a X-band EPR-spectrometer (Bruker EMX) and a split ring resonator (Bruker MD5). Quadruplicates of four different fiber types were analyzed, the incubation time of each alteration step was 336 h. The analyzed fiber types were DFOB altered fibers, DFOB altered fibers incubated in pH 7.4 and pH 3.0 blank solutions and pH 3.0 blank altered fibers incubated in a pH 3.0 blank solution. The detection of $HO^{\bullet}$ by DMPO in the presence of asbestos fibers has been frequently carried out before [35, 37, 43, 50, 121, 146, 174]. Accordingly, 11 mg of fibers were incubated for 0.5 h in 0.5 ml of a 125 mmol L^{-1} H_2O_2 and 12.5 mmol L^{-1} DMPO solution buffered at pH 7.3 with a 250 mmol L^{-1} chelex pre-treated phosphate buffer. After 25 min of incubation and 5 min of centrifugation at 14000 RPM at room temperature, 50 µl of the supernatant were aspirated into a glass capillary (intraMark Blaubrand) and afterwards sealed with Critoseal. The capillary was subsequently transferred into the resonator. The parameters of the EPR measurements were identical to the ones applied by Walter et al. (2018a) [146]. The mean signal intensity (Ipp, Intensity peak-to-peak) of the second peaks from the left in the DMPO/$HO^{\bullet}$ quadruplet of altered fibers (≙ the decreased HRFP) was expressed as the percentage of the mean Ipp of a quadruplicate of pristine fibers, which was measured each measurement session.

Data analysis and supplementary data

Synergistic metal mobilization was identified when a measured value of a combined treatment was not obtained by summing up the measured values of the respective separate treatments. Thereby, metal concentrations obtained from blank treatments were subtracted from concentrations obtained in the combined and the separate treatments.

For the statistical evaluation of EPR spin trapping results, a F-test was used to determine equal or unequal variance between samples. The analyzed samples had an equal variance, therefore a one-way

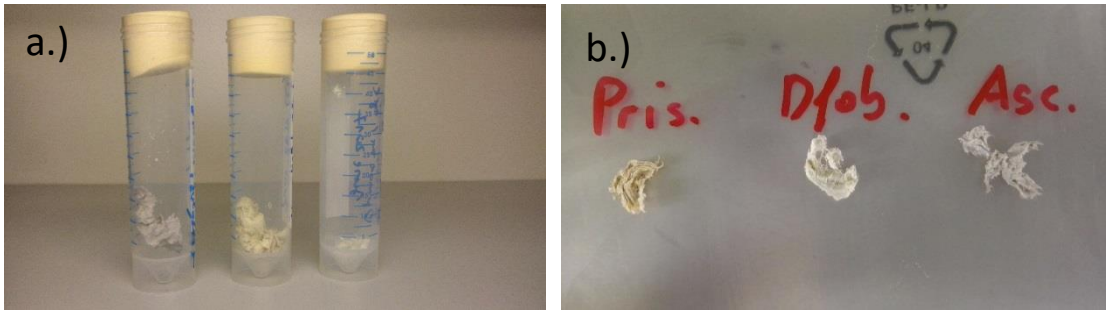

Figure 1.) *Alteration of fibers and the resulting colors. Panel a.) From left to right: Ascorbate altered fibers, blank altered fibers and DFOB altered fibers; Panel b.) From left to right: Pristine fibers, DFOB altered fibers and ascorbate altered fibers. The pale-pinkish color of ascorbate altered fibers was observed by incubating pristine, blank and DFOB altered fibers in pH 7.4 ascorbate solutions, the color change in DFOB altered fibers treatments from whitish to pale-pinkish however only occurred in later stages of the experiment.*

ANOVA (alpha 0.05) test was used to determine if there was a significant difference in the data. Applying a subsequent Turkey HSD test was not required.

All analyzed data reported in the figure can be found in Si-Table 2 to 6 respectively.

Results

Visible color change of altered fibers

The similar brownish color of pristine and blank altered fibers and the whitish color of DFOB altered fibers were already described by Walter et al. (2018b) [174]. However, the pale-pinkish color of ascorbate altered fibers (Figure 1) differed from these two fiber colors. By re-oxidizing ascorbate altered fibers, the pale-pinkish color disappeared and changed to a brownish to greyish color (SI-Figure 2).

Detection of Fe^{2+}[4] and redox cycling tetrahedral Fe on chrysotile surfaces

Since only 7% of the bulk-Fe of Shijiazhuang chrysotile was detected to be Fe^{3+}[4] (Table 1), and since only ≈30 µmol L^{-1} Fe were mobilized by DFOB from the first Mg and Si layer during dissolution at pH 7.4 (SI-Table 1), one can estimate the Fe^{3+}[4] concentration in the first Si layer to be ≈ 3 µmol g^{-1} fibers.

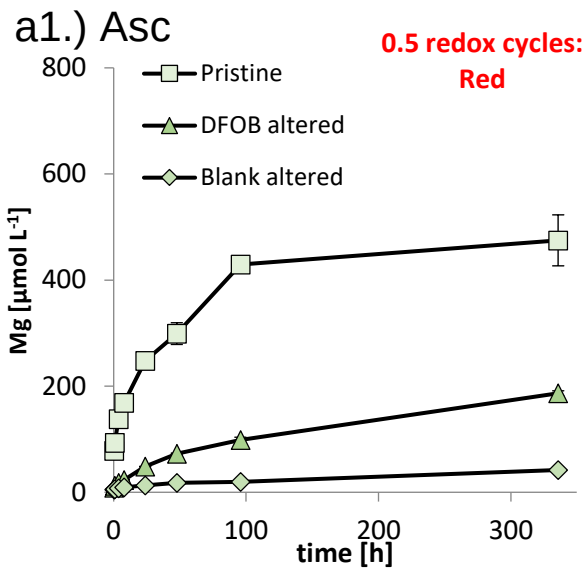
a1.) Asc
0.5 redox cycles:
Red
Pristine
DFOB altered
Blank altered
Mg [µmol L-1]
800
600
400
200
0
0
100
200
300
time [h]

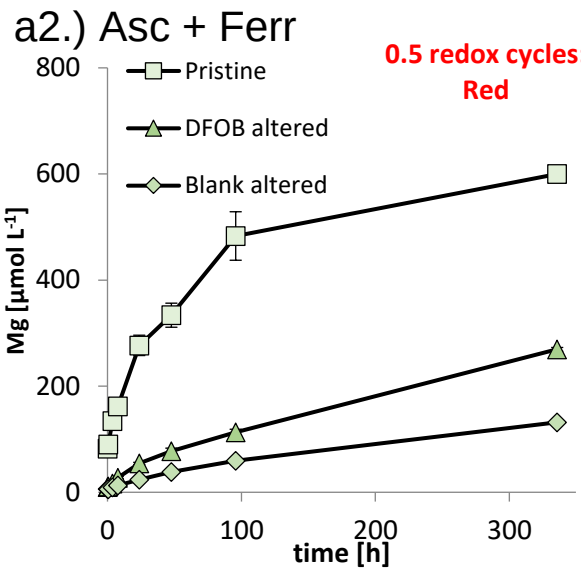
a2.) Asc + Ferr
0.5 redox cycles:
Red
Pristine
DFOB altered
Blank altered
Mg [µmol L-1]
800
600
400
200
0
0
100
200
300
time [h]

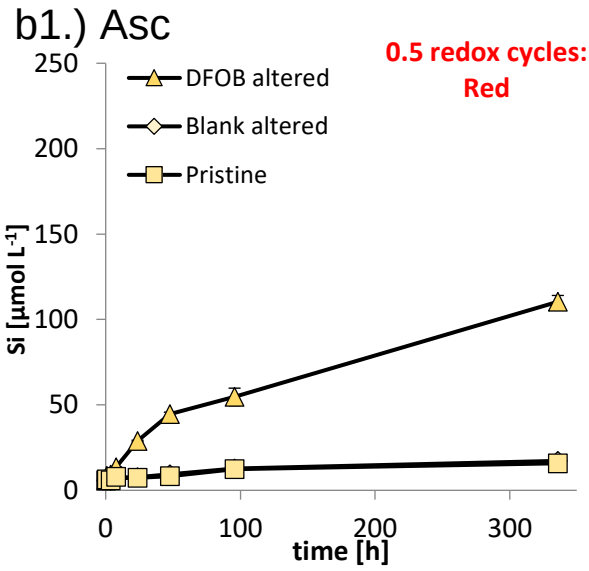
b1.) Asc
0.5 redox cycles:
Red
DFOB altered
Blank altered
Pristine
Si [µmol L-1]
250
200
150
100
50
0
0
100
200
300
time [h]

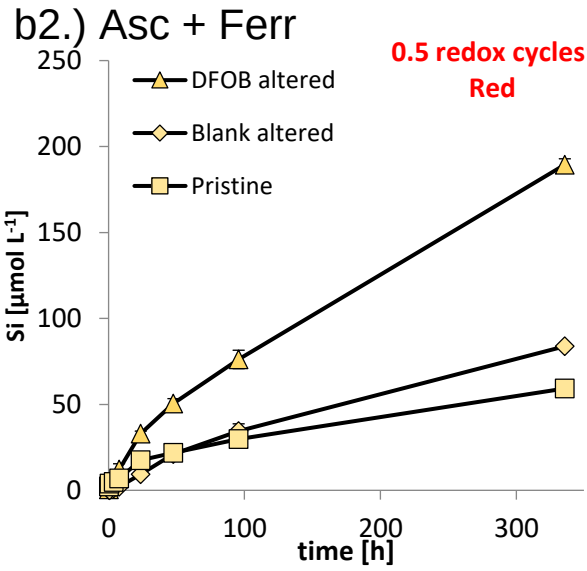
b2.) Asc + Ferr
0.5 redox cycles:
Red
DFOB altered
Blank altered
Pristine
Si [µmol L-1]
250
200
150
100
50
0
0
100
200
300
time [h]

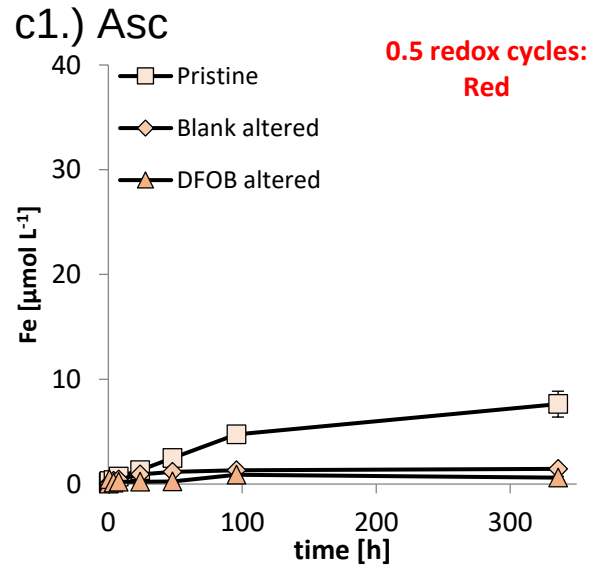
c1.) Asc
0.5 redox cycles:
Red
Pristine
Blank altered
DFOB altered
Fe [µmol L-1]
40
30
20
10
0
0
100
200
300
time [h]

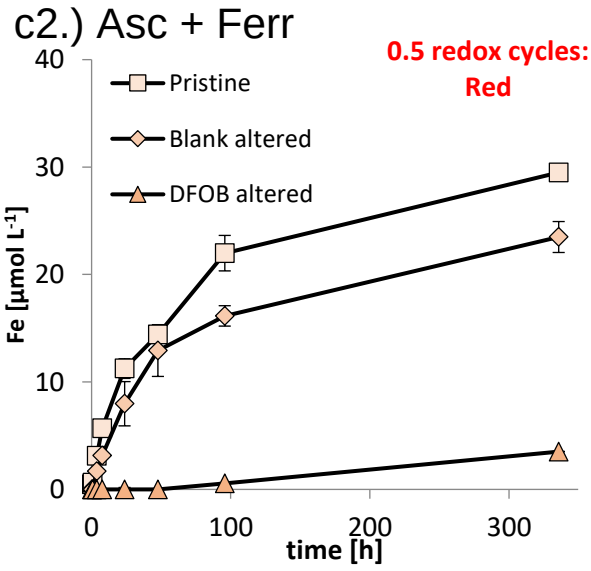
c2.) Asc + Ferr
0.5 redox cycles:
Red
Pristine
Blank altered
DFOB altered
Fe [µmol L-1]
40
30
20
10
0
0
100
200
300
time [h]

↑ ***Figure 2.)*** *Anoxic incubation of pristine fibers, blank altered fibers and DFOB altered fibers in either pH 7.4 buffered 1 mmol L^{-1} ascorbate or 1 mmol L^{-1} ascorbate + ferrozine solutions. Mobilized Mg (panel a), Si (panel b) and Fe (panel c) concentrations from ascorbate treatments can be found in the subpanels 1, from the ascorbate + ferrozine treatments in the subpanels 2. Incubation times were 0.5, 1, 4, 8, 24, 48, 96 and 336 h. Error bars indicate standard deviations (n = 2). The amount of redox cycles of Fe^{3+}[4] (and octahedral Fe) is indicated in red ("Red" = reduction). Additionally, the corresponding data of mobilized metal concentrations from the same fiber types in anoxic pH 7.4 buffered blank and 1 mmol L^{-1} ferrozine solutions can be found in SI-figure 1.*

Since Mössbauer spectroscopy is not sensitive enough to detect such low concentrations, we indirectly analyzed the presence of Fe^{2+}[4] under anoxic conditions via the metal and Si mobilization from chrysotile surfaces in the presence of a reductant (ascorbate) and/or ferrozine (Figure 2 and 3). Metal and Si concentrations mobilized from pristine, blank and DFOB altered fibers in anoxic pH 7.4 blank and ferrozine treatments were comparable or lower than the ones observed in ascorbate treatments and are exclusively presented in SI-Figure 1.

Mg concentrations mobilized from pristine fibers in the presence of ascorbate (Figure 2, Panel a1) followed the two dissolution stages of Mg described for pristine Shijiazhuang chrysotile fibers by Walter et al. (2018a) [146]: In the first rapid stage of Mg dissolution, large parts of the outermost exposed Mg layer dissolved during the early sampling times of the experiment (Figure 2, Panel a1). Later in the second stage, further Mg dissolution was hampered by the low solubility of the first exposed Si layer so that mobilized Mg concentrations did not exceed 500 - 600 µmol L^{-1} (which corresponds with the dissolution of the outermost Mg layer of Shijiazhuang chrysotile [146]). Contrarily, Mg concentrations mobilized from DFOB and blank altered fibers in the presence of ascorbate increased more linearly up to 187 µmol L^{-1} and 42 µmol L^{-1} respectively after 336 h of incubation (Figure 2, Panel a1). Mobilized Mg concentrations from DFOB and blank altered fibers in the presence of ascorbate and ferrozine also increased linearly (Figure 2, Panel a2), but were considerably higher than in the mere presence of ascorbate (e.g. 270 and 132 µmol L^{-1} respectively after 336 h). Si concentrations mobilized from pristine and blank altered fibers (Figure 2, Panel b1) were equally low in the presence of ascorbate (e.g. 16 - 17 µmol L^{-1} after 336 h), whereas they were considerably higher in DFOB altered fiber treatments (e.g. 110 µmol L^{-1} after 336 h). Comparably to Mg mobilization, mobilized Si concentrations were higher when ferrozine was added to the respective ascorbate treatment (Figure 2, Panel b2): Si concentrations mobilized from pristine, blank and DFOB altered fibers increased to 59, 84 and 189 µmol L^{-1} respectively after 336 h of incubation. By comparing the dissolution of DFOB and blank altered fibers in the presence of ascorbate + ferrozine (Figure 2, Panel a2 and b2), mobilized Mg and Si concentrations were stoichiometric (factor 1.5) at later sampling

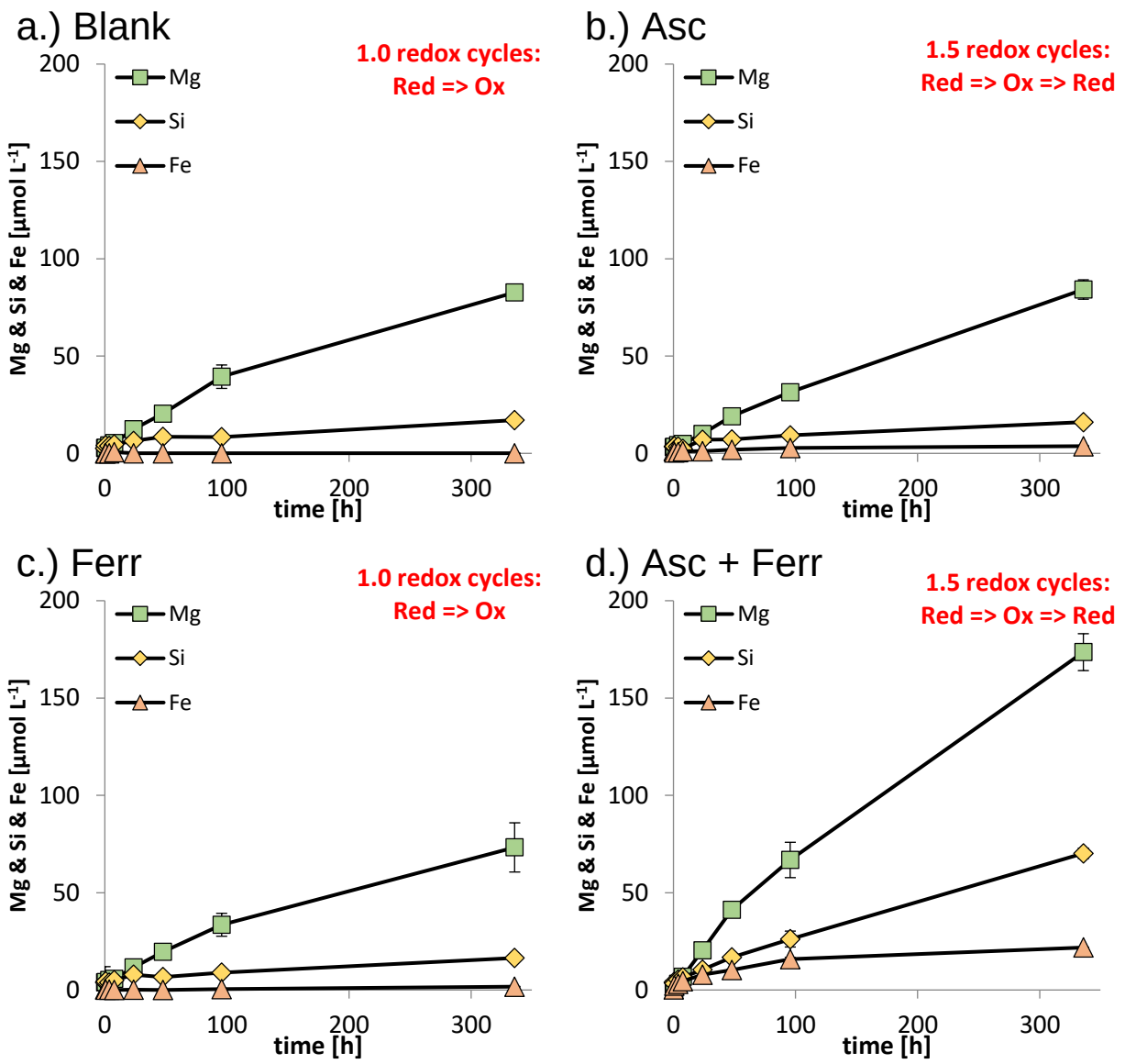

Figure 3.) *Mg, Si and Fe concentrations mobilized from re-oxidized ascorbate altered fibers. The fibers were incubated under anoxic conditions in a pH 7.4 buffered blank (panel a), 1 mmol L^{-1} ascorbate (panel b), 1 mmol L^{-1} ferrozine (panel c) and 1 mmol L^{-1} ascorbate + ferrozine solution for 0.5, 1, 4, 8, 24, 48, 96 and 336h. Error bars indicate standard deviations (n = 2). The amount of redox cycles of Fe^{3+}[4] (and octahedral Fe) is indicated in red ("Red" = reduction, "Ox" = oxidation).*

points of the experiments. Finally, mobilized Fe concentrations in the presence of ascorbate only increased in pristine fiber treatments up to 8 µmol L^{-1} after 336 h of incubation (Figure 2, Panel c1), whereas they increased to a clearly higher extent in pristine, blank and DFOB altered fiber treatments in the presence of ascorbate and ferrozine to 29, 23 and 4 µmol L^{-1} respectively (Figure 2, Panel c2).

Mg and Si concentrations mobilized from re-oxidized ascorbate altered fibers in blank and ferrozine treatments (Figure 3, Panel a and c) were similar (e.g. 73 and 83 µmol L^{-1} Mg and 16 and 17 µmol L^{-1} Si respectively after 336 h of incubation). In both treatments, the Fe^{3+}[4] content of the exposed Si layers

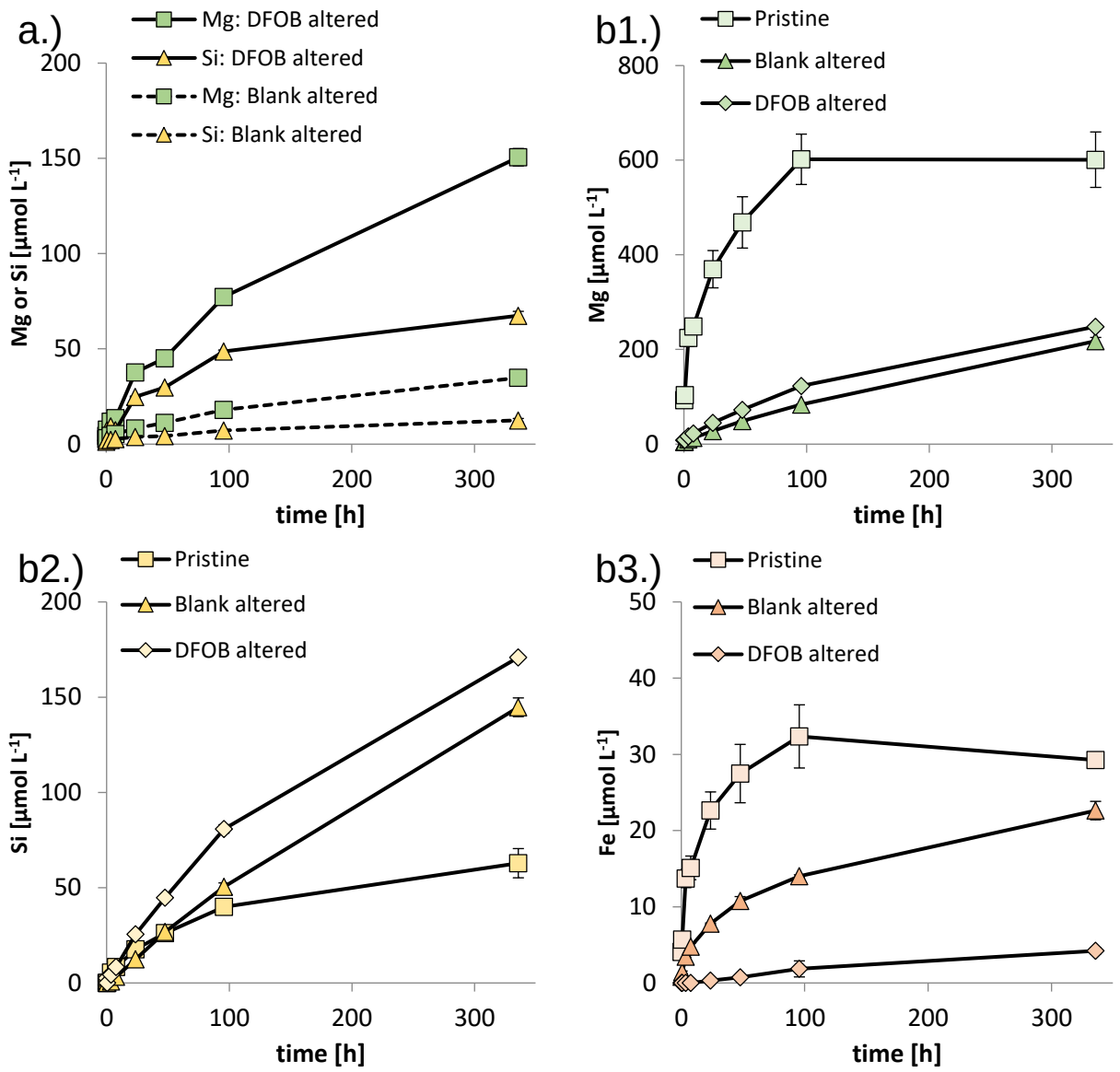

Figure 4.) *Incubation of pristine fibers, blank and DFOB altered fibers under oxic conditions. Panel a.) Mg and Si concentrations mobilized from blank and DFOB altered fibers in a pH 7.4 blank solution; Panel b.) Mobilized Mg (Panel b1), Si (Panel b2) and Fe (Panel b3) concentrations from pristine, blank and DFOB altered fibers. Incubation times were 0.5, 1, 4, 8, 24, 48, 96 and 336 h. Error bars indicate standard deviations (n = 2). Data of Mg, Si and Fe mobilization from pristine fibers by DFOB (Panel b1-3) were taken from Walter et al. (2018a) [146].*

had concluded one full redox cycle prior to the experiment. However, in the treatments containing ascorbate (Figure 3, Panel b and d), the Fe^{3+}[4] content of the surface exposed Si layer of re-oxidized ascorbate altered fibers had even concluded 1.5 redox cycles. Mg and Si concentrations mobilized from re-oxidized ascorbate altered fibers in ascorbate treatments were comparable to the ones mobilized in blank and ferrozine treatments (Figure 3, Panel b). Mobilized Fe concentrations however were higher (e.g. 4 µmol L^{-1} after 336 h). Finally, Mg, Si and Fe concentrations mobilized in the ascorbate +

ferrozine treatment (Figure 3, Panel d) were considerably higher than in all the other three treatments, increasing to 174, 70 and 22 µmol L^{-1} respectively after 336 h of incubation.

In both experiments, the blank corrected increased mobilized Mg, Si and Fe concentrations in ascorbate + ferrozine treatments constituted a synergistic increase relative to the sum of the blank corrected mobilized concentrations in the separate ferrozine and ascorbate treatments (Figure 2 and 3, SI-figure 1).

Loss of redox cycling tetrahedral Fe on chrysotile surfaces

In order to assess the loss of Fe^{3+}[4] from exposed Si layers of pristine and altered chrysotile fibers by redox cycling, at first the redox-independent loss of Fe^{3+}[4] by hydrolysis or direct complexation by ligands was assessed under oxic conditions (Figure 4). Regarding the latter, DFOB was used since it was observed to directly complex Fe^{3+}[4] from pristine fibers [146].

Mg and Si concentrations mobilized from blank altered fibers in pH 7.4 blank treatments (e.g. 35 and 13 µmol L^{-1} respectively after 336 h) were considerably lower than from DFOB altered fibers (e.g. 151 and 67 µmol L^{-1} respectively) (Figure 4, Panel a). Mobilized Mg and Si concentrations from both fiber types were not stoichiometric. Contrarily to blank treatments, mobilized Mg and Si concentrations from blank and DFOB altered fibers approximately increased linearly in the presence of DFOB (Figure 4, Panel b1 and b2). Thereby, mobilized Mg concentrations increased up to 218 and 248 µmol L^{-1}, whereas mobilized Si concentrations increased up to 145 and 171 µmol L^{-1} after 336 h of incubation respectively. Similarly as observed in blank and DFOB altered fiber treatments in the presence of ascorbate + ferrozine, mobilized Mg and Si concentrations from blank and DFOB altered fibers in the presence of DFOB were stoichiometric (factor 1.5) in late sampling points of the experiments. Mobilized Fe concentrations from pristine fibers reached a plateau of ≈30 µmol L^{-1} after 48 h of incubation (Figure 4, Panel b3), which represents the complete dissolution of the Fe content of the first Mg and Si layer of Shijiazhuang chrysotile [146]. However, Fe mobilization from blank and DFOB altered fibers did not reach this plateau and only increased to 23 and 4 µmol L^{-1} respectively after 336 h of incubation.

Mobilized Mg, Si and Fe concentrations after 96 and 336 h of incubation in the presence and absence of H_2O_2 and/or DFOB are presented in Figure 5 to compare the depletion of Fe[4] from chrysotile surfaces by redox cycling with H_2O_2 with the depletion of Fe[4] by hydrolysis or complexation. Because of high standard deviations, mobilized Mg concentrations from pristine fibers after 96 h of incubation (Figure 5, Panel a1) were similar in blank, DFOB, H_2O_2, and H_2O_2 + DFOB treatments (≈ 500 - 600 µmol L^{-1}), all represent the dissolution of the first Mg layer [146]. However, they were considerably

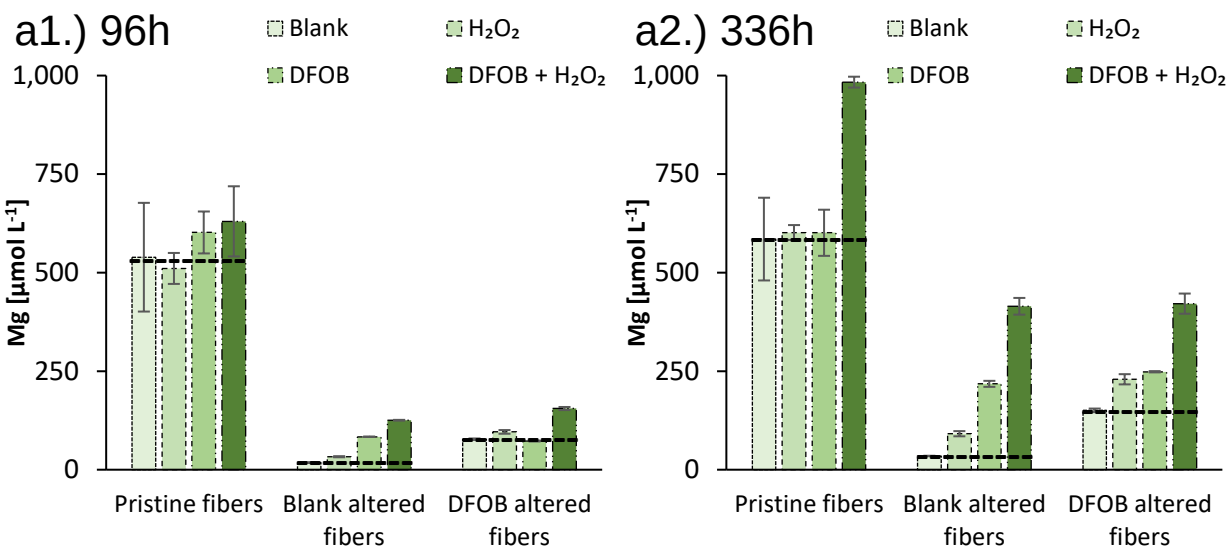
a1.) 96h
Blank
H₂O₂
DFOB
DFOB + H₂O₂
1,000
750
500
250
0
Mg [µmol L⁻¹]
Pristine fibers
Blank altered fibers
DFOB altered fibers

a2.) 336h
Blank
H₂O₂
DFOB
DFOB + H₂O₂
1,000
750
500
250
0
Mg [µmol L⁻¹]
Pristine fibers
Blank altered fibers
DFOB altered fibers

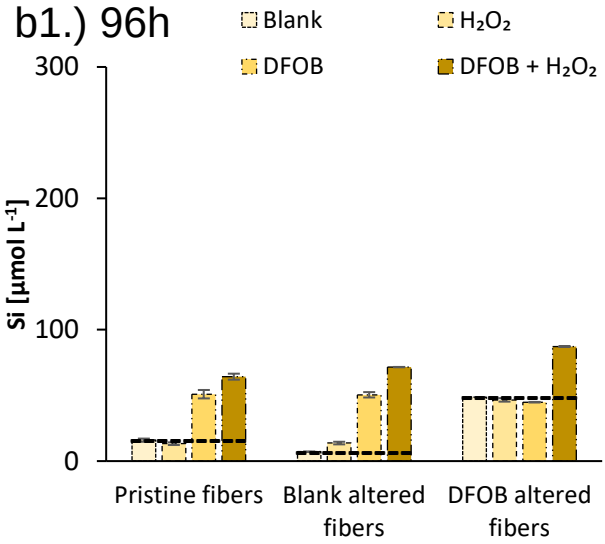
b1.) 96h
Blank
H₂O₂
DFOB
DFOB + H₂O₂
300
200
100
0
Si [µmol L⁻¹]
Pristine fibers
Blank altered fibers
DFOB altered fibers

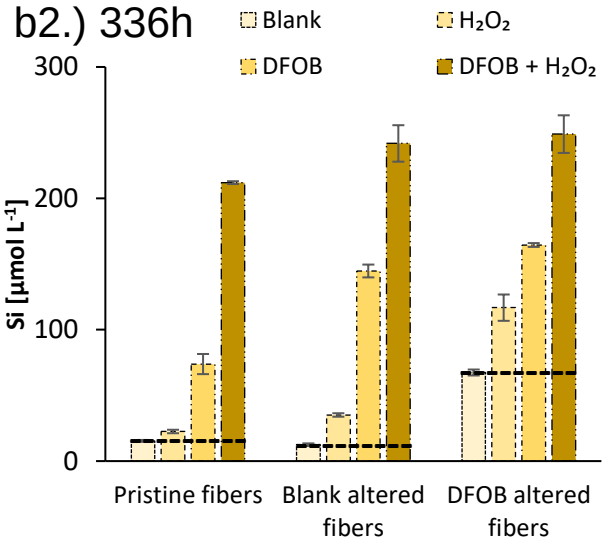
b2.) 336h
Blank
H₂O₂
DFOB
DFOB + H₂O₂
300
200
100
0
Si [µmol L⁻¹]
Pristine fibers
Blank altered fibers
DFOB altered fibers

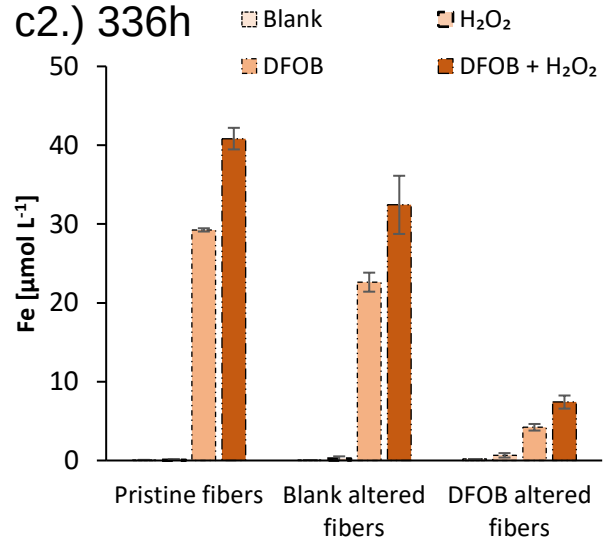
c2.) 336h
Blank
H₂O₂
DFOB
DFOB + H₂O₂
50
40
30
20
10
0
Fe [µmol L⁻¹]
Pristine fibers
Blank altered fibers
DFOB altered fibers

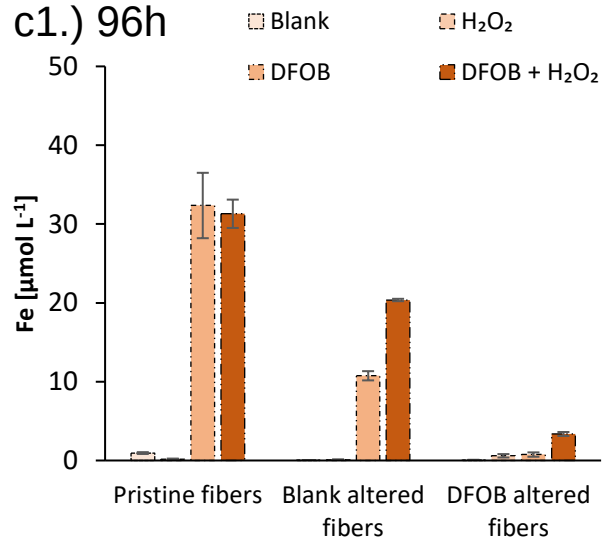
c1.) 96h
Blank
H₂O₂
DFOB
DFOB + H₂O₂
50
40
30
20
10
0
Fe [µmol L⁻¹]
Pristine fibers
Blank altered fibers
DFOB altered fibers

↑ ***Figure 5.)*** *Synergistic Mg (Panel a), Si (Panel b) and Fe (Panel c) concentrations after 96 h (Subpanels 1) and 336 h (Subpanels 2) of incubation mobilized from pristine fibers, blank altered fibers and DFOB altered fibers in oxic pH 7.4 buffered blank, 3.34 g L^{-1} H_2O_2, 1 mmol L^{-1} DFOB and 1 mmol L^{-1} DFOB + 3.34 g L^{-1} H_2O_2 solutions. 3.34 g L^{-1} was the starting concentration of all H_2O_2 incubations. Dashed lines approximately indicate the blank level of the respective metal or Si mobilization. Error bars indicate standard deviations (n = 2). Data of the blank and DFOB treatments of pristine fibers were taken from Walter et al. (2018a) [146], data of H_2O_2 treatments were taken from Walter et al. (2018b) [174]. The H_2O_2 decomposition of all H_2O_2 and DFOB + H_2O_2 treatments were reported by Walter et a. (2018b) [174].*

higher in the H_2O_2 + DFOB treatment (983 µmol L^{-1}) after 336 h of incubation (Figure 5, Panel a2). Mg concentrations mobilized from DFOB and blank altered fibers successively increased from blank to H_2O_2 to DFOB to H_2O_2 + DFOB treatments, this increase was more pronounced after 336 h than 96 h of reaction time (Figure 5, panel a1 and a2). Mobilized Mg concentrations started from a higher level in DFOB altered fiber treatments compared to blank altered and pristine fiber treatments since the labilized Si layers (from the fibers' pre-treatment) of DFOB altered fibers permitted a higher dissolution of Mg from structurally deeper layers (SI-Table 1). Si concentrations mobilized from pristine fibers after 336 h of incubation were low in blank and H_2O_2 treatments (all below 25 µmol L^{-1}), but increased in the presence of DFOB (74 µmol L^{-1}) and sharply increased to 212 µmol L^{-1} in H_2O_2 + DFOB treatments. A comparable sharp increase in mobilized Si concentrations was observed from blank altered fibers, in which 145 µmol L^{-1} of Si were mobilized by DFOB after 336 h, whereas 242 µmol L^{-1} were mobilized by H_2O_2 + DFOB (Figure 5, Panel b2). Mobilized Si concentrations from DFOB altered fibers also successively increased in blank, DFOB, H_2O_2, and H_2O_2 + DFOB treatments after 336 h, but again from a higher level as observed in the two other fiber treatments (Figure 5, Panel b2). Mobilized Si concentrations after 96h of incubation were only increased in DFOB and in H_2O_2 + DFOB treatments relative to blank and H_2O_2 treatments (Figure 5, Panel b1). Fe was only mobilized in DFOB and H_2O_2 + DFOB treatments, whereby Fe concentrations mobilized in H_2O_2 + DFOB treatments from all three fiber types were, apart from pristine fibers after 96 h, clearly higher than in DFOB treatments (Figure 5, Panel c1 and c2).

The blank corrected increased Mg, Si and Fe concentrations mobilized in H_2O_2 + DFOB treatments from all three fiber types mostly constituted a synergistic increase over the sum of the respective blank corrected concentrations mobilized in the separate H_2O_2 and DFOB treatments. This synergism was highest in pristine fibers and lowest in DFOB altered fibers (Figure 5).

To assess whether Fe^{2+}[4] can be complexed by ferrozine during the redox cycling of Fe[4] by H_2O_2 under oxic conditions and whether this initiates Si-labilization, metal and Si mobilization from pristine,

Table 2: *Mg, Si and Fe concentrations (in µmol L^{-1}) mobilized during 96 and 336 h of incubation from pristine, blank and DFOB altered fibers suspended in either 1 mmol L^{-1} DFOB or ferrozine and 3.34 g L^{-1} H_2O_2 solutions. Numbers in round brackets represent standard deviations (n = 2).*

Fiber type	Time [h]	Mg		Si		Fe	
		DFOB	Ferrozine	DFOB	Ferrozine	DFOB	Ferrozine
Pristine	96	630 (89.0)	430 (20.6)	64.3 (2.3)	10.4 (0.7)	31.3 (1.8)	0.9 (0.2)
	336	983 (13.8)	619 (0.0)	212 (1.1)	18.8 (2.6)	40.8 (1.4)	2.7 (0.1)
Blank altered	96	125 (0.9)	27.5 (3.0)	71.5 (0.1)	11.3 (0.4)	20.4 (0.2)	0.1 (0.1)
	336	415 (21.2)	81.3 (1.6)	242 (13.9)	33.4 (1.8)	32.4 (3.7)	1.0 (0.1)
DFOB altered	96	155 (3.9)	95.8 (2.4)	87.2 (0.0)	50.1 (0.4)	3.4 (0.3)	0.3 (0.0)
	336	421 (25.6)	228 (19.7)	249 (14.3)	127 (9.0)	7.7 (0.8)	0.4 (0.0)

blank and DFOB altered fibers in the presence of H_2O_2 + ferrozine was assessed (Table 2). Thereby, mobilized Mg, Si and Fe concentrations in all fiber treatments after 96 and 336 h of incubation were considerably lower as in the respective H_2O_2 + DFOB treatments. In fact, mobilized concentrations in H_2O_2 + ferrozine treatments can be well compared to the respective concentrations mobilized in the presence of H_2O_2 only (Figure 5).

Recovery of Fenton-active tetrahedral Fe on dissolving chrysotile surfaces

Incubating DFOB altered fibers with a HRFP of 9% for 336 h in a pH 7.4 buffered blank solution significantly increased the fibers' HRFP to 13% (Figure 6). However, incubating DFOB altered fibers for 336 h in a pH 3.0 buffered blank solution even increased the fibers' HRFP to 20%, a similar HRFP as obtained by incubating pristine fibers for two consecutive incubation times of 336 h in buffered pH 3.0 blank solutions, in which fibers had a HRFP of 21%.

Discussion

Detection of Fe^{2+}[4] and redox cycling tetrahedral Fe on chrysotile surfaces

The synergistic increase of mobilized Mg, Si and Fe concentrations exclusively in the presence of ascorbate + ferrozine indicates that both are, on their own, not able to cause a labilization of the Si

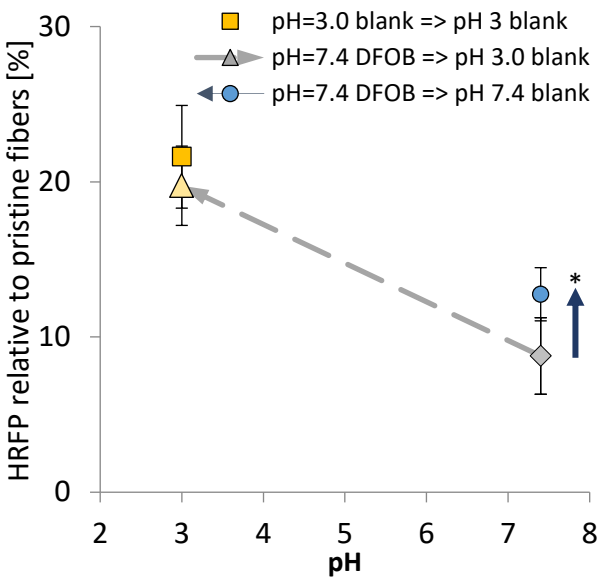

Figure 6.) *HRFP in % relative to the HRFP of pristine fibers (≙ 100%). DFOB altered fibers (grey diamond symbol) were incubated for 336 h in buffered pH 7.4 blank (blue circle, blue arrow) and pH 3.0 blank (yellow triangle, greyish dashed line) solutions under oxic conditions, whereby the HRFP increased. The rectangular yellow symbol indicates the HRFP of fibers incubated two consecutive times for 336 h in a buffered pH 3.0 solution. * indicates a significant increase determined in an ANOVA between the HRFP of DFOB altered fibers and DFOB altered fibers incubated for 336 h in a pH 7.4 buffered blank solution. Error bars indicate standard deviations (n = 4).*

layer of chrysotile. Ferrozine did, contrarily to DFOB [146], not complex Fe^{3+}[4] due to its Fe^{2+}-specificity (SI-Figure 1). As hypothesized, ascorbate however reduced Fe^{3+}[4] to Fe^{2+}[4] and hence enabled the complexation of tetrahedral Fe by ferrozine, being the causal mechanism of the observed synergism. Complexation of Fe^{2+}[4] by ferrozine thereby initiated Si labilization and increased Si and Mg mobilization from fibers (Figure 2, Panel a2 and b2). Since no Si labilization was observed in ascorbate treatments for up to 336 h (Figure 2, Panel b1), Fe^{2+}[4] consequently remained stable under anoxic conditions inside the exposed Si-lattice of chrysotile during this period. The complete back-oxidation of Fe^{2+}[4] to Fe^{3+}[4] by O_2 in re-oxidized ascorbate altered fibers was verified by the absence of an increased mobilized Si concentration (due to Si labilization) in ferrozine treatments, which indicates that no Fe^{2+}[4] was available for complexation (Figure 3, Panel c). The lack of Si labilization in the respective blank incubation of re-oxidized ascorbate altered fibers (Figure 3, Panel a) furthermore indicates that one full redox cycle of Fe^{3+}[4] did not damage the exposed Si layer of chrysotile. Even 1.5 full redox cycles of Fe^{3+}[4] in re-oxidized ascorbate altered fibers did not initiate Si labilization, which indicates that Fe^{2+}[4] was still located in the fibers' exposed Si layer in this treatment (Figure 3, Panel b and d). These experiments verify our hypothesis that Fe^{3+}[4] can undergo full redox cycles within the crystal lattice of chrysotile without initiating damage to the fibers' Si layers.

Analogously to the observed redox cycling of Fe^{3+}[4] by ascorbate and O_2, Fe^{3+}[4] redox cycled in exposed Si layers in the presence of H_2O_2 since H_2O_2 both reduces and oxidizes Fe in Haber-Weiss cycles [46]. This redox cycling of Fe[4] inside Si layers by H_2O_2 is likely a rationale for the high catalytic efficacy of Fe[4] in $HO^{\bullet}$ generation studies [146, 174]. Consistent with the redox cycling of Fe^{3+}[4] by ascorbate and O_2, redox cycling of Fe[4] by H_2O_2 did not induce Si labilization in pristine fiber treatments (Figure 5, Panel b1 and b2), even in the presence of high H_2O_2 concentrations (3.3 g L^{-1} starting concentration). However, mobilized Mg and Si concentrations in the presence of H_2O_2 were higher in blank and DFOB altered fiber treatments than in pristine fiber treatments. One explanation for this may be that H_2O_2 decomposition kinetics were highest in the presence of pristine fibers, but lowest in the presence of DFOB altered fibers [174], resulting in the highest mean H_2O_2 concentrations and consequently the highest potential amount of redox cycles of Fe^{3+}[4] in the latter fiber treatment. Hence, the total number of redox cycles may be proportional to Si labilization. However, Si labilization was only induced after a high number of redox cycles of Fe^{3+}[4], which were stimulated by a physiologically unrealistic high H_2O_2 concentration. Therefore, considering the low dissolution kinetics of Si layers at pH 7.4, Fe^{3+}[4] may be capable to redox cycle for an extended time under physiologic conditions without inducing Si labilization.

Redox cycling of octahedral Fe on chrysotile surfaces

As hypothesized, also octahedral Fe of the dissolved Mg layer completed one or 1.5 redox cycles during the re-oxidation experiment, but contrarily to Fe^{3+}[4] not inside the crystal lattice of chrysotile, but on its fiber surface (Figure 3). These redox cycles were governed by the reduction of Fe^{3+}[6] and the precipitation of ferric Fe as secondary Fe-minerals on the fiber surfaces during the fibers' re-oxidation (the latter was already observed by Walter et al. (2018a) [146]). Since only little (pristine fibers) or no (blank and DFOB altered fibers) Fe was measured in ascorbate treatments (Figure 2, Panel c1 and c2), we assume that Fe^{2+} was largely retained on the fiber surface under reductive conditions, most likely by adsorption on the exposed Si layers. Adsorption of Fe^{2+} to fiber surfaces may be supported by the pale-pinkish color of ascorbate altered fibers (Figure 1). Furthermore, adsorption is supported by calculating a mass balance of mobilized Fe concentrations in the ascorbate + ferrozine treatment of re-oxidized ascorbate altered fibers: Upon 1.5 redox cycles, 22 µmol L^{-1} of Fe^{2+} were still extracted by ferrozine (Figure 3d), representing an almost closed mass balance by considering the ≈30 µmol L^{-1} of Fe contained in the first Mg layer minus the 5 µmol L^{-1} of Fe^{2+} that had been mobilized during the ascorbate preconditioning (SI-Table 1). This indicates that the remaining Fe^{2+} in the ascorbate preconditioning had to adsorb to the fiber surface.

Loss of redox cycling tetrahedral Fe on chrysotile surfaces

As discussed, the redox cycling of Fe[4] only had minor implications on its dissolution from exposed Si layers of chrysotile (Figure 3 and 5). The synergistic increase of Si, Mg and Fe concentrations mobilized from all three analyzed fiber types in combined H_2O_2 + DFOB treatments (Figure 5) however indicates that, as hypothesized, redox cycling of Fe^{3+}[4] increased the likelihood for complexation of tetrahedral Fe by ligands and thus promoted Si labilization. The reduction to Fe^{2+}[4] and its complexation from Si layers can however be falsified as the causal mechanism for this observed synergism since ferrozine did not initiate Si labilization of redox cycling Fe[4] in the presence of H_2O_2 (Table 2). This suggests that the reduction of Fe^{3+}[4] to Fe^{2+}[4] is the rate limiting step in redox cycles of Fe[4] under oxic conditions, but not the Fenton-oxidation of Fe^{2+}[4] to Fe^{3+}[4]. Consequently, Fe^{2+}[4] may only be transiently exposed on chrysotile surfaces. Since the ligand-promoted dissolution of Fe^{3+}[4] was demonstrated to eventually take weeks [146], Fe^{2+}[4] may therefore be too short lived for complexation by Fe^{2+}-specific ligands during redox cycling by H_2O_2. Because of the increased ionic radius of Fe^{2+}[4] relative to Fe^{3+}[4] (63 vs. 49 pm [177]), the reduction of Fe^{3+}[4] may locally expand, but not destroy, the neighboring crystal lattice of the fibers' Si layer. Assuming that the Si lattice remains expanded after the back-oxidation of Fe^{2+}[4], Fe^{3+}[4] would consequently be located in an expanded Si-cage, which may sterically favor complexation by ligands like DFOB, and therefore promote Si labilization. This may explain the observed synergism (Figure 5).

Recovery of redox cycling tetrahedral Fe on dissolving chrysotile surfaces

By incubating DFOB altered fibers in oxic DFOB (Figure 4, Panel b3) or in anoxic ascorbate + ferrozine (Figure 2, Panel c2) treatments, no Fe was mobilized at the beginning of the experiments due to the metal depletion of the fiber surface during the fibers' preconditioning (SI-Table 1). However, Fe concentrations clearly increased at later sampling times of the experiments up to 4 µmol L^{-1} after 336 h of incubation (Figure 4, Panel b3). Because of the high mobilized Si and Mg concentrations in DFOB altered fiber treatments (Figure 2 and 4), this consequently suggests that also Fe from deeper Mg and Si layers became surface-exposed and consequently mobilized by the respective ligands. Als Fenton-active Fe^{3+}[4] of deeper Si layers becomes surface-exposed in this process, which was indicated by the significantly increased HRFP of DFOB altered fibers incubated for 336 h in a pH 7.4 blank solution (Figure 6). The HRFP of fibers even increased by more than a factor 2 by incubating DFOB altered fibers in pH 3.0 blank solutions, most likely because considerably higher amounts of Si and Mg were mobilized relative to the pH 7.4 incubation of DFOB altered fibers (SI-Table 1), which consequently caused a higher surface exposure of Fenton-active Fe^{3+}[4]. However, apart from the surface exposure

of Fenton-active Fe^{3+}[4 by the dissolution of Fe^{3+}[4]-depleted Si and structurally deeper Mg layers, the Fe content of dissolving Mg layers may also partly incorporate as Fe^{3+}[4] in vacancies of exposed Si layers and thereby increase the HRFP of the fibers. The observed stoichiometric Mg and Si dissolution from DFOB altered fibers at pH 7.4 that was exclusively observed in the presence of ligands (Figure 2 and 4) supports this mechanism: During oxic and anoxic blank incubations of DFOB altered fibers (Figure 4, SI-figure 1), Fe dissolving from Mg layers in the absence of ligands may have become incorporated in vacancies of the exposed Si layer, which decreased Si dissolution and consequently prevented the stoichiometric dissolution of the fibers. To conclude, our experiments verify our hypothesis that the depletion of redox cycling Fe from fiber surfaces is to a certain extent transient since, upon further dissolution, redox active Fe may be recovered on the fibers' surface.

Conclusions

The data discussed in this publication allows to causally explain the dominance of Fe^{3+}[4] in $HO^{\bullet}$ generation on chrysotile surfaces [174]. The capability of Fe^{3+}[4] to fully redox cycle inside Si layers of chrysotile may be a key determinant of the high catalytic efficacy of this Fe species in fiber-mediated Haber-Weiss cycles. Since redox cycling of Fe^{3+}[4] hardly damaged the fibers' crystal lattice, and since the dissolution kinetics of Si layers at circumneutral pH are slow [97, 146], Fe^{3+}[4] may likely be capable to redox cycle for an extended time on exposed chrysotile surfaces in vivo and thereby permanently catalyze the production of highly toxic $HO^{\bullet}$. Even if redox cycling Fe^{3+}[4]-sites get depleted from fiber surfaces (e.g. by ligands or hydrolysis), our data suggest that they will be recovered to a certain extent during further fiber dissolution. This demonstrates that redox cycling Fe^{3+}[4]-sites cannot be fully depleted from chrysotile surfaces and therefore will be capable of catalyzing the production of highly toxic $HO^{\bullet}$ as long as the fibers are present in vivo. The combination of the high catalytic efficacy and the high weathering resistance of redox-cycling Fe^{3+}[4]-sites inside the Si layers on dissolving chrysotile surfaces likely make Fe^{3+}[4] one of the most malignant metal species on chrysotile surfaces. Therefore, Fe^{3+}[4] may considerably contribute to asbestos induced injuries and fatalities. Apart from chrysotile, the capability of Fe^{3+}[4] to redox cycle within Si crystal lattices has to our knowledge only been described in non-pathogenic nontronites [163, 164, 165]. However, Fe^{3+}[4] has also been detected in other pathogenic minerals like quartz, talcum, amphiboles and in synthetic and natural zeolites [167, 168, 169, 170, 171, 172, 173]. Hence, redox cycling of Fe^{3+}[4] on their mineral surface and the resulting formation of $HO^{\bullet}$ may be a common pathogenic adverse mode of action in the pathology of these silicate minerals. The criterion of Fe to be tetrahedrally coordinated in crystalline Si lattices in order to

redox cycle and be catalytically active in Haber-Weiss cycles may eventually be demonstrated by the different carcinogenicity and toxicity of different silica polymorphs: Whereas crystalline silica is toxic and carcinogenic to humans (WHO-IARC group 1), the carcinogenicity of amorphous silica to humans is not classifiable (WHO-IARC group 3) [2, 178]. However, the crystalline and high-pressure silica-polymorph stishovite, in which Si is octahedrally and not tetrahedrally coordinated, seems to be non-pathogenic in vivo and in vitro as well and is not capable of producing radicals [179, 180, 181]. In both silica polymorphs, Fe^{3+}[4] can cristallographically be excluded, which may (apart from other reasons) be a determinant of the low pathogenicity of these minerals. Concluding, this study in combination with the studies of Walter et. al (2018a) and (2018b) [146, 174] demonstrate that the tetrahedral coordination environment of Fe^{3+}[4] in the Si lattice of chrysotile (and potentially other minerals) is a prerequisite for Fe to be highly catalytically active in fiber or particle-mediated $HO^{\bullet}$ generation.

Fourth Chapter

"Soil-pH and cement influence dissolution kinetics of, and radical generation by, chrysotile asbestos in sois"

Authors: Martin Walter[a], Walter D.C. Schenkeveld*[a]†, Gerald Geroldinger[b], Lars Gille[b], Stephan M. Kraemer[a]

Publication intended in: "Environmental Sciences & Technology"

[a] Department of Environmental Geosciences, University of Vienna
Althanstraße 14 (UZA II), 1090 Vienna, Austria
*Email: w.d.c.schenkeveld@uu.nl

[b] Institute of Pharmacology and Toxicology, University of Veterinary Medicine, Vienna
Veterinärplatz 1, 1210 Vienna, Austria

† current address:
Copernicus Institute of Sustainable Development, Faculty of Geosciences, Utrecht University Princetonlaan 8A, 3584 CB Utrecht, The Netherlands

Abstract

Chrysotile asbestos is a toxic and carcinogenic mineral that has abundantly been used in a variety of industrial applications. Much of the fibers and cement-containing asbestos waste has ended up in terrestrial environments, necessitating costly remediative actions. However, dissolution of chrysotile in soils and the potential for natural attenuation haven't been thoroughly examined yet. In this study we examined how soil properties influence dissolution rates of chrysotile and its hydroxyl radical forming potential (HRFP), which co-determines its toxicity. Chrysotile dissolution rates in soil suspensions increased with decreasing soil solution pH and were comparable to reported dissolution rates in soil-free systems. High dissolved organic carbon concentrations did not accelerate dissolution rates in acidic soils, whereas cement mixed with soil totally inhibited dissolution due to its high alkalinity. In soils with a circumneutral or mildly acidic pH, in which chrysotile dissolved relatively slowly, the HRFP decreased by 70 - 75% relative to pristine fibers. However, in acidic soils in which fibers rapidly dissolved, the decrease in HRFP was smaller. Cement mixed through the soils strongly decreased the HRFP of fibers by initiating the precipitation of redox-inactive Al phases on fiber surfaces.

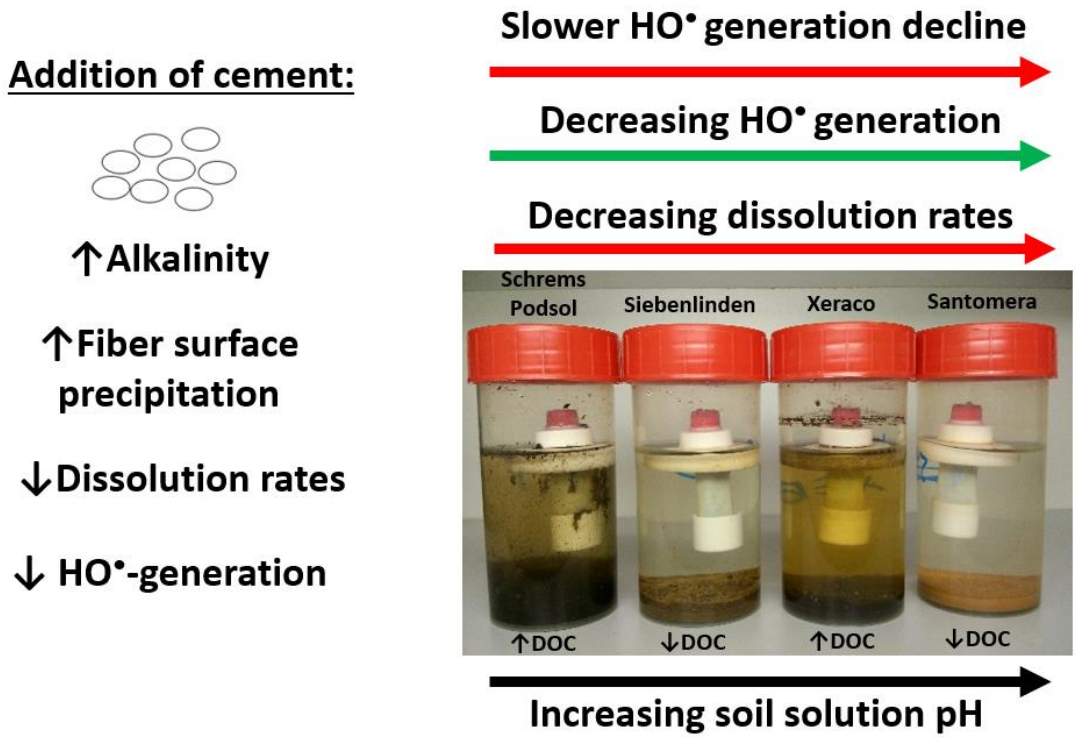

Introduction

Asbestos is a commercial term introduced for a group of fibrous silicate minerals used in a variety of industrial applications, especially in the building industry [1, 14, 16]. Five asbestos minerals belong to the amphibole group, whereas chrysotile asbestos belongs to the serpentine group [1]. Upon inhalation, asbestos fibers may induce pneumoconiosis, pleural plaques and effusions, lung cancers and mesotheliomas [2, 25, 29, 33, 144]. Fe in the structure of asbestos has been linked to the fiber pathogenicity for its ability to generate reactive radicals, which can damage DNA, proteins and lipids [3, 25, 33]. In EU countries, the use of asbestos has been banned since the late 1980s [21]. In northern American countries its application is still allowed [21] and in some Asian countries it even increases [20, 23]. Asbestos causes more than 100,000 fatalities each year, mostly following occupational exposure [27]. Apart from occupational exposure, terrestrial environments contaminated, either geogenically [75, 76, 77, 78, 79] or anthropogenically with loose asbestos (e.g. near asbestos mines or processing sites) [59, 63, 64, 66, 67, 69] or asbestos containing (cement)waste [59, 68, 70, 71, 73], are an additional source of exposure to asbestos in many countries and therefore present a health risk for residents [15, 59, 64, 70, 80]. Asbestos polluted environments are abundant: in the USA the release of friable asbestos into the environment was estimated at 6.2 million kg in 1999 (from 86 facilities) [182] and 4.0 million kg in 2009 [144]. In Europe, cases of fatalities induced by asbestos exposure from contaminated environments were reported for the Netherlands, Poland and Italy [68, 70, 71, 73]. In Israel, the western Galilee has 72 public areas with asbestos-polluted soil (≈150,000 m^3), necessitating remediative actions of 85 million dollars [183]. Apart from human health risks, asbestos in soils may have ecotoxicological implications for soil biota [15, 82, 83].

Chrysotile [$Mg_3Si_2O_5(OH)_4$] is the mostly used asbestos mineral (<95%) [13], and is most commonly found in asbestos-contaminated soils; hence, this study focuses on chrysotile. Chrysotile consists of octahedral Mg and tetrahedral Si layers which bundle together to a fiber with Mg hydroxide as the outer layer [97]. In the soil pH range (3.0 - 8.5), the outer Mg layer dissolves rapidly and the dissolution of Si layers becomes rate determining [94, 97, 146, 174, 184]. Dissolution rates of chrysotile are inversely related to pH [94, 96, 97, 98, 99, 146]. In the moderately acidic pH range (4.5 – 6.0) chrysotile dissolves congruently, whereas at strongly acidic (pH ≤ 3) and neutral pH it dissolves incongruently [94, 146]. Fe is the most abundant, redox-active metal in chrysotile (usually 2 - 4 wt%)[5]. During petrogenesis, Fe^{2+} and Fe^{3+} substitute into octahedral crystal sites, whereas only Fe^{3+} substitutes into tetrahedral sites (Fe^{3+}[4]) [38, 39, 146, 174, 184]. During dissolution in the soil pH range, surface Fe^{3+}[4] is the only Fe species generating highly toxic hydroxyl radicals ($HO^{\bullet}$) [174] while undergoing redox-cycling within the tetrahedral Si lattice of chrysotile [184], and hence determines the hydroxyl radical

forming potential (HRFP) of chrysotile. Ligand or proton-promoted dissolution of Fe^{3+}[4] labilizes the Si layers and thereby promotes overall Si dissolution [146].

In soils, chrysotile is exposed to processes, which may promote or inhibit dissolution. These processes may depend on soil properties (e.g. soil pH and dissolved organic carbon (DOC) concentration), on meteorological/hydrological conditions [121], and on the presence of organisms inducing bio-weathering reactions. Various organisms have been shown to accelerate dissolution of metals from asbestos by exuding metal-chelating ligands. Lichens, fungi, bacteria and plants can colonize and dissolve constituents of asbestos or asbestos bearing rocks and soils [50, 60, 106, 115, 120, 185, 186, 187]. Furthermore, DOC constituents like humic and fulvic acids in soil solution can chelate metals from minerals [188, 189] and thereby enhance dissolution rates.

The fate of chrysotile in soils has hardly been examined so far [15]. It is unknown how weathering rates from fiber-solution suspensions, as reported in previous studies, compare to weathering rates in suspensions additionally containing soil. Moreover, the effect of soil properties and the presence of cement (e.g. from asbestos cement waste) on the weathering rate and the HRFP of chrysotile have not yet been explored. In this study we have addressed these knowledge gaps.

Based on results from studies in soil-free systems [94, 96, 97, 99, 146], we hypothesize that the soil solution pH largely controls the weathering rate of chrysotile asbestos in soil, as well as the rate at which the HRFP decreases over time; for both rates an inverse relation with pH is predicted. Due to the natural occurrence of chelating ligands in soils, we predict larger dissolution rates in soil suspensions than observed in soil-free studies. Cement will increase the soil solution pH due to its high alkalinity (pH > 11) [103], and will therefore lower the dissolution rate and the rate of decline in HRFP. Analogously to soil-free experiments, the HRFP is predicted to reach a steady-state value rather than declining to zero [184]. These hypotheses were tested by incubating chrysotile asbestos in various soil suspensions and examining the elemental fluxes between asbestos, the soil solution and the soil solid phase and the HRFP as a function of time.

Materials and Methods

Material

Shijiazhuang chrysotile asbestos - Chrysotile asbestos was purchased from Shijiazhuang Mining IMP&EXP Trade Co, China and thoroughly characterized in a previous study [146]. Additionally, the Cr, Ni, Mn, Zn and Co content of the material were determined by fusion digestion and partly by a neutron

activation analysis (NAA). Bulk characteristics are summarized in Table 1a. Chemical reagents were bought in at least pro analysis quality from VWR (unless specifically mentioned).

Soils: Four soils differing in pH and soil organic matter (SOM) content (Table 1) were collected, air-dried and sieved over a 2 mm mesh before the experiment. The soils included were: an acidic, organic-rich A horizon from a podzol, collected in Schrems, Lower Austria (Latitude: 48°49'4.02"N; Longitude 15°3'24.77"E), an agricultural cambisol (0 - 20 cm) with a mildly acidic pH and low organic matter content, collected in Siebenlinden, Lower Austria (Latitude: 48°41'1.53"N; Longitude 15°0'3.00"E), an organic-rich, carbonaceous sandy soil (0 - 20 cm) from Xeraco, Spain, and an organic-poor, carbonaceous clay soil (0 - 20 cm) soil from Santomera (Latitude: 38°01'17.01"N; Longitude 1°10'43.69"W). These soils were used in several studies on Fe speciation in soil [190] and Fe acquisition by plants[191, 192, 193, 194, 195, 196, 197]. A summary of soil properties is presented Table 1b. All soils were air dried and sieved over a 2 mm mesh

Cement: Commercial cement ("ProBau® Schnellzement") was used for this study, its elemental composition is reported in SI-Table 1.

Dialysis devices: Chrysotile asbestos fibers were incubated in soil suspensions in 1 ml "Float-A-Lyzers" (Spectrum Laboratory Products) with dialysis-membranes with a 1000 kD molecular weight cut-off. Float-A-Lyzers are floating dialysis devices (see graphical abstract), which can be opened and closed with a screw cap.

Incubation of chrysotile asbestos in soil suspensions

To gain a better understanding of chrysotile weathering kinetics in soil, an incubation experiment was conducted. To examine dissolution of elements from chrysotile to the soil, the amounts present in the fibers, in soil solution and in the soil solid phase were monitored over time, aiming to arrive at a mass balance. Also, fiber surface reactivity and composition were investigated over time.

Chrysotile asbestos was added to Float-A-Lyzers to accommodate a fiber to solution ratio (FSR) of 2 g L^{-1} in soil suspensions with a soil to solution ratio (SSR) of 1:10. To examine how the effect of cement on the local chemical conditions impacts the dissolution rate of chrysotile asbestos, Schrems soil was mixed with cement in a 1:1 ratio. The effect of physical embedding of chrysotile fibers in a cement matrix on the dissolution rate was not explored in this study. A 300 mmol L^{-1} KCl background electrolyte solution was used to minimize the effect of chrysotile dissolution on the ionic strength and pH of the soil suspension, and to facilitate the comparison with previous dissolution studies with Shijiazhuang chrysotile at similar ionic strength [146, 174, 184]. The soil suspensions were prepared in 180 ml containers, 2 days prior to the start of the experiment to pre-equilibrate the dried soil [193]. Before

Table 1: *Section a.) Bulk characteristics of pristine Shijiazhuang chrysotile asbestos as previously reported in Walter et al. (2018a) [146], with exception of the Co, Cr, Mn, Ni and Zn content. Section b.) Soil characteristics of the soils used in the incubation experiment. Values in round brackets represent standard deviations.*

a) Composition of Shijiazhuang chrysotile asbestos

Bulk composition:		*Fusion digestion (n = 15)*	*NAA (n = 2)*[1]	**Fe-bulk speciation:**	*Mössbauer [%]*
Mg	[g kg^{-1}]	250 (7)		Fe^{2+}[6]	38.4
Si	[g kg^{-1}]	188 (3)		Fe^{3+}[6]	54.6
Fe	[g kg^{-1}]	19.0 (1.4)	21.4 (0.3)	Fe^{3+}[4]	7.0
Al	[g kg^{-1}]	8.0 (0.5)		Total Fe in chrysotile[2]	68.2
Mn	[g kg^{-1}]	0.8 (0.1)			
Ni	[g kg^{-1}]	1.2 (0.1)	1.2 (0.03)		
Cr	[g kg^{-1}]	1.4 (0.1)	1.3 (0.04)		
Zn	[mg kg^{-1}]		17.0 (1.1)		
Co	[mg kg^{-1}]		53.6 (1.0)		

b) Soils characteristics

Soil		Schrems	Siebenlinden	Xeraco	Santomera
Classification		Podzol	Cambisol	Entisol	Entisol
$CaCO_3$ content	[%]	0	0[##]	42[#]	52[#]
Clay content[4]	[%]	21	7	10[#]	26[#]
Soil solution pH [3]		3.0 ± 0.3	4.8 – 6.0	7.1 ± 0.3	7.5 ± 0.2
DOC in soil solution (1 day blank)[3]	[mg L^{-1}]	265 (5)	10.4 (0.4)	41.5 (0.9)	1.7 (0.1)
DOC in soil solution (56 days blank)[3]	[mg L^{-1}]	175 (7)	10.7 (0.4)	38.8 (0.2)	1.5 (0.1)

[1] Nuclear activation analysis
[2] Remaining Fe (31.8%) is in magnetite impurities
[3] SSR = 1:10 ; n = 4
[4] After removal of SOC with H_2O_2
[#] Schenkeveld et al. (2008)
[##] Walter et al. (2017) [192]

inserting chrysotile, the Float-A-Lyzers were washed with 10% ethanol to regenerate the dialysis-membranes, then rinsed and filled with 2 ml of ultra-pure water (UPW). Finally, 200 mg Shijiazhuang chrysotile asbestos were added, after which the Float-A-Lyzers were closed and put into the pre-equilibrated soil suspensions. The containers were placed on a horizontal shaker, shaking at 120 rounds per minutes (RPM), and were aerated once a week to prevent the soil suspensions from becoming anoxic. The experiment was carried out in a temperature-controlled room (20 ± 2°C) in the dark I n quadruplicates. Samples were taken destructively after 1, 4, 7, 14, 28 and 56 days. Two

replicates were used for an acid digestion, the other two replicates for the remaining fiber analyses. Collected fibers were either dried at 50°C (acid digestion) or were vacuum dried (fiber analyses), whereby the mass loss due to evaporation was recorded.

Additionally, "blank" soil suspensions without Float-A-Lyzers were prepared analogously and incubated for 1, 7, 28 and 56 days under the same conditions. Furthermore, empty Float-A-Lyzers were incubated for 56 days in duplicates exclusively in the presence of the four soil suspensions.

Sampling scheme

Fibers

The remaining amounts of elements associated with the fibers were determined through two digestions: an acid and fusion digestion. In the acid digestion all remaining Mg, Cr, Ni, Mn and Co was dissolved by extracting the complete Float-A-Lyzers with fiber content in acid. For these elements the recovery after digestion of pristine fibers was (near) complete (SI-Table 2). Si and Al did not sufficiently dissolve in acid (SI-Table 2), as already demonstrated by Rozalen et al. (2013) for Si [100]. Si not even dissolves from chrysotile in acids at elevated temperature [102]. Since the remaining Si bulk of fibers in soil suspensions was important to calculate overall fiber dissolution rates, fiber subsamples from two fiber replicates were homogenized and fusion digested to accurately determine the molar ratio between Mg and Si. The remaining amount of Si could then be calculated by dividing the remaining amount of Mg in chrysotile (acid digestions) by the molar Mg/Si ratio (fusion digestion).

Acid digestion - Per treatment, two fiber-filled Float-A-Lyzers were cleaned from soil particles sticking to the outside with UPW. Then they were opened (screw cap removed) and dried for 4 days at 50 °C. The dried fibers were then digested by adding 40 ml of 1.4 mol L^{-1} trace metal grade HNO_3 solution to 50 ml centrifugation tubes (VWR) containing the entire Float-A-Lyzers and shaking them in a horizontal shaker at 120 RPM for 336 h at 50°C, whereby the dialysis membranes dissolved. Empty Float-A-Lyzers incubated for 56 d were also digested to quantify the release of elements from the Float-A-Lyzers during the digestion (SI-Table 3). This release was very low to negligible relative to the net dissolved amounts of metals from fibers and accounted for maximally 2% of the net dissolved Mn and Cr, and ≈ 0% of the net dissolved Mg and Ni amounts.

Fusion digestion - From two replicate Float-A-Lyzers per treatment, 100 mg fibers were subsampled, dried and fusion-digested according to Walter et al. (2018a) [146] to determine Mg/Si-ratios. For the Schrems soil, time points were included, for the other soils only the 1 and 56 d samples.

Soil solid phase

To determine the reactive metal pools in the soil solid phase, soil samples were collected after decanting the soil solution. The samples were dried in an oven at 50 °C for 7 days and mass losses due to evaporation were recorded. Reactive metal pools in the sampled soil were determined by a 0.43 mol L^{-1} HNO_3 extraction for 2 h in a SSR of 1:10 (ISO 17586). Carbonate minerals were dissolved before the extraction by addition of an aliquot of 5 mol L^{-1} HNO_3 solution. In Schrems and Siebenlinden treatments, all sample times were included; for Santomera and Xeraco treatments, as well as for the blank (soil only) controls, only the 1 and 56 day samples were included.

Soil solution

To determine the metal concentration in soil solution, solution samples were collected and filtered over 0.45 µm Satorius cellulose acetate filters. The pH of two replicate filtrates was measured (SI-Table 4). For soil and fiber samples that had been dried, the amount of metals and Si present in digests and extracts were corrected for the amounts that had been present in the remaining soil solution phase after sampling, by subtracting the product of the soil solution concentration and the evaporation loss.

Fiber surface composition

pH 7.4- and alkaline extraction - To quantify the amount of exposed metals at chrysotile fiber surfaces, subsamples of dried fibers were extracted in a solution buffered at pH 7.4 (50 mmol L^{-1} MOPS (3-(*N*-morpholino)propanesulfonic-acid)) containing 1 mmol L^{-1} HEDTA (hydroxyethylenediaminetriacetic acid) for 336 h. To quantify the amount of amorphous siliceous material associated with the dissolving chrysotile fibers [100, 198], subsamples of dried fibers were extracted for 4 h in a 0.1 mol L^{-1} NaOH. Both extractions were carried out in an end-over-end shaker at 15 RPM in a FSR of 1 g L^{-1} at 20 20 ± 2°C in the dark.

Analysis

Si and metal concentrations in soil solution, extracts and digests were determined by ICP-OES (Optima 5300-DV, Perking Elmer). Calibration standards were matrix-matched with the samples. Before analysis, samples were filtered over 0.45 µm filters (Sartorius) and acidified with trace metal grade HNO_3 to 0.14 mol L^{-1}, with exception of the fusion digest samples. For a selected set of solution samples, DOC concentrations were determined in non-acidified subsamples with a TOC-L Shimadzu analyzer.

The HRFP of fibers was quantified through EPR spin-trapping analyses with the spin-trap 5-5'-dimethyl-1-pirroline-N-oxide (DMPO) using a X-band EPR-spectrometer (Bruker EMX) and a split ring resonator (Bruker MD5). This method has frequently been applied for quantifying the HRFP of chrysotile [35, 37, 43, 50, 121]; the analytical procedure is described in more detail in Walter et. al (2018a) [146]. The mean signal intensity (Ipp, Intensity peak-to-peak) was expressed as the percentage of the mean Ipp

of pristine fibers, which were analyzed as a reference each measuring day. Two fiber subsamples from each sampled experimental replicate were analyzed.

Calculation of dissolution rates, statistical analyses and supplementary information

Surface normalized net Mg dissolution rates were calculated by dividing the slopes of linear regression lines of the dissolved Mg concentrations obtained in the sample period between 4 d to 56 d as a function of time by the FSR and the BET specific surface area of pristine fibers. The dissolved Mg concentration was calculated in two ways: 1) based on the decrease in remaining amount of Mg in the fibers (acid digestion), and 2) based on the increase in amount of Mg in the soil solid phase (nitric acid extraction) and in soil solution combined. For the latter, changes in background concentrations (blanks) over time were accounted for. Net Si dissolution rates were only calculated from the change in amount of Si in the fibers (calculation analogously to the Mg dissolution rates).

An ANOVA was carried out to statistically test whether HRFPs increased in samples of the Schrems podzol as a function of time. Prior to the statistical evaluation, a F-test was used to determine equal or unequal variance between samples. If samples had an equal variance, a one-way ANOVA (alpha 0.05) test was used to determining significant differences between samples. If a significant difference was found between more than three samples, a Tukey HSD post-hoc test (alpha 0.05) was used to confirm differences between samples. If samples had unequal variance, a non-parametric Kruskal-Wallis (alpha 0.05) test was used to determine significance between samples. If a significant difference was found between more than three samples, a Dunn post-hoc test with a Bonferroni correction (alpha 0.0167) was subsequently used to test and identify differences between samples. All statistical tests apart from the Dunn post-hoc test were performed using the StatPlus:mac Pro software (Build 6.3.05/Core v6.2.30, AnalystSoft Inc). The Dunn post-hoc test was performed using XLSTAT Base (v2018, Addinsoft).

All data presented in Figure 1 - 4 are reported in SI-Table 5 - 8 respectively.

Results and discussion

Soil suspension properties

The pH of soil suspensions with Schrems, Xeraco and Santomera soil, with and without chrysotile, were well-buffered and remained constant within ± 0.3 pH units throughout the experiment (Table 1, SI-Table 5). The pH of Siebenlinden soil suspensions increased as a result of chrysotile asbestos

weathering, from 4.9 after 1 day to 6.0 after 56 days; in the control without chrysotile the pH remained constant. Amending the Schrems soil with cement also increased the soil suspension pH from 3.0 to 9.2 ± 0.7 in treatments with chrysotile and to 8.2 ± 0.6 in blanks.

DOC concentrations varied by two orders of magnitude among the soils (Table 1, SI-Table 9); except for Schrems soil the concentration remained constant. In Schrems soil suspensions, which had the highest DOC concentrations, the concentration declined by approximately 30 percent in absence of, and by 50 percent in presence of cement. Organic ligands present in DOC may enhance chrysotile dissolution rates [146, 188].

Except for Santomera soil, fungal colonies developed in all soil suspensions (with and without chrysotile), starting within a few days after the start of the experiment (SI-Figure 1). Fungi can enhance mineral weathering rates by exuding organic acids and siderophores via fungal hyphae [199, 200]. Fungal hyphae were found to associate with the Float-A-Lyzers, suggesting fungi might attempt to acquire nutrients from chrysotile. As the average diameters of fungal hyphae is in the low µm range [201], direct contact between hyphae and chrysotile can be excluded considering the average pore size of 0.1 µm of the 1000 kDa MWCO Float-A-Lyzer membrane.

Chrysotile weathering

For the purpose of comparability, (changes in) amounts of elements in all phases (fiber, soil solid phase and soil solution) are expressed per soil solution volume.

Mg dissolution

In the Schrems soil, Mg dissolution from the fibers was relatively rapid (Figure 1a): after 1 day, fiber-Mg had decreased from 19.7 to 18.9 mmol L^{-1}. The ≈1 mmol L^{-1} of dissolved Mg (FSR of 2 g L^{-1}) corresponds with the initial fast dissolution of ≈0.5 mmol L^{-1} Mg (FSR of 1 g L^{-1}) observed in a previous study with Shijiazhuang chrysotile [146]. This concentration presumably represents the dissolution of the outer Mg layer of the fibers [146]. Mg dissolution continued and after 56 days fiber-Mg had decreased to 15.7 mmol L^{-1}. The dissolved Mg had predominantly partitioned into soil solution (≈90%), and to a lesser degree to the soil solid phase (≈10%). The mass balance for Mg was closed (Figure 1a). As a consequence, Mg dissolution rates calculated from the decrease in fiber-Mg (16.4 pmol m^{-2} s^{-1}) and from the increase of Mg in soil solution and the soil solid phase (15.0 pmol m^{-2} s^{-1}) were very similar (Table 2).

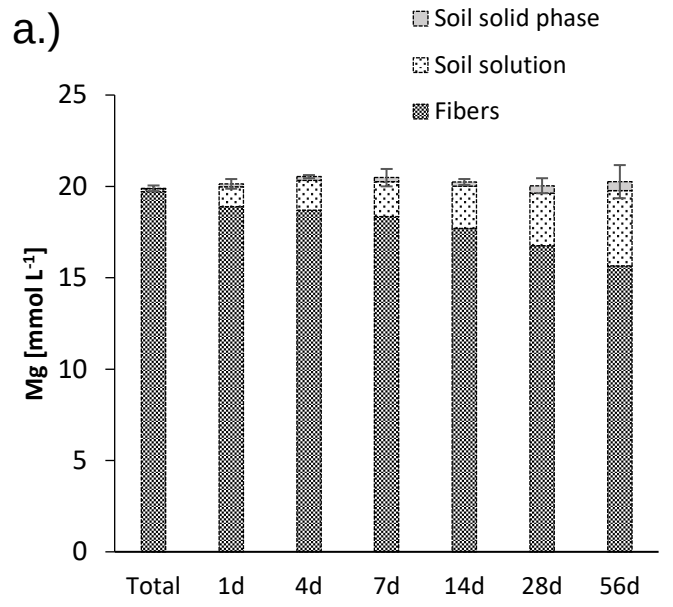

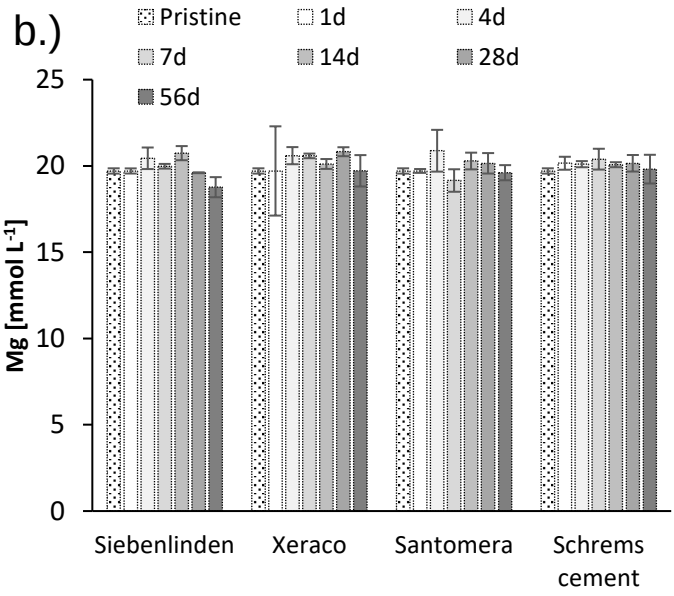

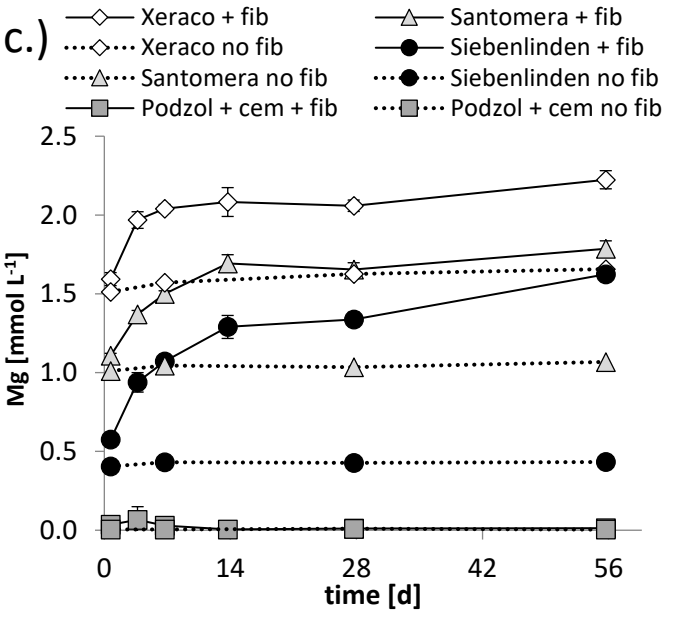

In Siebenlinden soil, a limited decrease in fiber-Mg, from 19.7 to 18.8 mmol L^{-1}, was only observed after 56 days (Figure 1b). This decrease was comparable to the Mg concentrations that partitioned into soil solution (≈1.2 mmol L^{-1}, Figure 1c) plus the soil solid phase (≈0.15 mmol L^{-1}, SI-Figure 2) and corresponded with the Mg content of the outer Mg layer of Shijiazhuang chrysotile (≈1.0 mmol L^{-1} in 2 g L^{-1} [146]). Because fiber-Mg only significantly decreased towards the end of the experiment, Mg dissolution rates were exclusively calculated from Mg soil solutions concentration (6.42 pmol m^{-2} s^{-1}) and in soil solution and the soil solid phase (7.9 pmol m^{-2} s^{-1}) (Table 2).

For Xeraco , Santomera and the cement-amended Schrems soil, neither a decrease in fiber-Mg nor an increase in soil solid phase Mg was observed (Figure 1b). The latter was partly caused by the limited precision of the acid digestion method and the high Mg content of these soils (SI-Table 10). However, in Xeraco and Santomera soil, Mg concentrations in soil solution were elevated up to ≈500 µmol L^{-1} after 56 days in the treatments with chrysotile asbestos, relative to the corresponding blank control (Figure 1c). Mg dissolution rates were calculated solely from the solution concentrations as a lower estimate of the actual rate: 0.96 pmol m^{-2} s^{-1} for Xeraco soil and 3.2 pmol m^{-2} s^{-1} for Santomera soil (Table 2). For Schrems and

↑ ***Figure 1:*** *Mg dissolution from chrysotile in soil suspensions. Panel a.) Mass balance for Mg during dissolution of chrysotile asbestos in Schrems soil. For all phases (fibers, soil solution and soil solid phase) Mg is expressed as an equivalent concentration in soil solution for the conditions of the incubation experiment (SSR = 1:10 and FSR = 2 g L^{-1}); Panel b.) Fiber-Mg (expressed as solution concentration) as a function of time in Siebenlinden, Xeraco, Santomera and Schrems cement soils; Panel c.) Mg concentration in soil solution as a function of time in the same soils as in Panel b. Error bars indicate standard deviations: Panel a: error bars represent standard deviations summed (squared addition) for the three phases; Panel b: n = 2; Panel c: n = 2 in blanks and n =4 in fiber incubations.*

Siebenlinden the Mg fraction that partitioned to the soil solid phase was limited, suggesting that these values might not deviate much from the actual rate. However, carbonate minerals may act as a sink for Mg in the soil solid phase in Xeraco, Santomera and cement-amended Schrems soil. For the cement-amended Schrems soil, no increases in Mg solution concentration were observed (Figure 1c), strongly contrasting the relatively fast Mg dissolution in the (non-cement-amended) Schrems soil (Figure 1a). This suggests that not even the outer Mg layer dissolved and that no chrysotile asbestos weathering took place. In a soil-free study on chrysotile dissolution also no Mg mobilization from the outer Mg layer occurred at alkaline pH (pH 11.5) [146], which is generally associated with cement [103]. The pH of the soil solution of fiber incubations in the cement-amended Schrems soil was however lower (pH ≈ 9), and the same soil-free study demonstrated dissolution of the outer Mg layer at pH 8.5. These results support our hypothesis that cement in the direct vicinity of chrysotile in soils inhibits fiber dissolution by increasing the local soil solution pH, but also suggest that additional factors may have played a role in inhibiting Mg mobilization.

Similarly as in the soil-free studies [94, 96, 97, 99, 146], Mg dissolution rates decreased with increasing pH (Table 2). This supports our hypothesis that the soil solution pH largely controls the weathering rate of chrysotile. However, Mg dissolution rates in the soil suspensions were consistently lower than in soil-free studies, by a factor of two to six. Differences in experimental setup, specifically the use of a dialysis membranes and the milder way of shaking in the current study, reduced the speed of mixing and may have contributed to lower dissolution rates.

The hypothesized enhanced dissolution rate due to the ability of natural organic substances to chelate metals from minerals [188, 189] and facilitate ligand-controlled dissolution was not established. Instead, the lower dissolution rates in soil suspensions may in part be related to an inhibitory effect of dissolved organic matter adsorbing to chrysotile surfaces on dissolution. E.g. Yoon at al. observed that particularly in the lower pH range (2.0 – 4.5) adsorption of humic substances to boehmite lowered

Table 2: *Mg and Si dissolution rates for chrysotile asbestos in soil suspensions (SSR = 1:10; 1 g L^{-1} chrysotile). Mg dissolution rates were calculated from the increase in soil solution concentrations ("Mg solution"), from the increase in concentration in soil solution and the soil solid phase combined ("Mg soil + solution") and from the decrease in fiber-Mg ("fiber Mg"). Si dissolution rates were calculated from the decrease in fiber-Si ("Fiber Si") and from the decrease in fiber-Si plus the increase in amorphous siliceous matter ("Fiber-Si + amorphous Si"). In accordance with Walter et al. (2018a) [146], only data points of the second stage of Mg dissolution from pristine chrysotile fibers were used for the derivation of dissolution rates (all data points excluding t = 1d). Numbers in round brackets indicate the R^2 values of the respective linear regressions used. Stoichiometric dissolution is marked with *. Rates with n.d. were not determined.*

Soil	**Dissolution rate [pmol m^{-2} s^{-1}]**						
	Mg solution	**Mg soil + solution**	**Fiber Mg**	**Fiber Si**	**Fiber-Si + amorphous Si**	**Walter et al. (2018a) [146] Mg**	**Si**
Schrems	13.0 (0.99)	15.0 (0.99)	16.4* (0.96)	5.33 (0.89)	12.0* (0.93)	47.3 (pH 3.0)	17.3 (pH 3.0)
Siebenlinden	6.42 (0.91)	7.92 (0.90)	n.d.	n.d.	n.d.	18.2 (pH 4.5) 13.3 (pH 6.0)	12.1(pH 4.5) 7.5 (pH 6.0)
Xeraco	0.96 (0.45)	n.d.	n.d.	n.d.	n.d.	5.6 (pH 7.5)	0.4 (pH 7.5)
Santomera	3.24 (0.66)	n.d.	n.d.	n.d.	n.d.	5.6 (pH 7.5)	0.4 (pH 7.5)
Schrems cement	n.d.	n.d.	n.d.	n.d.	n.d.	n.d. (pH 11.5)	n.d. (pH 11.5)

dissolution rates and attributed this to steric protection of surface sites, by strong outer-sphere association of humic molecules preventing access of protons to the surface sites and hence slowing down proton-promoted dissolution [202]. A similar effect might lower the dissolution rate of chrysotile. Because of the aforementioned difference in experimental setup, the role of ligands occurring in NOM on chrysotile dissolution remains somewhat unclear. It however seems unlikely that they have a strong enhancing effect.

Similarly, it remains uncertain to what extent the fungal colonies observed in most soils (SI-Figure 1) have affected Mg dissolution rates. Fungi have been demonstrated to promote dissolution of metals from asbestos through the exudation of ligands [107, 114, 115, 117]. Direct contact between fibers and fungal hyphae had been largely impaired by the dialysis membrane. By analogy to ligands occurring in NOM, a strong enhancing effect appears unlikely, as Mg dissolution rates were lower than in the soil-free studies.

a.) Fusion digestion

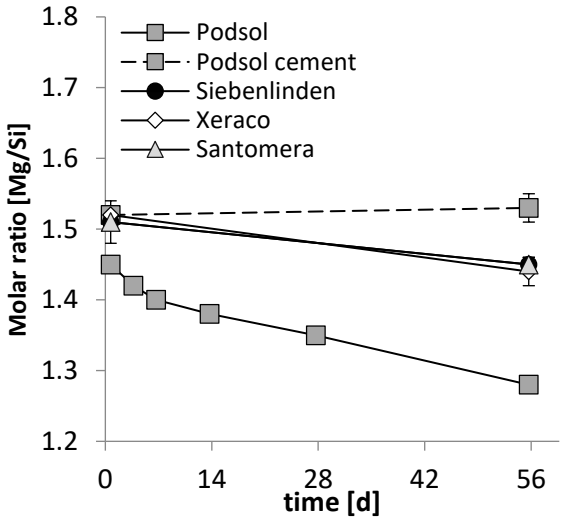

b.) Alkaline extraction

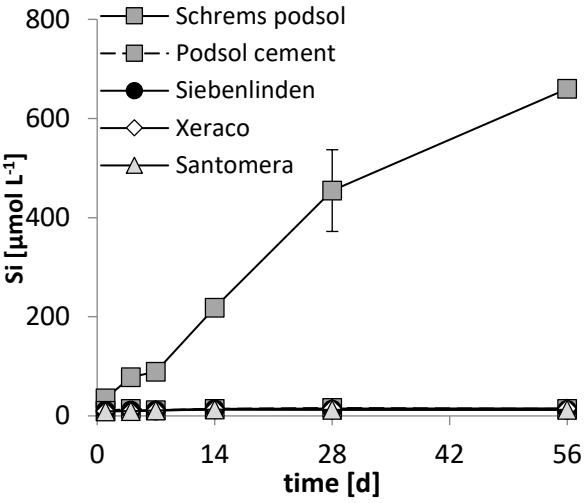

c.) Si mass balance

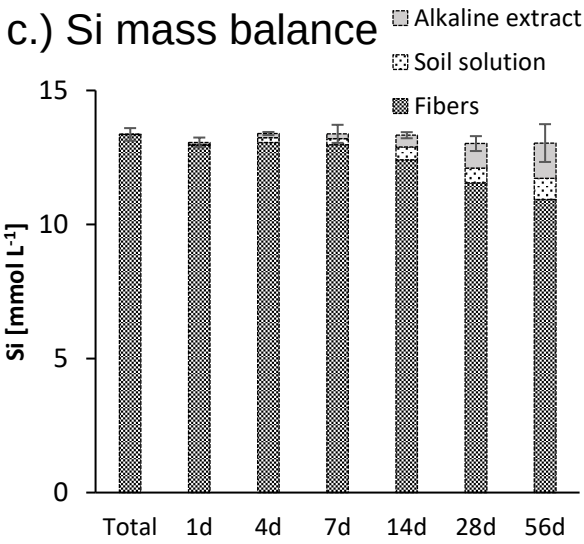

Si dissolution

In Schrems soil, the Mg/Si-ratio gradually decreased from 1.52 to 1.28 after 56d, illustrating that dissolution is non-stoichiometric (Figure 2a). Fiber-Si, which had been calculated by dividing fiber-Mg by the Mg/Si ratio, was used for calculating the Si dissolution rate. The calculated Si dissolution rate was 5.33 pmol m^{-2} s^{-1}, which was over a factor two lower than would be expected for stoichiometric dissolution considering the Mg dissolution rate (Table 2).

In Siebenlinden, Xeraco and Santomera soil, the molar Mg/Si-ratio decreased from 1.52 to approximately 1.45 after 56d (Figure 2a). Assuming that no Si had dissolved, this decrease corresponds with ≈ 950 µmol L^{-1} of mobilized Mg i.e. dissolution of the outermost Mg layer [146]. Among these treatments, only in Siebenlinden soil the Si soil solution concentration had slightly increased relative to the blank control (≈ 70 µmol L^{-1} after 56d, SI-Figure 3). Therefore, the equal Mg/Si-ratios in these three treatments may indicate that, apart from the outermost Mg layer, the fibers did not substantially dissolve.

The Mg/Si-ratio of fibers sampled from the cement-amended Schrems soil after 56 d was identical to the ratio of pristine fibers (≈1.52). This further strengthens the idea that not even the outer Mg layer had dissolved and further supports our hypothesis that dissolution of chrysotile asbestos is greatly impaired in the presence of cement.

↑ ***Figure 2:*** *Si dissolution from chrysotile in soil suspensions: Panel a.) Molar Mg/Si ratio of chrysotile incubated in soil suspensions as a function of time determined in fusion digestions; Panel b.) Si extracted with 0.1 mol L^{-1} NaOH for 4 h from chrysotile that had been incubated in soil suspensions, as a function of incubation time. The extracted Si has been expressed as a solution concentration in the incubation experiment (1 g L^{-1} fibers); Panel c.) Si mass balance for chrysotile incubated in Schrems soil. For all phases (fibers, soil solution and alkaline extractable Si contents) Si is expressed as an equivalent concentration in soil solution for the conditions of the incubation experiment (SSR = 1:10 and FSR = 2 g L^{-1}). Error bars indicate standard deviations (Panel a: n = 2; Panel b: n = 4; Panel c: error bars represent standard deviations summed (squared addition) for the three phases.*

In alkaline extractions, Si was only mobilized from chrysotile that had been exposed to Schrems soil, up to a concentration of 660 µmol L^{-1} after incubation for 56 days (Figure 3b). In a soil-free supplementary experiment, substantial Si mobilization also only occurred in alkaline extractions from chrysotile asbestos that had been pretreated at pH 3.0, and not at higher pH (SI-Figure 4). This suggest that the solution pH is the main driver for the formation of amorphous siliceous material. At pH 4.5 chrysotile dissolution was shown to be congruent [146], implying that the formation of this amorphous siliceous material starts between pH 3.0 and pH 4.5.

By subtracting the Si concentrations mobilized in the alkaline extraction of fibers sampled from Schrems soil (Figure 2b) from the corresponding fiber-Si (Figure 2c), a new Si dissolution rate (12.0 pmol m^{-2} s^{-1}) was calculated that was approximately stoichiometric to the calculated Mg dissolution rate (16.4 pmol m^{-2} s^{-1}) (Table 2). This suggests that chrysotile dissolution under acidic conditions (pH ≤ 3.0) is congruent as long as the formation of amorphous siliceous material is considered. Although the Si flux to the soil solid phase of Schrems soil could not be determined through the nitric acid extraction, the three other quantifiable Si pools (fiber bulk, amorphous siliceous material and soil solution Si) constituted a closed mass balance (Figure 2c), indicating that the flux to soil was small.

Dissolution of other elements

Because overall chrysotile dissolution was fastest in Schrems soil, the clearest trends in dissolution of the trace elements Ni, Cr and Mn and their partitioning to the soil solid phase and soil solution were also observed for this soil (Figure 3). Results for the dissolution of other trace elements in Schrems soil and for the dissolution of trace metals to the soil solution and solid soil phase in other soil treatments are presented in SI-Figure 2, 3 and 5.

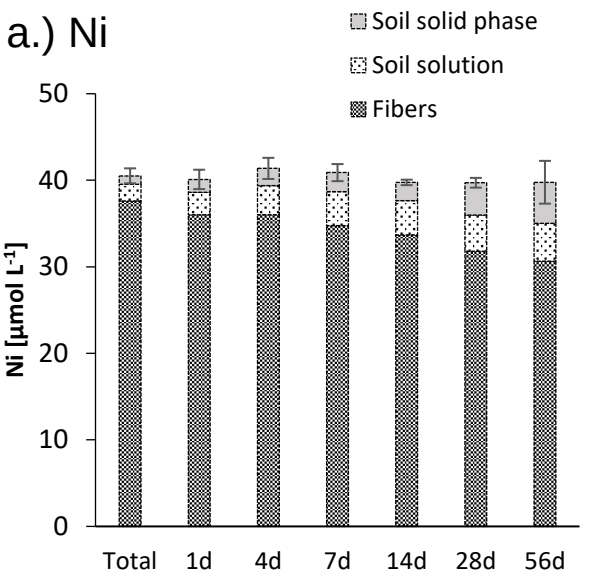

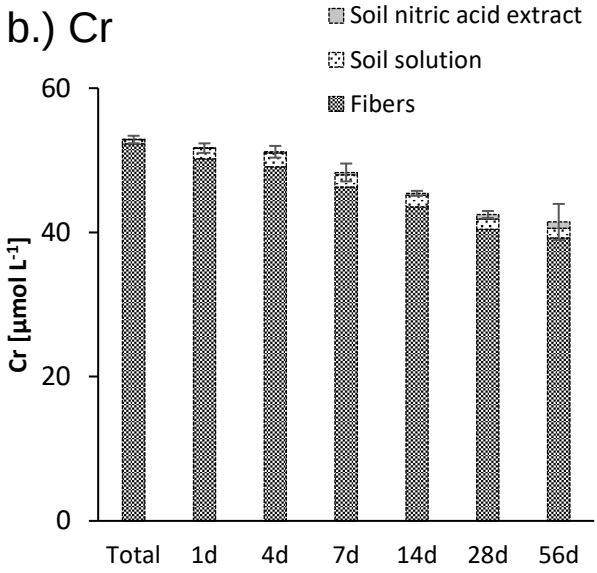

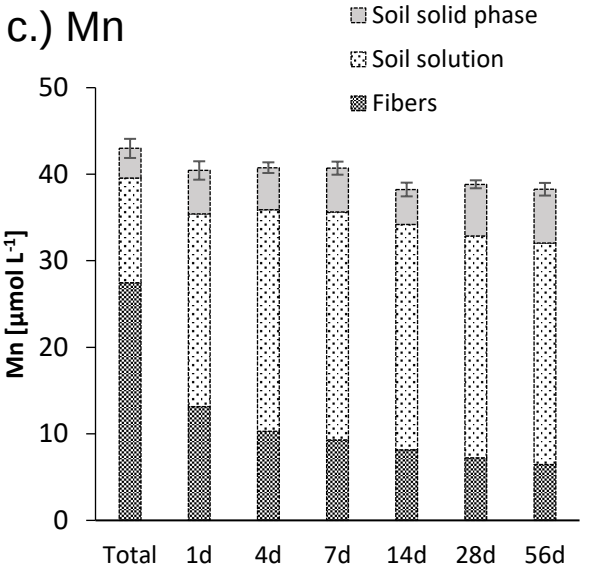

For Ni dissolution in Schrems soil the mass balance was closed (Figure 3a). Fiber-Ni gradually decreased from 37.6 µmol L^{-1} in pristine fibers to 30.7 µmol L^{-1} after 56 d. Ni preferentially partitioned to the soil solid phase over soil solution.

Similarly to Ni, fiber-Cr gradually decreased from 52.3 to 39.3 µmol L^{-1} after 56 d, however, soil solution concentrations of Cr were low, and Cr that partitioned to the solid soil phase was not recovered in nitric acid digestions of the Schrems soil (Figure 3b).

Approximately half of the fiber-Mn dissolved within 1 day (from 27.5 µmol L^{-1} to 13.2 µmol L^{-1}). Mn dissolution gradually continued until approximately a quarter of the initial fiber-Mn (6.4 µmol L^{-1}) remained after 56 days. This rapid initial dissolution is presumably associated with Mn enrichment in the outer Mg layer of Shijiazhuang chrysotile relative to deeper layers and the dissolution of this outer Mg layer within the first day. The dissolution of Mn from fibers in Schrems had an almost closed mass balance, most of the dissolved Mn partitioned to, and remained in, the soil solution (Figure 3c).

In pH 7.4-extractions of fibers sampled from Schrems soil, Mg, Fe, Mn and Cr were extracted to a lower extent than from fibers incubated in other soils. This suggests a faster depletion of these metals from fiber surfaces, probably because of the faster dissolution in the Schrems soil (SI-Figure 6).

↑ *Figure 3: Mass balance for Ni (Panel a), Cr (Panel b) and Mn (Panel c) during dissolution of chrysotile asbestos in Schrems soil. For all phases (fibers, soil solution and soil solid phase) Ni, Cr or Mn are expressed as an equivalent concentration in soil solution for the conditions of the incubation experiment (SSR = 1:10 and FSR = 2 g L^{-1}). Error bars represent standard deviations summed (squared addition) for the three compartments.*

Apart from metals dissolving from chrysotile fibers in soils, metals from the soil solution also accumulated on the fiber surface, as e.g. demonstrated for Zn, (SI-Figure 3, 5). Exclusively in the cement-amended Schrems soil, a strong accumulation of Al on the chrysotile fibers occurred (SI-Figure 5), up to 2.2 mmol L^{-1} after 56d of incubation, corresponding with 4 times the amount present in pristine fibers and largely exceeded the amount of Al required for complete surface coverage of the fiber surfaces. The cement-induced elevation in pH had increased the Al concentrations in soil solution (data not shown), which presumable had led to precipitation of secondary Al-bearing phases which had coated the fiber surfaces. This coating of the fiber surfaces may have contributed to inhibiting Mg dissolution (vide supra).

The HRFP of chrysotile fibers in soil suspensions

Incubation in soil suspensions led to a decline in HRFP of chrysotile asbestos. The rate of decline was soil-dependent and was largest for Schrems soil: after 1d the HRFP had decreased to 24%, while for the other soils it ranged from 53 to 87% (Figure 4). The rapid initial decrease in HRFP with Schrems soil presumably resulted from the fast dissolution of the outermost Mg layer (Figure 1a) and the subsequent rapid dissolution of Fe^{3+}[4] from the first exposed Si layer. For steady-state dissolution in the soil pH range (pH 3 - 9), Fe^{3+}[4] has been shown to be the principal Fe species generating hydoxyl radicals [174]. The chrysotile dissolution kinetics in Siebenlinden, Xeraco and Santomera soil were slower (Figure 2), and it required longer before steady state dissolution was reached, explaining the slower decline in HRFP. For the latter three soils, no difference in rate of decline in HRFP at later incubation times (≥ 1 week) could be discerned. Hence, the results only partly support our hypothesis that the rate of decline in HRFP decreases with increasing soil-pH.

After 14d, the HRFP of fibers from Siebenlinden, Xeraco and Santomera soils had converged to 25 - 30%, after which it remained approximately constant, supporting our hypothesis that the HRFP of chrysotile asbestos weathering in soils does not become zero. In Schrems soil, the HRFP even significantly increased from 24% after 1d to 39% at the end of the experiment. This increase may be related to the high Fe-content in the soil solution of Schrems treatments: As external Fe was demonstrated to incorporate in vacancies of the fibers' exposed Si layers as Fenton-active Fe^{3+}[4] [174],

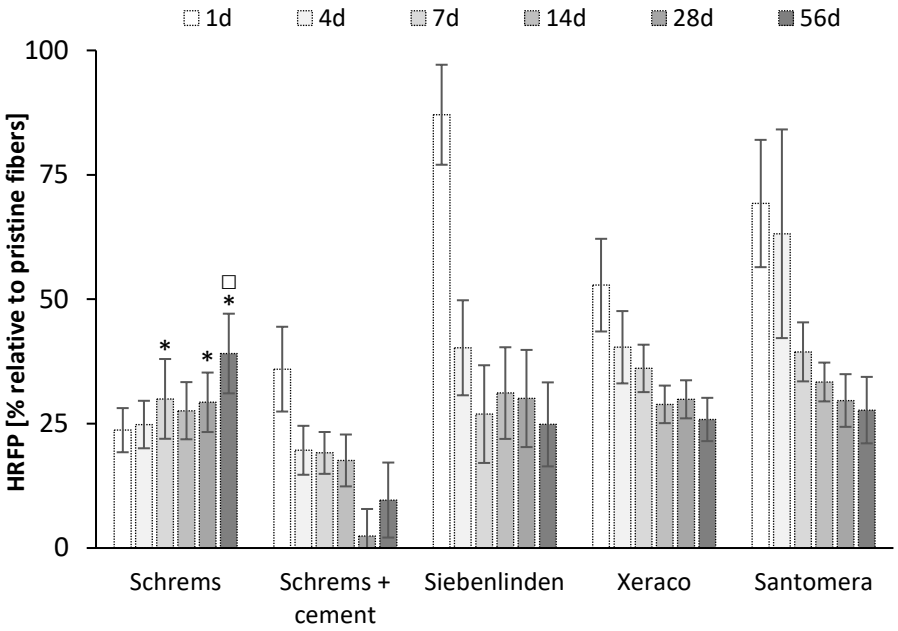

Figure 4: *Hydroxyl radical forming potential (HRFP) of chrysotile asbestos incubated in Schrems, cement-amended Schrems, Siebenlinden, Xeraco and Santomera soil as a function of time (HRFP of pristine fibers ≙ 100 %). Error bars indicate standard deviations (n = 4). An ANOVA was carried out to statistically test whether HRFPs increased in samples of the Schrems podzol as a function of time. * indicates a significant increase of the HRFP relative to the HRFP of the respective 1d sample, □ indicates a significant increase of HRFP relative to the HRFP of the directly preceding sample.*

Fe from the soil solution may have successively increased the fibers HRFP in Schrems treatments by this process. The decline in HRFP to ≈25 - 30% was reproduced in soil-free systems in a supplementary experiment at pH 7.4 after 56d of incubation (SI-Figure 7). Drying and rewetting is likely to occur in soil environments as a result of fluctuations in soil moisture content. However, whether fibers were biweekly dried and resuspended or not did not affect how the HRFP developed over time in this experiment.

In the cement-amended Schrems soil the HRFP strongly decreased, reaching values well below the 25 - 30% window of unamended soils. This effect was unexpected and opposed our hypothesis that at the alkaline pH associated with cement (pH 11.5), a decrease in HRFP would be inhibited. In soil-free experiments it was observed that at pH 11.5 the outer Mg layer of chrysotile hardly dissolved and that the HRFP remained at ≈ 100%. The pH of cement-amended Schrems soil was somewhat lower (pH ≈ 9) and dissolution of the outer Mg layer would be expected, resulting in a HRFP in the 25 - 35% window. However, as mentioned, large amounts of Fenton-inactive Al had accumulated on the chrysotile fibers,

presumably coating the fiber surfaces and shielding the surface Fe, preventing it from generating hydroxyl radicals.

Environmental implications

An understanding of the rates and mechanisms of chrysotile asbestos weathering in soils and the impact of weathering reactions on the hazard of the material is essential for making meaningful estimates of its residence time in terrestrial environments and for performing risk assessments of asbestos-polluted sites. The results from this incubation study contribute to this understanding and demonstrate that weathering rates of chrysotile asbestos depend on the specifics of the soil and that particularly the soil pH plays an important role. As a consequence, the time required for natural attenuation of friable asbestos in soil will be shorter in more acidic soils. Potentially, in certain soils this time span can be shortened by applying soil amendments that lower the soil pH, or by introducing vegetation or applying nutrients that have an acidifying effect on the soil. However, soil acidification does not reduce the potential of chrysotile asbestos to generate toxic hydroxyl radicals.

In the environment, asbestos is often encountered in association with cement. In this study we demonstrated that the presence of cement may strongly alter reaction conditions and dramatically decrease the rate of chrysotile weathering, almost to a complete stop, thereby hugely increasing the time required for natural attenuation. The effect of cement on lowering the weathering rate appears to be twofold: an intrinsic decrease in weathering rate related to a cement-induced increase in soil solution pH, and precipitation of Al phases on chrysotile fiber surfaces, inhibiting dissolution. Presumably this formation of Al surface coating was also responsible for shielding the Fenton-active Fe surface sites, causing the potential of chrysotile fibers to generate hydroxyl radicals to drop. It remains to be explored if this surface passivation also occurs when chrysotile asbestos and cement are actually embedded in the soil and if the passivation is lasting under physiological conditions, upon inhalation. Also, the influence of physical embedding of asbestos fibers in a cement matrix and of DOC on dissolution rates remain to be explored. Some of these issues will be addressed in a follow-up pot trial study in which also the potential of plants that exude organic ligands for enhancing chrysotile dissolution rates in soil will be examined.

Fifths Chapter

"Weathering of chrysotile in a long-term microcosm experiment: The influence of soil type, plants and cement on dissolution kinetics and radical generation of asbestos in polluted soils"

Authors: Martin Walter[a], Walter D.C. Schenkeveld*[a]†, Gerald Geroldinger[b], Lars Gille[b], Stephan M. Kraemer[a]

Publication intended in: "Environmental Sciences & Technology"

[a] Department of Environmental Geosciences, University of Vienna
Althanstraße 14 (UZA II), 1090 Vienna, Austria
*Email: w.d.c.schenkeveld@uu.nl

[b] Institute of Pharmacology and Toxicology, University of Veterinary Medicine, Vienna
Veterinärplatz 1, 1210 Vienna, Austria

† current address:
Copernicus Institute of Sustainable Development, Faculty of Geosciences, Utrecht University Princetonlaan 8A, 3584 CB Utrecht, The Netherlands

Abstract

Chrysotile is the most abundantly used asbestos mineral. Respiratory exposure to the fibers induces malignant and non-malignant diseases. Because of its worldwide industrial use, many soils were polluted by chrysotile, which possesses a health risk for residents. The dissolution of chrysotile in polluted environments has only been assessed in simplified laboratory experiments. Hence, we designed a long-term microcosm experiment to better study the effect of soil type, cement (in asbestos waste) and plants on fiber weathering in polluted soils. Mg and Si dissolution rates of chrysotile in an acidic podzol were 13 and 6 times lower than in batch dissolution and soil suspension experiments of previous publications. In a mildly acidic agricultural and a calcareous soil, dissolution rates were below detection. Radical generation by fibers maximally decreased by ≈75%, but only in soils with low mobile Fe contents. This decrease took years compared to days or weeks in published batch dissolution and soil suspension studies. Cement near fibers in soils antagonized metal dissolution from, and the decrease of the radical generation by, chrysotile surfaces. Plants had more subtle effects than cement and soil type and increased metal dissolution from fibers, and transiently decreased radical generation of chrysotile fibers in soils.

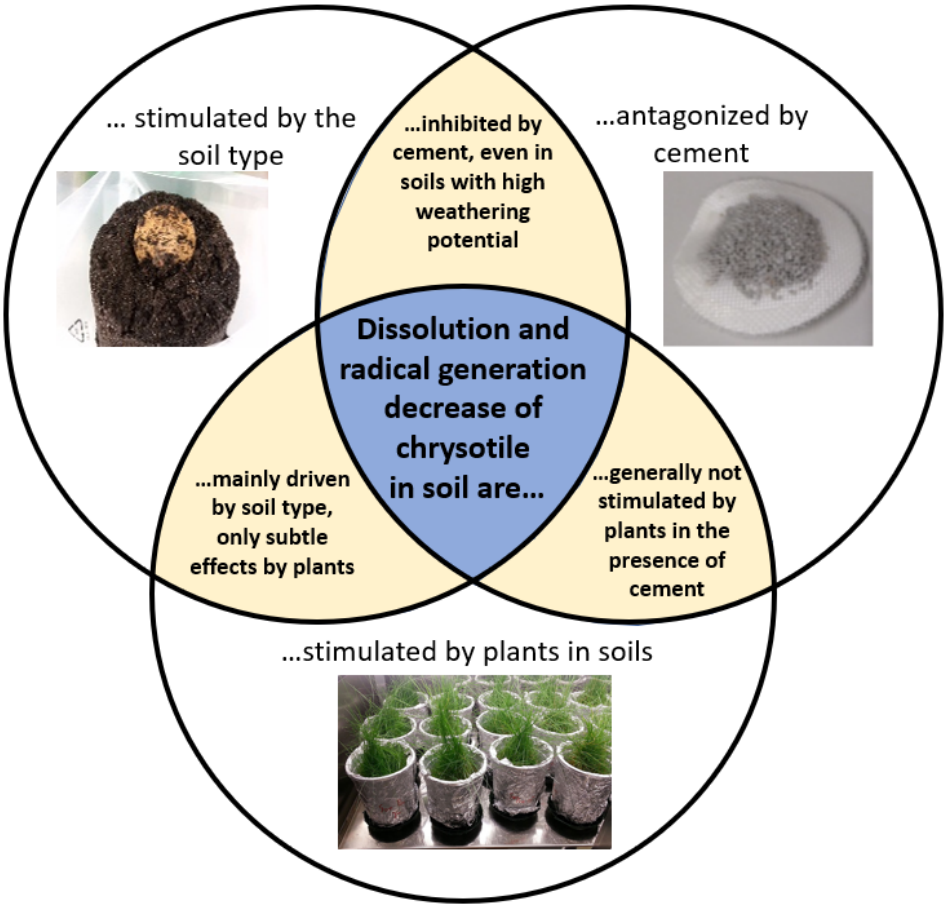

Introduction

Asbestos is a commercial term that has been introduced for six fibrous silicate minerals, which were used in a variety of industrial applications [1, 15, 16, 144]. Upon inhalation, asbestos may induce pneumoconiosis and pleural diseases, but also malignant lung carcinomas and mesotheliomas [3, 25, 29, 33, 144]. Exposure to asbestos causes more than 100,000 fatalities each year, mostly due to occupational exposure [27]. Consequently, asbestos was banned in EU countries from the late 1980s onwards [21]. However, its use has not been banned in northern American countries and even increases in some Asian countries [20, 21, 23]. Environmental exposure to asbestos from either geogenic [59, 63, 64, 66, 67, 69] or anthropogenic sources possesses a health risk to residents [15, 59, 64, 70, 75, 76, 80, 203] and can be associated to approximately 400 casualties per year worldwide [27]. Anthropogenic contamination can result from the release of either loose asbestos (e.g. from asbestos mines or processing sites) [63, 64, 66, 67, 69] or asbestos containing (cement) wastes [68, 70, 71, 73]. Environmental pollution may reach considerable dimensions: The release of friable asbestos in the USA was estimated to be 6.2 million kg in 1999 [65] and 4.0 million kg in 2009 [144]. In Israel, 72 public areas and an estimated 150,000 m^3 of soil near a former cement plant were polluted with industrial asbestos cement waste, which required remediation expenses of 85 million dollars [74].

The serpentine mineral chrysotile [$Mg_3Si_2O_5(OH)_4$] dominated the historic asbestos use (< 95%) [13], consequently this mineral is the most abundant asbestos pollutant in the environment. Hence, we focus on chrysotile in this study. Chrysotile consists of sheets of octahedral Mg hydroxide and tetrahedral Si layers which bundle together to a fiber with an exposed outer Mg hydroxide layer [6, 7]. Dissolution of chrysotile is inversely related to pH [94, 96, 97, 98, 99] and increases at a wide pH range in the presence of biogenic ligands such as citrate, oxalate and siderophores [146]. The dissolution of Si layers is rate determining, whereas Mg layers readily dissolve from acidic up to circumneutral pH [94, 96, 97, 146]. At alkaline cement pH [103], the fibers do not dissolve due to the low solubility of the Mg layers [97, 99, 146]. In soil suspensions, dissolution rates of chrysotile were ≈3x lower than in soil-free experiments at the same pH [146, 204]. The soil solution pH was the decisive pedochemical parameter that influenced dissolution rates [204].

The malignancy of asbestos is to a clear extent determined by structural Fe that generates reactive radicals in Fenton reactions, which can harm DNA, proteins and lipids [3, 25, 33, 43]. During dissolution, tetrahedrally substituted Fe in the fibers' Si layers (Fe^{3+}[4]) is the only causal Fenton-active Fe species on fiber surfaces which generates highly toxic hydroxyl radicals ($HO^{\bullet}$) out of H_2O_2 [174] by fully redox-cycling inside the fibers' crystal lattice [184]. Ligand or proton-promoted dissolution of Fe^{3+}[4] decrease the hydroxyl radical forming potential (HRFP) of chrysotile [146, 174, 184] and forms

vacancies in Si layers, which enhance Si dissolution rates [146]. In soil suspensions, HRFPs of chrysotile maximally decreased to a value of 25 - 30% of the HRFP of pristine fibers [204].

Apart from geochemical [204] and physical [121] fiber weathering, also biota may increase dissolution rates of asbestos: Fungi, bacteria, lichens and plants can colonize and dissolve constituents of asbestos or asbestos bearing rocks and soils by the release of metal chelating agents [50, 60, 106, 115, 120, 185, 186, 187].

To our knowledge, dissolution rates of chrysotile in soils have only been estimated in simplified batch, flow-through or soil suspension studies. Considering that dissolution rates of silicates may be orders of magnitudes lower in the field than determined in simplified laboratory experiments[205, 206, 207], representative dissolution rates of chrysotile in soils have not been published yet. Similarly, the HRFP decrease kinetics and the maximal HRFP decrease level of chrysotile have only been determined in batch dissolution and soil suspension experiments. As cement is a common constituent in asbestos waste, its influence on dissolution rates of, and radical generation by, chrysotile in soils may be considerable. However, this has to our knowledge only been assessed in simplified laboratory experiments. Finally, the effect of plants on chrysotile weathering has only been described by a serpentinite-endemic Ni hyperaccumulator in a column experiment [120]. Accordingly, it is not known if non-serpentinite endemic plants can influence fiber dissolution or the HRFP of chrysotile in soils.

In this publication, we address these research gaps in a long-term microcosm experiment. We thereby hypothesize that dissolution kinetics and the kinetics of the HRFP decrease of chrysotile in soils are considerably slower than determined in simplified laboratory approaches. We predict that both rates are inversely related to the soil solution pH and antagonized by the spatial vicinity of cement near the fibers in soil because of its high alkalinity [103]. Furthermore, we hypothesize that plants contribute to fiber weathering by increasing the ligand-promoted metal dissolution from fiber surfaces in soils. Since this may also affect Fenton active metals, we predict that plants accelerate the HRFP decrease kinetics of chrysotile in polluted soils. Finally, we hypothesize that the HRFP of chrysotile under realistic soil conditions maximally decreases to 25 - 30% of the HRFP of pristine fibers, as demonstrated in batch dissolution and soil suspension experiments before [146, 184, 204].

All hypotheses were tested by ICP-OES, DOC (dissolved organic carbon), TN (total nitrogen) and EPR analyses.

Materials and methods

Materials

Fibers: Commercial chrysotile was purchased from Shijiazhuang Mining IMP&EXP Trade Co, China. Phase and bulk analyses of Shijiazhuang chrysotile were carried out by Walter et al. (2018a) or Walter et al. (2018d) [146, 204] (Table 1). Additionally, the bulk metal and Si content of Shijiazhuang fibers was determined by fusion digestions according to Walter et al. (2018a) [146] (Table 1). Thereby, new data and published data by Walter et al. (2018a) were combined [146].

Soils: Three geochemically different soils were used (Table 1). An acidic B horizon of a podzol with high DOC soil solution contents was collected in Schrems, Lower Austria (Latitude: 48°49'4.02"N; Longitude 15°3'24.77"E). An agricultural cambisol (0 – 20 cm) with mildly acidic pH and low DOC soil solution contents was collected in Siebenlinden, Lower Austria (Latitude: 48°41'1.53"N; Longitude 15°0'3.00"E). Finally, a calcareous entisol (0 – 20 cm) with a high clay, but low DOC soil solution content, was collected in Santomera, Spain (Latitude: 38°01'17.01"N; Longitude 1°10'43.69"W). Plants grow chlorotic on Santomera soil [208]. These soils were used in several studies on Fe speciation in soil [190] and Fe acquisition by plants [191, 192, 193, 194, 195, 196, 197]. Suspensions of all three soils were furthermore used in the fiber dissolution study of Walter et al. (2018d) [204]. To improve root penetration in Santomera soil, it was amended with quartz sand in a ratio of 3:1. Prior to the microcosm experiment, the soils were airdried and sieved (4 mm mesh). Pictures of the colleting sites of the soil can be seen in SI-Figure 1.

Cement: Commercial cement powder ("ProBau® Schnellzement") was hardened with deionized water (DIW), dried for two days, and then crushed into particles. To prevent agglomeration, the particles were equilibrated for one day in DIW, dried again, and selectively sieved to a particle fraction of 0.7 - 1 mm. The bulk composition of the cement was determined by Walter et al. (2018d) [204].

Plants: Three plant species were used: White lupines exude up to millimolar amounts of citrate [209], especially under stress situations (e.g. P deficiency) [210]. Lupinus albus cv. Multolupa was especially prone in exuding citrate [211]. Since this cultivar was not available, the cultivar Multitalia, an Italian line of Multolupa, was used. Sheep sorrel exudes oxalate, especially as adaptive stress mechanism (e.g. against Al toxicity) [212]. Sorrel seeds (rumex acetosella sp) were obtained from a commercial supplier in Germany (Templiner Kräutergarten). Both lupines and sorrel were grown on Siebenlinden soil. Finally, the Kentucky bluegrass poa pratensis cv. Baron was used to represent graminaceous strategy II plants. It exudes elevated amounts of Fe chelating phytosiderophores [213], and was grown on

Table 1: *Section a.) Bulk concentrations determined in fusion digestions and an NAA; Section b.) Soil properties. Abbreviations are fiber to solution ratio (FSR), soil to solution ratio (SSR), fiber to soil ratio (FSoR), water holding capacity (WHC), neutron activation analysis (NAA), white lupine (LUP), sorrel (SORR), poa pratensis (POA). Numbers in round braces are standard deviations.*

a.) Bulk analyses		*Fusion digestion*[1]	*NAA*[2]		*Mössbauer [%]*
Mg	[g kg^{-1}]	253 (8.9)		Fe^{2+}[6][4]	38.4[*]
Si	[g kg^{-1}]	193 (6.4)		Fe^{3+}[6][4]	54.6[*]
Fe	[g kg^{-1}]	19.0 (1.2)	21.4 (0.3)[*]	Fe^{3+}[4]	7.0[*]
Al	[g kg^{-1}]	7.4 (0.8)		Total Fe in chrysotile	68.2[*]
Mn	[g kg^{-1}]	0.8 (0.06)			
Ni	[g kg^{-1}]	1.3 (0.10)	1.2 (0.03) [**]		
Cr	[g kg^{-1}]	1.4 (0.11)	1.3 (0.04) [**]		
Zn	[mg kg^{-1}]		17.0 (1.1) [**]		

b.) Soil and soil solution properties:		Schrems	Siebenlinden	Santomera
Classification		Podzol	Cambisol	Entisol
$CaCO_3$ content	[%]	0 [**]	0 [**]	52 [***]
Clay content	[%]	21 [**]	7 [**]	26 [***]
Nitric acid Mg[3]	[mmol L^{-1}]	0.17 (0.01)	0.61 (0.04)	15.6 (0.6)
Estimated WHC	[ml kg^{-1}]	1.24	0.35	0.21
FSR	[g L^{-1}]	1.18	2.57	4.29
SSR		1:0.62	1:0.175	1:0.105
FSoR	[g kg^{-1}]	0.73	0.45	0.45
Soil solution pH[2]		3.5 (0.1)	4.2 (0.1)	7.2 (0.1)
Soil solution pH planted soils[2]			LUP: 4.6 (0.4)	POA: 7.7 (0.2)
			SORR: 4.8 (0.1)	
Soil solution DOC[2]	[mg L^{-1}]	893 (159)	45.6 (13.8)	29.3 (8.4)
Soil solution DOC planted soils[2]	[mg L^{-1}]		LUP: 72.4 (24.7)	POA: 146 (68.5)
			SORR: 187 (35.9)	

[1] n = 32
[2] n = 2
[3] n = 4
[4] Octahedrally coordinated ferrous or ferric Fe
[*] Walter et al. (2018a) [146]
[**] Walter et al. (2028d) [204]
[***] Schenkeveld et al. (2008) [197]

Santomera soil. Seeds were obtained from a commercial supplier in Italy (Fratelli-Ingegnoli, Milano). Citrate, oxalate and phytosiderophores were demonstrated to increase the ligand-promoted dissolution of metals from chrysotile at a wide pH range [146].

Experimental procedure of the microcosm experiment

Incubation: Fibers were incubated in Nylon-membrane based "fiber incubation bags" in soils: Two nylon membranes (diameter 47mm, pore size 0.45µm, Magna) were glued together on the rims using specifically suited plastics glue ("Patex Kunststoffkleber®"). 450 mg fibers were filled into bags, which were closed by further gluing. These bags were tearproof, even after prolonged incubation in soils. For each bag, a cement replicate was manufactured: A further layer that contained 2.5 g of cement particles was retained on each side of the fiber incubation bags by gluing a nylon mesh ("Siebgewebe", VWR) on the rims of the bags. The fiber to cement ratio thereby corresponded with the ratio that was used in Eternit (≈1:10) [4]. Both bag types were incubated some centimeters above the bottom of pots containing the soils which were wetted to 50% of their estimated water holding capacity (WHC, Table 1) with DIW. The corresponding fiber to solution ratio (FSR), soil to solution ratio (SSR) and fiber to soil ratio of all treatments are listed in Table 1. Fiber bags (cement and no cement) were incubated in four replicates of unplanted "blank microcosms" for 0.5; 1; 1.75 and 2.5 years. Every second week, evaporated water was compensated with DIW. To avoid rapid evaporation, the pots were covered with perforated plastic wraps. All blank pots were kept in a temperature-controlled room (20 ± 2 °C) in the dark. Fiber bags were analogously incubated in planted pots in Fitotron growing chambers for 1, 1.75 and 2.5 years at 20 ± 1 °C. Because of evapotranspiration, the water loss had to be compensated three times per week with DIW by considering the estimated weight of the plants. The day/night cycle consisted of 14 hours light per day. The transparent pots were wrapped in Al foil. Per pot, 5 lupines were planted, the number of plants was successively reduced to allow the growth of one strong plant. Once it faded away (≈1 year), a new planting cycle was started. The other plant species were planted according to growth density, whereby sorrel was never re-panted, but Kentucky bluegrass after the first year. The latter grew chlorotic after prolonged incubation. To avoid accumulation of water on the bottom, the pots were placed on a mesh-wire above saucers. Occasionally leaking water was retained in the saucers and poured back into the pots. Pictures of the experimental setup can be seen in SI-Figure 2, of the chlorotic Kentucky bluegrass in SI-Figure 3.

Sampling: Sampled fiber bags were cleaned on one edge and then cut open to sample the fibers, which were vacuum dried in a desiccator. The soil was airdried and stored.

Processing of sampled fibers, soil solutions and soils

Soil solution analyses: After 1, 1.75 and 2.5 years, homogenized aliquots of the soils were immediately centrifuged in two-compartment centrifuge tubes for 10 minutes at 7000 rounds per minutes according to Schenkeveld et al. (2008) [197]. The pH and the metal, P, DOC and TN content of the filtrate was analyzed.

Fusion digestions: To determine the metal and Si bulk of sampled fibers, 100 mg of fibers sampled from all microcosms were fusion digested according to Walter et al. (2018a) [146].

Alkaline extractions: To detect amorphous siliceous material that formed during fiber weathering [100, 101], 1 g L^{-1} of fibers from all microcosms were subjected to alkaline extractions according to Walter et al. (2018d) [204] for 4 h in a 0.1 mol L^{-1} NaOH. In the same extractions, desorbed DOC and TN was analyzed.

pH 7.4 extraction: For analyzing surface metal contents of sampled chrysotile, 1 g L^{-1} of fibers from all microcosms were incubated according to Walter et al. (2018d) [204] for 336 h in a pH 7.4 buffered solution (buffered with 50 mmol L^{-1} MOPS (3-(*N*-morpholino)propanesulfonic-acid)) containing 1 mmol L^{-1} of the metal chelator HEDTA (hydroxyethylenediaminetriacetic-acid).

Nitric acid extraction: Dried soils of the Schrems and Siebenlinden blank treatments were homogenized and analyzed in nitric acid extractions (ISO 17586), whereby metals were extracted from soil in a 0.43 mol L^{-1} HNO_3 for 2 h at a SSR of 1:10.

Analytical procedures and corresponding sample preparations

Metal, Si, P and DOC analyses: All extraction samples were incubated in a temperature-controlled room (20 ± 2°C) in the dark. Soil and fiber suspensions were filtered over 0.45 µm Sartorius cellulose acetate syringe filters, aliquots of the obtained filtrates were acidified with trace metal grade HNO_3 to 0.14 mol L^{-1}. Fusion digestion samples were neither filtered nor acidified. The Si, P and metal content of samples was analyzed by ICP-OES spectrometry (Optima 5300-DV, Perking-Elmer), calibration standards were matrix-matched with the samples. DOC samples were only acidified during analysis (TOC-L Shimadzu).

EPR spin trapping analysis: The generation of $HO^{\bullet}$ in Fenton reactions out of H_2O_2 was quantified using a Bruker X-band EPR spectrometer with 5-5'-dimethyl-1-pirroline-N-oxide (DMPO) as spin trap. This technique has been frequently used before in this context [35, 37, 43, 50, 121, 146, 174, 184, 204] and was carried out according to Walter et al. (2018a) [146]. Per treatment, eight replicates were analyzed (2 per pot). The decreased signal intensity of sampled fibers (the decreased HRFP) was expressed as % relative to the intensity of pristine fibers. Intensities of DMPO/$HO^{\bullet}$ spectra were quantified by the height of the second peak from the left in the quadruplet.

Data Processing and supplementary information

Dissolution rates: Surface normalized Mg and Si dissolution rates were calculated by dividing the slopes of linear regressions of dissolved Mg and Si concentrations as a function of time by the BET surface area of pristine fibers [146]. Dissolved Mg concentrations were either determined by the sum of Mg

that partitioned to the soil solution and soil or by the molar Mg/Si ratios of sampled fibers. Regarding the latter, molar Mg/Si ratios of Shijiazhuang chrysotile with known Mg dissolution determined by Walter et al. (2018d) [204] in Schrems podzol suspensions were used for calibrating the Mg/Si ratios of fibers from this study to dissolved Mg contents. Si dissolution was calculated by dividing the dissolved Mg contents determined in both approaches through the corresponding molar Mg/Si ratios. Alkaline extractable Si contents from sampled fibers were added to the calculated dissolved Si contents to account for the formation of amorphous siliceous material during fiber dissolution [204].

Statistics: An ANOVA was carried out with the StatPlus:mac Pro (Build 6.3.05/Core v6.2.30, AnalystSoft Inc) and XLSTAT Base (v2018, Addinsoft) software. A F-test was used to determine equal or unequal variance between samples. For equal variance, a one-way ANOVA (alpha 0.05) test was used to determining significant differences between samples. If a significant difference was found between more than three samples, a Tukey HSD post-hoc test (alpha 0.05) was used to confirm differences between samples. For unequal variance, a non-parametric Kruskal-Wallis (alpha 0.05) test was used to determine significance between samples. If a significant difference was found between more than three samples, a Dunn post-hoc test with a Bonferroni correction (alpha 0.0167) was used to test and identify differences between samples.

All data presented in Figure 1 - 3 are reported in SI-Table 1 - 3 respectively, the results of all statistical analyzes are summarized in SI-Table 4.

Results and discussion

Effect of soils

Bulk Si contents of 100 mg chrysotile fibers sampled from Schrems microcosms linearly increased by 10.0% per year (relative to pristine fibers), whereas Mg contents decreased by 13.2% (Figure 1a). This indicates incongruent dissolution of fibers in Schrems soil, with Si accumulating and Mg dissolving. The Cr and Ni bulk contents of digested fibers from Schrems microcosms similarly decreased as Mg relative to pristine fibers (SI-Table 5). The Mn bulk contents of chrysotile rapidly decreased and equilibrated at a level of 27% (relative to pristine fibers) after 1.75 years of incubation. A similar fast dissolution of the Mn bulk of chrysotile has already been described in the soil suspension experiments of Walter et al. (2018d) [204]. The authors of this study concluded that Mn is enriched in the outer Mg layers of Shijiazhuang chrysotile, and that the dissolution of these layers caused the depletion of a high fraction of the total Mn bulk. The molar Mg/Si ratios of fibers sampled in Schrems microcosms linearly

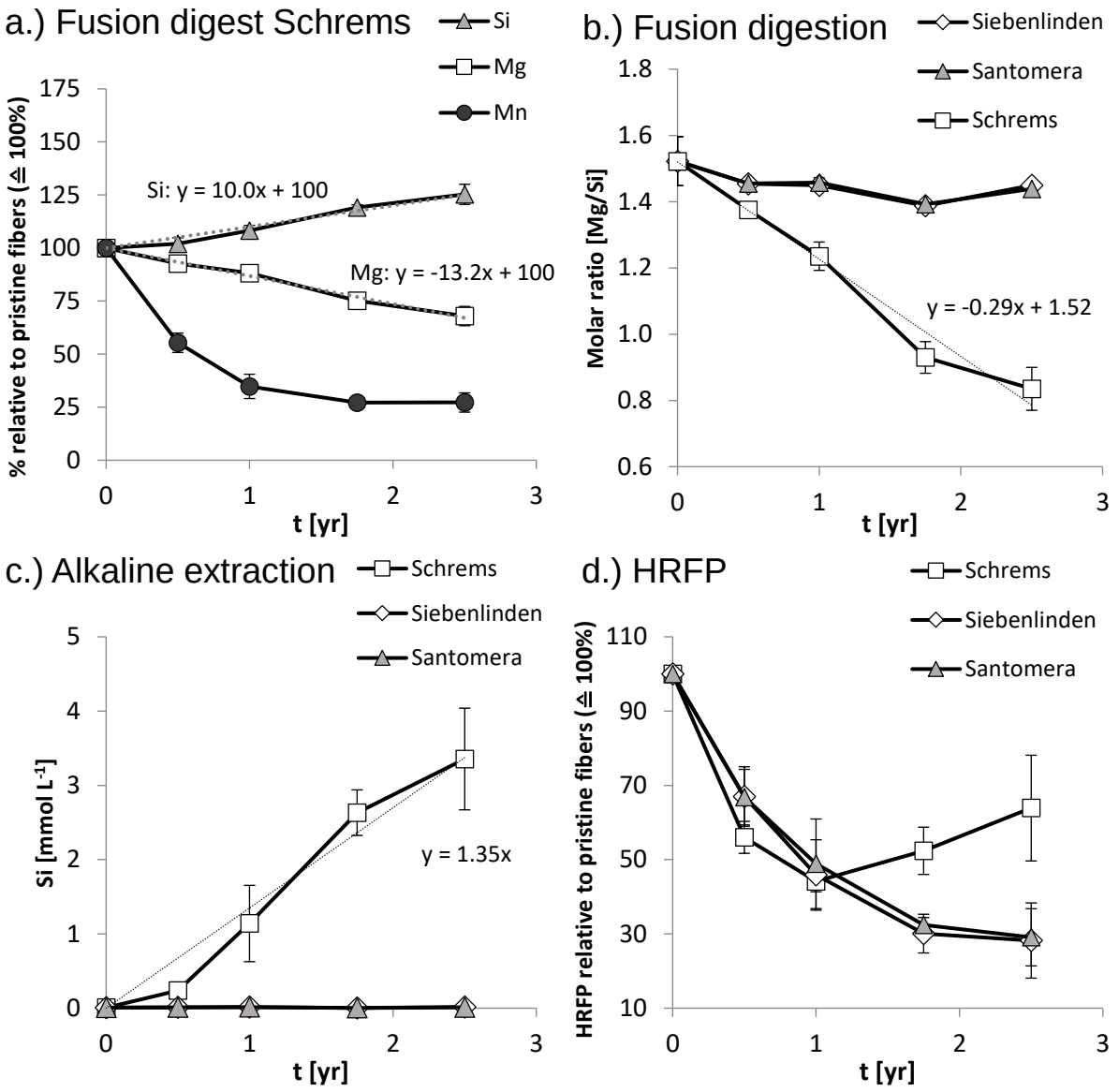

Figure 1: *Effect of soils. Panel a.) Si, Mg and Mn bulk of fibers in the Schrems microcosms as a function of time in % relative to pristine fibers (≙ 100%); Panel b.) Molar Mg/Si ratios of fibers from Schrems, Siebenlinden and Santomera microcosms as a function of time. Panel c.) Alkaline extracted Si contents of fibers from Schrems, Siebenlinden and Santomera microcosms as a function of time. Panel d.) HRFP of fibers from Schrems, Siebenlinden and Santomera microcosms in % relative to the HRFP of pristine fibers (≙ 100%). Error bars indicate standard deviations (Panel a – c: n = 3; Panel d: n = 8).*

decreased from 1.52 (pristine fibers) by approximately 0.29 per year (Figure 1b). Mg and Si dissolution rates of fibers in Schrems microcosms that were calculated by these ratios were 3.63 and 0.80 pmol m^{-2} s^{-1}, which indicates incongruent fiber dissolution (stoichiometric Mg/Si ratio of ≈1.5). These rates correspond to the total dissolution of 22.3% and 5.7% of the Mg and Si fiber-bulk per year respectively (Table 2). All these observations verify out hypothesis: Mg dissolution rates in Schrems soils were approximately 4.5 times lower than determined in Schrems soil suspensions [204], and more than an

Table 2: *Surface normalized Mg and Si dissolution rates of fibers incubated in Schrems no cement microcosms. Rates were calculated by Mg/Si ratios of fibers ("Mg/Si ratios") and by the summed Mg concentrations that partitioned to the soil solution and to soil ("Soil & solution"). For Si dissolution rates, alkaline extractable siliceous material ("+ alk extract") was added to dissolved Si contents. * indicates congruent dissolution (within 25%). Values in round braces indicate R^2 values of the linear regressions used, values in square brackets the bulk dissolution in % after one year of incubation calculated by the respective rates. n.d.: not determined.*

	Origin of data	Mg dissolution [pmol m^{-2} s^{-1}]		Si dissolution [pmol m^{-2} s^{-1}]			
		Mg/Si ratios	Soil & solution	Mg/Si ratios	Soil & solution	Mg/Si ratios + alk extract	Soil & solution + alk extract
This study	Microcosm experiments	3.63* (0.96) [22.3 % yr^{-1}]	2.94 (0.95) [18.0 % yr^{-1}]	0.80 (0.98) [7.46 % yr^{-1}]	0.61 (0.98) [5.69 % yr^{-1}]	2.92* (0.98) [27.2 % yr^{-1}]	2.57 (0.99) [24.0 % yr^{-1}]
Walter et al. (2018d) [204]	Fiber/Soil suspension experiments	16.4* [i] (0.96) [101 % yr^{-1}]	15.0 (0.99) [91.9 % yr^{-1}]	5.33 [i] (0.89) [49.9 % yr^{-1}]	n.d.	12.0* (0.93) [112 % yr^{-1}]	n.d.
Walter et al. (2018a) [146]	Fiber batch dissolution experiments	n.d.	47.3 at pH=3.0 [ii] [290 % yr^{-1}]	n.d.	17.3 at pH=3.0 [ii] [161 % yr^{-1}]	n.d.	n.d.

[i] Note that these dissolution rates were determined by quantitative acid digestions of fibers in soil suspensions

[ii] Note that dissoluton rates were determined in soil free systems

order of magnitude (≈ factor 13) lower than rates determined in batch dissolution experiments at a similar pH [146] (Table 2). The molar Mg/Si ratios of fibers from Siebenlinden and Santomera microcosms did not statistically differ and equilibrated at a mean level of 1.45 between 0.5 and 2.5 years of incubation (Figure 1b). This either indicates that the fibers did not sufficiently dissolve, or that they dissolved congruently. Even though congruent dissolution of Shijiazhuang chrysotile was observed at pH 4.5 [146] and 7.4 [184] in batch dissolution experiments, the fibers did not dissolve apart from the outermost Mg layer in quantitative soil suspension dissolution experiments of the same soils [204]. The low decreases of the bulk-Mn of fibers sampled from Siebenlinden and Santomera soils support that the high Mg/Si ratios were caused by low dissolution rates (e.g. 76% of the bulk-Mn was still present in fibers from Siebenlinden and 93% in Santomera microcosms after 2.5 years of incubation, SI-Table 6). The molar Mg/Si ratio of 1.45, which corresponds to ≈0.85 mmol L^{-1} of dissolved Mg (under the assumption that no Si had

dissolved), approximately represents the dissolution of the outermost Mg layer and the brucite phase contamination in Shijiazhuang chrysotile (≙ 406 and 771 ± 360 µmol g^{-1} respectively) [146]. This calculation further suggests that maximally the outermost Mg layer of chrysotile dissolved in Siebenlinden and Santomera microcosms. Since fiber weathering was equally inefficient in both microcosms despite the high difference in their soil solution pH (Table 1), fiber weathering in soil was not exclusively a function of the mere soil solution pH. Chrysotile pollution was demonstrated to increase the pH of contaminated soils [84]. Since Siebenlinden soil has a low buffer capacity (as observed in chrysotile soil suspension dissolution studies [204]), the soil solution in Siebenlinden microcosms most likely did not sufficiently buffer fiber dissolution. Contrarily, the Schrems podzol must have buffered fiber dissolution, explaining the high dissolution rates in this treatment. Considering this, we need to modify our hypothesis: Dissolution of chrysotile in soils is inversely related to the soil solution pH only at a sufficiently high soil buffer capacity.

The alkaline extractable amount of Si from fibers of Siebenlinden and Santomera microcosms was in the low µmol L^{-1} background range (Figure 1c). However, alkaline extractable Si contents linearly increased by approximately 1.35 mmol L^{-1} per year from 1 g L^{-1} of fibers sampled in Schrems microcosms, indicating that the fibers weathered and transformed into a secondary amorphous siliceous material. Apart from Si, a similar increase was also observed for Al (SI-Table 7). By summing up extracted Si contents and calculated dissolved Si contents, the Si dissolution rate of fibers in Schrems microcosms were 2.92 pmol m^{-2} s^{-1}, which corresponds to 27.2% of total dissolution of the Si bulk per year. This rate is approximately stoichiometric to its corresponding Mg dissolution rate (within 25%), indicating that fibers weathered congruently in Schrems microcosms when considering the formation of amorphous siliceous material (Table 2).

The HRFPs of fibers from Siebenlinden and Santomera microcosms did not statistically differ and decreased to approximately 30% after 1.75 years and remained at that level until 2.5 years (Figure 1d). This HRFP represents the lowest possible HRFP of Shijiazhuang chrysotile dissolving in the absence of (high concentrations of) Fe^{3+}[4]-chelating ligands [146, 184, 204]. However, this decrease took years in microcosms, whereas it maximally took weeks in soil suspensions and dissolution studies [146, 204]. This verifies our hypothesis that the HRFP of chrysotile decreases considerably slower in more realistic soil rather than simplified laboratory conditions. This decrease in HRFP indicates that the highly Fenton-active Fe^{3+}[4] content of the fibers' exposed Si layers slowly, but successively, dissolved in Siebenlinden and Santomera microcosms, rendering Fe^{3+}[4]-surface-depleted fibers. The maximum HRFP-decrease level of 25 - 30% likely constitutes an equilibrium between the hydrolytic Fe^{3+}[4] dissolution and the consequent Si labilization, which causes the re-exposure of Fe^{3+}[4] from deeper layers. The HRFP of fibers from Schrems microcosms did however not decrease to 25 - 30% (Figure 1d).

It first decreased to 56% after 0.5 years, which constituted a significantly faster decrease than observed in Siebenlinden and Santomera microcosms (≈67%). The HRFP then significantly further decreased to a minimum of 44% after 1 year of incubation, but significantly increased again to 63% after 2.5 years. An increased HRFP of chrysotile has also been observed for fibers that were incubated in soil suspensions of the Schrems podzol by Walter et al. (2018d) [204]. A rationale for the increase in HRFP was discussed by the authors of the aforementioned study to be the Fe-rich soil solution in the Schrems podzol. Also in Schrems microcosms, the mean value of Fe in soil solution was high (163 µmol L^{-1}, SI-Table 8). Fe from the soil solution may have incorporated as Fe^{3+}[4] into vacancies of the fibers' Si layer, which had been formed after the hydrolytic dissolution of Fe^{3+}[4] or tetrahedral Al [146]. A similar incorporation of external Fe into Si vacancies of hrysotile has already been observed in batch-dissolution experiments [174]. In soil microcosms, this incorporation of Fe^{3+}[4] likely took years, which may explain the initial decrease in HRFP for up to 1 years of incubation. As a consequence, the HRFP of chrysotile fibers that weather in soils with a high mobile Fe content cannot decrease to the minimum equilibrium HRFP of 25 - 30%. This partly falsifies our hypotheses: Only in the absence of mobile Fe in soil solutions, the HRFPs of fibers in soils decrease to a minimum value of 25 - 30%. This decrease seems to be inversely related to the soil solution pH (as observed in this study for up to 0.5 years and in the soil suspension study of Walter et al. (2018d) [204]).

The surface metal content on fibers from soil microcosms was investigated in pH 7.4 extractions. The extracted contents of Mg, Fe, Mn, Ni and Cr were consistently lower for fibers of Schrems microcosms than for fibers of Siebenlinden and Santomera microcosms (Figure 2a, SI-Figure 4). This was probably caused by the enhanced fiber dissolution kinetics in Schrems microcosms. Apart from dissolution, elements also accumulated on fiber surfaces in soils. Zn accumulated on fibers in Schrems and Siebenlinden microcosms relative to pristine fibers, e.g. by a factor 6.4 and 3.7 respectively after 2.5 years (SI-Figure 5). A similar accumulation of Zn in soil suspensions was already observed by Walter et al. (2018d) [204]. Furthermore, DOC accumulated on fibers from Schrems microcosms by up to a factor ≈7 more than on fibers from Siebenlinden and Santomera microcosms (SI-Figure 5).

Effect of cement

Cement near fibers in soils did not influence the molar Mg/Si ratios of fibers in Siebenlinden and Santomera microcosms (Figure 2b). However, cement near fibers completely inhibited the decrease of molar Mg/Si ratios that was observed in Schrems no cement microcosms: The ratios only decreased to a mean level of 1.44, which was identical with the mean ratios of fibers from microcosms in which only the outermost Mg layer dissolved. Similarly, the bulk-Mn did by far not decrease as drastically as

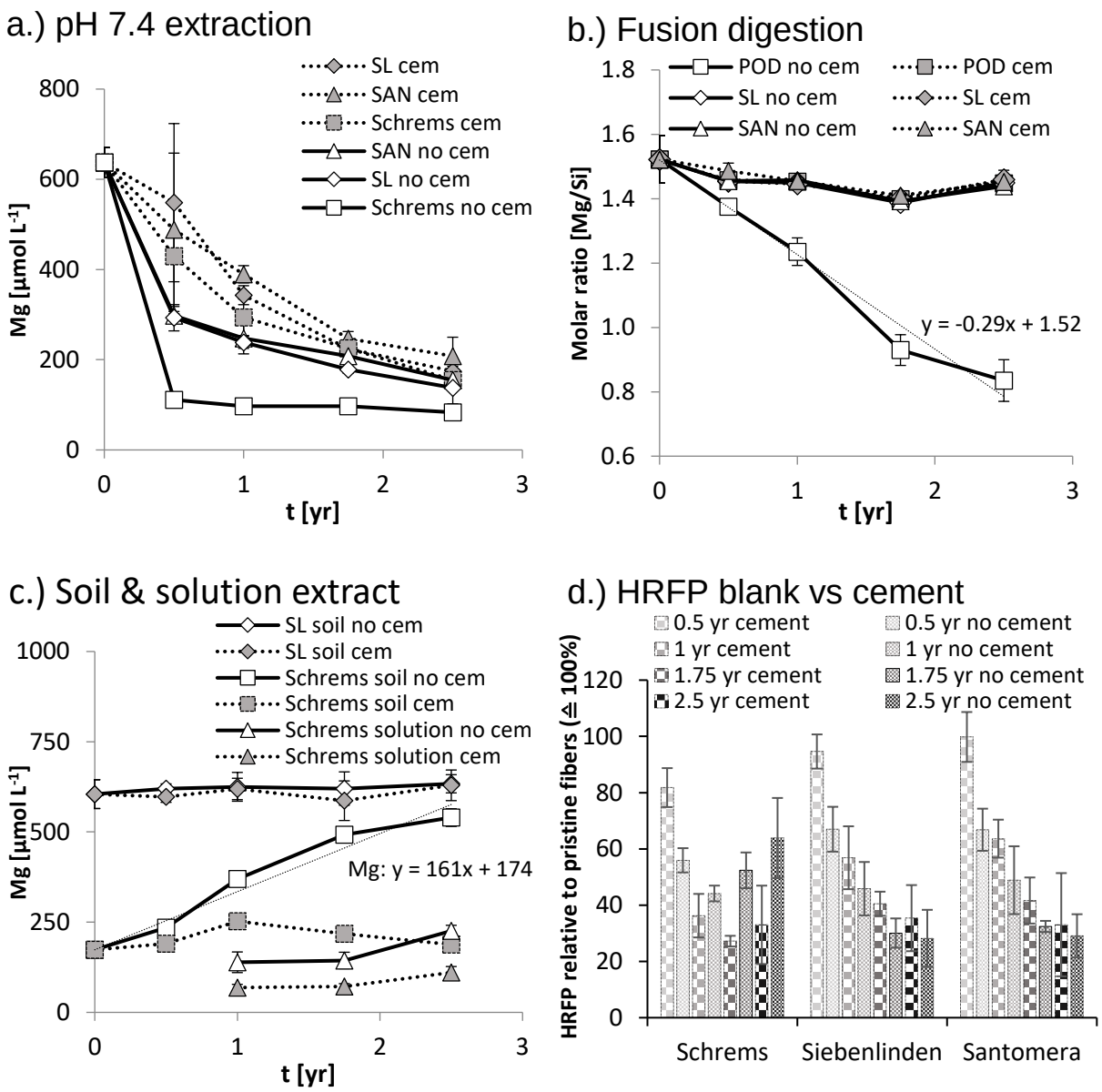

Figure 2: *Effect of cement. Panel a.) Mg contents extracted from fibers sampled in Schrems, Siebenlinden and Santomera cement and no cement microcosms (n = 4); Panel b.) Molar Mg/Si ratios of fibers from Schrems, Siebenlinden and Santomera cement and no cement microcosms (n = 4). Panel c.) Nitric acid extractable Mg contents from soils of the Schrems and Siebenlinden cement and no cement microcosms (n = 4), and Mg contents of the soil solutions in Schrems cement and no cement microcosms (n = 2). Panel d.) HRFP of fibers from Schrems, Siebenlinden and Santomera cement and no cement microcosms (n = 8) relative to the HRFP of pristine fibers (≙ 100%). Error bars indicate standard deviations. "POD" indicates Schrems podzol, "SL" Siebenlinden, "SAN" Santomera soil and "cem" cement.*

observed for fibers of no cement treatments (SI-Table 6). The inhibition of fiber dissolution in the Schrems cement microcosms was furthermore supported in alkaline and nitric acid extractions of fibers: The alkaline-extractable Si (and Al, SI-Table 7) contents were up to three orders of magnitude

lower than extracted contents of fibers from the no cement microcosms (data not shown), which indicates that the fibers did not weather into a secondary amorphous siliceous material in the presence of cement. Furthermore, the nitric acid extractable Mg contents of soils from Schrems treatments only increased in no cement microcosms (by approximately 161 µmol L^{-1} per year), whereas they remained constant in their cement analogs (Figure 2c), which indicates that fibers did not dissolve in the latter treatments. Additionally, nitric acid extractable Cr and Ni concentrations were significantly higher in soils from Schrems no cement compared to cement microcosms (SI-Table 9). Apart from metal accumulation in soils, soil solution Mg contents were at all sampling times higher in no cement Schrems microcosms than in their cement analogs (Figure 2c). The same trend was also observed for Cr (SI-Figure 6). All these observations verify our hypothesis that fiber weathering in soils is greatly inhibited in the presence of cement.

The calculated Mg dissolution rates of the sum of the dissolved Mg contents that partitioned to the soil solid phase and soil solution were comparable to the Mg dissolution rates calculated before (2.94 vs. 3.63 pmol m^{-2} s^{-1} respectively, Table 2). This validates our calculation of Mg dissolution rates by molar Mg/Si ratios and indicates that the Mg mass balance in Schrems microcosms was closed.

The Mg contents in nitric acid extractions of soils from Siebenlinden cement and no cement microcosms did not statistically differ (Figure 2c). This supports our conclusion that fibers in Siebenlinden no cement microcosms did, apart from their outermost Mg layer, not substantially dissolve. Analogously, the soil solution Mg contents of cement and no cement microcosms did not statistically differ in Siebenlinden and Santomera treatments (SI-Table 8).

Cement near fibers caused significantly higher mobilized Mg (Figure 3a) and Ni, Cr, Mn and Fe contents from fibers of Schrems, Siebenlinden and Santomera microcosms in pH 7.4 extractions (SI-Figure 7), most likely because it antagonized their dissolution from fibers in soils. The highest inhibitory effect by cement addition was observed in Schrems treatments.

In Siebenlinden and Santomera microcosms, the addition of cement significantly slowed down the decrease in HRFP of fibers to the minimum equilibrium HRFP level of 25 - 30% for up to 1.75 years (Figure 2d), likely because it antagonized the hydrolytic dissolution of Fe^{3+}[4] from exposed Si layers of chrysotile due to its alkalinity. In Schrems microcosms, cement only antagonized the HRFP decreased of fibers after 0.5 years of incubation. After 1.75 and 2.5 years, HRFPs of fibers from cement microcosms were significantly lower than HRFPs from no cement microcosms. This can be related to the observation that the HRFPs of fibers in Schrems no cement microcosms did not decrease to the equilibrium HRFP of 25 - 30% (Figure 1d), whereas the HRFPs of fibers in cement microcosms did after 1.75 years, despite the high mobile Fe contents of the soil solution in Schrems microcosms. The

rationale for this may have been a locally increased soil solution pH by cement, which permitted the incorporation of external Fe from the soil solution into vacancies of exposed Si layers due to the drastically decreased Fe^{3+} solubility and hence delivery of Fe to the fiber surfaces.

The observed effects of cement on fiber weathering and the fibers' HRFPs can all be explained by an increased local soil solution pH due to the spatial vicinity of the alkaline cement particles. Thereby, the local soil solution pH in the cement-fiber incubation bags probably increased up to circumneutral or mildly alkaline values, since the outermost Mg layer still dissolved and the HRFP decreased down to the minimum equilibrium HRFP of 25 - 30%. If cement had equilibrated the soil solution pH up to cement values (pH 11 and higher [103]), the outermost Mg layer would not have dissolved and, as a consequence, the HRFP would have remained unchanged [146]. An accumulation of Al on chrysotile, as described for soil suspension with added cement powder [204], was not observed, probably because the cement had been hardened before the experiment.

Cement furthermore inhibited the accumulation of Zn and TN on fibers from Schrems soil, but not of DOC (SI-Figure 5). This may indicate that the accumulation of Zn and TN was independent of DOC.

Effect of plants

The molar Mg/Si ratios of fibers from planted and unplanted Siebenlinden and Santomera no cement and cement microcosms did not statistically differ (Figure 3a, SI-Figure 8). The Mn bulk of fibers sampled from planted treatments did not decrease relative to the Mn bulk of fibers that were sampled in their blank microcosms analogs (SI-Table 6). Hence, we conclude that the high molar Mg/Si ratios of fibers from planted microcosms indicate low dissolution rates rather than congruent dissolution.

Plants generally decreased the soil solution contents of TN, Mg, Na, Al, K, Ca, V, Mn, Ni and Zn, whereas they generally increased the soil solution pH and contents of DOC, Fe, P, Cr, Cu and Ti (Table 1, SI-Table 8). The depletion of metals from soil solutions may be demonstrated by Mg contents, which decreased by a factor 121 from 6.19 to 0.05 mmol L^{-1} in lupine-, and by a factor 46 to 0.14 mmol L^{-1} in sorrel-planted Siebenlinden microcosms after 2.5 years of incubation (Figure 3b). Contrarily, soil solution Fe contents significantly increased in planted Siebenlinden treatments, e.g. from approximately 1 to 12 µmol L^{-1} in sorrel planted microcosms (Figure 3b).

Similarly to metal contents in soil solutions, the contents of extracted Mg, Fe, Cr, Ni and Mn from fibers of planted microcosms in pH 7.4 extractions were in many treatments significantly lower than from fibers of the corresponding unplanted microcosms (Figure 3c, SI-Table 10): E.g. extracted Mg contents of fibers from lupine planted microcosms were a factor 2.5 (after 1.75 years) and a factor 3.5 (after 2.5

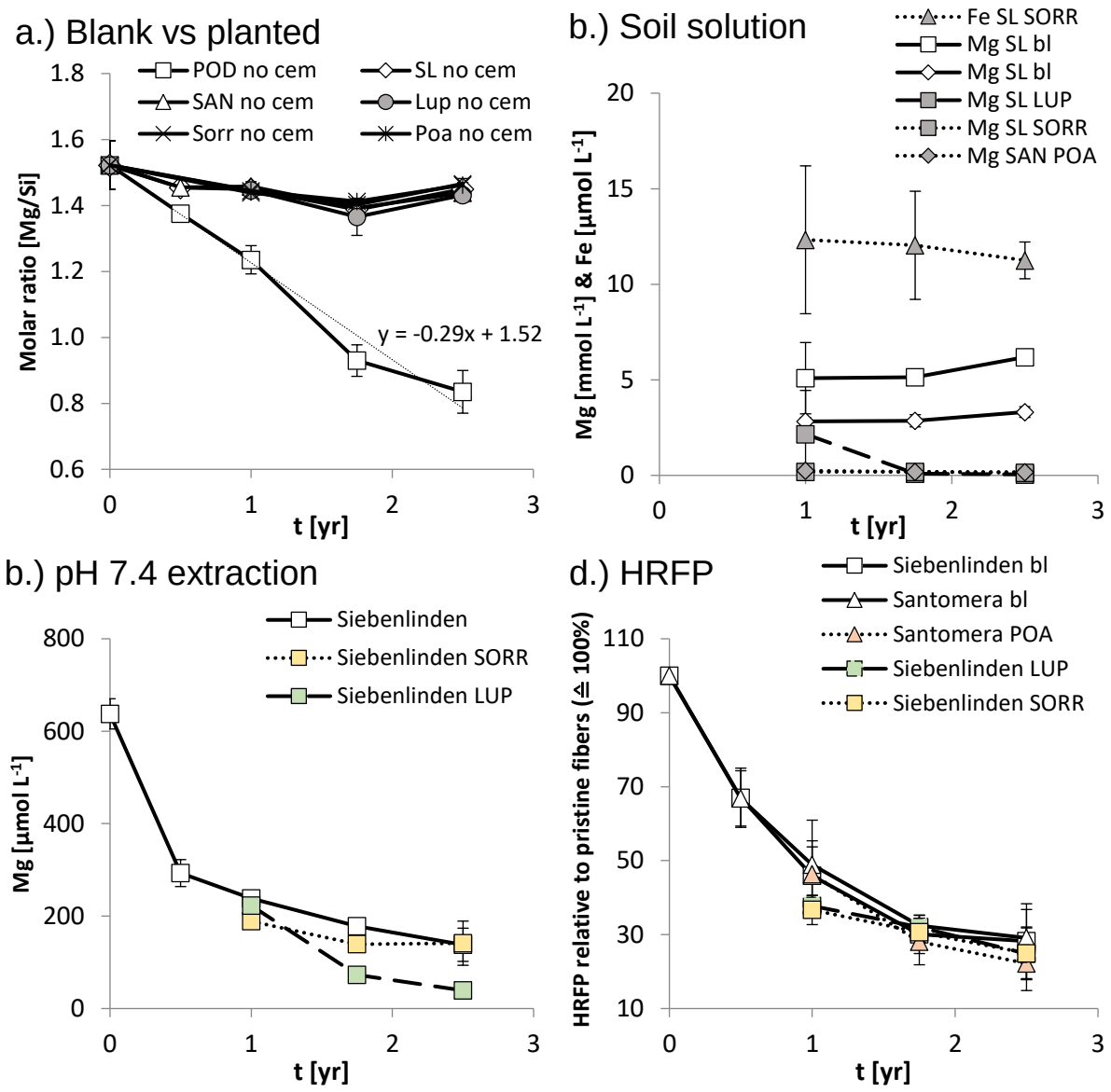

Figure 3: *Effect of plants. Panel a.) Molar Mg/Si ratios of fibers from Siebenlinden and Santomera no cement blank and planted microcosms (n = 4). The molar Mg/Si ratios of fibers from Schrems microcosms were added as a reference; Panel b.) Soil metal contents of Siebenlinden and Santomera no cement blank and planted microcosms (n = 2). Fe concentrations in the soil solutions of Siebenlinden blank treatments did not exceed 2 µmol L^{-1}; Panel c.) Mg contents extracted from fibers of Siebenlinden no cement blank and planted microcosms (n = 4); Panel d.) HRFP of fibers from Siebenlinden and Santomera no cement blank and planted microcosms (n = 8). Error bars indicate standard deviations. "bl" indicates blank, "cem" cement "LUP" white lupine, "SORR" sorrel and "POA" Kentucky bluegrass.*

years) lower than in unplanted microcosms (Figure 3c). Similarly, extracted Fe from fibers of lupine and sorrel planted microcosms after 2.5 years was by 50% (10.7 vs. 16.1 µmol L^{-1}) and by 35% (11.3 vs. 15.3 µmol L^{-1} respectively) significantly lower than in unplanted microcosms (SI-Table 10). A similar depletion was observed in desorbed TN contents in alkaline extractions of fibers from all planted

relative to unplanted microcosms (SI-Figure 5). These observations verify our hypothesis that plants can dissolve metals (and non-metals like TN) from chrysotile in soils. The enhanced dissolution of low soluble metals like Fe was likely the consequence of the exudation of metal chelating ligands by plants. This may be supported by the significantly increased DOC and consequently increased Fe contents in soil solutions of planted microcosms (Table 1, Figure 3b, SI-Table 8). Furthermore, desorbed DOC levels from fibers of planted microcosms were higher than in unplanted microcosms, which supports an interaction of plant-borne DOC with fibers (SI-Figure 5). Moreover, roots of all plant species were observed to attach to the fiber incubation bags, lupine roots even penetrated an asbestos cement bag after 1.75 years of incubation and proliferated inside the bag (SI-Figure 9). All these observations indicate that plants use chrysotile as a source for metal acquisition in soils.

The HRFP of fibers from lupine and sorrel planted microcosms were by ≈20% significantly lower than the HRFP of fibers from unplanted microcosms after 1 year of incubation (Figure 3d). Considering that plants facilitated metal dissolution from fibers, they may have as well enhanced the dissolution of Fenton-active Fe^{3+}[4]. However, this difference already perished after 1.75 and 2.5 years, since in both planted and unplanted Siebenlinden microcosms the HRFPs of fibers equally decreased to the minimum equilibrium HRFP of 25 - 30%. However, fibers sampled from planted Kentucky bluegrass microcosms had a significantly lower mean HRFP (also by ≈20%) after 2.5 years than fibers from unplanted microcosm, which suggests that plants may decrease the HRFP of chrysotile in soil even further than the minimum equilibrium HRFP. As the Kentucky bluegrass became increasingly chlorotic towards the end of the microcosm experiment (SI-Figure 3), this decreased HRFP was possibly a consequence of an enhanced exudation of phytosiderophores by the poa pratensis grass to counteract Fe limitation. Phytosiderophores have a high Fe affinity [118, 119, 193] and may therefore effectively deplete chrysotile surfaces from Fe^{3+}[4] and consequently decrease the HRFP of chrysotile in soil.

Cement near fibers inhibited the effect of plants on the decrease of the HRFP of chrysotile in soils (SI-Figure 10). Furthermore, it inhibited the effect of plants on the dissolution of metals from chrysotile fiber surfaces in soils (SI-Table 10). This was likely caused by an increase of the local soil solution pH to circumneutral or mildly alkaline values, at which plant borne ligands like oxalate or citrate were demonstrated to not or only inefficiently complex and remove metals from chrysotile surfaces [146].

Environmental implications

Even though chrysotile rapidly weathered in acidic soils with a sufficiently high buffer capacity, weathering in soils with circumneutral pHs and acidic pHs with a low buffer capacity was inefficient. Hence, chrysotile fibers that pollute similar soils should be considered as weathering resistant. The

inhibition of the HRFP decrease of fibers in soils due to high soil solution Fe contents implies that HRFPs of fibers do not necessarily decrease in soils during weathering. Regarding the potent antagonizing effect of cement on fiber weathering in soils and its consequences on the fibers' HRFP, the presence of cement should always be considered in risk assessments of asbestos polluted environments as an inhibitory factor to natural attenuation processes. Plants increased metal dissolution from fibers in soils, but to a minor extent compared to the extensive dissolution of fibers in potent soils like the Schrems podzol. Furthermore, plants were demonstrated to decrease the HRFP of fibers in soils, but this decrease did not exceed 20% relative to the HRFP of fibers from unplanted soils. As a consequence of these observations, plants only have a low potential for bioremediation practices of asbestos polluted soils. Nevertheless they are highly important for avoiding aeolian soil erosion and thereby fibers from getting airborne from asbestos polluted sites [15, 111].

Summary

The most important results from this project are summarized in this section to provide a short and comprehensive overview, which may serve as a basis for future research on chrysotile asbestos:

First Chapter

In accordance with many published dissolution studies on chrysotile asbestos, fiber dissolution was indirectly related to pH, with Mg dissolution rates in the tens of pmol m^{-2} s^{-1} at low pH and at single digit pmol m^{-2} s^{-1} values at circumneutral and mildly alkaline pH. Si dissolution rates at acidic (pH 3.0) and circumneutral pH were lower than predicted by stoichiometry. The fibers dissolved in a step-wise manner, in which the Mg layers readily dissolved at a wide pH range (in acidic conditions within minutes to hours and in circumneutral conditions within hours to days), and in which the dissolution of the Si layers was rate-determining. However, Si layers hardly dissolved at circumneutral pH, explaining the slow overall dissolution rates of chrysotile fibers in this pH range. At alkaline pH (pH 11.5), which represents the pH in the vicinity of cement (e.g. in asbestos cement waste), fibers did not dissolve at all due to the very low solubility of the outermost brucite-like Mg layer. As the Fe content of the insoluble outermost Mg layer did not change its coordination environment at that pH, fibers that were incubated at pH 11.5 had the same HRFP (hydroxyl radical forming potential) as unaltered pristine fibers. However, at acidic to circumneutral pH values and in the absence of Fe-chelating ligands, octahedrally coordinated ferrous and ferric Fe (Fe^{2+}[6] and Fe^{3+}[6] respectively), that were substituted in the readily dissolving Mg layers of chrysotile, co-dissolved and/or oxidized and precipitated as secondary Fenton-inactive Fe phases on the fiber surface. The third structural Fe species in chrysotile asbestos, tetrahedrally coordinated ferric iron (Fe^{3+}[4]), turned out to be highly important in fiber dissolution, but also in fiber mediated radical generation, and was therefore thoroughly investigated throughout the whole thesis. The investigation of the pivotal role of Fe^{3+}[4] is one of the most relevant contributions of this dissertation to research on asbestos (Figure 1).

Fe^{3+}[4] only made 7% of the total bulk-Fe in Shijiazhuang chrysotile (total bulk-Fe ≈ 2 wt%), resulting in only 0.14 wt% of Fe^{3+}[4] in chrysotile. Despite its low abundancy, the ligand-promoted dissolution of Fe^{3+}[4] (and potentially Al^{3+}[4]) was identified to labilize Si layers of chrysotile by the formation of vacancies in Si layers of chrysotile, which considerably increased Si dissolution from the fibers over the respective blank treatments. This consequently also increased Mg dissolution from underlying Mg layers. Fe^{3+}[4] was most efficiently complexed by the siderophore DFOB and the synthetic metal-chelate HEDTA (which may serve as proxy for phytosiderophores) from acidic up to mildly alkaline pH values. Even at an alkaline cement pH (pH 11.5), the synthetic metal chelates HEDTA and HBED

complexed Fe^{3+}[4] and thereby initiated Si labilization. The depletion of Fe^{3+}[4] from exposed Si-layers by ligands like DFOB decreased fiber-mediated $HO^{\bullet}$ generation by Fenton reactions to almost background values. Other ligands (oxalate and citrate) did not decrease $HO^{\bullet}$ generation over blank treatments. However, compared to the respective blank treatments they increased Si- and Mg dissolution, indicating that they also influenced Si labilization, but potentially via the complexation of Al^{3+}[4] only. In the absence of Fe^{3+}[4]-chelating ligands at circumneutral pH values, Fe^{3+}[4] remained in situ in the hardly dissolving exposed Si layer of the fibers and was Fenton-active throughout the experiment (two weeks). Additionally, on an atom basis, exposed Fe^{3+}[4] was more than 10 times as Fenton-active as the exposed octahedral Fe in the first Mg layer of pristine Shijiazhuang chrysotile fibers. Apart from ligand promoted dissolution of Fe^{3+}[4], also proton promoted dissolution of Fe^{3+}[4] (and potentially Al^{3+}[4]) was hypothesized to initiate Si labilization. This was discussed to be the rationale for the observed inverse relationship between Si dissolution rates and pH in ligand free treatments. Since Al substitution into the Si layers has been detected in chrysotile [127], but not in Shijiazhuang chrysotile (so far), the contribution of the proton- or ligand-promoted dissolution of Al^{3+}[4] to Si labilization can only be postulated.

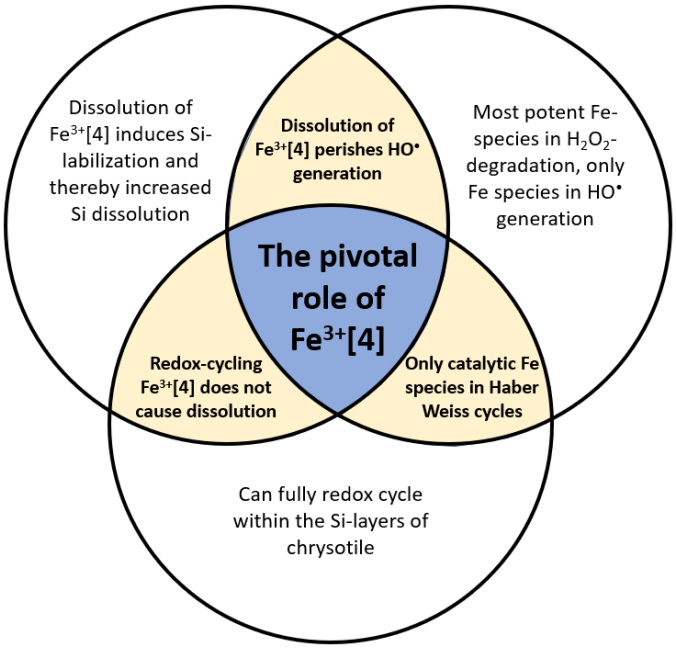

Figure 1: *The pivotal role of Fe^{3+}[4] in chrysotile. Fe^{3+}[4] is a very potent catalyst in fiber mediated Haber Weiss cycles, whereas the hydrolytic or ligand-promoted dissolution of Fe^{3+}[4] enhances overall dissolution rates of chrysotile fibers.*

Second Chapter

Based on the high weathering resistance of Fe^{3+}[4] on chrysotile surfaces and the high efficacy of Fe^{3+}[4] to generate $HO^{\bullet}$ radicals, as summarized in chapter 1, chapter 2 specifically focused on the catalytic properties of this Fe species to produce $HO^{\bullet}$ in fiber mediated Haber-Weiss cycles at circumneutral pH.

As hypothesized in chapter 1, the complexation of Fe^{3+}[4] and potentially Al^{3+}[4] by ligands (e.g. DFOB) at circumneutral pH formed vacancies in exposed Si layers of chrysotile. External ^{57}Fe that was added to fibers became reincorporated in these vacancies and thereby coordinated tetrahedrally, as verified by Mössbauer spectroscopy. This tetrahedral reincorporation of external Fe increased the $HO^{\bullet}$ generation by fibers from almost background to an equal level as generated by exposed Si layers which contained the original amount of Fe^{3+}[4] (HRFP of 50 ± 10%). The reincorporation of Fe^{3+}[4] furthermore stabilized the outermost Si layer of the fibers and thereby decreased Si and Mg dissolution by up to 50%. As this decrease was only observed up to a certain amount of added external Fe (30 $\mu mol\ g^{-1}$ fibers), the reincorporation of Fe^{3+}[4] was hypothesized to become saturated once all available Si vacancies had been filled with external Fe. All these observations demonstrated that the depletion of Fe^{3+}[4] (e.g. by ligands) is a reversible process. An important consequence of this is that fibers or particles that were depleted in, or that lack, bulk-Fe^{3+}[4] can become Fenton active upon incorporation of Fe^{3+}[4] in tetrahedral vacancies of crystalline Si lattices. This may especially be relevant for the pathogenicity of fibrous zeolites (e.g. erionite), which commonly lack total bulk-Fe, but are even more carcinogenic than asbestos [25]. Indeed, zeolites were demonstrated to bind Fenton-active Fe, which may support this hypothesis [37]. The addition of Fe to chrysotile fibers which contained the original amount of Fe^{3+}[4] in situ in exposed Si layers (with no Si vacancies present) did not significantly increase (nor decrease) $HO^{\bullet}$ generation by chrysotile fiber surface. This was even the case by precipitating more than a 100x as much Fe on the fiber surface as the expected amount of Fe^{3+}[4] in exposed Si layers. Since no vacancies were available in the exposed Si layers, the added Fe had not been tetrahedrally incorporated and thus precipitated as Fenton-inactive Fe phases on the fiber surface (as demonstrated by Mössbauer spectroscopy).

Differently from $HO^{\bullet}$ generation, Fe^{3+}[6]-containing precipitates on chrysotile fiber surfaces contributed to fiber mediated H_2O_2 degradation. Experiments in chapter 2 demonstrated that the potency of Fe^{3+}[4] to degrade H_2O_2 was at least 10 times as high as the potency of Fe^{3+}[6] in secondary Fe precipitates on dissolving chrysotile surfaces. This indicates that, on an atom basis, Fe^{3+}[4] was the dominating Fe species in H_2O_2 degradation on dissolving chrysotile fiber surfaces. At a precipitation

level of more than 100x as much Fe as the expected amount of Fe^{3+}[4] in exposed Si layers, the contribution of the Fe-precipitates on the fiber surfaces to the overall H_2O_2 degradation was only ≈ 2.5 higher than the one of the exposed Fe^{3+}[4] sites. To conclude, both the prerequisite (H_2O_2 degradation into reductants) and the last step ($HO^{\bullet}$ generation) of fiber-mediated Haber-Weiss cycles were to a high extent or exclusively dominated by the presence of Fe^{3+}[4] on the fiber surface of chrysotile. As only ferric Fe is substituted tetrahedrally in silicates, Fe^{3+}[4] was postulated in chapter 2 to be reduced to ferrous tetrahedral Fe (Fe^{2+}[4]), which thereby becomes the ultimate Fenton-active Fe species on chrysotile asbestos surfaces.

Apart from Fe-mediated H_2O_2 degradation on chrysotile surfaces, also a remanent mode of H_2O_2 degradation was discovered, which was similarly efficient in overall H_2O_2 degradation as the two Fe-related degradation modes and was discussed to potentially be caused by functional groups of exposed Si layers of chrysotile. The molecular mechanism for this mode of H_2O_2-degradation was however not identified.

Third Chapter

In chapter 3, the redox cycling of Fe^{3+}[4] in chrysotile, which was postulated in chapter 2 to be required for the observed high catalytic efficacy of Fe^{3+}[4] in fiber mediated Haber-Weiss cycles, was examined at circumneutral pH in more detail.

Fe^{3+}[4] was reduced and oxidized for up to 1.5 redox cycles by ascorbate and oxygen in a step-by-step manner. During this procedure, no Si labilization and hence increased Si and Mg dissolution from the chrysotile fibers was detected. Multiple redox cycles of tetrahedral Fe by H_2O_2 did not or only marginally induce Si labilization of the fibers' exposed Si layers. This observation and the fact that redox cycling of Fe^{3+}[4] did not change the $HO^{\bullet}$ generation by the fibers (e.g. through dissolution and subsequent precipitation of Fe^{3+}[6] in Fenton-inactive phases) led to the conclusion that redox cycling of Fe^{3+}[4] occurs inside the Si layers of chrysotile. Fe that was not incorporated in the Si layer of chrysotile redox cycled on the surface of the fibers. These redox cycles were governed by the precipitation of Fe^{3+}[6] in secondary Fe phases on the fiber surfaces under oxidative conditions, and by the adsorption of Fe^{2+} onto the fiber surface under reductive conditions.

The ligand promoted dissolution of Fe^{3+}[4] by DFOB induces Si labilization, and as a consequence increased Si and Mg dissolution rates (as described in chapter 1). In the presence of H_2O_2 and DFOB however, mobilized Si and Mg concentrations at circumneutral pH were higher than the sum of Si and

Mg concentrations that were mobilized in the separate DFOB and H_2O_2 treatments. The rationale for this synergism was hypothesized to be the local expansion of the crystalline lattice of Fe[4] tetrahedra during redox cycling by H_2O_2, as the ionic radius of Fe[4] increases after reduction to Fe^{2+}[4]. After back-oxidation to Fe^{3+}[4] (e.g. Fenton oxidation) and the respective decrease of the ionic radius, the expanded Si lattice was hypothesized to sterically enhance the complexation of Fe^{3+}[4], which consequently increased Si labilization.

The capability of tetrahedrally coordinated Fe to fully redox cycle within Si layers of chrysotile was considered a key requirement for the high catalytic efficacy of Fe^{3+}[4] in fiber mediated Haber-Weiss cycles (as described in chapter 2). Since redox cycling of exposed Fe^{3+}[4] on pristine fiber surfaces at circumneutral pH by high concentrations of H_2O_2 did not initiate Si labilization (only in the presence of Fe^{3+}[4]-chelators), and since Fe^{3+}[4] was on an atom basis the most potent metal species in H_2O_2-degradation on chrysotile surfaces (chapter 2), Fe^{3+}[4] likely redox cycled within the Si layer of chrysotile throughout the experiments and thereby constantly degraded H_2O_2 (e.g. to $HO^{\bullet}$ radicals).

Furthermore, the experiments of chapter 3 demonstrated that the depletion of Fe^{3+}[4] from exposed Si layers of chrysotile (e.g. by DFOB) and the corresponding sharp decrease of fiber-mediated $HO^{\bullet}$ generation close to background values were to a certain extend reversible: By incubating fibers with exposed Fe^{3+}[4]-depleted Si layers (e.g. by DFOB pretreatments) in a pH 3.0 solution, the HRFP of the fibers increased from 9% to 21%. Two reasons were hypothesized for this increased HRFP: After dissolving 1 g L^{-1} of these fibers for some days, Fe was again mobilized from the fiber surface by Fe[4]-complexing ligands up to a concentration of 4 µmol L^{-1} (after two weeks). This indicated that Fe from structurally deeper layers became exposed once the Fe^{3+}[4]-depleted Si layers dissolved. Hence, also Fe^{3+}[4] became exposed, which thereby increased the HRFP of the fibers. Another reason for the increased HRFP was hypothesized to result from Fe, which originated from structurally deeper dissolving Mg layers, that was incorporated in Si vacancies of Fe^{3+}[4]-depleted Si layers and thereby became Fenton active (as demonstrated in chapter 2 with external Fe on modified fiber surfaces).

Fourth Chapter

Apart from investigating the pivotal role of Fe^{3+}[4] in chrysotile dissolution and radical generation, a second key focus of the dissertation was the investigation of dissolution rates and HRFPs of chrysotile fibers in polluted soils.

In the fourth chapter, dissolution rates of chrysotile were measured in a soil-suspensions setup using four geochemically different soils: An acidic and DOC rich podzol (pH ≈ 3.0), a mildly acidic agricultural soil (pH ≈ 4.5 – 6.0) with low DOC and a low buffer capacity and two calcareous soils (pH ≈ 7.5) with a high and low DOC respectively. Mg dissolution rates of chrysotile determined in podzol soil suspensions (16.4 pmol m^2 s^{-1}) were a factor 3 lower compared to the dissolution rates determined in chapter 1 at the same pH in batch dissolution experiments with only fibers and a buffered pH. Mg dissolution rates were inversely related to pH and were in the low single digit pmol m^2 s^{-1} range in circumneutral soil suspensions (pH ≈ 7.5). Molar Mg/Si ratios of fibers incubated in the two carbonaceous soil treatments indicated that even at an incubation time of 8 weeks, only the outermost Mg layer of the fibers had dissolved. Si dissolution rates were exclusively determined in acidic soil suspensions (12.0 pmol m^2 s^{-1}), in mildly acidic and circumneutral soil suspensions they were not quantifiable because of the low dissolution kinetics of the fibers. The Si dissolution rates of fibers incubated in the podzol treatments were congruent to Mg dissolution rates, but only if the formation of siliceous amorphous material during dissolution was considered: alkaline extractions of fibers (in a 0.1 mol L^{-1} NaOH) that were sampled from all four soil suspensions and from fibers that were incubated at a pH range from 3.0 - 7.4 revealed that extractable siliceous amorphous material only formed during the dissolution of fibers at acidic pH values (pH 3.0 in batch experiments or in the podzol suspensions).

Apart from the different dissolution rates, also the fiber surface metal content, as extracted in pH 7.4 solutions in the presence of the metal chelate HEDTA, differed among fibers incubated in the four tested soil suspensions: Extracted Mg, Fe, Mn and Cr contents of fibers sampled from the acidic podzol suspensions were considerably lower compared to fibers sampled from the other three soil suspensions, which indicated a more efficient depletion from the fiber surfaces during the incubation. The addition of cement to the acidic podzol soil suspension (in a ratio 1:1) completely inhibited dissolution of chrysotile fibers and consequently increased the extraction of metals from fibers by HEDTA at pH 7.4, likely because of the sharply increased soil solution pH up to alkaline values (at which the dissolution of the first Mg layer was inhibited, chapter 1).

The HRFP of fibers sampled in mildly acidic to circumneutral soil suspensions, in which fiber dissolution was governed by the low dissolution rate of the first Si layer, decreased to a similar value (on average 25 ± 5%) after weeks of incubation. This HRFP was also measured in long term batch dissolution experiments at pH 7.4 (also chapter 4, up to 8 weeks) and in short term batch dissolution experiments at pH 3.0 (chapter 1, 2 weeks). A similar HRFP was also measured in chapter 3 upon dissolving fibers with exposed Fe^{3+}[4]-depleted Si layers (after DFOB pretreatments) in a pH 3.0 solution for 2 weeks. The conclusion of all these observations was that this HRFP (25 ± 5%) was the minimum HRFP level that may be reached during dissolution of chrysotile in the absence of (high concentrations of) Fe^{3+}[4]-

chelating ligands. The addition of cement to podzol soil suspensions decreased the HRFP of fibers to background values, which contradicted the observations of chapter 1 that HRFPs of fibers in alkaline (pH 11.5) solutions are equal to HRFPs of pristine fibers. However, bulk analyses revealed that the addition of cement to the podzol suspension caused a complete surface coating of the fibers with up to ≈2 mmol L^{-1} Al (per 2 g L^{-1} fibers), which likely inhibited radical generation by Fe^{3+}[4] on chrysotile surfaces. This coating may have been caused by the cement-induced elevation in pH, which had increased the Al concentrations in soil solution and thus may have led to the precipitation of secondary Al-bearing phases on the fiber surfaces.

Fifths Chapter

In chapter 5, dissolution rates of fibers were determined in a long-term soil microcosm experiment. Thereby, the effect of soil type, cement and plants on fiber weathering were examined (Figure 2).

Mg dissolution rates were approximately 13 times lower than rates determined in batch experiments (at the same pH) and a factor 4.5 lower than in soil suspension experiments (chapter 1 and 4 respectively). In microcosms of the same acidic podzol that was used for the soil suspension experiments in chapter 4, Mg dissolution rates were ≈3.63 pmol m^2 s^{-1}, and Si dissolution rates were 2.92 pmol m^2 s^{-1}. Si dissolution was thereby to a large extent governed by the formation of amorphous siliceous material (as described in chapter 4). Based on the low dissolution kinetics of chrysotile in mildly acidic and circumneutral soils, dissolution rates of fibers were not quantifiable in these microcosms. However, analyses of molar Mg/Si ratios of fibers sampled from these soils suggested that only the first Mg layer of chrysotile dissolved during incubation for up to 2.5 years. In batch experiments and in soil suspension experiments this was a matter of hours or weeks respectively. These results indicate that chrysotile fibers are de facto resistant towards weathering in polluted mildly acidic soils (with a low buffering capacity) to circumneutral soils. Furthermore, also the kinetics of the decrease in HRFP of fibers sampled from the soil microcosms were considerably slower than determined in batch incubation experiments and soil suspensions (chapter 1 and 4). The HRFP of fibers sampled in mildly acidic to circumneutral soils successively decreased for up to 1.75 years to a minimum HRFP of ≈25 ± 5% and then remained at that HRFP for another 0.75 years of incubation. In batch dissolution and soil suspension studies at circumneutral pH, this decrease was already measured after weeks (chapter 4). Interestingly, the HRFP of fibers that weathered in the podzol (pH 3.0) was clearly higher (≈64%) than the HRFPs of fibers sampled from mildly acidic and circumneutral soils (≈25 ± 5%), which hardly dissolved at all apart from the first Mg layer. The reason for this observation was

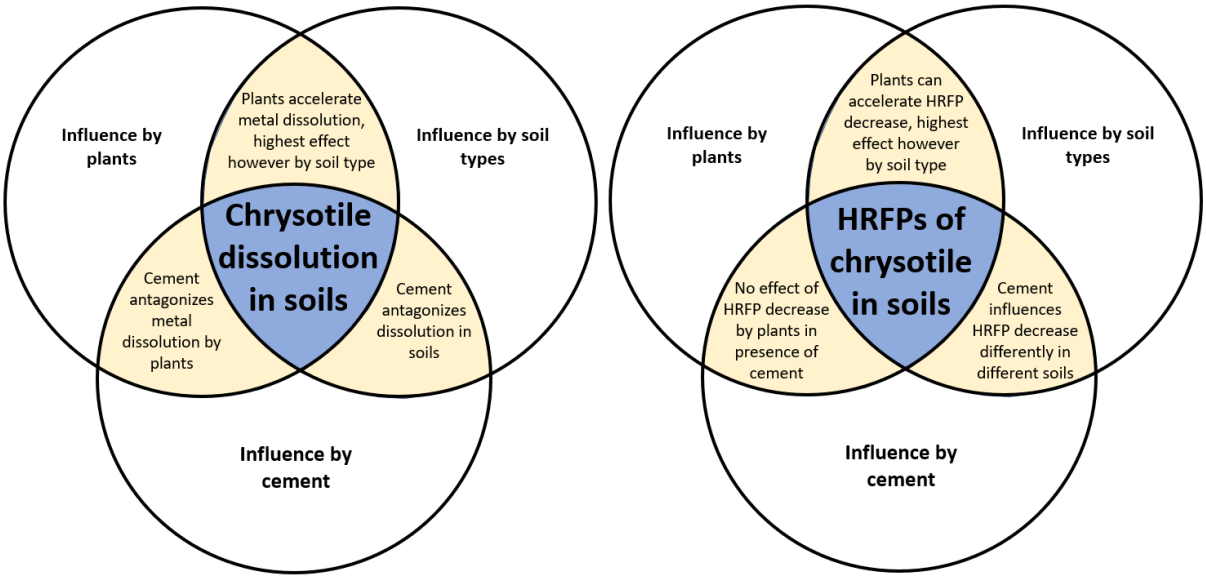

Figure 2: *Implications of the basic parameters (soil type, cement and plants) on the dissolution of chrysotile fibers in soils (left panel) and radical generation of the fibers (right panel).*

hypothesized to be the high Fe soil-solution concentrations in the podzol microcosms. As demonstrated in chapter 2, external Fe reincorporates as Fe^{3+}[4] in vacancies of exposed Si layers and becomes Fenton-active. Hence, soluble Fe in the soil-solution of podzol microcosms may have become incorporated in Si vacancies of chrysotile fibers that were incubated in soil and thereby increased the overall HRFP of the fibers.

Cement near the fibers in the soil microcosms inhibited fiber dissolution. This was best observed in podzol microcosms, in which Mg/Si-ratios indicated that only the outermost Mg layer dissolved, whereas in the absence of cement more than half of the fiber bulk dissolved after 2.5 years. In all tested soil microcosms, the presence of cement close to the fibers caused increased extractable metal contents from fibers by HEDTA in pH 7.4 solutions relative to fibers that were sampled from their no cement analogs. This was likely caused by an increased local soil solution pH in cement treatments, which inhibited the dissolution of these metals from the fibers. Cement near fibers in mildly acidic to circumneutral carbonaceous soil microcosms slowed down the HRFP decrease kinetics for up to 2.5 years. This possibly resulted from the locally increased soil solution pH in the vicinity of the fibers, which decreased the hydrolytic removal of Fe^{3+}[4] from exposed Si layers chrysotile. However, the HRFP of fibers that were incubated in podzol cement treatments were lower as the HRFP of fibers from their no cement analogs (after 1.75 and 2.5 years of incubation). This was hypothesized to be related to the increased local soil solution pH around the fibers near the cement, which dropped the local Fe-solubility in the soil solution and hence inhibited the incorporation of external Fe into vacancies of exposed Si layers, which thus caused a decreased HRFP of the fibers.

Finally, the three tested plant species did not increase the overall dissolution rates of chrysotile in soil microcosms. However, the white lupine (lupinus albus cv multitalia) was observed to effectively deplete fiber surfaces from metals (e.g. Mg, Fe, Mn and Cr) and extractable total nitrogen. Other plants (rumex acetosella sp and poa pratensis cv baron) were also effective in depleting some metals. Possibly the exudation of metal chelating agents by plants into the soil contributed to this surface depletion. This was supported by high soil solution DOC concentrations and significantly higher soil solution concentrations of metals (e.g. Fe) in planted microcosms, that were otherwise insoluble in unplanted microcosms. The interaction of plant borne DOC with chrysotile fiber surfaces was also hypothesized to have influenced the HRFP of fibers in soils. The presence of plants thereby caused a significantly lower HRFP of the fibers in mildly acidic soils by approximately 20% after one year of incubation, which was likely caused by the removal of Fe^{3+}[4] from fiber surfaces by plant borne metal chelates. At longer incubation times, this effect perished since the HRFP of fibers in planted and in non-planted microcosms decreased to a common HRFP of ≈25 ± 5% (as observed in chapter 4). However, after 2.5 years of incubation, a significantly lower HRFP (by ≈20%) than the common HRFP of ≈25 ± 5% was observed for fibers in microcosms that were planted with strategy II grasses. This decreased HRFP may have originated from the exudation of phytosiderophores by the grass, which may have depleted the fiber surfaces from Fe^{3+}[4]. The data presented in chapter 5 indicate that plant-born metal chelates can interact with fiber surfaces in polluted soils, but the extent of this was not enough to increase total dissolution rates of chrysotile in polluted soils within the precision of the analyses in chapter 5, or to strongly decrease the HRFPs of fibers in planted soils to background levels.

Concluding notes on the relevance of the research carried out in this dissertation

The research carried out in this project demonstrated that chrysotile asbestos has some special properties when compared to other minerals, which are important determinants of the hazard of the fibers.

The examined key role of Fe^{3+}[4] in both radical generation by, and dissolution of, chrysotile will likely have implications for the research among other silicates. The fact that Fe^{3+}[4] was shown to be the only relevant catalytic Fe species in chrysotile mediated Haber-Weiss cycles at the physiological lung pH and the natural soil pH-zone will be highly important for future investigations of the adverse redox properties of other pathogenic minerals. Furthermore, the demonstrated incorporation of Fe^{3+}[4] in vacancies of Si lattices may be especially relevant in the investigation of pathogenic particles which

commonly lack bulk-Fe (e.g. erionite). Fe^{3+}[4] can redox-cycle for a prolonged time inside tetrahedral Si layers of chrysotile and thereby produce high amounts of $HO^{\bullet}$ radicals by the degradation of H_2O_2. The combination of H_2O_2 in vivo as a consequence of asbestos induced chronic inflammation and surface exposed Fe^{3+}[4] in chrysotile may thereby lead to a high level of cellular oxidative stress, which may be a key contribution to the pathological mode of action of the fibers.

Apart from the investigation of the pathogenicity of asbestos, the high redox reactivity of Fe^{3+}[4] and its high degradation rates of H_2O_2 may also be relevant for technical applications and engineering. Fe^{3+}[4] may be interesting for the synthesis of highly Fenton active materials that may be used for forced oxidative degradation applications of organic contaminants (e.g. in waste water sewage treatment plants). As both redox conditions of Fe[4] (Fe^{3+}[4] and Fe^{2+}[4]) were stable in the Si layer of chrysotile fibers at circumneutral pH under anoxic conditions, a Fe[4]-doted tetrahedral Si-matrix which is able to host the two redox states of Fe[4] may furthermore be considered as a potential material for information storage (the redox state of Fe[4] would in that context be the bit).

Regarding weathering of chrysotile fibers in polluted environments, the fact that dissolution rates of fibers in soil were more than an order of magnitude lower than determined under simplified batch dissolution conditions may be highly relevant for competent authorities performing risk assessments of polluted terrestrial sites. Since the dissolution of chrysotile was only above the analytical precision in acidic podzol microcosms, dissolution in soils with a non-acidic pH may be considered negligible, even in prolonged time frames (years or even decades). Therefore, chrysotile fibers in non-acidic polluted soils should be regarded as de facto resistant towards weathering by competent authorities. Consequently, dissolution rates determined under simplified laboratory conditions should not be considered as representative values for risk assessments, strategies and decisions on asbestos polluted soils. The presence of cement near chrysotile asbestos fibers in soils even further inhibited fiber dissolution. Hence, the presence of cement in asbestos polluted sites should always be examined in the frame of risk assessments of asbestos polluted soils. Finally, plants did not markedly influence dissolution rates of chrysotile asbestos in soils, even though they decreased metal concentrations on fiber surfaces and the HRFP of fibers (transiently). However, plants that grow on asbestos polluted soils may nevertheless be highly important in risk strategies for avoiding aeolian erosion of asbestos polluted soils and thereby fibers from becoming airborne.

German summary

Chrysotil-Asbest ist ein giftiges und krebserregendes Mineral, welches im zwanzigsten Jahrhundert in hoher Quantität für industrielle und technische Anwendungen verwendet wurde. Die gesundheitlichen Folgen von Asbestexposition gehen zum Teil auf die hohe Redox-Reaktivität von strukturellem Fe in Asbest zurück: Fe^{2+} und Fe^{3+} substituieren Mg in oktaedrischen Mg-Schichten, während Fe^{3+} Si in tetraedrischen Si-Schichten substituiert (Fe[4]). Oberflächenexponiertes Fe katalysiert dabei den Zerfall von H_2O_2 zu hochreaktiven Hyroxylradikalen ($HO^{\bullet}$) in Haber-Weiss Reaktionen. Neben der überwiegenden Exposition von Asbestfasern am Arbeitsplatz gelangten auch hohe Mengen von Asbestfasern und -abfällen in die Umwelt, wo sie ein Gesundheitsrisiko für Anrainer darstellen. Einige Mechanismen bezüglich der Faserlöslichkeit und der Produktion von $HO^{\bullet}$-Radikalen sind nicht ausreichend erforscht, besonders in Betracht von Asbestkontaminationen in der Umwelt. Die vorliegende Doktorarbeit nahm sich deshalb zum Ziel, diese zwei Aspekte in größerem Detail zu studieren. Dabei wurden Experimente mit simplifizierten Versuchsaufbau sowie komplexere Bodensuspensionen- und Bodenmikrokosmos-Experimente durchgeführt. Fe[4] spielte eine außerordentliche Rolle in der Löslichkeit von Fasern und der $HO^{\bullet}$-Produktion: Die protonen- und ligandengestützte Lösung von Fe[4] initiierte eine Labilisierung der Si-Schichten der Fasern und erhöhte dabei die Löslichkeit von Si und Mg. Ferner war Fe[4] die einzige katalytisch-aktive Fe-Spezies in der Produktion von $HO^{\bullet}$-Radikalen auf der Faseroberfläche, indem es in den Si-Schichten der Fasern redoxzyklierte. Die Faserlöslichkeitsraten nahmen mit niedrigeren pH-Werten zu und waren mehr als eine Größenordnung niedriger in sauren Böden als wie in simplifizierten Löslichkeitsexperimenten. Weiters waren die Löslichkeitsraten in leicht-sauren und kalkigen Böden unter der Quantifizierungsgrenze. Zement inhibierte die Löslichkeit von Fasern in Böden, während Pflanzen durch pflanzliche Liganden die Faseroberflächen von Metallen abreicherten. Die $HO^{\bullet}$-Produktion von Fasern in Böden nahm generell um 75% ab, eine höhere Abnahme wurde jedoch generell nicht gemessen. Die Ergebnisse dieser Doktorarbeit sind von großer Bedeutung für WissenschaftlerInnen und RisikobewerterInnen, welche sich mit der Gesundheitsgefährdung von Asbestfasern und Asbestkontaminationen in der Umwelt beschäftigen.

Abbreviations

The following list contains all abbreviations that were used in the thesis in an alphabetic order. Element symbols as well as physical units and trade names were not added to this list, however, abbreviations of elements with a specific coordination and chemical formulas were added.

ADP: Adenosine diphosphate; Al^{3+}[4]: Tetrahedrally coordinated aluminum; ANOVA: Analysis of variances; a.u.: arbitrary unit; BET: Brunauer, Emmet, Teller; DFOB: desferrioxamine-B; DMPO: 5-5'-dimethyl-1-pirroline-N-oxide; DMPO-$HO^{\bullet}$: Adduct of DMPO and $HO^{\bullet}$; DNA: Deoxyribonucleic acid; EDTA ethylenediaminetetraacetic acid; EDS: Electron dispersive X-ray spectroscopy; EPR: Electron paramagnetic resonance; Fe[4]: tetrahedrally coordinated Fe; Fe^{3+}[4]: ferric tetrahedral Fe; Fe^{2+}[4]: ferrous tetrahedral Fe; Fe^{3+}[6]: ferric octahedral Fe; Fe^{2+}[6]: ferrous octahedral Fe; FeDFOB: Fe complexed by DFOB; HBED: N,N'-di(2-hydroxybenzyl)ethylenediamine-N,N'-diacetic-acid; FSR: Fiber to solution ratio; FSoR: Fiber to soil ratio; HEDTA: hydroxyethylenediaminetriacetic-acid; HEPES: 4-(2-hydroxyethyl)-1-piperazineethanesulfonic acid; HCl: Hydrochloric acid; HNO_3: Nitric acid; $HO^{\bullet}$: hydroxyl radical; H_2O_2: Hydrogen peroxide; $HO_2^{\bullet}$: Hydroperoxyl radical; HRFP: Hydroxyl radical forming potential; ICP-OES: Inductively coupled plasma optical emission spectrometry; ICP-MS: Inductively coupled plasma mass spectrometry; IGF-1: Insulin like growth factor 1; Ipp: Intensity peak-to-peak; IS: Ionic strength; KCl: Potassium chloride; $KMnO_4$: Potassium permanganate; $Li_2B_4O_7$: Di-lithium-Tetraborate; LOD: Limit of detection; LOQ: Limit of quantification; MES: 2-(*N*-morpholino)ethanesulfonic-acid; MOPS: 3-(*N*-morpholino)propanesulfonic-acid; NAA: Neutron activation analysis; NaCl: Sodium chloride; NFκB: Nuclear factor kappa-light-chain-enhancer of activated B cells; NOM: Natural organic matter; $O_2^{\bullet-}$: Superoxide anion radical; p.a.: quality: pro analysis quality of chemical reagents; PDGF: Platelet derived growth factor; PIPPS: 1,4-Piperazinedipropanesulfonic-acid; PP: Polypropylene; RPM: Rounds per minute; p53: Tumor protein 53; SD: Standard deviation; SI: Supplementary information; SOC: Soil organic carbon; SOD: Superoxide dismutase; SSR: Solid to solution ratio (in chapter 1) and soil to solution ratio (in chapter 4 and 5); TGFα and ß: Transforming growth factor α and ß; TNFα: Tumor necrosis factor α; Turkeys HSD test: Turkeys hones significant difference test; UPW: Ultrapure water; UV-VIS: Ultra violet and visible light; WC: Tungsten-carbide; WHO: World health organization; WHO-IARC: World health organization, international agency for research on cancer; WHO-IPCS: World health organization, international program on chemical safety; XRD: X-ray diffraction; 8-OHdG DNA adducts: 8-hydroxy-2'-deoxyguanosine; 95% CI: 95% confidence interval

References

1. Catherine H, Skinner W. Mineralogy of asbestos minerals. Indoor and Built Environment. 2003;12 6:385-9; doi: 10.1177/1420326x03037003.
2. WHO-IARC. Arsenic, metals, fibres and dusts. IARC monographs on the evaluation of carcinogenic risks to humans. 2012;100 C:219-94.
3. Aust AE, Cook PM, Dodson RF. Morphological and chemical mechanisms of elongated mineral particle toxicities. Journal of Toxicology and Environmental Health-Part B-Critical Reviews. 2011;14 1-4:40-75; doi: 10.1080/10937404.2011.556046.
4. Pye AM. A review of asbestos substitute materials in industrial applications. Journal of Hazardous materials. 1979;3 2:125-47; doi: 10.1016/0304-3894(79)80001-1.
5. Bowes DR, Farrow CM. Major and trace element compositions of the UICC standard asbestos samples. American Journal of Industrial Medicine. 1997;32 6:592-4; doi: 10.1002/(sici)1097-0274(199712)32:6<592::aid-ajim3>3.0.co;2-s.
6. Bales RC, Morgan JJ. Surface-charge and adsorption properties of chrysotile asbestos in natural-waters. Environmental Science & Technology. 1985;19 12:1213-9; doi: 10.1021/es00142a013.
7. Evans BW. The serpentinite multisystem revisited: Chrysotile is metastable. International Geology Review. 2004;46 6:479-506; doi: 10.2747/0020-6814.46.6.479.
8. Oury TD, Sporn TA, Roggli VL, (Editors). Pathology of asbestos associated diseases. 2014; doi: 10.1007/978-3-642-41193-9.
9. Chrysotile asbestos in serpentinite quarries: a case study in Valmalenco, Central Alps, Northern Italy. Environ Sci: Processes Impacts. 2013:15, 1341.
10. Van Gosen BS. The geology of asbestos in the United States and its practical applications. Environmental & Engineering Geoscience. 2007;13 1:55-68; doi: 10.2113/gseegeosci.13.1.55.
11. Hendrickx M. Naturally occurring asbestos in eastern Australia: a review of geological occurrence, disturbance and mesothelioma risk. Environmental Geology. 2009;57 4:909-26; doi: 10.1007/s00254-008-1370-5.
12. S Van Gosen B. The Geology of Asbestos in the United States and Its Practical Applications. Environmental & Engineering Geoscience. 2007;13:55-68; doi: 10.2113/gseegeosci.13.1.55.
13. Landrigan PJ. Asbestos - Still a carcinogen. New England Journal of Medicine. 1998;338 22:1618-9; doi: 10.1056/nejm199805283382209.
14. Frank A. The History of the Extraction and Uses of Asbestos. 2005:1-7; doi: 10.1201/9781420038149.ch1.
15. Schreier H: Asbestos in the natural environment. vol. Studies in environmental science 37. Amsterdam: Elsevier; 1989.

16. Frank AL, Joshi TK. The Global Spread of Asbestos. Annals of Global Health. 2014;80 4:257-62; doi: 10.1016/j.aogh.2014.09.016.
17. Neuberger M, Kundi M. Individual asbestos exposure: smoking and mortality--a cohort study in the asbestos cement industry. British Journal of Industrial Medicine. 1990;47 9:615-20.
18. Marsili D, Angelini A, Bruno C, Corfiati M, Marinaccio A, Silvestri S, et al. Asbestos Ban in Italy: A Major Milestone, Not the Final Cut. International Journal of Environmental Research and Public Health. 2017;14 11:1379; doi: 10.3390/ijerph14111379.
19. Albino GV. Iron-rich and aluminum-rich serpentinite and chlorite from the boundary ultramafic complex, Cape-Smith belt, New-Quebec. Canadian Mineralogist. 1995;33:559-68.
20. Nicholson WJ. The carcinogenicity of chrysotile asbestos - A review. Industrial Health. 2001;39 2:57-64; doi: 10.2486/indhealth.39.57.
21. Nishikawa K, Takahashi K, Karjalainen A, Wen CP, Furuya S, Hoshuyama T, et al. Recent Mortality from Pleural Mesothelioma, Historical Patterns of Asbestos Use, and Adoption of Bans: A Global Assessment. Environmental Health Perspectives. 2008;116 12:1675-80; doi: 10.1289/ehp.11272.
22. Commission Directive 1999/77/EC of 26 July 1999 adapting to technical progress for the sixth time Annex I to Council Directive 76/769/EEC on the approximation of the laws, regulations and administrative provisions of the Member States relating to restrictions on the marketing and use of certain dangerous substances and preparations (asbestos).
23. Le GV, Takahashi K, Park EK, Delgermaa V, Oak C, Qureshi AM, et al. Asbestos use and asbestos-related diseases in Asia: Past, present and future. Respirology. 2011;16 5:767-75; doi: 10.1111/j.1440-1843.2011.01975.x.
24. Virta RL. Worldwide asbestos supply and consumption trends from1900 through 2003. USGS Circular 1298; 2006.
25. Hardy JA, Aust AE. Iron in asbestos chemistry and carcinogenicity. Chemical Reviews. 1995;95 1:97-118; doi: 10.1021/cr00033a005.
26. Currie GP, Watt SJ, Maskell NA. An overview of how asbestos exposure affects the lung. The BMJ. 2009;339; doi: 10.1136/bmj.b3209.
27. WHO, International programme on chemical safety: Chrysotile asbestos, ISBN: 978 92 4 156481 6. 2014.
28. DGUV-Statistiken für die Praxis 2012, Paderborn: Deutsche Gesetzliche Unfallversicherung. 2013.
29. Baur X. Asbestos: Socio-legal and Scientific Controversies and Unsound Science in the Context of the Worldwide Asbestos Tragedy - Lessons to be Learned. Pneumologie. 2016;70 6:405-12; doi: 10.1055/s-0042-103580.

30. Cullen MR. The amphibole hypothesis of asbestos-related cancer--gone but not forgotten. American Journal of Public Health. 1996;86 2:158-9.
31. Stayner LT, Dankovic DA, Lemen RA. Occupational exposure to chrysotile asbestos and cancer risk: a review of the amphibole hypothesis. American Journal of Public Health. 1996;86 2:179-86; doi: 10.2105/AJPH.86.2.179.
32. Kamp DW, Graceffa P, Pryor WA, Weitzman SA. The role of free-radicals in asbestos-induced diseases. Free Radical Biology and Medicine. 1992;12 4:293-315; doi: 10.1016/0891-5849(92)90117-y.
33. Kamp DW, Weitzman SA. The molecular basis of asbestos induced lung injury. Thorax. 1999;54 7:638-52; doi: 10.1136/thx.54.7.638.
34. Stanton MF, Layard M, Tegeris A, Miller E, May M, Morgan E, et al. Relation of particle dimension to carcinogenicity in amphibole asbestoses and other fibrous minerals. J Natl Cancer Inst. 1981;67 5:965-75.
35. Fubini B, Mollo L. Role of iron in the reactivity of mineral fibers. Toxicology Letters. 1995;82-3:951-60; doi: 10.1016/0378-4274(95)03531-1.
36. Mossman BT, Churg A. Mechanisms in the pathogenesis of asbestosis and silicosis. American Journal of Respiratory and Critical Care Medicine. 1998;157 5:1666-80.
37. Fubini B, Mollo L, Giamello E. Free-radical generation at the solid/liquid interface in iron-containing minerals. Free Radical Research. 1995;23 6:593-614; doi: 10.3109/10715769509065280.
38. Ristic M, Czako-Nagy I, Music S, Vertes A. Spectroscopic characterization of chrysotile asbestos from different regions. Journal of Molecular Structure. 2011;993 1-3:120-6; doi: 10.1016/j.molstruc.2010.10.005.
39. Stroink G, Blaauw C, White CG, Leiper W. Mössbauer characteristics of UICC* standard reference asbestos samples. Canadian Mineralogist. 1980;18:285-90. <Go to ISI>://WOS:000208518700004.
40. Shannon RD. Revised effective ionic-radii and systematic studies of interatomic distances in halides and chalcogenides. Acta Crystallographica Section A. 1976;32 SEP1:751-67; doi: 10.1107/s0567739476001551.
41. Luys M-J, De Roy GL, Adams F, Vansant EF. Cation site population in amphibole asbestos. A Mossbauer study. Journal of the Chemical Society, Faraday Transactions 1: Physical Chemistry in Condensed Phases. 1983;79 6:1451-9; doi: 10.1039/F19837901451.
42. Winterbourn CC. Toxicity of iron and hydrogen peroxide: The Fenton reaction. Toxicology Letters. 1995;82-3:969-74; doi: 10.1016/0378-4274(95)03532-x.

43. Gazzano E, Turci F, Foresti E, Putzu MG, Aldieri E, Silvagno F, et al. Iron-loaded synthetic chrysotile: A new model solid for studying the role of iron in asbestos toxicity. Chemical Research in Toxicology. 2007;20 3:380-7; doi: 10.1021/tx600354f.
44. Iguchi H, Kojo S, Ikeda M. Nitric oxide (NO) synthase activity in the lung and NO synthesis in alveolar macrophages of rats increased on exposure to asbestos. Journal of Applied Toxicology. 1996;16 4:309-15; doi: 10.1002/(sici)1099-1263(199607)16:4<309::aid-jat345>3.0.co;2-z.
45. Fenoglio I, Prandi L, Tomatis M, Fubini B. Free radical generation in the toxicity of inhaled mineral particles: the role of iron speciation at the surface of asbestos and silica. Redox Report. 2001;6 4:235-41; doi: 10.1179/135100001101536382.
46. Haber F, Weiss J. Über die Katalyse des Hydroperoxydes. Naturwissenschaften, 1932, Vol20(51), pp948-950.948.
47. Shen ZH, Parker VD, Aust AE. Mediated, thin-layer cell, coulometric determination of redox-active iron on the surface of asbestos fibers. Analytical Chemistry. 1995;67 2:307-11; doi: 10.1021/ac00098a013.
48. Lund LG, Aust AE. Iron mobilization from asbestos by chelators and ascorbic-acid. Archives of Biochemistry and Biophysics. 1990;278 1:60-4; doi: 10.1016/0003-9861(90)90231-m.
49. De Laat J, Gallard H. Catalytic decomposition of hydrogen peroxide by Fe(III) in homogeneous aqueous solution: Mechanism and kinetic modeling. Environmental Science & Technology. 1999;33 16:2726-32; doi: 10.1021/es981171v.
50. Turci F, Favero-Longo SE, Tomatis M, Martra G, Castelli D, Piervittori R, et al. A biomimetic approach to the chemical inactivation of chrysotile fibres by lichen metabolites. Chemistry-a European Journal. 2007;13 14:4081-93; doi: 10.1002/chem.200600991.
51. Mohanty SK, Gonneau C, Salamatipour A, Pietrofesa RA, Casper B, Christofidou-Solomidou M, et al. Siderophore-mediated iron removal from chrysotile: Implications for asbestos toxicity reduction and bioremediation. Journal of Hazardous materials. 2018;341:290-6; doi: 10.1016/j.jhazmat.2017.07.033.
52. Weitzman SA, Graceffa P. Asbestos catalyzes hydroxyl and superoxide radical generation from hydrogen-peroxide. Archives of Biochemistry and Biophysics. 1984;228 1:373-6; doi: 10.1016/0003-9861(84)90078-x.
53. Morgan A, Gold C, Holmes A. Studies of solubility of constituents of chrysotile asbestos in-vivo using radioactive tracer techniques. Environmental Research. 1971;4 6:558-&; doi: 10.1016/0013-9351(71)90016-8.

54. Szabó C, Ischiropoulos H, Radi R. Peroxynitrite: biochemistry, pathophysiology and development of therapeutics. Nature Reviews Drug Discovery. 2007;6:662; doi: 10.1038/nrd2222.
55. Barlow CA, Lievense L, Gross S, Ronk CJ, Paustenbach DJ. The role of genotoxicity in asbestos-induced mesothelioma: an explanation for the differences in carcinogenic potential among fiber types. Inhalation Toxicology. 2013;25 9:553-67; doi: 10.3109/08958378.2013.807321.
56. Camargo MC, Stayner LT, Straif K, Reina M, Al-Alem U, Demers PA, et al. Occupational Exposure to Asbestos and Ovarian Cancer: A Meta-analysis. Environmental Health Perspectives. 2011;119 9:1211-7; doi: 10.1289/ehp.1003283.
57. Marsh GM. Critical review of epidemiologic studies related to ingested asbestos. Environmental Health Perspectives. 1983;53:49-56.
58. Cantor KP. Drinking Water and Cancer. Cancer Causes & Control. 1997;8 3:292-308.
59. Liu B, van Gerwen M, Bonassi S, Taioli E. Epidemiology of Environmental Exposure and Malignant Mesothelioma. Journal of Thoracic Oncology. 2017;12 7:1031-45; doi: 10.1016/j.jtho.2017.04.002.
60. Daghino S, Turci F, Tomatis M, Girlanda M, Fubini B, Perotto S. Weathering of chrysotile asbestos by the serpentine rock-inhabiting fungus Verticillium leptobactrum. FEMS Microbiology Ecology. 2009;69 1:132-41; doi: 10.1111/j.1574-6941.2009.00695.x.
61. Ferrante D, Bertolotti M, Todesco A, Mirabelli D, Terracini B, Magnani C. Cancer Mortality and Incidence of Mesothelioma in a Cohort of Wives of Asbestos Workers in Casale Monferrato, Italy. Occupational and environmental medicine. 2007;115:1401-5; doi: 10.1289/ehp.10195.
62. Goswami E, Craven V, Dahlstrom DL, Alexander D, Mowat F. Domestic Asbestos Exposure: A Review of Epidemiologic and Exposure Data. International Journal of Environmental Research and Public Health. 2013;10 11:5629-70; doi: 10.3390/ijerph10115629.
63. Magnani C, Agudo A, González CA, Andrion A, Calleja A, Chellini E, et al. Multicentric study on malignant pleural mesothelioma and non-occupational exposure to asbestos. British Journal Of Cancer. 2000;83:104; doi: 10.1054/bjoc.2000.1161.
64. Bourdès V, Boffetta P, Pisani P. Environmental exposure to asbestos and risk of pleural mesothelioma: review and meta-analysis. European Journal of Epidemiology. 2000;16 5:411-7; doi: 10.1023/A:1007691003600.
65. ATSDR Toxicological Profile for Asbestos, US Deptartment of Health & Human Services. vol. TP-61; 2001.

66. Anastasiadou K, Gidarakos E. Toxicity evaluation for the broad area of the asbestos mine of northern Greece. Journal of Hazardous materials. 2007;139 1:9-18; doi: 10.1016/j.jhazmat.2006.06.031.
67. Mensi C, Riboldi L, De Matteis S, Bertazzi PA, Consonni D. Impact of an asbestos cement factory on mesothelioma incidence: Global assessment of effects of occupational, familial, and environmental exposure. Environment International. 2015;74:191-9; doi: 10.1016/j.envint.2014.10.016.
68. Musti M, Pollice A, Cavone D, Dragonieri S, Bilancia M. The relationship between malignant mesothelioma and an asbestos cement plant environmental risk: a spatial case–control study in the city of Bari (Italy). International Archives of Occupational and Environmental Health. 2009;82 4:489-97; doi: 10.1007/s00420-008-0358-5.
69. Kurumatani N, Kumagai S. Mapping the Risk of Mesothelioma Due to Neighborhood Asbestos Exposure. American Journal of Respiratory and Critical Care Medicine. 2008;178:624-9; doi: 10.1164/rccm.200801-063OC.
70. Driece HAL, Siesling S, Swuste PHJJ, Burdorf A. Assessment of cancer risks due to environmental exposure to asbestos. Journal Of Exposure Science And Environmental Epidemiology. 2009;20:478; doi: 10.1038/jes.2009.56.
71. Szeszenia-Dabrowska N, Wilczyńska U, Szymczak W, Laskowicz K. Environmental exposure to asbestos in asbestos cement workers: a case of additional exposure from indiscriminate use of industrial wastes. International journal of occupational medicine and environmental health. 1998;11 2:171-7.
72. Szeszenia-Dąbrowska N, Sobala W, Świątkowska B, Stroszejn-Mrowca G, Wilczyńska U. Environmental asbestos pollution — Situation in Poland. International journal of occupational medicine and environmental health. 2012;25 1:3-13; doi: 10.2478/s13382-012-0003-0.
73. Ferrante D, Mirabelli D, Tunesi S, Terracini B, Magnani C. Pleural mesothelioma and occupational and non-occupational asbestos exposure: a case-control study with quantitative risk assessment. Occupational and environmental medicine. 2016;73 3:147-53; doi: 10.1136/oemed-2015-102803.
74. Israel Environment Bulletin vol. 37: Israel Ministry of Environmental Protection; September 2011.
75. Baumann F, Buck BJ, Metcalf RV, McLaurin BT, Merkler DJ, Carbone M. The Presence of Asbestos in the Natural Environment is Likely Related to Mesothelioma in Young Individuals and Women from Southern Nevada. Journal of Thoracic Oncology. 2015;10 5:731-7; doi: 10.1097/jto.0000000000000506.

76. Buck BJ, Goossens D, Metcalf RV, McLaurin B, Ren M, Freudenberger F. Naturally Occurring Asbestos: Potential for Human Exposure, Southern Nevada, USA. Soil Science Society of America Journal. 2013;77:2192-204; doi: 10.2136/sssaj2013.05.0183.
77. Pan XL, Day HW, Wang W, Beckett LA, Schenker MB. Residential proximity to naturally occurring asbestos and mesothelioma risk in California. American Journal of Respiratory and Critical Care Medicine. 2005;172 8:1019-25; doi: 10.1164/rccm.200412-1731OC.
78. Luce D, Brochard P, Quenel P, Salomon-Nekiriai C, Goldberg P, Billon-Galland MA, et al. Malignant pleural mesothelioma associated with exposure to tremolite. Lancet. 1994;344 8939-8940:1777; doi: 10.1016/S0140-6736(94)92919-X.
79. Emri S, Demir A, Dogan M, Akay H, Bozkurt B, Carbone M, et al. Lung diseases due to environmental exposures to erionite and asbestos in Turkey. Toxicology Letters. 2002;127 1:251-7; doi: 10.1016/S0378-4274(01)00507-0.
80. Metintas M, Özdemir N, Hillerdal G, Uçgun I, Metintas S, Baykul C, et al. Environmental asbestos exposure and malignant pleural mesothelioma. Respiratory Medicine. 1999;93 5:349-55; doi: 10.1016/S0954-6111(99)90318-9.
81. Carbone M, Baris YI, Bertino P, Brass B, Comertpay S, Dogan AU, et al. Erionite exposure in North Dakota and Turkish villages with mesothelioma. Proceedings of the National Academy of Sciences. 2011;108 33:13618-23; doi: 10.1073/pnas.1105887108.
82. Schreier H, Timmenga HJ. Earthworm response to asbestos-rich serpentinitic sediments. Soil Biology and Biochemistry. 1986;18 1:85-9; doi: 10.1016/0038-0717(86)90107-0.
83. Bordeleau LM, Lalande R, De Kimpe CR, Zizka J, Tabi M. Effects des poussieres d'amiante sur la microflore tellurique. Plant and Soil. 1977;46 3:619-27; doi: 10.1007/BF00015920.
84. DeKimpe C, Tabi M, Zizka J. Influence of basic material on soil genesis in the Thetford-Black Lake area, Province of Quebec Canadian Journal of Soil Science. 1973;53:27-35.
85. Schreier H. Asbestos fibres introduce trace metals into streamwater and sediments. Environmental Pollution. 1987;43 3:229-42; doi: 10.1016/0269-7491(87)90159-X.
86. Schreier H, Shelford JA, Nguyen TD. Asbestos fibers and trace metals in the blood of cattle grazing in fields inundated by asbestos-rich sediments. Environmental Research. 1986;41 1:99-109; doi: 10.1016/S0013-9351(86)80172-4.
87. Paglietti F, Malinconico S, della Staffa BC, Bellagamba S, De Simone P. Classification and management of asbestos-containing waste: European legislation and the Italian experience. Waste Manag. 2016;50:130-50; doi: 10.1016/j.wasman.2016.02.014.
88. Commission Regulation No 1357/2014 of 18 December 2014 replacing Annex III to Directive 2008/98/EC of the European Parliament and of the Council on waste repealing certain

Directives. https://eur-lex.europa.eu/legal-content/EN/TXT/HTML/?uri=CELEX:32014D0955&from=EN.

89. Commision Decision of 18 December 2014 amending Decision 2000/532/EC on the list of waste pursuant to Directive 2008/98/EC of the European Parliament and of the Council.
90. Council Directive 1999/31/EC of 26 April 1999 on the landfill of waste.
91. Swartjes FA, Tromp PC. A Tiered Approach for the Assessment of the Human Health Risks of Asbestos in Soils. Soil and Sediment Contamination: An International Journal. 2008;17 2:137-49; doi: 10.1080/15320380701870484. 10.1080/15320380701870484.
92. Dutch soil remediation circular, Rijkswaterstaat, Ministry of Infrastructure and Water Management. 2009. http://esdat.net/Environmental%20Standards/Dutch/ENGELSE%20versie%20circulaire%20Bodemsanering%202009.pdf.
93. European Environment Agency, Progress in management of contaminated sites. 2014. http://www.eea.europa.eu/data-and-maps/indicators/progress-inmanagement-of-contaminated-sites-3/assessment
94. Gronow JR. The dissolution of asbestos fibers in water. Clay Minerals. 1987;22 1:21-35; doi: 10.1180/claymin.1987.022.1.03.
95. Morgan A. Acid leaching studies of chrysotile asbestos from mines in the Coalinga region of California and from Quebec and British Columbia. Annals of Occupational Hygiene. 1997;41 3:249-68; doi: 10.1016/S0003-4878(97)00001-X.
96. Thom JGM, Dipple GM, Power IM, Harrison AL. Chrysotile dissolution rates: Implications for carbon sequestration. Applied Geochemistry. 2013;35:244-54; doi: 10.1016/j.apgeochem.2013.04.016.
97. Bales RC, Morgan JJ. Dissolution kinetics of chrysotile at pH=7 to 10. Geochimica et Cosmochimica Acta. 1985;49 11:2281-8; doi: 10.1016/0016-7037(85)90228-5.
98. Choi I, Smith RW. Kinetic study of dissolution of asbestos fibers in water. Journal of Colloid and Interface Science. 1972;40 2:253-&; doi: 10.1016/0021-9797(72)90014-8.
99. Rozalen M, Ramos ME, Fiore S, Gervilla F, Huertas FJ. Effect of oxalate and pH on chrysotile dissolution at 25 degrees C: An experimental study. American Mineralogist. 2014;99 4:589-600; doi: 10.2138/am.2014.4636.
100. Rozalen M, Huertas FJ. Comparative effect of chrysotile leaching in nitric, sulfuric and oxalic acids at room temperature. Chemical Geology. 2013;352:134-42; doi: 10.1016/j.chemgeo.2013.06.004.
101. Clark SG, Holt PF. Dissolution of chrysotile asbestos in water, acid and alkali. Nature. 1960;185 4708:237-; doi: 10.1038/185237a0.

102. Teir S, Revitzer H, Eloneva S, Fogelholm C-J, Zevenhoven R. Dissolution of natural serpentinite in mineral and organic acids. International Journal of Mineral Processing. 2007;83 1:36-46; doi: 10.1016/j.minpro.2007.04.001.
103. McPolin DO, Basheer PAM, Long AE, Grattan KTV, Sun T. New test method to obtain pH profiles due to carbonation of concretes containing supplementary cementitious materials. Journal of Materials in Civil Engineering. 2007;19 11:936-46; doi: 10.1061/(asce)0899-1561(2007)19:11(936).
104. Favero-Longo SE, Girlanda M, Honegger R, Fubini B, Piervittori R. Interactions of sterile-cultured lichen-forming ascomycetes with asbestos fibres. Mycological Research. 2007;111 4:473-81; doi: 10.1016/j.mycres.2007.01.013.
105. Favero-Longo SE, Turci F, Fubini B, Castelli D, Piervittori R. Lichen deterioration of asbestos and asbestiform minerals of serpentinite rocks in Western Alps. International Biodeterioration & Biodegradation. 2013;84:342-50; doi: 10.1016/j.ibiod.2012.07.018.
106. Bhattacharya S, John PJ, Ledwani L. Bacterial Weathering of Asbestos. Silicon. 2015;7 4:419-31; doi: 10.1007/s12633-014-9260-9.
107. Daghino S, Martino E, Fenoglio I, Tomatis M, Perotto S, Fubini B. Inorganic materials and living organisms: Surface modifications and fungal responses to various asbestos forms. Chemistry-a European Journal. 2005;11 19:5611-8; doi: 10.1002/chem.200500046.
108. Favero-Longo SE, Turci F, Tomatis M, Castelli D, Bonfante P, Hochella MF, et al. Chrysotile asbestos is progressively converted into a non-fibrous amorphous material by the chelating action of lichen metabolites. Journal of Environmental Monitoring. 2005;7 8:764-6; doi: 10.1039/b507569f.
109. Christensen S. Epilithic lichen vegetation of corrugated asbestos-cement roof tiles in the Copenhagen area. 2004.
110. Favero-Longo SE, Castelli D, Salvadori O, Belluso E, Piervittori R. Pedogenetic action of the lichens Lecidea atrobrunnea, Rhizocarpon geographicum gr. and Sporastatia testudinea on serpentinized ultramafic rocks in an alpine environment. International Biodeterioration & Biodegradation. 2005;56 1:17-27; doi: 10.1016/j.ibiod.2004.11.006.
111. Favero-Longo SE, Siniscalco C, Piervittori R. Plant and lichen colonization in an asbestos mine: Spontaneous bioattenuation limits air dispersion of fibres. Plant Biosystems - An International Journal Dealing with all Aspects of Plant Biology. 2006;140 2:190-205; doi: 10.1080/11263500600756546.
112. Favero-Longo SE, Castelli D, Fubini B, Piervittori R. Lichens on asbestos–cement roofs: Bioweathering and biocovering effects. Journal of Hazardous materials. 2009;162 2:1300-8; doi: 10.1016/j.jhazmat.2008.06.060.

113. Favero-Longo SE, Piervittori R. Cultivation of isidia and transplantation of adult thalli of Xanthoparmelia tinctina in an abandoned asbestos mine. The Lichenologist. 2012;44 6:840-4; doi: 10.1017/S0024282912000485.
114. Elena M, Laura P, Ivana F, Paola B, Silvia P, Bice F. Soil Fungal Hyphae Bind and Attack Asbestos Fibers. Angewandte Chemie International Edition. 2003;42 2:219-22; doi: doi:10.1002/anie.200390083.
115. Martino E, Cerminara S, Prandi L, Fubini B, Perotto S. Physical and biochemical interactions of soil fungi with asbestos fibers. Environmental Toxicology and Chemistry. 2004;23 4:938-44; doi: 10.1897/03-266.
116. Daghino S, Turci F, Tomatis M, Favier A, Perotto S, Douki T, et al. Soil Fungi Reduce the Iron Content and the DNA Damaging Effects of Asbestos Fibers. Environmental Science & Technology. 2006;40 18:5793-8; doi: 10.1021/es060881v.
117. Daghino S, Martino E, Perotto S. Fungal weathering and implications in the solubilization of metals from soil and from asbestos fibres. Current Research, Technology and Education Topics in Applied Microbiology and Microbial Biotechnology. 2010:329-38.
118. Schenkeveld WDC, Schindlegger Y, Oburger E, Puschenreiter M, Hann S, Kraemer SM. Geochemical Processes Constraining Iron Uptake in Strategy II Fe Acquisition. Environmental Science and Technology. 2014;48 21:12662-70; doi: 10.1021/es5031728.
119. Walter M, Kraemer SM, Schenkeveld WDC. The effect of pH, electrolytes and temperature on the rhizosphere geochemistry of phytosiderophores. Plant Soil. 2017:1-19; doi: 10.1007/s11104-017-3226-9.
120. Chardot-Jacques V, Calvaruso C, Simon B, Turpault MP, Echevarria G, Morel JL. Chrysotile Dissolution in the Rhizosphere of the Nickel Hyperaccumulator Leptoplax emarginata. Environmental Science & Technology. 2013;47 6:2612-20; doi: 10.1021/es301229m.
121. Favero-Longo S, Turci F, Tomatis M, Compagnoni R, Piervittori R, Fubini B. The Effect of Weathering on Ecopersistence, Reactivity, and Potential Toxicity of Naturally Occurring Asbestos and Asbestiform Minerals. Journal of Toxicology and Environmental Health-Part a-Current Issues. 2009;72 5:305-14; doi: 10.1080/15287390802529864.
122. Schwertmann U, Cornell RM. Iron oxides in the laboratory. 2., completely rev. and extended ed. edn. Weinheim [u.a.]: Wiley-VCH; 2000.
123. Churg A. Deposition and clearance of chrysotile asbestos. Annals of Occupational Hygiene. 1994;38 4:625-33; doi: 10.1093/annhyg/38.4.625.
124. Kidd DR, Ryan MH, Haling RE, Lambers H, Sandral GA, Yang ZJ, et al. Rhizosphere carboxylates and morphological root traits in pasture legumes and grasses. Plant Soil. 2016;402 1-2:77-89; doi: 10.1007/s11104-015-2770-4.

125. Stroink G, Blaauw C, White CG, Leiper W. Mössbauer characteristics of UICC standard reference asbestos samples. Canadian Mineralogist. 1980;18:285-90.
126. Morgan A, Holmes A, Gold C. Studies of the solubility of constituents of chrysotile asbestos in vivo using radioactive tracer techniques. Environmental Research. 1971;4 6:558-70; doi: 10.1016/0013-9351(71)90016-8.
127. Viti C, Mellini M. Contrasting chemical compositions in associated lizardite and chrysotile in veins from Elba, Italy. European Journal of Mineralogy. 1997;9:585-96.
128. Cervini-Silva J, Sposito G. Steady-state dissolution kinetics of aluminum-goethite in the presence of desferrioxamine-B and oxalate ligands. Environmental Science and Technology. 2002;36 3:337-42; doi: 10.1021/es010901n.
129. Welch SA, Ullman WJ. Feldspar dissolution in acidic and organic solutions: Compositional and pH dependence of dissolution rate. Geochimica et Cosmochimica Acta. 1996;60 16:2939-48; doi: 10.1016/0016-7037(96)00134-2.
130. Wypych F, Adad LB, Mattoso N, Marangon AAS, Schreiner WH. Synthesis and characterization of disordered layered silica obtained by selective leaching of octahedral sheets from chrysotile and phlogopite structures. Journal of Colloid and Interface Science. 2005;283 1:107-12; doi: 10.1016/j.jcis.2004.08.139.
131. Fischer BE, Haring UK, Tribolet R, Sigel H. Metal ion-buffer interactions - Stability of binary and ternary complexes containing 2-amino-2(hydroxymethyl)1-3-Propanediol (Tris) and adenosine 5'-triphosphate (ATP). European Journal of Biochemistry. 1979;94 2:523-30; doi: 10.1111/j.1432-1033.1979.tb12921.x.
132. Kraemer SM. Iron oxide dissolution and solubility in the presence of siderophores. Aquatic Sciences. 2004;66 1:3-18; doi: 10.1007/s00027-003-0690-5.
133. Pokrovski GS, Schott J. Experimental study of the complexation of silicon and germanium with aqueous organic species: implications for germanium and silicon transport and Ge/Si ratio in natural waters. Geochimica et Cosmochimica Acta. 1998;62 21:3413-28; doi: 10.1016/S0016-7037(98)00249-X.
134. Baronnet A. Equilibrium and kinetic processes for polytype and polysome generation. vol. 1. Budapest: EMU Notes in Mineralogy; 1997.
135. Lindsay WL. Chemical equilibria in soils. N.Y.: John Wiley and Sons; 1979.
136. Saldi GD, Kohler SJ, Marty N, Oelkers EH. Dissolution rates of talc as a function of solution composition, pH and temperature. Geochimica et Cosmochimica Acta. 2007;71 14:3446-57; doi: 10.1016/j.gca.2007.04.015.

137. Falini G, Foresti E, Gazzano M, Gualtieri AE, Leoni M, Lesci IG, et al. Tubular-shaped stoichiometric Chrysotile nanocrystals. Chemistry-a European Journal. 2004;10 12:3043-9; doi: 10.1002/chem.200305682.
138. Turci F, Tomatis M, Lesci IG, Roveri N, Fubini B. The Iron-Related Molecular Toxicity Mechanism of Synthetic Asbestos Nanofibres: A Model Study for High-Aspect-Ratio Nanoparticles. Chemistry-a European Journal. 2011;17 1:350-8; doi: 10.1002/chem.201001893.
139. Kandegedara A, Rorabacher DB. Noncomplexing tertiary amines as "better" buffers covering the range of pH 3-11. Temperature dependence of their acid dissociation constants. Analytical Chemistry. 1999;71 15:3140-4; doi: 10.1021/ac9902594.
140. Lopez-Rayo S, Hernandez D, Lucena JJ. Chemical Evaluation of HBED/Fe3+ and the Novel HJB/Fe3+ Chelates as Fertilizers to Alleviate Iron Chlorosis. Journal of Agricultural and Food Chemistry. 2009;57 18:8504-13; doi: 10.1021/jf9019147.
141. Parkhurst DL, Appelo CAJ. User's Guide to PHREEQC (version 2). A Computer Program for Speciation, Batch Reaction, One-Dimensional Transport, and Inverse Geochemical Calculations. U.S. Geological Survey Water-Resources Investigations Report. 1999.
142. Reay A. The effect of disk mill grinding on some rock-forming minerals. Mineralogical Magazine. 1981;44 334:179-82; doi: 10.1180/minmag.1981.044.334.10.
143. Mørup S, Both E. Interpretation of Mossbauer-spectra with broadened lines. Nuclear Instruments and Methods. 1975;124 2:445-8; doi: 10.1016/0029-554x(75)90595-9.
144. Asbestos (chrysotile, amosite, crocidolite, tremolite, actinolite, and anthophyllite), IARC Monographs on the Evaluation of Carcinogenic Risks to Humans 100C, International Agency for Research on Cancer. 2012.
145. J Olsen N, Franklin P, Reid A, Klerk N, J Threlfall T, Shilkin K, et al. Increasing incidence of malignant mesothelioma after exposure to asbestos during home maintenance and renovation. Medical Journal of Australia. 2011;195:271-4; doi: 10.5694/mja11.10125.
146. Walter M, Schenkeveld WDC, Reissner M, Gille L, Kraemer SM. The effect of pH and biogenic ligands on the weathering of chrysotile asbestos; the pivotal role of tetrahedral Fe in dissolution kinetics and radical formation. This dissertation. 2018a:29 - 53.
147. Eberhardt MK, Román-Franco AA, Quiles MR. Asbestos-induced decomposition of hydrogen peroxide. Environmental Research. 1985;37 2:287-92; doi: 10.1016/0013-9351(85)90108-2
148. Ghio A, E. Taylor D, G. Stonehuerner J, Piantadosi C, L. Crumbliss A. The release of iron from different asbestos structures by hydrogen peroxide with concomitant O2 generation. Biometals. 1998;11/1:41-7; doi: 10.1023/A:1009257323963.

149. Ghio AJ, Kennedy TP, Stonehuerner JG, Crumbliss AL, Hoidal JR. DNA strand breaks following in-vitro exposure to asbestos increase with surface complexed Fe3+. Archives of Biochemistry and Biophysics. 1994;311 1:13-8; doi: 10.1006/abbi.1994.1202.
150. Ghio AJ, Kennedy TP, Whorton AR, Crumbliss AL, Hatch GE, Hoidal JR. Role of surface complexed iron in oxidant generation and lung inflammation induced by silicates. American Journal of Physiology. 1992;263 5:L511-L8.
151. Ghio AJ, LeFurgey A, Roggli VL. In vivo accumulation of iron on crocidolite is associated with decrements in oxidant generation by the fiber. Journal of Toxicology and Environmental Health. 1997;50 2:125-42.
152. Doulias PT, Christoforidis S, Brunk UT, Galaris D. Endosomal and lysosomal effects of desferrioxamine: Protection of HeLa cells from hydrogen peroxide-induced DNA damage and induction of cell-cycle arrest. Free Radical Biology and Medicine. 2003;35 7:719-28; doi: 10.1016/s0891-5849(03)00396-4.
153. Geroldinger G, Tonner M, Hettegger H, Bacher M, Monzote L, Walter M, et al. Mechanism of ascaridole activation in Leishmania. Biochemical Pharmacology. 2017;132:48-62; doi: 10.1016/j.bcp.2017.02.023.
154. ThomasArrigo LK, Mikutta C, Byrne J, Kappler A, Kretzschmar R. Iron(II)-Catalyzed Iron Atom Exchange and Mineralogical Changes in Iron-rich Organic Freshwater Flocs: An Iron Isotope Tracer Study. Environmental Science & Technology. 2017;51 12:6897-907; doi: 10.1021/acs.est.7b01495.
155. Stookey LL. Ferrozine---a new spectrophotometric reagent for iron. Analytical Chemistry. 1970;42 7:779-81; doi: 10.1021/ac60289a016.
156. Murad E, Schwertmann U. The Mössbauer spectrum of ferrihydrite and its relations to those of other iron-oxides. American Mineralogist. 1980;65 9-10:1044-9.
157. Eisenberg GM. Colorimetric determination of hydrogen peroxide. Industrial and Engineering Chemistry-Analytical Edition. 1943;15:327-8; doi: 10.1021/i560117a011.
158. Zhao GH, Chasteen ND. Oxidation of Good's buffers by hydrogen peroxide. Analytical Biochemistry. 2006;349 2:262-7; doi: 10.1016/j.ab.2005.10.005.
159. Dominguez-Vera JM. Iron(III) complexation of Desferrioxamine B encapsulated in apoferritin. Journal of Inorganic Biochemistry. 2004;98 3:469-72; doi: 10.1016/j.jinorgbio.2003.12.015.
160. Machala Z, Tarabova B, Hensel K, Spetlikova E, Sikurova L, Lukes P. Formation of ROS and RNS in Water Electro-Sprayed through Transient Spark Discharge in Air and their Bactericidal Effects: Formation of ROS/RNS in Water Sprayed through Spark in Air. Plasma Processes and Polymers, 07/2013, Vol10(7), pp649-659.649.

161. Murad E, Cashion J. Mössbauer Spectroscopy of Environmental Materials and Their Industrial Utilization. 2004.
162. Mello R, González Núñez ME. Reactions of Peroxides on Solid Surfaces. PATAI'S Chemistry of Functional Groups: John Wiley & Sons, Ltd; 2009.
163. Russell JD. Infrared and Mössbauer Studies of Reduced Nontronites. Clays and Clay Minerals, 1979, Vol27(1), pp63-71.63; doi: 10.1346/CCMN.1979.0270108.
164. Jaisi DP, Kukkadapu RK, Eberl DD, Dong H. Control of Fe(III) site occupancy on the rate and extent of microbial reduction of Fe(III) in nontronite. Geochimica et Cosmochimica Acta. 2005;69 23:5429-40; doi: 10.1016/j.gca.2005.07.008.
165. Merola RB, McGuire MM. Crystallographic site distribution and redox activity of Fe in nontronites determined by optical spectroscopy. Clays and Clay Minerals, December 2009, Vol57(6), pp771-778.771; doi: 10.1346/CCMN.2009.0570609
166. Steinhoff D, Mohr U, Hahnemann S. Carcinogenesis studies with iron oxides. Experimental pathology. 1991;43 3:189-94; doi: 10.1016/S0232-1513(11)80116-7.
167. Roquemalherbe R, Diazaguila C, Regueraruiz E, Fundoralliteras J, Lopezcolado L, Hernandezvelez M. The state of iron in natural zeolites - A Mossbauer study. Zeolites. 1990;10 7:685-9; doi: 10.1016/0144-2449(90)90080-b.
168. Taylor GL, Ruotsala AP, Keeling RO. Analysis of iron in layer silicates by Mossbauer Spectroscopy. Clays and Clay Minerals. 1968;16 5:381-&; doi: 10.1346/ccmn.1968.0160507.
169. Martin F, Micoud P, Delmotte L, Marichal C, Le Dred R, De Parseval P, et al. The structural formula of talc from the Trimouns deposit, Pyrenees, France. Canadian Mineralogist. 1999;37:997-1006.
170. Di Benedetto F, D'Acapito F, Fornaciai G, Innocenti M, Montegrossi G, Pardi LA, et al. A Fe K-edge XAS study of amethyst. Physics and Chemistry of Minerals. 2010;37 5:283-9; doi: 10.1007/s00269-009-0332-0.
171. Weil JA. EPR of iron centers in silicon dioxide. Applied Magnetic Resonance. 1994;6 1-2:1-16; doi: 10.1007/BF03162478
172. Dennen WH. Stoichiometric substitution in natural quartz. Geochimica et Cosmochimica Acta. 1966;30 12:1235-&; doi: 10.1016/0016-7037(66)90122-0.
173. Goldfarb D, Strohmaier KG, Vaughan DEW, Thomann H, Poluektov OG, Schmidt J. Studies of framework iron in zeolites by pulsed ENDOR at 95 GHz. Journal of the American Chemical Society. 1996;118 19:4665-71; doi: 10.1021/ja953903e.
174. Walter M, Schenkeveld WDC, Geroldinger G, Gille L, Reissner M, Kraemer SM. Identifying the reactive sites of hydrogen peroxide decomposition and hydroxyl radical formation on chrysotile asbestos surfaces. This dissertation. 2018b:54 - 76.

175. Hsieh YHP, Hsieh YP. Kinetics of Fe(III) reduction by ascorbic acid in aqueous solutions. Journal of Agricultural and Food Chemistry. 2000;48 5:1569-73; doi: 10.1021/jf9904362.
176. Bui MH, Sauty A, Collet F, Leuenberger P. Dietary vitamin-c intake and concentrations in the body-fluids and cells of male smokers and nonsmokers. Journal of Nutrition. 1992;122 2:312-6; doi: 10.1093/jn/122.2.312.
177. Shannon RD. Revised effective ionic radii and systematic studies of interatomic distances in halides and chalcogenides. Acta Crystallographica Section A. 1976;32 5:751-67; doi: 10.1107/S0567739476001551.
178. WHO-IARC. Silica, some silicates, coal dust and paramid fibrils. IARC monographs on the evaluation of carcinogenic risks to humans. 1997;68:1-475.
179. Cerrato G, Fubini B, Baricco M, Morterra C. Spectroscopic, structural and microcalorimetric study of stishovite, a non-pathogenic polymorph of SiO2. Journal of Materials Chemistry. 1995;5:1935-41 doi: 10.1039/JM9950501935.
180. Driscoll KE, Guthrie GD. 8.17 - Crystalline Silica and Silicosis A2 - McQueen, Charlene A. Comprehensive Toxicology (Second Edition). Oxford: Elsevier; 2010. p. 331-50.
181. Bríeger H, Gross P. On the Theory of Silicosis, II. Stishovite. Archives of Environmental Health: An International Journal. 1967;15 6:751-7; doi: 10.1080/00039896.1967.10664993.
182. ATSDR Toxicological Profile for Asbestos Edited by Services UDoHH, vol. TP-612001.
183. Israel Environment Bulletin vol. 37: Israel Ministry of Environmental Protection; September 2011.
184. Walter M, Schenkeveld WDC, Geroldinger G, Gille L, Kraemer SM. Presence, loss and recovery of redox cycling tetrahedral iron on chrysotile asbestos surfaces during dissolution. This dissertation. 2018c:77 - 98.
185. Favero-Longo SE, Turci F, Tomatis M, Castelli D, Bonfante P, Hochella MF, et al. Chrysotile asbestos is progressively converted into a non-fibrous amorphous material by the chelating action of lichen metabolites. Journal of Environmental Monitoring. 2005;7 8:764-6; doi: 10.1039/b507569f.
186. Favero-Longo SE, Siniscalco C, Piervittori R. Plant and lichen colonization in an asbestos mine: Spontaneous bioattenuation limits air dispersion of fibres. Plant Biosystems. 2006;140 2:190-205; doi: 10.1080/11263500600756546.
187. Favero-Longo SE, Castelli D, Fubini B, Piervittori R. Lichens on asbestos-cement roofs: Bioweathering and biocovering effects. Journal of Hazardous Materials. 2009;162 2-3:1300-8; doi: 10.1016/j.jhazmat.2008.06.060. <Go to ISI>://WOS:000263370200099.

188. Baker WE. Role of humic acids from tasmanian podzolic soils in mineral degradation and metal mobilization. Geochimica et Cosmochimica Acta. 1973;37 2:269-81; doi: 10.1016/0016-7037(73)90134-8.

189. Boxma R. Mobility of iron in estuaries of rhine and ems relevant to plant-availability problems. Plant and Soil. 1976;44 2:407-22; doi: 10.1007/bf00015892.

190. Neubauer E, Schenkeveld WDC, Plathe KL, Rentenberger C, von der Kammer F, Kraemer SM, et al. The influence of pH on iron speciation in podzol extracts: Iron complexes with natural organic matter, and iron mineral nanoparticles. Science of the Total Environment. 2013;461:108-16; doi: 10.1016/j.scitotenv.2013.04.076.

191. Walter M, Oburger E, Schindlegger Y, Hann S, Puschenreiter M, Kraemer SM, et al. Retention of phytosiderophores by the soil solid phase - adsorption and desorption. Plant and Soil. 2016;404 1-2:85-97; doi: 10.1007/s11104-016-2800-x.

192. Walter M, Kraemer SM, Schenkeveld WDC. The effect of pH, electrolytes and temperature on the rhizosphere geochemistry of phytosiderophores. Plant and Soil. 2017:1-19; doi: 10.1007/s11104-017-3226-9. .

193. Schenkeveld WDC, Kimber RL, Walter M, Oburger E, Puschenreiter M, Kraemer SM. Experimental considerations in metal mobilization from soil by chelating ligands: The influence of soil-solution ratio and pre-equilibration - A case study on Fe acquisition by phytosiderophores. Science of the Total Environment. 2017;579:1831-42; doi: 10.1016/j.scitotenv.2016.11.168.

194. Schenkeveld WDC, Schindlegger Y, Oburger E, Puschenreiter M, Hann S, Kraemer SM. Geochemical Processes Constraining Iron Uptake in Strategy II Fe Acquisition. Environmental Science & Technology. 2014;48 21:12662-70; doi: 10.1021/es5031728. <Go to ISI>://WOS:000344449100023.

195. Oburger E, Gruber B, Wanek W, Watzinger A, Stanetty C, Schindlegger Y, et al. Microbial decomposition of 13C- labeled phytosiderophores in the rhizosphere of wheat: Mineralization dynamics and key microbial groups involved. Soil Biology and Biochemistry. 2016;98:196-207; doi: 10.1016/j.soilbio.2016.04.014.

196. Oburger E, Gruber B, Schindlegger Y, Schenkeveld WDC, Hann S, Kraemer SM, et al. Root exudation of phytosiderophores from soil-grown wheat. New Phytologist. 2014;203 4:1161-74; doi: 10.1111/nph.12868.

197. Schenkeveld WDC, Dijcker R, Reichwein AM, Temminghoff EJM, van Riemsdijk WH. The effectiveness of soil-applied FeEDDHA treatments in preventing iron chlorosis in soybean as a function of the o,o-FeEDDHA content. Plant and Soil. 2008;303 1-2:161-76; doi: 10.1007/s11104-007-9496-x.

198. G. Clark S, F. Holt P. Dissolution of Chrysotile Asbestos in Water, Acid and Alkali. Nature. 1960;185 4708:237-; doi: 10.1038/185237a0.
199. van Schöll L, Kuyper TW, Smits MM, Landeweert R, Hoffland E, Breemen Nv. Rock-eating mycorrhizas: their role in plant nutrition and biogeochemical cycles. Plant and Soil. 2008;303 1:35-47; doi: 10.1007/s11104-007-9513-0.
200. Hoffland E, Kuyper TW, Wallander H, Plassard C, Gorbushina AA, Haselwandter K, et al. The role of fungi in weathering. Frontiers in Ecology and the Environment. 2004;2 5:258-64; doi: 10.1890/1540-9295(2004)002[0258:TROFIW]2.0.CO;2.
201. Steele GC, Trinci AP. Morphology and growth kinetics of hyphae of differentiated and undifferentiated mycelia of Neurospora crassa. Journal of General Microbiology. 1975;91 2:362-8; doi: 10.1099/00221287-91-2-362.
202. Yoon TH, Johnson SB, Brown GE, Jr. Adsorption of organic matter at mineral/water interfaces. IV. Adsorption of humic substances at boehmite/water interfaces and impact on boehmite dissolution. Langmuir. 2005;21 11:5002-12; doi: 10.1021/la0476276.
203. Burilkov T, Michailova L. Asbestos content of the soil and endemic pleural asbestosis. Environmental Research. 1970;3 5:443-51; doi: 10.1016/0013-9351(70)90037-X.
204. Walter M, Schenkeveld WDC, Geroldinger G, Gille L, Kraemer SM. Soil-pH and cement influence dissolution kinetics of, and radical formation by, chrysotile asbestos in soils. This dissertation. 2018d:99 - 117.
205. White AF, Brantley SL. The effect of time on the weathering of silicate minerals: why do weathering rates differ in the laboratory and field? Chemical Geology. 2003;202 3:479-506; doi: 10.1016/j.chemgeo.2003.03.001.
206. Ganor J, Roueff E, Erel Y, Blum JD. The dissolution kinetics of a granite and its minerals—Implications for comparison between laboratory and field dissolution rates. Geochimica et Cosmochimica Acta. 2005;69 3:607-21; doi: 10.1016/j.gca.2004.08.006.
207. Swoboda-Colberg NG, Drever JI. Mineral dissolution rates in plot-scale field and laboratory experiments. Chemical Geology. 1993;105 1:51-69; doi: 10.1016/0009-2541(93)90118-3.
208. Schenkeveld WDC, Temminghoff EJM, Reichwein AM, van Riemsdijk WH. FeEDDHA-facilitated Fe uptake in relation to the behaviour of FeEDDHA components in the soil-plant system as a function of time and dosage. Plant and Soil. 2010;332 1-2:69-85; doi: 10.1007/s11104-009-0274-9.
209. Jones DL. Organic acids in the rhizosphere - a critical review. Plant and Soil. 1998;205 1:25-44; doi: 10.1023/a:1004356007312.

210. Neumann G, Massonneau A, Langlade N, Dinkelaker B, Hengeler C, Romheld V, et al. Physiological aspects of cluster root function and development in phosphorus-deficient white lupin (Lupinus albus L.). Annals of Botany. 2000;85 6:909-19; doi: 10.1006/anbo.2000.1135.
211. Garcia JAL, Barbas C, Probanza A, Barrientos ML, Manero FJG. Low molecular weight organic acids and fatty acids in root exudates of two Lupinus cultivars at flowering and fruiting stages. Phytochemical Analysis. 2001;12 5:305-11.
212. Schottelndreier M, Norddahl MM, Strom L, Falkengren-Grerup U. Organic acid exudation by wild herbs in response to elevated Al concentrations. Annals of Botany. 2001;87 6:769-75; doi: 10.1006/anbo.2001.1405.
213. Ueno D, Rombola AD, Iwashita T, Nomoto K, Ma JF. Identification of two novel phytosiderophores secreted by perennial grasses. New Phytologist. 2007;174 2:304-10; doi: 10.1111/j.1469-8137.2007.02056.x.

Danksagung (Acknowledgements)

Viele Personen haben zum Erfolg dieser Arbeit beigetragen, ich möchte mich an dieser Stelle recht herzlich bei allen dafür bedanken!

An erster Stelle möchte ich diejenigen hervorheben, die als Forschende an diesem Projekt mitgearbeitet haben und als Coautoren jeweils in den Kapiteln Erwähnung finden:

Da wären zuallererst meine zwei Betreuer an der Uni Wien in der Forschungsgruppe für Umwelt-Biogeochemie und Isotopen-Geochemie, Stephan Krämer und Walter Schenkeveld. Stephan Krämer möchte ich als meinen Erstbetreuer besonders für sein Vertrauen und für die vielen anregenden Diskussionen während den vier Jahren dieses Projektes danken. Vom Schreiben des Antrags für die uni:docs Finanzierung bis hin zur Fertigstellung der Doktorarbeit hatte ich immer das Gefühl, dass meine Arbeit wertgeschätzt wurde. Ich bedanke mich vor allem für das große Vertrauen in meine Arbeit, welches mir ermöglichte, den Großteil des Projektes selbstständig und eigenverantwortlich zu erarbeiten und vor allem auch eigenen Ideen einbringen und nachgehen zu können. Bezüglich der Finanzierung von Experimenten will ich mich bedanken, dass Stephan für alle meine Ideen zugänglich war und auch Experimente dieses Projektes finanzierte, wenn das uni:docs Sachmittelbudget schon erschöpft war. Zum Abschluss will ich mich noch für die Korrekturarbeit an den vielen Manuskripten dieses Projektes bedanken. Meinem Zweitbetreuer Walter Schenkeveld möchte ich besonders dafür danken, mir während meines Masters (der in der selben Forschungsgruppe stattfand) das notwendige Handwerk gelernt zu haben, wie man erfolgreich Experimente plant, ausführt und anschließend auswertet. Der Erfolg dieses Projektes geht auf diese Einschulung während meines Masters zurück. Analog will ich mich auch dafür bedanken, dass Walter mich im wissenschaftlichen Schreiben während meines Doktoratsstudiums einschulte und Manuskriptentwürfe erstkorrigierte. Weiters möchte ich mich dafür bedanken, dass mir vor jedem großen Vortrag und Interview Probedurchgänge meiner Präsentationen von ihm angeboten wurden. Ich möchte mich auch für die Hilfe beim Beantragen der uni:docs Finanzierung während meines Masters bedanken. Letztendlich will ich mich noch für sein Interesse an dem Projekt, den vielen Diskussionen zu Experimenten und deren Ergebnissen und dem Korrekturlesen des allgemeinen Teils der Dissertation bedanken.

Neben meinem Erst- und Zweitbetreuer will ich mich besonders bei Lars Gille (Veterinärmedizinische Universität Wien) und Michael Reissner (Technische Universität Wien) bedanken. Ihre Kooperation ermöglichte mir den Einsatz von zwei analytischen Techniken, die für den Erfolg dieses Projektes von maßgeblicher Bedeutung waren; die ESR und die Mößbauer Spektroskopie. Ich möchte mich recht herzlich bei Lars Gille für die vielen Messungen an der ESR bedanken, und für das Vertrauen, dass er von Anfang an in mich gehabt hat. Ferner möchte ich mich für die vielen netten Diskussionen und Gespräche während unseren langen ESR-Messsessions bedanken, und dafür, dass Lars mir den postgraduellen Toxikologie-Master auf der Medizinischen Uni Wien empfohlen hat, der mir fachlich

auch für dieses Projekt und die Dissertation sehr nützlich war. Ein letzter Dank an Lars geht noch an sein Vertrauen in mich, dass ich auch bei seinen eigenen Projekten mitarbeiten durfte, was eine nette Abwechslung zu der Arbeit mit den Asbestfasern war. Ein herzlicher Dank geht auch an Michael Reissner für die Mößbauer-Analysen meiner Proben. Dabei möchte ich mich für sein Vertrauen zu dieser Kooperation bedanken, vor allem jedoch auch für unsere Diskussionen zu den jeweiligen Ergebnissen. Ich möchte mich auch für seine Bereitschaft bedanken mir zu erklären, wie man Proben für die Mößbauer-Analysen herstellt. Die Mößbauer-Spektroskopie war enorm wichtig für die Erforschung von tetraedrisch-koordiniertem Eisen in Chrysotil-Asbest, welches eine zentrale Rolle in der Erforschung von den verschiedensten Eigenschaften dieses gefährlichen Minerals in dieser Arbeit hatte. Deswegen waren die Mößbauer Untersuchungen auf der Technischen Universität Wien von größter Bedeutung, ich möchte ich mich nochmals herzlich dafür bedanken.

Anschließend will ich mich auch noch bei Gerald Geroldinger (VetMed Uni Wien) und Carolina Reyes (Uni Wien) für ihre Mitarbeit an diesem Projekt bedanken. Für die langen ESR Messsessions und seine Geduld darin will ich mich herzlich bei Gerald bedanken. Nicht nur dafür dass wir erfolgreich den „Fünf-Minutentakt“ während den ESR Messungen einführten (und dadurch mehr Proben an den jeweiligen Messtagen messen konnten), sondern auch für die netten Gespräche und die nette Atmosphäre während den Messungen und seine Verständnis, wenn ich wieder mit vielen Proben ankam. Ich war immer sehr gern bei euch auf der VetMed, vielen Dank für die gute Freundschaft! Zu guter Letzt bedanke ich mich noch herzlich bei Carolina Reyes, die alle statistischen Analysen dieses Projektes durchführte. Vor allem die statistische Auswertung des fünften Kapitels wäre für mich am Schluss dieses Projektes zeitlich schwer zu erledigen gewesen, deshalb herzlichen Dank!

Neben jenen sechs Personen, die als Forschende an dem Projekt mitgearbeitet haben und in den Kapiteln als Coautoren geführt werde, will ich besonders die beiden Labormanager Wolfgang Obermaier und Herwig Lenitz hervorheben und Ihnen meinen größten Dank aussprechen. Mit beiden entstand neben der Laborarbeit auch eine gute Freundschaft.

Wolfgang war maßgeblich bei der Messung des Großteils der analytischen Daten in dieser Arbeit beteiligt. Abgesehen von Daten aus ESR-, Mössbauer- und Photospektrometrie-Analysen führte ich alle Metallanalysen und Si-Analysen anhand ICP-OES Messungen unter seiner Aufsicht durch. Neben den ICP-OES Analysen erlernte mir Wolfgang auch Schmelzaufschlüsse von Festkörpern, die in dieser Arbeit vor allem im vierten und fünften Kapitel von entscheidender Bedeutung waren. Neben der Laborarbeit bedanke ich mich für die vielen Diskussionen und die gute Stimmung bei den jeweiligen Messungen. Falls technische Probleme an der Maschine aufgekommen sind, hatte er auf MacGyver-Style jedes Mal die passende Lösung parat, auch wenn die Situation schon ausweglos schien. Ich war immer gerne ICP-OES messen und Schmelzaufschlüsse machen, dafür bedanke ich mich herzlich! Neben der Arbeit

waren die gemeinsamen Mittagessen beim Resnicek und Orlik Wirtn und in da Mensa Highlights meines Doktoratsstudiums.

Bei Herwig Lenitz möchte ich mich ähnlich bedanken! Seine Mitarbeit und sein Know-How erleichterten mir viele Experimente. Herwig war immer für Hilfe im Labor bereit, und analysierte mir auch hin und wieder Proben mit der ICP-MS. Neben der Laborarbeit entstand auch mit Herwig eine gute Freundschaft; bald nachdem er im Labor zu arbeiten begann war er schnell in der Mittagsessen-Gang mit Wolfgang dabei. Vielen Dank auch dafür, dass er das Schokoladensystem in der Forschungsgruppe eingeführt hat, während harten und langen Experimenten war das immer sehr hilfreich.

Besonders Danken möchte ich dann noch Andreas Maier (Forschungsgruppe Für Geoökologie, Universität Wien), der für mich die DOC und TN-Messungen durchgeführt hat. Während der Probenbereitung bei ihm im Labor hatte ich immer eine gute Zeit, vielen Dank auch für unsere Gespräche übers Reisen, Wandern, Campen und Trekken.

Ein großer Dank geht an Kyounglim Kang, Herwig Lenitz und Sebastian Pontz, die mir oft während meiner Urlaube die Pflanzen vom Microcosm Experiment gossen und somit überhaupt erst das fünfte Kapitel ermöglichten! Vielen Dank dafür! Bei Kyounglim Kang möchte ich mich ferner für das Bereitstellen ihrer synthetisierten Ferrihydrite für Experimente im zweiten Kapitel bedanken.

Für die Probencharakterisierung der Chrysotil-Asbestfasern möchte ich mich bei Andreas Attac für die Raman-Messungen bedanken, bei Christian Lengauer und Dominik Taller für die Pulferdiffraktometrie Untersuchungen, und bei Dieter Mader für sein großzügiges Angebot, für uns vier Proben anhand einer Neutronenaktivierungsanalyse zu untersuchen. Bei Melanie Kah und Gabriel Sigmund möchte ich mich für ihre Einschulung für die BET Messungen bedanken. Für die elektronenmikroskopische Untersuchung der Fasern möchte ich mich bei Christian Baal für die Einschulung am REM bedanken, bei Wolfgang Knierzinger für die Hilfe am REM, bei Gerlinde Habler für die Einführung wie man Proben mit Kohlenstoff coated, und bei Christa Hofmann für das zur Verfügung stellen von REM-Probetischen.

Einen besonderen Dank möchte ich auch Paolo Annicchiarico vom Centro di Ricerca per le Produzioni Foraggere e Lattiero-Casearie in Italien ausrichten, der mir nach sehr langer Suche Samen der Varietät Multolupa (oder besser gesagt Multitalia) der Weißen Lupine zur Verfügung gestellt hat. Für den Versand der Samen nach Österreich hat er nichts verlang, was ich cool fand.

Weiters möchte ich noch den verschiedensten Personen meinen Dank aussprechen: Bei Thilo Hofmann möchte ich mich für gelegentliche Hilfestellungen und für die Möglichkeit bedanken, dass ich in seiner Forschungsgruppe Laborinventar und Messgeräte nutzen durfte. Frank von der Kammer möchte ich für die gelegentliche labortechnische und administrative Hilfe danken, den Gärtner Thomas Joch der

Uni Wien für Beratungen zum Microcosm Experiment im fünften Kapitel, Christoph Schuster für seine Einschulung auf der ICP-MS während meines Masters und für seine Hilfestellungen im Labor, Susanne Gier für das Bereitstellen von Sieben für Manuskript vier und fünf, Bernhard Groiss für das Bereitstellen von Feldgeräten wie Pürckhauer, Petra Körner und Anna Kastlunger für verschiedene labortechnische Hilfestellungen, Markus Puschenreiter von der BOKU für seine telefonischen Ratschläge zum fünften Manuskript und Jan Wiederhold für Diskussionen und Zusendungen von interessanten Themen bezüglich meiner Doktorarbeit. Ferner möchte ich mich bei Matthias Tonner und Katrin Staniek von der VetMed für die gute Unterhaltung und für die netten Gespräche bei den ESR Messsessions bedanken. Bei Matthias möchte ich mich besonders dafür bedanken, dass ich öfters seinen Laborplatz während den ESR Messungen besetzen durfte. Bei meiner Cousine Theresa Walter und auch bei Tamina Buttinger, Martina Salomon und Cloe Pretret möchte ich mich bei ihrer Hilfe beim Bodensammeln für das vierte und fünfte Manuskript bedanken, vor allem dafür, dass wir mehr al 60 kg vom einen wenigen Centimeter mächtigen A Horizont eines Podsols sammelten. Weiters möchte ich Laurent Charlet danken für sein Interesse an meiner Forschung nach meinem Vortrag auf der Goldschmidt 2017. Ich möchte auch den freundlichen Menschen von Anafi, Nisyros, Symi und Karpathos in Griechenland danken, wo ich Teile dieser Arbeit geschrieben habe. Mein Dank geht außerdem auch an die administrativen MitarbeiterInnen an der Fakultät für Erdwissenschaften, Geographie und Astronomie der Uni Wien, vor allem Franz Mikysek aka Frens Mike, Doris Herzog und Brigitte Notter, jedoch auch Tobias Reckling und David Zuser vom DoktorandInnenzentrum und Martin Zuschin als Doktorats-SPL. Meinen Dank möchte ich auch Bettina Grasl-Kraupp und Wolfgang Huber aussprechen dafür dass ich an der Medizinischen Uni Wien am postgraduellen Masterprogramm Toxikologie teilnehmen durfte. Diese zusätzliche Ausbildung beeinflusste auch meine Doktoratsausbildung maßgeblich.

Ganz besonders möchte ich noch Francisco Javier Huertas (Universität Granada), Brenda Buck (University of Nevada), Brenda Casper (University of Pennsylvania) und Stefano Cesco (Universität Bozen) für ihre Bereitschaft danken, diese Arbeit zu begutachten. Die letzten zwei wurden zur Begutachtung dieser Arbeit vom Studienpräses der Universität Wien ausgewählt. Ich möchte mich für ihr Interesse an diesem Projekt und für ihre Gutachterarbeit bedanken!

Abschließend möchte ich noch allen KollegInnen am Department für Umweltgeowissenschaften an der Uni Wien, die noch nicht genannt wurden, für die gute Zusammenarbeit danken.

Zu allerletzt geht mein größter Dank jedoch an meine Familie, Freunde und Freundinnen, die mich immer in meiner akademischen Ausbildung unterstützt haben.

Tabular curriculum vitae

Contact details:

Martin Walter MSc

Florianigasse 23/10

1080 Vienna, Austria

Tel.: +43676-81429763

martinwalter1990@gmx.at

Personal Data:

First name:	Martin
Surname:	Walter
Date and place of birth:	25.11.1990, Bad Ischl (Austria)
Nationality:	Austrian

Languages:

German:	Mother tongue
English:	Excellent, both oral and written
French:	Good, A-levels
Farsi:	Basic understanding (A2 level, Language Center of the University of Vienna)

Education and working experience:

1997 - 2001: Primary School	Volksschule Steinbach am Attersee
2001 - 2005: Secondary School	Hauptschule Schörfling am Attersee

2005 - 2009: High School	Oberstufenrealgymnasium Vöcklabruck. A-level exam ("Matura") with honors
2006, 2007: Waiter	Summer jobs, Steinbach am Attersee. Variable durations (1 to 1.5 months)
2008, 2009, 2010: Sandoz (Novartis)	Unterach am Attersee. Summer internships in the sterile production of cytostatic drugs. Variable durations (1.5 to 3 months)
2009 - 2014: Study of Environmental Earth Sciences	University of Vienna (2012-2014), graduation with honors within the minimum duration of studies. Master thesis: "The influence of geochemical parameters on metal mobilization from a calcareous soil by the phytosiderophore DMA"
2014 - 2018: Doctoral study of Environmental sciences	University of Vienna, research group for environmental biogeochemistry and environmental isotope geochemistry. Project funded by an uni:docs scholarship of the University of Vienna[1]. Doctoral thesis: "Studies on the radical generation and dissolution mechanisms of chrysotile asbestos – From the Laboratory to the Environment"
2015-2018: Post-gradual Master study of Toxicology	Medical University of Vienna, accredited by ASTOX and EUROTOX (Austrian/European Society of Toxicology). Lectures on toxicology, biochemistry, analytics and regulatory affairs. Master thesis: "The potential contribution of hexavalent chromium, nickel and pro-oxidants to the carcinogenicity of chrysotile asbestos"

[1] "The uni:docs fellowship program offers individual scholarships which aim at financing excellent doctoral candidates", https://forschung.univie.ac.at/en/services/funding/early-career-researchers/unidocs-fellowship-programme/

Analytical and laboratory experience:

ICP-MS	Four years of extended experience in inductively coupled plasma mass spectrometry, specifically in elemental analyses and method development
ICP-OES	Four years of extended experience in inductively coupled plasma optical emission spectrometry, specifically in elemental analyses of inorganic and biologic samples and method development
EPR	Three years of laboratory experience in electron spin resonance spectroscopy, especially in spin trapping methods in radical chemistry
Solid state analyses	Three years of laboratory experience in analyses of solid materials, including different digestion methods (fusion digestions, microwave digestions) with subsequent ICP-OES/MS analyses, Mössbauer spectroscopy, infrared spectroscopy and electron microscopy including electron dispersive X-ray spectroscopy
Chromatography	Basic laboratory experience of different chromatographic methods (HPLC, GC), also coupled to mass spectrometry
Others	Extended laboratory experience in UV/VIS photospectrometry and basic laboratory analytical methods

Peer-reviewed scientific publications:

2017: Gille L, Geroldinger G, Tonner M, Hettegger H, Bacher M, Monzote L, Walter M, Staniek, K, Rosenau T (2017) P 045 - The activation of the endoperoxide ascaridole in Leishmania, *Free Radical Biology & Medicine,* 108, S32. doi: https://doi.org/10.1016/j.freeradbiomed.2017.04.130

Walter M, Kraemer SM, Schenkeveld WDC (2017) The effect of pH, electrolytes and temperature on the rhizosphere geochemistry of phytosiderophores. Plant Soil: 1-19. doi: 10.1007/s11104-017-3226-9.

Geroldinger G, Tonner M, Hettegger H, Bacher M, Monzote L, Walter M, Staniek K, Rosenau T, Gille L (2017) Mechanism of ascaridole activation in Leishmania. Biochemical pharmacology 132: 48-62. doi: 10.1016/j.bcp.2017.02.023

Schenkeveld WDC, Kimber RL, Walter M, Oburger E, Puschenreiter M, Kraemer SM (2017) Experimental considerations in metal mobilization from soil by chelating ligands: The influence of soil-solution ratio and pre-equilibration – A case study on Fe acquisition by phytosiderophores. Science of The Total Environment 579: 1831-1842. doi: 10.1016/j.scitotenv.2016.11.168.

2016: Walter M, Oburger E, Schindlegger Y, Hann S, Puschenreiter M, Kraemer SM, Schenkeveld WDC (2016) Retention of phytosiderophores by the soil solid phase - adsorption and desorption. Plant Soil 404: 85-97. doi: 10.1007/s11104-016-2800-x

Scientific publications in preparation:

Walter M, Schenkeveld WDC, Reissner M, Gille L, Kraemer SM; The effect of pH and biogenic ligands on the weathering of chrysotile asbestos; the pivotal role of tetrahedral Fe in dissolution kinetics and radical formation

Walter M, Schenkeveld WDC, Geroldinger G, Gille L, Reissner M, Kraemer SM; Identifying the reactive sites of hydrogen peroxide decomposition and hydroxyl radical formation on chrysotile asbestos surfaces

Walter M, Schenkeveld WDC, Geroldinger G, Gille L, Kraemer SM; Presence, loss and recovery of redox cycling tetrahedral iron on chrysotile asbestos surfaces during dissolution

Walter M, Schenkeveld WDC, Geroldinger G, Gille L, Kraemer SM; Soil-pH and cement influence dissolution kinetics and radical formation of chrysotile asbestos in soils

Walter M, Schenkeveld WDC, Geroldinger G, Gille L, Kraemer SM; Weathering of chrysotile in a long-term microcosm experiment: The influence of soil-type, plants and cement on dissolution kinetics and radical generation of asbestos in polluted soils

Walter M, Schenkeveld WDC, Geroldinger G, Gille L, Kraemer SM; The potential contribution of hexavalent chromium and nickel to the carcinogenicity of chrysotile asbestos

Walter M, Schenkeveld WDC, Geroldinger G, Gille L, Kraemer SM; Mobilization of iron from chrysotile asbestos by the pro-oxidants citrate and ADP

In public media:

Falter, Heureka: "JungforscherInnen", 05. November 2014

Falter, Heureka: Wie kommt Asbest wieder aus dem verseuchtem Erdboden? 18. May 2016

Conference contributions:

2017: Localizing crystal-sites of long-term radical formation in altered chrysotile asbestos (*Oral presentation*), 7th International Conference on Medical Geology, August 2017, Moscow, Russia

Radical generation and transition metals on chrysotile asbestos surfaces (*Oral presentation*), Goldschmidt 2017, August 2017, Paris, France

2016: The effect of rhizosphere variables on the geochemistry of phytosiderophores *(Poster presentation)*, International Symposium on Iron Nutrition and Interactions in Plants, June 2016, Madrid, Spain

Dissolution of chrysotile asbestos and its implications on the fibers' iron surface speciation and radical forming potential: A complementary ICP-OES, EPR and 57Fe Mössbauer study *(Poster presentation)*, International Symposium on the Industrial Applications of the Mössbauer Effect, September 2016, Cape town, South Africa

Understanding the radical forming potential (RFP) of pristine and (environmentally) altered asbestos fibers *(Poster presentation)*, Advanced Lecture Course on Redox Regulation of Metabolic Processes, September 2016, Spetses, Greece

2015: Quantifying the radical forming potential of environmentally weathered asbestos fibers by means of EPR spectroscopy *(Poster presentation)*, Summer School of the European Federation of EPR groups on Advanced EPR, August 2015, Berlin, Germany

Addendum

Containing to supplemtary data to chapter one to five

Addendum

Supporting Information to Chapter 1

"The effect of pH and biogenic ligands on the weathering of chrysotile asbestos; the pivotal role of tetrahedral Fe in dissolution kinetics and radical formation"

Supporting information to the data material presented on page 29 to 53.

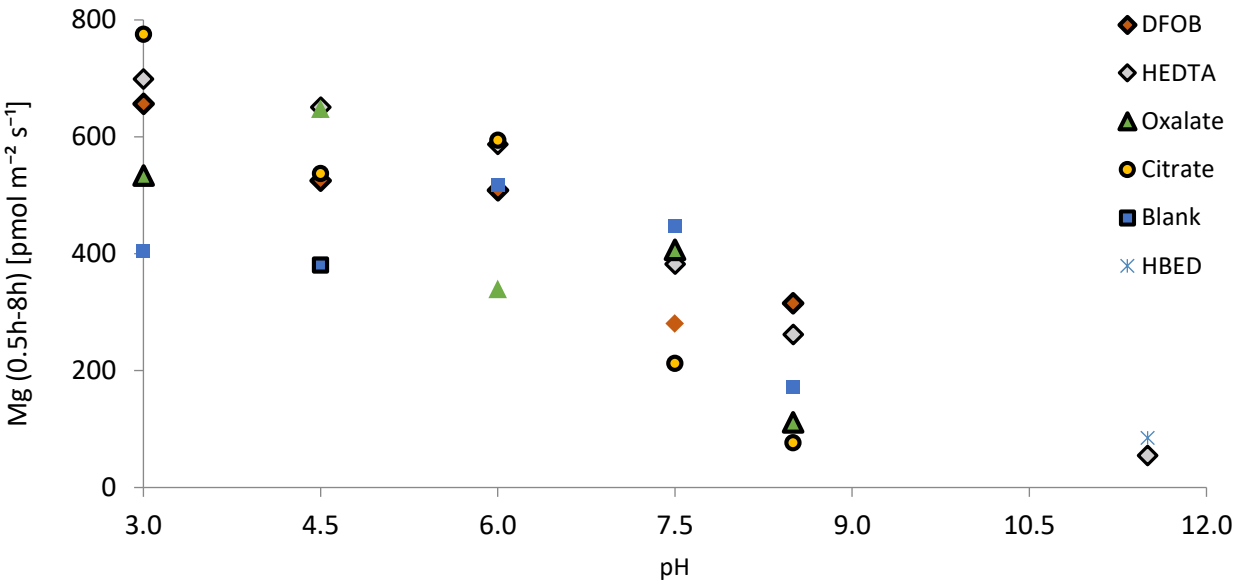

SI-Figure 1: *Mg dissolution rates during the initial stage (0.5 - 8 h). Concentration data underlying this figure is presented in SI-Table 2. Unframed symbols indicate rates for treatments in which the outermost Mg layer had not completely dissolved until the first 8 h.*

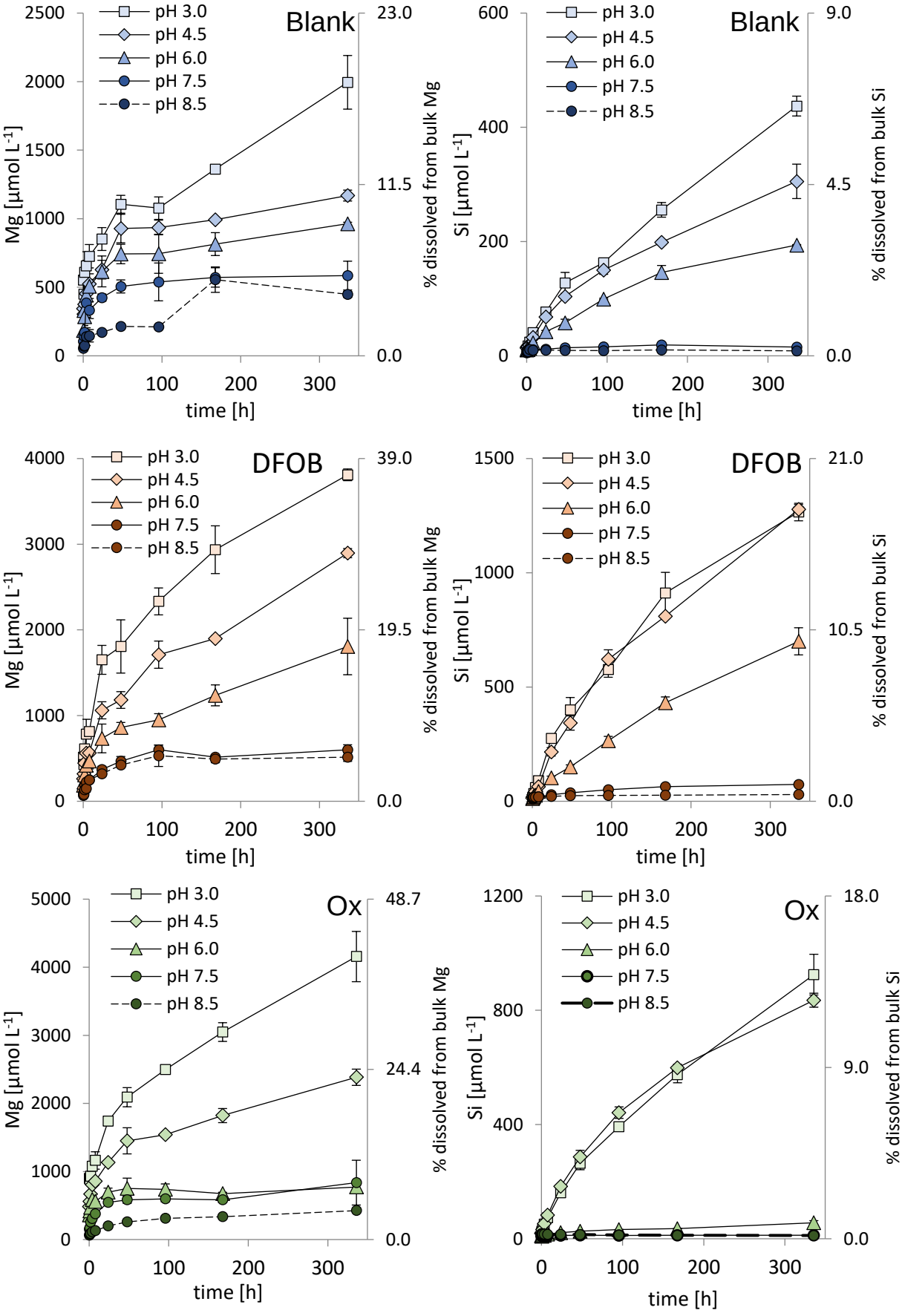
Blank
pH 3.0
pH 4.5
pH 6.0
pH 7.5
pH 8.5
Mg [µmol L-1]
% dissolved from bulk Mg
time [h]
Blank
Si [µmol L-1]
% dissolved from bulk Si
time [h]
DFOB
Mg [µmol L-1]
% dissolved from bulk Mg
time [h]
DFOB
Si [µmol L-1]
% dissolved from bulk Si
time [h]
Ox
Mg [µmol L-1]
% dissolved from bulk Mg
time [h]
Ox
Si [µmol L-1]
% dissolved from bulk Si
time [h]

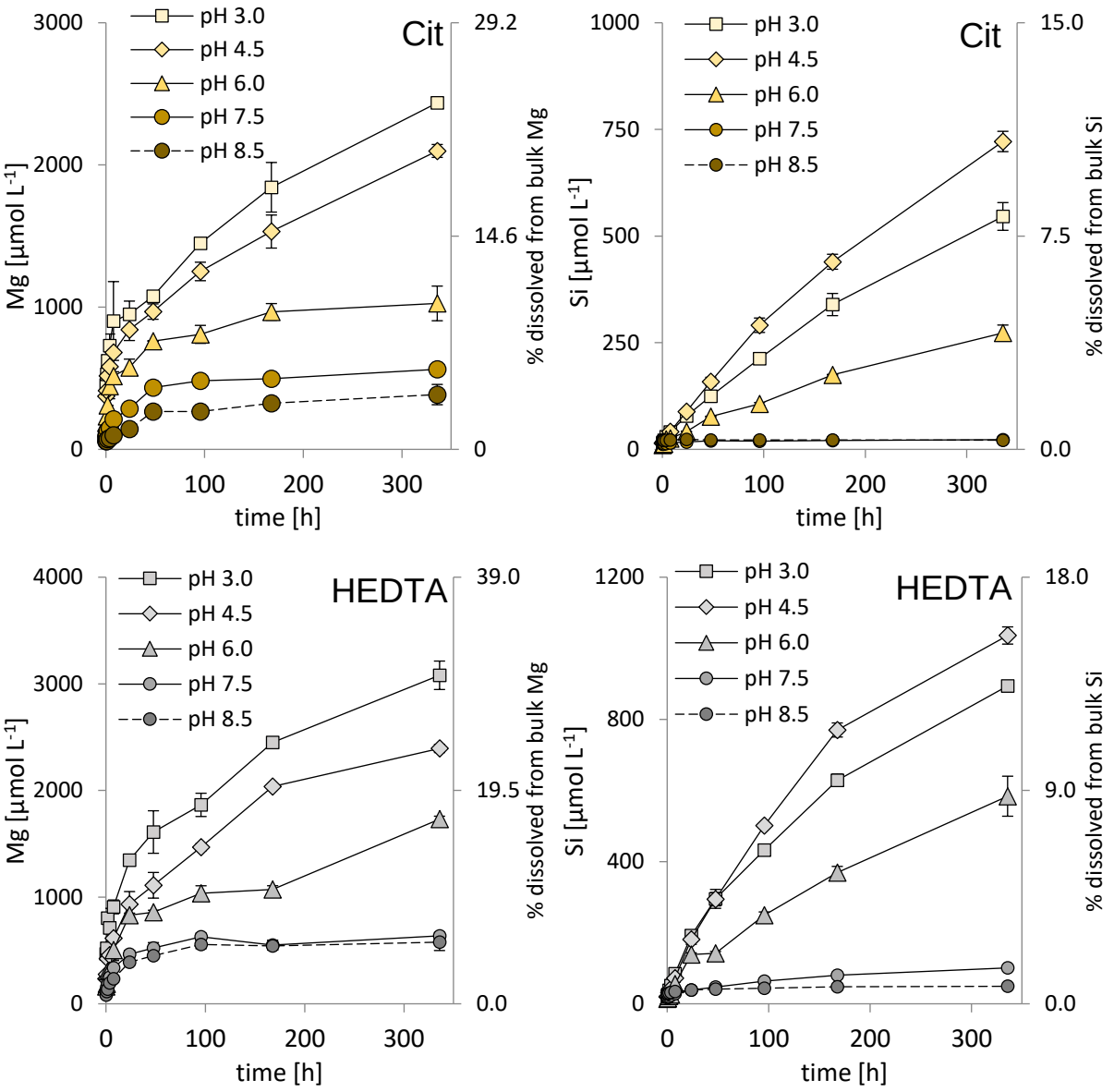

SI-Figure 2: *Mobilized Mg and Si concentrations at pH 3.0; 4.5; 6.0; 7.5 and 8.5 after 0.5; 1; 2; 4; 8; 24; 48; 96; 168 and 336 h of incubation. Ligand concentrations were 1 mmol L^{-1}. For comparison, the percentage of the total bulk dissolved is indicated on the secondary y-axis. Error bars indicate standard deviations (n = 2)*

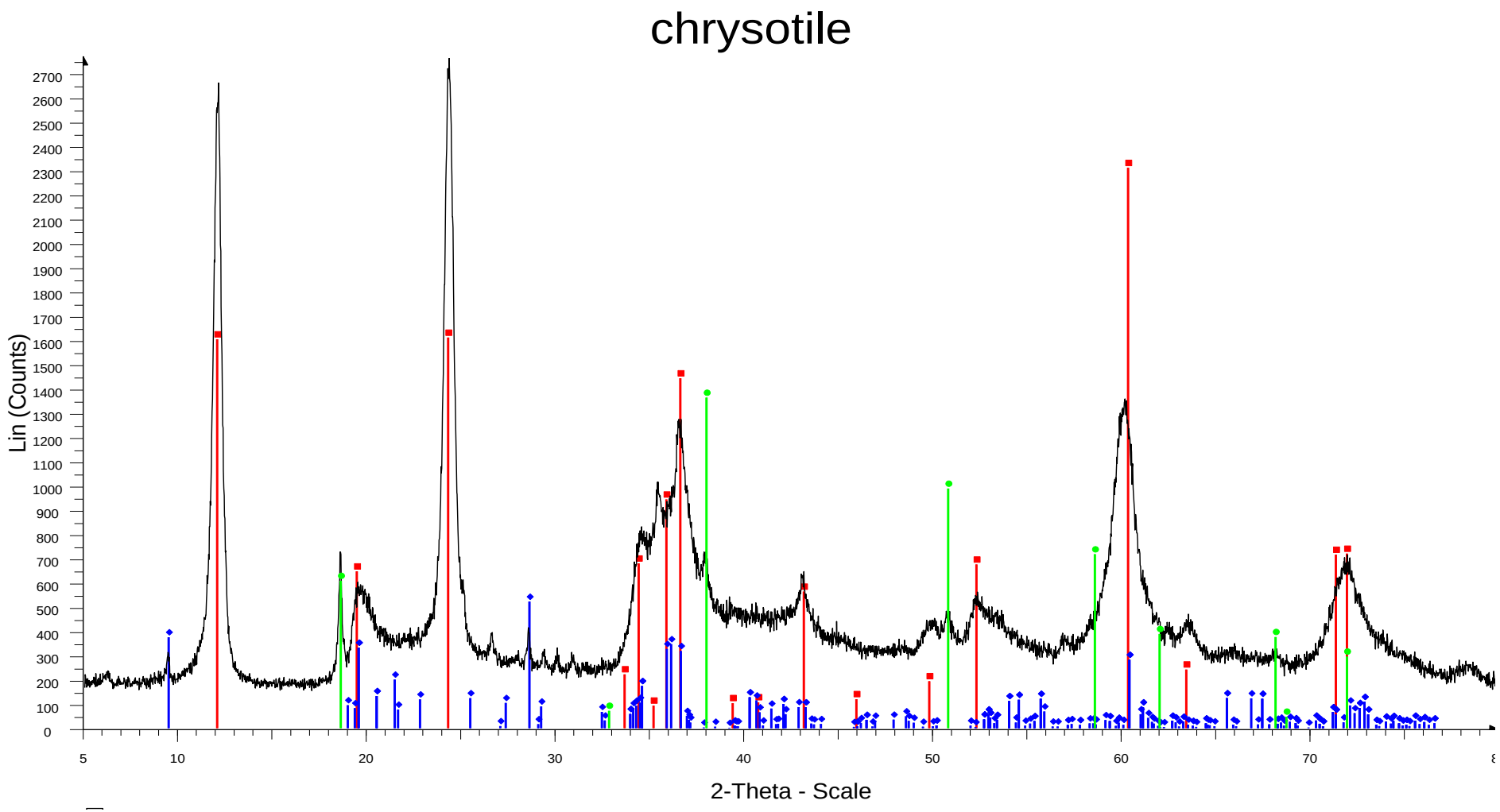

SI-Figure 3: *XRD-Rietveld diffractogram of 1 g chrysotile, ground for 3 min in a WC ball mill at 30 strokes per minute. The Rietveld-analysis identified chrysotile (86.4 ± 4.6%), brucite (4.5 ± 2.1%), talc (3.4 ± 2.0%), chlorite (2.4 ± 2.9%), magnetite (1.5 ± 0.2%), quartz (1.0 ± 0.2%) and calcite (0.8 ± 0.2%). Red arrows indicate chrysotile, blue ones talc and green ones brucite. Step time was 2 s, temperature 25 °C, theta1 5° and theta2 2.5°.*

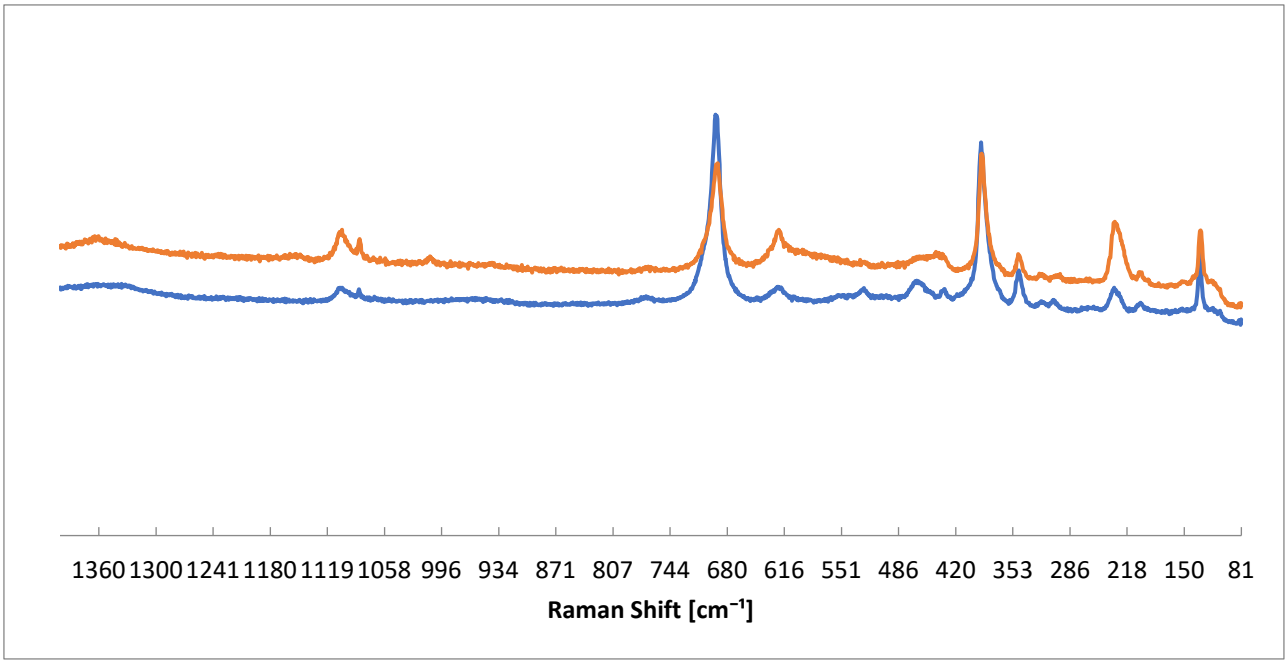

SI-Figure 4: *Raman spectrum of two single Shijiazhuang chrysotile fibers. The Raman database identified the single fiber specimens as chrysotile. Peaks were measured at 130 cm^{-1}, 332 cm^{-1}, 303 cm^{-1}, 321 cm^{-1}, 346 cm^{-1}, 389 cm^{-1}, 435 cm^{-1}, 535 cm^{-1}, 622 cm^{-1}, 693 cm^{-1}, 1085 cm^{-1}, 1103 cm^{-1}.*

SI-Table 1: *First and second stage Mg and Si dissolution rates of chrysotile at different pH values and in presence and absence of ligands. Congruency is expressed by the rate ratio of the Mg-rate divided by the Si rate; rate ratios are presented next to second stage Mg dissolution rates. If the rate ratio deviated by less than 10% from the Mg/Si ratio in chrysotile of 1.5, dissolution was considered congruent (indicated in green).*

Mg and Si dissolution rates of chrysotile at different pHs and in the presence of different ligands. Values in pmol m^{-2} s^{-1}.

Initial Mg dissolution rates:

	Blank	DFOB	Oxalate	Citrate	HEDTA	HBED
3	404	657	534	776	699	
4.5	381	525	648	537	651	
6	518	509	340	594	588	
7.5	446	281	407	213	383	
8.5	172	315	113	77.6	262	
11.5					55.3	85.1

Si-dissolution rates:

	Blank	Dfob	Oxalate	Citrate	HEDTA	HBED
3	17.3	52.9	37.3	22.1	36.7	
4.5	12.1	53.1	34.5	29.7	44	
6	7.9	28.6	1.8	10.9	23.5	
7.5	0.4	2.7		0.4	3.5	
8.5		0.5			0.8	
11.5						0.91

Mg dissolution rates (24-336 h), rates in which second stage dissolution is not reached in round brackets:

pH	Blank	Congruency	DFOB	Congruency	Oxalate	Congruency	Citrate	Congruency	HEDTA	Congruency	HBED	Congruency
3	47.3	2.7	95.6	1.8	103	2.8	65.2	3	74.9	2		
4.5	18.2	1.5	79	1.5	50.6	1.5	54.4	1.8	64.4	1.5		
6	13.3	1.7	46.6	1.6	1.8	1.0	17.2	1.6	39.1	1.7		
7.5	5.6	14	(7.4)	2.7	11.9		(9.3)	23.3	5.7	1.6		
8.5					(8.8)		(8.6)		(6.9)	(8.6)		
11.5							(0.5)		(3.2)		(8.5)	9.3

SI-Table 2: *Mobilized Mg and Si concentrations in µmolL^{-1} as a function of time (in h) in all treatments (ligand concentrations in mmol L^{-1}) at all pH values. SD indicates standard deviation (n = 2). Data with n.d. were not determined.*

Mg Blank [h]	pH 3.0	SD	pH 4.5	SD	pH 6.0	SD	pH 7.5	SD	pH 8.5	SD	pH 11.5	SD
0.5	552	144	344	61.7	186	2.0	105	0.1	55.0	6.1	Below LOQ	Below LOQ
1	451	22.1	305	84.2	331	110	145	20.7	71.4	2.4	Below LOQ	Below LOQ
2	611	49.2	376	13.2	285	34.1	172	17.4	73.8	1.2	Below LOQ	Below LOQ
4	657	103	455	29.5	443	29.9	386	64.9	140	64.5	Below LOQ	Below LOQ
8	726	85.3	525	32.0	508	89.9	333	61.5	146	45.3	Below LOQ	Below LOQ
24	852	83.4	629	68.0	616	113	425	26.6	172	12.9	Below LOQ	Below LOQ
48	1106	65.1	928	104	743	71.2	506	47.7	215	19.8	Below LOQ	Below LOQ
96	1077	81.9	936	53.4	744	142	539	138	211	4.2	Below LOQ	Below LOQ
168	1363	6.3	992	1.3	815	83.5	572	70.6	556	92.8	Below LOQ	Below LOQ
336	1995	195	1169	39.9	964	10.7	585	105	448	22.3	Below LOQ	Below LOQ

Si Blank [h]	pH 3.0	SD	pH 4.5	SD	pH 6.0	SD	pH 7.5	SD	pH 8.5	SD	pH 11.5	SD
0.5	10.6	0.7	14.0	0.1	10.3	0.0	5.5	0.2	9.4	0.6	17.5	0.0
1	11.6	1.1	16.1	0.2	12.8	0.7	6.8	1.0	8.8	0.7	9.0	0.1
2	17.3	0.3	16.2	1.4	11.4	0.0	6.8	0.1	7.5	1.1	7.8	0.9
4	24.1	2.0	18.8	0.5	13.2	0.3	7.5	0.5	11.4	4.9	8.4	0.3
8	40.9	0.5	32.4	1.1	23.0	0.3	10.7	0.4	10.1	1.3	6.1	0.3
24	76.9	1.5	68.3	0.1	42.5	1.9	11.4	0.1	10.0	0.1	13.0	0.2
48	128	18.4	104	1.4	57.7	6.4	14.2	0.6	9.5	0.5	16.7	0.4
96	163	5.4	150	7.4	99.5	1.3	15.9	1.2	9.2	1.5	15.1	1.4
168	256	12.8	199	4.9	146	12.1	19.1	1.0	10.4	0.8	7.9	0.5
336	437	17.4	305	30.1	194	0.8	15.4	0.7	8.5	0.2	9.4	0.2

Mg DFOB [h]	pH 3.0	SD	pH 4.5	SD	pH 6.0	SD	pH 7.5	SD	pH 8.5	SD	pH 11.5	SD
0.5	516	47.6	262	20.5	189	42.0	93.3	2.6	68.4	1.0	19.1	1.6
1	429	45.9	321	59.0	224	42.6	104	7.9	80.0	8.6	17.9	0.5
2	612	11.8	444	14.3	308	12.2	180	1.1	135	6.0	22.9	0.8
4	783	174	562	44.2	419	18.0	225	18.2	150	15.1	25.6	0.4
8	815	30.9	564	30.1	471	92.9	249	10.9	248	16.3	28.2	0.0
24	1650	169	1062	99.7	734	168	370	39.5	320	15.3	29.4	1.3
48	1807	311	1182	97.3	863	57.4	469	54.2	424	11.3	28.1	0.3
96	2333	157	1711	159	949	73.1	602	53.2	532	125	28.1	0.3
168	2936	279	1899	33.6	1236	122	514	12.0	492	41.6	28.8	0.3
336	3810	68.1	2896	53.5	1807	329	601	58.6	516	50.1	22.5	0.3

Si DFOB [h]	pH 3.0	SD	pH 4.5	SD	pH 6.0	SD	pH 7.5	SD	pH 8.5	SD	pH 11.5	SD
0.5	16.1	0.5	14.4	1.1	11.7	1.4	10.9	0.4	16.1	0.0	18.3	1.0
1	19.6	0.7	20.4	1.8	16.6	0.5	10.9	0.3	16.5	0.7	11.3	0.7
2	33.9	1.4	28.3	2.6	21.0	0.2	15.7	0.8	17.8	0.3	10.2	0.9
4	60.3	12.9	42.8	1.4	27.0	0.1	16.4	1.2	18.3	1.5	10.3	0.8
8	89.6	1.7	63.9	3.4	43.6	1.4	19.3	1.0	19.3	0.7	7.7	0.5
24	275	16.3	216	18.4	102	7.9	28.7	2.0	21.8	0.2	13.4	1.7
48	400	54.1	342	31.2	150	9.0	37.2	0.5	25.0	0.9	16.9	1.2
96	577	34.1	621	41.6	265	19.4	50.9	3.2	25.3	0.1	18.7	0.2
168	911	90.8	810	10.2	432	25.0	63.9	8.0	26.9	0.0	10.3	0.4
336	1266	38.4	1278	20.5	700	59.3	73.9	7.7	29.5	1.8	6.0	1.5

Mg Oxalat [h]	pH 3.0	SD	pH 4.5	SD	pH 6.0	SD	pH 7.5	SD	pH 8.5	SD	pH 11.5	SD
0.5	896	103	482	1.7	361	18.5	150	21.5	64.5	9.3	Below LOQ	Below LOQ
1	884	265	558	2.3	419	19.5	170	2.0	82.0	2.8	Below LOQ	Below LOQ
2	930	120	667	9.0	472	2.1	254	2.6	88.9	2.5	Below LOQ	Below LOQ
4	1075	35.7	804	5.9	586	24.2	309	34.6	114	2.1	Below LOQ	Below LOQ
8	1161	128	856	29.3	558	3.7	379	23.8	130	0.3	Below LOQ	Below LOQ
24	1739	67.4	1130	29.6	696	59.7	544	16.0	201	17.6	Below LOQ	Below LOQ
48	2091	140	1450	192	750	152	584	51.4	260	20.4	Below LOQ	Below LOQ
96	2498	67.1	1540	34.5	737	80.2	598	45.1	310	19.8	Below LOQ	Below LOQ
168	3048	137	1821	104	673	21.6	583	40.8	336	13.6	Below LOQ	Below LOQ
336	4157	369	2384	119	771	57.4	836	329	425	14.4	Below LOQ	Below LOQ

Si Oxalat [h]	pH 3.0	SD	pH 4.5	SD	pH 6.0	SD	pH 7.5	SD	pH 8.5	SD	pH 11.5	SD
0.5	20.7	1.9	18.5	1.0	10.6	0.5	10.7	0.8	18.4	0.1	18.5	0.4
1	26.0	3.2	21.9	0.4	9.3	0.1	10.1	1.0	16.6	0.2	10.0	0.5
2	32.7	6.2	32.1	0.6	12.2	0.4	10.1	0.0	17.2	0.5	9.8	0.0
4	51.6	5.1	53.4	0.2	12.3	0.3	11.1	1.4	16.8	0.3	8.5	0.0
8	73.6	6.0	82.7	2.0	16.8	0.1	10.9	1.1	15.6	1.0	6.6	0.0
24	161	6.3	184	2.0	21.8	1.7	11.5	0.4	15.6	0.9	12.1	0.3
48	264	22.5	287	22.7	26.4	1.3	12.5	0.6	14.6	0.4	16.4	0.0
96	392	5.5	442	20.1	32.2	0.5	11.5	0.0	13.3	0.3	17.0	0.9
168	574	28.3	599	11.5	35.7	0.0	12.5	0.6	12.1	0.3	7.2	1.1
336	925	71.3	835	24.5	56.0	7.5	12.1	1.3	11.5	0.7	6.6	0.4

Mg Citrate [h]	pH 3.0	SD	pH 4.5	SD	pH 6.0	SD	pH 7.5	SD	pH 8.5	SD	pH 11.5	SD
0.5	453	5.0	374	7.1	186	2.1	89.6	7.9	57.5	4.2	Below LOQ	Below LOQ
1	528	2.6	413	1.5	233	14.3	106	4.5	57.6	7.0	Below LOQ	Below LOQ
2	623	8.7	518	3.3	309	1.7	132	5.5	73.3	8.2	Below LOQ	Below LOQ
4	730	81.0	583	74.2	445	89.2	150	7.7	79.8	6.1	Below LOQ	Below LOQ
8	903	277	683	8.6	516	30.0	213	1.5	99.4	3.6	Below LOQ	Below LOQ
24	951	91.8	842	76.5	577	58.0	287	15.0	144	3.9	Below LOQ	Below LOQ
48	1078	32.8	969	54.0	762	1.4	434	11.5	265	9.8	Below LOQ	Below LOQ
96	1449	3.9	1251	65.0	809	63.4	483	21.9	265	30.0	Below LOQ	Below LOQ
168	1843	174	1532	116	967	58.6	497	12.0	324	11.7	Below LOQ	Below LOQ
336	2437	22.4	2099	45.4	1026	122	563	21.6	385	71.2	Below LOQ	Below LOQ

Si Citrate [h]	pH 3.0	SD	pH 4.5	SD	pH 6.0	SD	pH 7.5	SD	pH 8.5	SD	pH 11.5	SD
0.5	15.4	0.1	14.8	0.1	10.3	0.4	12.4	1.3	22.0	0.6	17.3	0.2
1	17.3	0.1	16.1	0.7	11.4	0.9	12.5	0.5	21.7	0.1	9.6	0.4
2	21.4	1.3	19.5	1.3	13.5	0.3	13.3	0.7	21.0	0.1	9.0	0.8
4	29.6	1.0	25.2	3.3	23.5	8.9	13.6	0.7	21.4	0.1	8.6	0.1
8	40.7	6.0	41.2	1.9	25.9	0.1	15.3	0.6	22.5	0.4	7.6	0.7
24	78.6	4.7	89.0	5.2	41.8	0.2	17.6	0.1	23.4	1.7	14.7	0.8
48	124	0.8	159	10.2	76.9	0.8	19.8	0.4	22.4	2.6	19.4	0.7
96	213	2.9	291	16.9	107	3.0	19.2	1.3	22.4	1.0	22.4	2.1
168	339	26.0	440	17.6	175	0.9	20.9	0.3	22.1	0.1	10.7	0.1
336	546	32.5	722	23.8	273	18.5	22.7	0.6	21.6	0.2	4.9	1.0

Mg HEDTA [h]	pH 3.0	SD	pH 4.5	SD	pH 6.0	SD	pH 7.5	SD	pH 8.5	SD	pH 11.5	SD
0.5	468	42.7	233	14.3	163	8.4	117	5.9	83.2	2.3	35.3	0.5
1	521	61.5	275	27.4	189	21.7	158	5.6	115	27.1	46.1	3.2
2	804	91.2	424	119	303	38.5	188	14.5	136	6.7	57.1	7.2
4	711	42.2	458	39.9	312	28.3	250	30.3	195	1.0	64.1	4.5
8	909	64.5	614	32.7	504	98.3	339	83.3	233	7.5	70.2	4.6
24	1347	26.6	934	119	830	20.3	465	34.8	389	21.8	100	0.9
48	1611	199	1111	120	859	18.1	523	50.9	452	23.5	110	17.3
96	1865	109	1469	33.8	1035	71.3	630	32.4	556	39.9	137	17.3
168	2451	30.9	2037	17.4	1071	36.1	551	45.4	543	39.5	142	1.4
336	3080	133	2394	38.4	1731	28.1	638	32.7	578	78.6	177	12.1

Si HEDTA [h]	pH 3.0	SD	pH 4.5	SD	pH 6.0	SD	pH 7.5	SD	pH 8.5	SD	pH 11.5	SD
0.5	23.0	0.0	19.7	1.4	14.2	0.3	16.8	1.7	28.3	1.3	19.3	0.9
1	26.5	0.3	21.5	1.2	15.3	1.6	18.6	0.4	28.7	0.9	17.0	1.3
2	38.1	0.2	31.3	5.4	21.7	3.0	20.6	1.3	30.5	0.4	17.2	0.2
4	50.9	2.0	42.2	3.1	26.3	2.3	24.2	2.3	31.9	0.2	20.5	0.1
8	84.5	0.8	71.9	3.7	55.2	5.2	28.6	2.4	34.6	2.1	20.3	0.1
24	192	11.2	181	13.2	139	4.7	38.9	0.4	38.5	2.4	21.3	0.3
48	295	26.5	294	18.9	142	5.4	47.2	0.2	41.3	0.1	27.1	0.0
96	432	11.5	501	2.6	249	9.2	63.8	0.9	44.0	0.5	26.5	0.0
168	629	17.2	770	19.8	369	17.3	80.4	0.8	47.7	1.2	19.2	0.1
336	894	14.5	1036	24.1	584	56.3	101	3.1	49.2	3.9	20.9	3.6

Mg HBED [h]	pH 3.0	SD	pH 4.5	SD	pH 6.0	SD	pH 7.5	SD	pH 8.5	SD	pH 11.5	SD
0.5	n.d.	n.d.	n.d.	n.d.	n.d.	n.d.	n.d.	n.d.	n.d.	n.d.	32.1	0.7
1	n.d.	n.d.	n.d.	n.d.	n.d.	n.d.	n.d.	n.d.	n.d.	n.d.	39.9	2.1
2	n.d.	n.d.	n.d.	n.d.	n.d.	n.d.	n.d.	n.d.	n.d.	n.d.	52.3	3.6
4	n.d.	n.d.	n.d.	n.d.	n.d.	n.d.	n.d.	n.d.	n.d.	n.d.	65.8	0.9
8	n.d.	n.d.	n.d.	n.d.	n.d.	n.d.	n.d.	n.d.	n.d.	n.d.	80.9	5.6
24	n.d.	n.d.	n.d.	n.d.	n.d.	n.d.	n.d.	n.d.	n.d.	n.d.	134	2.6
48	n.d.	n.d.	n.d.	n.d.	n.d.	n.d.	n.d.	n.d.	n.d.	n.d.	235	18.1
96	n.d.	n.d.	n.d.	n.d.	n.d.	n.d.	n.d.	n.d.	n.d.	n.d.	298	21.1
168	n.d.	n.d.	n.d.	n.d.	n.d.	n.d.	n.d.	n.d.	n.d.	n.d.	327	19.3
336	n.d.	n.d.	n.d.	n.d.	n.d.	n.d.	n.d.	n.d.	n.d.	n.d.	369	12.1

Si HBED [h]	pH 3.0	SD	pH 4.5	SD	pH 6.0	SD	pH 7.5	SD	pH 8.5	SD	pH 11.5	SD
0.5	n.d.	n.d.	n.d.	n.d.	n.d.	n.d.	n.d.	n.d.	n.d.	n.d.	16.6	0.3
1	n.d.	n.d.	n.d.	n.d.	n.d.	n.d.	n.d.	n.d.	n.d.	n.d.	14.8	0.3
2	n.d.	n.d.	n.d.	n.d.	n.d.	n.d.	n.d.	n.d.	n.d.	n.d.	10.0	0.1
4	n.d.	n.d.	n.d.	n.d.	n.d.	n.d.	n.d.	n.d.	n.d.	n.d.	11.1	0.5
8	n.d.	n.d.	n.d.	n.d.	n.d.	n.d.	n.d.	n.d.	n.d.	n.d.	13.1	0.2
24	n.d.	n.d.	n.d.	n.d.	n.d.	n.d.	n.d.	n.d.	n.d.	n.d.	23.0	0.0
48	n.d.	n.d.	n.d.	n.d.	n.d.	n.d.	n.d.	n.d.	n.d.	n.d.	11.7	1.8
96	n.d.	n.d.	n.d.	n.d.	n.d.	n.d.	n.d.	n.d.	n.d.	n.d.	14.7	0.6
168	n.d.	n.d.	n.d.	n.d.	n.d.	n.d.	n.d.	n.d.	n.d.	n.d.	34.8	1.9
336	n.d.	n.d.	n.d.	n.d.	n.d.	n.d.	n.d.	n.d.	n.d.	n.d.	32.7	0.7

SI-Table 3: *Dissolution experiment of chrysotile (fiber to solution ratio = 0.25) at pH=3.0 in blank and 1 mmol L^{-1} DFOB, oxalate and citrate treatments. Apart from the blank treatment, where Si and Mg dissolution rates were congruent, dissolution of chrysotile was not congruent in any ligand treatment. Congruency is expressed by the rate ratio of the Mg-rate divided by the Si-rate.*

	Mg	Si		Congruency (Rate ratio Mg/Si)
Blank	8.9	5.6	pmol $m^{-2}s^{-1}$	1.6
DFOB	25	12	pmol $m^{-2}s^{-1}$	2.1
Oxalate	41	12	pmol $m^{-2}s^{-1}$	3.4
Citrate	16	7	pmol $m^{-2}s^{-1}$	2.3

SI-Table 4: *Mobilized Fe concentrations in µmol L^{-1} in all treatments (ligand concentrations 1 mmol L^{-1}) at all pH values and incubation times. SD indicates standard deviations (n = 2).*

pH=3 [h]	Blank	SD	DFOB	SD	Oxalate	SD	Citrate	SD	HEDTA	SD
0.5	15.5	2.4	26.1	1.7	36.8	3.9	16.4	0.4	27.4	2.8
1	12.6	0.8	21.3	2.5	32.5	10.1	18.5	0.9	28.6	2.9
2	13.2	0.2	28.5	0.6	31.6	4.6	20.1	0.5	42.2	5.6
4	11.8	1.6	33.2	7.3	32.0	0.8	22.7	5.1	33.4	2.8
8	10.9	1.5	31.4	1.9	32.5	4.1	22.3	4.0	38.1	2.7
24	8.7	1.5	50.3	9.4	41.8	0.6	21.2	3.0	46.5	1.2
48	7.4	0.8	49.2	10.0	46.5	2.5	20.1	0.6	50.7	7.2
96	6.4	0.4	56.5	0.1	50.9	1.6	25.0	0.2	50.5	3.5
168	5.7	0.2	65.9	6.5	61.3	4.4	30.3	3.4	61.9	0.1
336	8.3	1.6	85.6	3.6	79.9	9.8	40.6	0.2	74.0	2.7

pH=4.5 [h]	Blank	SD	DFOB	SD	Oxalate	SD	Citrate	SD	HEDTA	SD
0.5	1.2	0.3	11.0	1.1	22.5	0.2	15.8	0.7	17.3	0.6
1	0.9	0.0	15.5	2.6	24.0	0.3	16.9	0.4	19.6	1.9
2	0.8	0.2	22.0	1.0	26.6	0.1	19.2	0.4	28.5	8.0
4	1.2	0.2	28.2	0.5	29.7	0.3	20.0	2.0	27.4	2.3
8	0.7	0.3	25.9	0.7	28.8	1.3	21.6	0.9	32.3	2.2
24	0.7	0.2	36.9	1.7	29.4	0.0	21.3	2.6	39.2	5.9
48	0.9	0.3	37.4	4.4	31.0	1.1	21.8	1.7	40.2	5.1
96	1.2	0.4	46.5	3.0	33.1	0.6	25.1	0.8	43.3	0.7
168	1.2	0.1	46.4	1.3	36.0	1.1	27.6	1.6	55.4	0.3
336	0.8	0.8	69.5	3.1	39.4	1.9	38.1	4.1	58.9	0.9

pH=6 [h]	Blank	SD	DFOB	SD	Oxalate	SD	Citrate	SD	HEDTA	SD
0.5	0.1	0.0	5.8	1.3	11.8	0.0	6.3	0.1	11.8	0.9
1	0.3	0.1	8.9	1.7	12.4	0.5	8.8	0.3	14.6	1.8
2	0.0	0.1	14.0	0.4	12.7	0.1	12.2	0.3	23.4	2.9
4	0.4	0.2	19.4	0.8	12.9	0.4	14.8	2.0	22.0	2.0
8	0.1	0.1	21.9	4.3	12.0	0.5	15.9	0.6	28.4	6.5
24	0.2	0.0	32.4	6.3	9.8	0.2	15.3	1.4	38.3	1.7
48	0.1	0.1	35.3	2.3	8.8	0.5	18.0	0.3	37.6	2.1
96	0.1	0.0	33.8	3.6	6.9	0.5	16.4	1.5	41.6	4.3
168	0.0	0.0	40.7	4.4	5.4	0.3	16.5	0.7	37.3	1.6
336	0.0	0.1	51.8	11.2	3.4	0.2	15.4	2.4	51.5	4.7

pH=7.5 [h]	Blank	SD	DFOB	SD	Oxalate	SD	Citrate	SD	HEDTA	SD
0.5	0.2	0.0	4.1	0.3	0.1	0.1	1.9	0.3	8.3	0.2
1	0.0	0.0	5.7	0.4	0.1	0.0	2.7	0.2	12.1	0.5
2	0.1	0.1	10.6	0.0	0.1	0.1	4.5	0.4	14.7	1.5
4	0.1	0.1	13.7	1.2	0.0	0.1	5.0	0.4	18.3	2.0
8	0.1	0.0	15.1	1.5	0.1	0.0	7.0	0.4	23.4	5.6
24	0.0	0.1	22.6	2.4	0.1	0.1	8.6	0.1	28.3	1.9
48	0.1	0.0	27.5	3.8	0.1	0.1	10.6	0.3	30.1	2.4
96	0.1	0.1	32.4	4.1	0.1	0.0	9.9	0.5	35.5	1.1
168	0.0	0.0	27.3	0.1	0.2	0.2	9.6	0.2	30.3	2.2
336	0.9	0.0	29.3	0.2	0.1	0.1	9.3	0.5	32.4	0.5

pH=8.5 [h]	Blank	SD	DFOB	SD	Oxalate	SD	Citrate	SD	HEDTA	SD
0.5	0.1	0.1	3.6	0.0	0.1	0.1	0.6	0.1	5.3	0.2
1	0.0	0.1	5.6	0.9	0.0	0.1	0.8	0.1	7.9	1.7
2	0.0	0.0	9.5	0.4	0.1	0.1	1.3	0.2	9.7	0.5
4	0.2	0.2	10.9	1.0	0.1	0.1	1.5	0.0	14.1	0.1
8	0.0	0.0	17.9	1.0	0.1	0.1	1.8	0.2	16.5	0.5
24	0.0	0.0	21.6	1.0	0.0	0.0	2.6	0.1	25.2	1.7
48	0.0	0.1	26.3	2.2	0.0	0.0	4.2	0.2	27.8	0.5
96	0.0	0.0	30.7	5.2	0.0	0.1	4.2	0.0	33.3	2.0
168	0.0	0.0	27.4	0.9	0.1	0.1	4.5	0.1	31.9	1.5
336	0.1	0.1	30.5	3.2	0.1	0.0	4.4	0.6	33.3	4.2

pH=11.5 [h]	Blank	SD	DFOB	SD	Oxalate	SD	Citrate	SD	HEDTA	SD	Blank	SD
0.5	0.1	0.1	0.4	0.0	0.0	0.0	Below LOQ	Below LOQ	1.1	0.0	1.4	0.2
1	0.1	0.1	0.4	0.0	0.0	0.0	Below LOQ	Below LOQ	1.6	0.1	2.1	0.0
2	0.0	0.1	0.7	0.2	0.1	0.1	Below LOQ	Below LOQ	2.6	0.4	3.5	0.5
4	0.0	0.1	0.9	0.0	0.0	0.0	Below LOQ	Below LOQ	3.6	0.3	5.0	0.2
8	0.0	0.1	1.0	0.2	0.1	0.0	Below LOQ	Below LOQ	4.4	0.4	6.7	0.6
24	0.0	0.1	0.8	0.2	0.1	0.0	Below LOQ	Below LOQ	6.9	0.0	11.9	0.1
48	0.1	0.1	0.6	0.1	0.0	0.0	Below LOQ	Below LOQ	8.1	1.0	20.0	1.8
96	0.1	0.0	0.7	0.1	0.0	0.1	Below LOQ	Below LOQ	10.1	1.0	24.5	1.7
168	0.0	0.1	0.3	0.0	0.1	0.0	Below LOQ	Below LOQ	10.6	0.1	26.3	1.7
336	0.0	0.1	Below LOQ	0.1	0.1	0.0	Below LOQ	Below LOQ	13.0	1.1	28.2	0.7

SI-Table 5: *Mobilized Al concentrations in µmol L^{-1} in all treatments (ligand concentrations 1 mmol L^{-1}) at all pH values and incubation times. SD indicates standard deviation (n = 2).*

pH=3 [h]	Blank	SD	DFOB	SD	Oxalate	SD	Citrate	SD	HEDTA	SD
0.5	4.8	1.9	4.9	0.3	6.6	0.3	4.9	0.2	6.4	0.3
1	4.2	0.4	2.4	0.2	6.4	2.2	4.5	0.6	6.4	1.1
2	5.5	1.6	3.3	3.5	6.5	1.2	5.8	0.8	7.4	1.3
4	6.2	1.0	6.4	2.8	6.2	0.4	6.7	0.8	8.4	1.4
8	7.2	0.4	5.2	0.9	7.4	0.2	5.6	0.7	9.8	0.2
24	6.9	1.8	13.7	3.0	11.9	0.9	7.0	0.4	12.0	0.7
48	9.7	0.3	15.4	2.3	15.7	0.2	7.8	1.7	14.2	0.6
96	9.9	1.5	17.7	3.2	21.8	0.3	10.2	0.7	17.4	1.4
168	11.2	0.3	34.6	7.9	29.7	0.9	14.0	1.5	24.0	0.7
336	18.1	3.4	50.0	3.2	44.9	3.1	17.5	2.9	32.7	0.4

pH=4.5 [h]	Blank	SD	DFOB	SD	Oxalate	SD	Citrate	SD	HEDTA	SD
0.5	2.5	0.3	1.1	0.0	3.3	0.5	3.8	0.5	4.1	0.5
1	3.1	0.9	1.8	0.2	5.0	1.2	4.4	0.4	5.2	0.1
2	3.2	0.0	3.1	0.3	3.8	0.3	4.0	0.2	6.3	0.8
4	3.0	0.5	2.2	3.4	5.5	0.1	4.3	0.5	6.5	1.8
8	3.3	0.1	3.4	1.9	5.5	0.0	3.5	0.0	7.4	0.6
24	4.1	0.1	7.8	0.3	7.7	0.0	5.9	1.7	8.8	0.6
48	4.1	0.3	8.3	1.8	8.6	1.6	6.3	0.6	10.5	0.7
96	3.3	0.6	12.6	3.3	9.6	0.3	8.4	0.6	12.3	0.6
168	2.4	0.2	17.4	1.3	12.6	0.2	9.5	0.2	16.5	0.3
336	1.3	0.8	30.9	2.5	15.2	0.5	14.2	0.3	21.3	0.6

pH=6 [h]	Blank	SD	DFOB	SD	Oxalate	SD	Citrate	SD	HEDTA	SD
0.5	1.1	0.5	Below LOQ	Below LOQ	1.4	0.1	2.1	0.6	3.1	0.3
1	0.0	1.3	Below LOQ	Below LOQ	1.2	0.6	2.4	0.6	3.8	0.4
2	0.8	0.2	Below LOQ	Below LOQ	2.5	0.0	3.3	0.2	3.1	0.0
4	1.0	0.2	0.4	0.4	2.7	1.0	3.7	0.5	3.7	0.3
8	0.7	1.1	1.8	1.1	3.0	0.9	3.2	1.8	5.3	1.4
24	0.4	0.2	3.1	0.2	3.8	0.7	4.0	1.0	6.8	0.4
48	0.5	0.3	3.3	1.4	3.7	1.1	3.9	0.0	7.9	0.4
96	1.1	0.6	5.0	0.8	2.2	1.0	5.1	0.6	8.1	0.3
168	0.9	1.1	8.5	2.0	4.8	0.8	5.1	0.2	9.2	0.5
336	1.4	0.1	15.2	2.5	3.1	1.6	7.6	0.7	11.4	0.8

pH=7.5 [h]	Blank	SD	DFOB	SD	Oxalate	SD	Citrate	SD	HEDTA	SD
0.5	0.4	0.1	Below LOQ	Below LOQ	Below LOQ	Below LOQ	0.7	0.7	3.3	0.7
1	Below LOQ	0.4	Below LOQ	Below LOQ	Below LOQ	Below LOQ	1.3	0.4	3.1	0.2
2	0.0	0.8	Below LOQ	Below LOQ	Below LOQ	Below LOQ	1.9	0.6	3.9	0.2
4	Below LOQ	0.5	Below LOQ	Below LOQ	Below LOQ	Below LOQ	1.4	0.7	3.6	0.3
8	0.7	0.4	1.2	0.2	Below LOQ	Below LOQ	2.8	1.0	3.5	0.1
24	0.4	1.4	2.5	1.0	Below LOQ	Below LOQ	2.4	0.3	4.3	1.6
48	0.5	0.5	1.1	0.3	Below LOQ	Below LOQ	2.8	0.1	5.1	0.5
96	1.4	0.7	3.6	2.0	Below LOQ	Below LOQ	2.1	0.9	5.7	2.0
168	0.0	0.0	4.5	1.0	Below LOQ	Below LOQ	3.9	0.1	5.5	0.2
336	1.4	0.4	2.5	0.1	Below LOQ	Below LOQ	2.5	0.7	6.2	0.6

pH=8.5 [h]	Blank	SD	DFOB	SD	Oxalate	SD	Citrate	SD	HEDTA	SD
0.5	0.3	1.1	Below LOQ	Below LOQ	Below LOQ	Below LOQ	1.4	0.2	3.1	0.3
1	1.4	0.2	Below LOQ	Below LOQ	Below LOQ	Below LOQ	0.7	0.3	3.2	0.3
2	Below LOQ	Below LOQ	1.2	0.5	Below LOQ	Below LOQ	1.4	0.6	3.8	0.8
4	0.7	0.0	Below LOQ	Below LOQ	Below LOQ	Below LOQ	1.5	0.3	3.8	1.3
8	1.1	0.5	0.4	0.4	Below LOQ	Below LOQ	1.1	0.6	3.6	0.6
24	0.6	0.6	2.4	0.4	Below LOQ	Below LOQ	0.4	0.1	4.2	1.0
48	0.9	0.8	2.9	0.6	Below LOQ	Below LOQ	1.5	0.6	5.1	0.8
96	1.1	0.2	2.1	2.3	Below LOQ	Below LOQ	1.1	1.3	3.8	1.1
168	0.8	0.9	3.5	1.3	Below LOQ	Below LOQ	1.8	0.2	3.2	0.0
336	0.5	1.1	3.6	0.9	Below LOQ	Below LOQ	1.8	0.1	3.4	0.3

pH=11.5 [h]	Blank	SD	DFOB	SD	Oxalate	SD	Citrate	SD	HEDTA	SD	HBED	SD
0.5	1.2	0.0	Below LOQ	Below LOQ	Below LOQ	Below LOQ	0.7	0.1	2.1	1.1	3.2	0.6
1	0.4	1.0	Below LOQ	Below LOQ	Below LOQ	Below LOQ	1.2	0.7	0.8	0.8	3.0	0.6
2	0.3	0.7	Below LOQ	Below LOQ	Below LOQ	Below LOQ	0.4	0.4	1.1	2.7	2.9	1.0
4	0.7	0.4	Below LOQ	Below LOQ	Below LOQ	Below LOQ	1.2	0.2	1.5	0.4	2.9	0.1
8	1.3	0.3	Below LOQ	Below LOQ	Below LOQ	Below LOQ	0.8	0.6	2.5	0.3	2.6	1.1
24	0.5	0.8	Below LOQ	Below LOQ	Below LOQ	Below LOQ	0.1	0.2	2.6	0.3	3.8	1.2
48	1.0	1.1	Below LOQ	Below LOQ	Below LOQ	Below LOQ	1.0	0.4	2.0	0.2	5.4	2.0
96	1.2	1.8	Below LOQ	Below LOQ	Below LOQ	Below LOQ	1.1	0.4	2.6	0.2	5.0	0.8
168	0.5	0.5	Below LOQ	Below LOQ	Below LOQ	Below LOQ	1.2	0.4	1.4	0.7	6.2	1.1
336	0.9	1.1	Below LOQ	Below LOQ	Below LOQ	Below LOQ	0.3	1.2	2.0	1.5	5.2	0.4

SI-Table 6: *Mössbauer hyperfine parameters of pristine and pH 3.0 blank and 1 mmol L^{-1} DFOB altered fibers. eQVzz/4 refers to quadrupole splitting, CS to the center shift relative to ^{57}Co**Rh**, and Γ to the line widths. Two fits of blank altered fibers are presented: One without and one without ferrihydrite (FH).*

		B_{hf}	B_{hf}	$eQV_{zz}/4$	CS	Γ/2	Area
Pristine		mm/s	kG	mm/s	mm/s	mm/s	%
S1	Fe^{II}[6]			1.29	1.05	0.22	26
S2	Fe^{III}[6]			0.33	0.19	0.38	37
S3	FeI^{II}[4]			0.22	0.09	0.3	5
S4	Fe_3O_4_1	15.84	493		0.17	0.25	18
S5	Fe_3O_4_2	14.62	455		0.52	0.25	14
DFOB							
S1	Fe^{II}[6]			1.29	1.05	0.22	26
S2	Fe^{III}[6]			0.33	0.19	0.38	37
S3	Fe^{III}[4]			0.22	0.09	0.3	5
S4	Fe_3O_4_1	15.84	493		0.17	0.25	18
S5	Fe_3O_4_2	14.62	455		0.52	0.25	14
Blank without FH („original species“)							
Fe^{II}[6]	Fe^{II}[6]			1.29	1.05	0.22	22
Fe^{III}[6]	Fe^{III}[6]			0.33	0.19	0.38	47
Fe^{III}[4]	Fe^{III}[4]			0.22	0.09	0.3	4
Fe_3O_4_1	Fe_3O_4_1	15.84	493		0.17	0.25	14
Fe_3O_4_2	Fe_3O_4_2	14.62	455		0.52	0.25	12
Blank with FH							
S1	Fe^{II}[6]			1.29	1.05	0.22	22
S2	Fe^{III}[6]			0.33	0.19	0.38	41
S3	Fe^{III}[4]			0.22	0.09	0.3	4
S4	Fe_3O_4_1	15.84	493		0.17	0.25	15
S5	Fe_3O_4_2	14.62	455		0.52	0.25	12
S6	Ferrihydrite			0.355	0.23	0.228	6

SI-Table 7: *Calculation of the estimated available amount of Fe for ferrihydrite precipitation during weathering at pH 3.0 in a blank treatment. Elemental concentrations were measured in solution after fiber alteration for 336 h at pH=3.0 in blank treatments for preparing Mössbauer specimens (SI-Table 8). The total amount of available Fe for precipitation in the blank treatment at pH=3.0 was estimated by multiplying the mobilized Fe concentration in the corresponding DFOB treatment with the ratio of the mobilized Si concentrations of the blank and the DFOB treatments, under the assumption that Fe is homogenously distributed in the fiber. The calculated amount of Fe available for ferrihydrite precipitation was 28.8 µmol L^{-1}, whereas the ferrihydrite fraction in the pH 3.0 blank altered fibers by the Mössbauer analysis calculated 23.2 µmol L^{-1}. Both results have a clear degree of uncertainty, therefore the same order of magnitude constitutes a satisfying match.*

Calculating the available amount of Fe for ferrihydrite-precipitation in a pH=3.0 blank solution (336h)		
68	% of Bulk-Fe in chrysotile (Mössbauer measurements)	
0.68		
454	µmol L^{-1} Si mobilized in pH=3.0 blank alteration	
1266	µmol L^{-1} Si mobilized in DFOB alteration	
96.2	Fe in DFOB, multiply times (Si_{blank}/Si_{DFOB})-ratio	
34.5	µmol L^{-1} Fe probably mobilized in pH=3.0 blank	
5.7	µmol L^{-1} Fe mobilized during alteration	
28.8	**µmol L^{-1} of Fe calculated to be available at pH=3.0 for ferrihydrite precipitation**	
6.4	% of Fe in ferrihydrite (Mössbauer analysis)	
0.064		
Total Fe content	Fe:	M(Fe) = 55.845 g/mol
19.0	g kg^{-1} measured in fusion digestion	
21.5	g kg^{-1} measured in NAA	
20.3	g kg^{-1} (mean from digestion and NAA)	
0.363	mmol L^{-1} bulk-Fe in chrysotile per gram	
0.023	mmol L^{-1} bulk-Fe in ferrihydrite per gram	
23.2	**µmol L^{-1} calculated in ferrihydrite**	

SI-Table 8: *Mobilized Fe, Mg, Si and Al concentrations in µmol L^{-1} after 336 h of interaction between chrysotile material and solutions containing 1 mmol L^{-1} ligand. Weathered chrysotile samples were used for EPR and Mössbauer experiments. SD indicates standard deviation (n = 2).*

	Blank EPR alteration 336h							
pH	Fe	SD	Mg	SD	Si	SD	Al	SD
3.0	6.4	1.6	1509	67.8	305	10.2	14.6	0.2
4.5	0.6	0.2	1099	71.0	214	0.4	2.9	0.9
6.0	Below LOQ	Below LOQ	895	32.3	135	4.6	1.5	1.3
7.5	Below LOQ	Below LOQ	592	11.0	16.7	0.9	2.1	0.4
8.5	Below LOQ	Below LOQ	357	58.5	6.8	0.3	2.0	0.2
11.5	Below LOQ	Below LOQ	5.1	0.0	9.3	0.0	1.5	0.0

	DFOB EPR alteration 336h							
pH	Fe	SD	Mg	SD	Si	SD	Al	SD
3.0	86.6	0.7	3574	4.0	1136	2.9	41.0	0.8
4.5	60.1	2.8	2516	43.3	1122	4.7	24.9	0.9
6.0	46.2	3.0	1626	102	633	17.4	14.1	0.1
7.5	41.3	2.8	778	24.8	93.2	1.1	8.2	0.5
8.5	33.7	4.6	580	56.5	24.1	0.2	5.8	0.5
11.5	0.3	0.0	15.8	0.8	10.1	0.6	2.0	0.1

	Oxalate EPR alteration 336h							
pH	Fe	SD	Mg	SD	Si	SD	Al	SD
3.0	88.7	1.1	3791	65.4	865	0.1	51.2	0.7
4.5	51.7	0.8	2251	24.7	860	28.4	22.9	0.9
6.0	5.8	0.7	723	49.8	65.7	2.3	7.9	0.1
7.5	Below LOQ	Below LOQ	623	0.6	13.4	0.8	1.6	1.0
8.5	Below LOQ	Below LOQ	513	18.1	7.0	0.7	1.3	0.1
11.5	Below LOQ	Below LOQ	5.3	0.4	8.1	0.5	1.3	0.4

	Citrate EPR alteration 336h							
pH	Fe	SD	Mg	SD	Si	SD	Al	SD
3.0	43.8	1.5	2251	25.8	494	7.1	22.4	0.7
4.5	41.8	1.1	2021	8.4	713	25.1	17.6	0.9
6.0	28.5	9.6	1522	478	291	48.7	10.5	1.0
7.5	15.1	1.8	773	137	25.6	1.2	6.2	0.3
8.5	7.7	1.7	465	65.5	10.4	0.1	3.3	0.6
11.5	Below LOQ	Below LOQ	7.5	0.8	13.4	0.5	1.4	1.0

	HBED EPR alteration 336h							
pH	Fe	SD	Mg	SD	Si	SD	Al	SD
11.5	31.4	0.7	420	18.0	45.2	3.9	3.7	1.0

	EPR-kinetic experiment							
	Fe	SD	Mg	SD	Si	SD	Al	SD
pH=7.5 Blank 0.5h	0.4	0.5	109	2.1	2.8	0.0	2.9	0.4
pH=7.5 Blank 2h	Below LOQ	Below LOQ	164	19.9	4.5	0.2	1.9	0.3
pH=7.5 Blank8h	1.1	1.7	340	33.1	7.0	1.2	2.7	0.3
pH=7.5 Blank 24h	Below LOQ	Below LOQ	528	31.9	9.5	0.2	3.0	0.6
pH=7.5 Blank 48h	Below LOQ	Below LOQ	490	17.2	12.1	2.3	2.8	0.2
pH=7.5 DFOB 0.5h	4.8	0.4	113	2.5	6.3	1.6	3.4	0.5
pH=7.5 DFOB 2h	10.3	0.3	183	7.3	10.3	0.3	3.1	0.3
pH=7.5 DFOB 8h	22.0	2.8	375	45.2	19.4	0.9	4.5	0.2
pH=7.5 DFOB24h	28.3	1.8	506	30.7	30.3	0.7	5.7	0.5
pH=7.5 DFOB 48h	29.5	0.2	536	18.0	41.5	3.7	6.3	0.7

	pH=3.0 blank and DFOB alteration Mössbauer experiments							
treatment	Fe	SD	Mg	SD	Si	SD	Al	SD
pH=3.0 DFOB	96.2	2.0	4031	97.8	1399	37.6	53.5	2.2
pH=3.0 blank	5.7	0.4	1771	66.6	454	7.4	18.4	1.1

SI-Table 9: *HRFPs in % (relative to unaltered fibers) of fibers altered in blank and 1 mmol L^{-1} DFOB, oxalate, citrate and HBED treatments for 336 h at various pH values. SD indicates standard deviations (n = 4). Data with n.d. were not determined.*

pH	Blank	SD	DFOB	SD	Oxalate	SD	Citrate	SD	HBED	SD
3.0	31.5	3.5	17.1	2.8	32.6	2.6	38.0	2.5	n.d.	n.d.
4.5	50.3	5.3	16.8	2.8	25.8	2.9	41.5	3.3	n.d.	n.d.
6.0	40.7	3.7	12.2	2.7	32.4	3.6	41.5	6.1	n.d.	n.d.
7.5	60.3	2.9	8.7	2.7	57.9	3.1	76.6	4.2	n.d.	n.d.
8.5	79.6	8.3	16.5	2.9	75.7	6.1	98.1	5.2	n.d.	n.d.
11.5	103	10.7	87.6	7.5	105	6.5	112	5.6	21.9	3.9

SI-Table 10: *HRFPs in % (relative to unaltered fibers) of fibers altered in blank and 1 mmol L^{-1} DFOB treatments for 0.5, 2, 8, 24, 48 and 336 h at different pH 7.5. SD indicates standard deviations (n = 4).*

pH	DFOB	SD	Blank	SD
0.5	53.7	5.2	76.5	7.3
2	41.6	6.1	75.6	7.4
8	31.6	3.2	56.9	5.6
24	25.0	3.1	51.6	5.4
48	17.7	2.3	53.4	7.5
336	8.5	2.6	60.3	2.9

Supporting Information to Chapter 2

"Identifying the reactive sites of hydrogen peroxide decomposition and hydroxyl radical formation on chrysotile asbestos surfaces"

Supporting information to the data material presented on page 54 to 76.

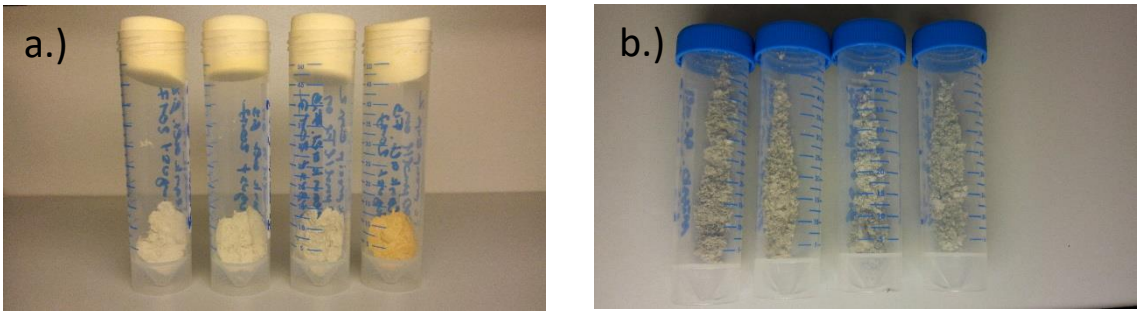

SI-Figure 1.) Alteration of fibers and the resulting colors. Panel a.) From left to right: Blank altered fibers 0 µmol g^{-1} Fe, blank altered fibers 3 µmol g^{-1} Fe, blank altered fibers 30 µmol g^{-1} Fe and blank altered fibers 300 µmol g^{-1} Fe; Panel b.) Fiber preparation for Mössbauer analyses, from left to right: Blank altered fibers 3 µmol g^{-1} ^{57}Fe, blank altered fibers 0 µmol g^{-1} ^{57}Fe, DFOB altered fibers 0 µmol g^{-1} ^{57}Fe, blank altered fibers 3 µmol g^{-1} ^{57}Fe.

SI-Table 1: *Mobilized Mg, Si and Fe concentrations in µmol L^{-1} during pretreatment (no duplicates available). Fibers were pretreated at pH 7.4 for 336 h without further additions (blank) and with 1 mmol L^{-1} DFOB (required for H_2O_2 decomposition, $HO^{\bullet}$ generation experiments and Mössbauer experiments), or for 24 hours under magnetic stirring with addition of Fe.*

Fiber pretreatment	**Mg**	**Si (µmol L^{-1})**	**Fe**
336 h pH=7.4 blank pretreatment: H_2O_2 decomp + $HO^{\bullet}$ gen Exp.	530	13.2	0.0
336 h pH=7.4 DFOB pretreatment: H_2O_2 decomp + $HO^{\bullet}$ gen Exp.	604	80.9	28.5
24 h Fe addition DFOB-alt. fib: H_2O_2 decomp + $HO^{\bullet}$ gen Exp. 0 µmol L^{-1} Fe	97.2	54.2	0.7
24 h Fe addition DFOB-alt. fib: H_2O_2 decomp + $HO^{\bullet}$ gen Exp. 3 µmol L^{-1} Fe	62.7	53.1	0.4
24 h Fe addition DFOB-alt. fib: H_2O_2 decomp + $HO^{\bullet}$ gen Exp. 30 µmol L^{-1} Fe	54.5	27.0	0.4
24 h Fe addition DFOB-alt. fib: H_2O_2 decomp + $HO^{\bullet}$ gen Exp. 300 µmol L^{-1} Fe	86.7	46.2	0.4
24 h Fe addition blank-alt. fib: H_2O_2 decomp + $HO^{\bullet}$ gen Exp. 0 µmol L^{-1} Fe	20.5	22.5	0.0
24 h Fe addition blank-alt. fib: H_2O_2 decomp + $HO^{\bullet}$ gen Exp. 3 µmol L^{-1} Fe	16.3	22.6	0.0
24 h Fe addition blank-alt. fib: H_2O_2 decomp + $HO^{\bullet}$ gen Exp. 30 µmol L^{-1} Fe	39.3	43.8	0.0
24 h Fe addition blank-alt. fib: H_2O_2 decomp + $HO^{\bullet}$ gen Exp. 300 µmol L^{-1} Fe	13.4	28.2	0.0
336 h pH=7.4 blank pretreatment: Mössbauer Exp.	533	11.3	0.1
336 h pH=7.4 DFOB pretreatment: Mössbauer Exp.	684	84.1	31.6
24 h Fe addition DFOB-alt. fib: Mössbauer Exp. 0 µmol L^{-1} Fe	111	77.6	1.1
24 h Fe addition DFOB-alt. fib: Mössbauer Exp. 3 µmol L^{-1} Fe	91.4	66.9	1.5
24 h Fe addition blank-alt. fib: Mössbauer Exp. 0 µmol L^{-1} Fe	31.0	55.7	0.3
24 h Fe addition blank-alt. fib: Mössbauer Exp. 3 µmol L^{-1} Fe	28.6	16.4	0.3

SI-Table 2: *Mössbauer hyperfine parameters of DFOB and blank altered fibers with 0 or 3 µmol g^{-1} ^{57}Fe precipitated on the fiber surface, analyzed in the narrow (Table a) and wide (Table b) velocity range. The spectra of Figure b in the main text were created out of data from the wide velocity range. The magnetite content in the narrow velocity range was not accordingly measured over the whole relevant velocity range, thus magnetite intensities should only be taken from the wide velocity range. B_{hf} refers to the magnetic hyperfine splitting, eQVzz/4 to the quadrupole splitting, CS to the chemical shift rel. to ^{57}Co**Rh**, and Γ to the line widths.*

Table a: Narrow velocity range:

Specimen	#	Fe species	B_{hf} mm/s	$eQV_{zz}/4$ mm/s	CS mm/s	Γ/2 mm/s	Area %
	1	Fe^{2+}[6]	0	1.181	1.172	0.191	16.2
Blank altered fibers	2	Fe^{3+}[6]	0	0.412	0.196	0.301	68.4
0 µmol g^{-1} ^{57}Fe	3	Fe^{3+}[4]	0	0.237	0.091	0.222	5.25
Narrow $\vec{v}$ range	4	Fe_3O_4_1	15.84	-0.009	0.171	0.191	4.98
	5	Fe_3O_4_1	14.62	0.052	0.53	0.225	5.24
	6	Ferrihydrite	0	0.355	0.23	0.228	7.9
	1	Fe^{2+}[6]	0	1.272	1.079	0.194	19.1
Blank altered fibers	2	Fe^{3+}[6]	0	0.379	0.183	0.289	54.3
3 µmol g^{-1} ^{57}Fe	3	Fe^{3+}[4]	0	0.21	0.089	0.218	4.37
Narrow $\vec{v}$ range	4	Fe_3O_4_1	15.94	-0.009	0.171	0.25	7.36
	5	Fe_3O_4_2	14.77	0.052	0.53	0.28	6.71
	6	Ferrihydrite	0	0.355	0.219	0.222	8.13
	1	Fe^{3+}[6]	0	1.271	1.07	0.168	25.3
DFOB altered fibers	2	Fe^{3+}[6]	0	0.385	0.172	0.317	53.4
0 µmol g^{-1} ^{57}Fe	3	Fe^{3+}[4]	0	0.219	0.078	0.266	3.13
Narrow $\vec{v}$ range	4	Fe_3O_4_1	15.91	-0.045	0.169	0.247	10.0
	5	Fe_3O_4_2	14.71	0.028	0.516	0.248	8.18
	1	Fe^{2+}[6]	0	1.27	1.082	0.169	15.8
Blank altered fibers	2	Fe^{3+}[6]	0	0.361	0.186	0.359	60.5
3 µmol g^{-1} ^{57}Fe	3	Fe^{3+}[4]	0	0.236	0.091	0.271	5.28
Narrow $\vec{v}$ range	4	Fe_3O_4_1	15.84	0	0.167	0.24	8.1
	5	Fe_3O_4_2	14.62	0	0.505	0.245	7.19
	6	Ferrihydrite	0	0.347	0.231	0.223	3.14

Table b: Wide velocity range:

Specimen	#	Fe species	B_{hf} mm/s	$eQV_{zz}/4$ mm/s	CS mm/s	Γ/2 mm/s	Area %
	1	Fe^{2+}[6]	0	1.279	1.02	0.199	14.2
Blank altered fibers	2	Fe^{3+}[6]	0	0.386	0.173	0.317	49.8
0 µmol g^{-1} ^{57}Fe	3	Fe^{3+}[4]	0	0.205	0.087	0.226	3.92
Wide $\vec{v}$ range	4	Fe_3O_4_1	15.935	-0.009	0.17	0.186	13.1
	5	Fe_3O_4_1	14.773	0.053	0.523	0.233	12.3
	6	Ferrihydrite	0	0.358	0.224	0.231	6.76
	1	Fe^{2+}[6]	0	1.285	1.007	0.203	15.7
Blank altered fibers	2	Fe^{3+}[6]	0	0.38	0.172	0.314	40.1
3 µmol g^{-1} ^{57}Fe	3	Fe^{3+}[4]	0	0.202	0.087	0.226	3.26
Wide $\vec{v}$ range	4	Fe_3O_4_1	15.87	-0.009	0.171	0.246	19.8
	5	Fe_3O_4_2	14.8	0.052	0.53	0.272	15.1
	6	Ferrihydrite	0	0.354	0.23	0.219	6.08
	1	Fe^{3+}[6]	0	1.301	1.021	0.182	19.7
DFOB altered fibers	2	Fe^{3+}[6]	0	0.384	0.171	0.326	34.0
0 µmol g^{-1} ^{57}Fe	3	Fe^{3+}[4]	0	0.216	0.08	0.274	2.18
Wide $\vec{v}$ range	4	Fe_3O_4_1	15.91	-0.045	0.169	0.247	24.4
	5	Fe_3O_4_2	14.71	0.028	0.516	0.248	16.7
	1	Fe^{2+}[6]	0	1.292	1.027	0.181	15.1
Blank altered fibers	2	Fe^{3+}[6]	0	0.35	0.171	0.396	41.1
3 µmol g^{-1} ^{57}Fe	3	Fe^{3+}[4]	0	0.22	0.088	0.279	3.66
Wide $\vec{v}$ range	4	Fe_3O_4_1	15.84	0	0.167	0.24	22.1
	5	Fe_3O_4_2	14.62	0	0.505	0.245	16.2
	6	Ferrihydrite	0	0.347	0.231	0.223	1.96

SI-Table 3: *Mobilized Mg and Si concentrations from 1 g L^{-1} pristine and altered fibers incubated atpH=7.4 (50 mM MOPS) with addition of 3.34 g L^{-1} H_2O_2 (Data is plotted in Figure 3 in the main text; SD = standard deviation with n = 2).*

Panel a1: Mg.)

Time [h]	Pristine fibers (µmol L^{-1})	SD	Blank-altered fibers (µmol L^{-1})	SD	DFOB-altered fibers (µmol L^{-1})	SD
0,5	82.1	4.9	2.9	0.0	9.5	2.3
1	97.9	6.7	3.2	0.4	8.7	0.4
4	150	14.6	4.8	0.4	15.8	0.9
8	199	21.9	7.9	0.6	20.0	0.8
24	332	24.9	13.5	0.2	38.0	0.7
48	437	25.4	20.6	0.2	51.4	0.5
96	511	39.3	32.9	1.4	95.9	4.7
168	614	28.2	47.8	1.2	137	4.1
336	602	18.9	91.3	6.6	229	13.0

Panel a2: Si.)

Time [h]	Pristine fibers (µmol L^{-1})	SD	Blank-altered fibers (µmol L^{-1})	SD	DFOB-altered fibers (µmol L^{-1})	SD
0.5	6.2	0.5	4.5	0.5	6.9	0.8
1	5.2	0.0	3.9	0.0	5.3	0.0
4	6.8	0.4	3.4	0.4	6.5	0.2
8	6.1	1.0	3.5	1.0	9.5	0.2
24	7.7	0.9	6.1	0.9	17.1	0.4
48	8.6	0.8	8.1	0.8	25.6	1.1
96	13.2	1.0	13.7	1.0	46.6	1.3
168	14.1	0.0	16.1	0.0	72.0	2.9
336	22.5	1.3	35.1	1.3	117	10.0

Panel b1: Mg.)

Time [h]	DFOB-altered fibers + 0 µmol g^{-1} Fe (µmol L^{-1})	SD	DFOB-altered fibers + 3 µmol g^{-1} Fe (µmol L^{-1})	SD	DFOB-altered fibers + 30 µmol g^{-1} Fe (µmol L^{-1})	SD	DFOB-altered fibers + 300 µmol g^{-1} Fe (µmol L^{-1})	SD
0.5	2.9	0.2	2.7	1.1	1.0	0.2	1.9	0.1
1	4.6	0.5	3.4	0.5	1.4	0.2	3.3	0.4
4	7.9	1.0	6.1	0.6	3.6	0.3	5.4	0.3
8	12.6	0.4	9.4	1.2	5.1	0.4	8.9	0.5
24	25.7	1.0	16.7	0.2	11.3	1.1	14.7	0.2
48	48.9	1.0	27.6	0.4	18.2	1.4	22.6	0.2
96	76.1	2.1	46.4	0.1	31.6	0.8	36.6	1.0
168	112	1.9	72.0	1.8	51.8	2.2	53.0	0.4
336	198	1.3	151	10.8	108	1.7	103	1.6

Panel b2: Si.)

Time [h]	DFOB-altered fibers + 0 µmol g^{-1} Fe ($\mu mol\ L^{-1}$)	SD	DFOB-altered fibers + 3 µmol g^{-1} Fe ($\mu mol\ L^{-1}$)	SD	DFOB-altered fibers + 30 µmol g^{-1} Fe ($\mu mol\ L^{-1}$)	SD	DFOB-altered fibers + 300 µmol g^{-1} Fe ($\mu mol\ L^{-1}$)	SD
0.5	5.6	0.6	5.7	0.4	5.5	0.4	6.6	0.2
1	4.1	0.1	4.3	0.7	4.4	0.6	5.7	0.5
4	6.3	0.3	5.7	0.2	5.5	0.6	8.1	0.1
8	8.2	0.1	7.4	0.7	5.6	0.4	8.9	0.4
24	16.6	0.7	13.2	1.2	8.4	1.7	13.1	1.6
48	29.7	0.3	18.1	0.0	11.2	0.8	16.4	0.3
96	45.8	2.2	29.3	0.4	19.1	0.5	24.8	0.5
168	65.4	2.8	41.1	0.3	27.4	0.2	30.4	0.9
336	112	0.4	81.6	5.1	53.6	0.6	53.4	2.0

Panel c1: Mg.)

Time [h]	blank-altered fibers + 0 µmol g^{-1} Fe ($\mu mol\ L^{-1}$)	SD	blank-altered fibers + 3 µmol g^{-1} Fe ($\mu mol\ L^{-1}$)	SD	blank-altered fibers + 30 µmol g^{-1} Fe ($\mu mol\ L^{-1}$)	SD	blank-altered fibers + 300 µmol g^{-1} Fe ($\mu mol\ L^{-1}$)	SD
0.5	2.4	0.4	3.2	0.2	2.2	0.1	2.1	0.0
1	2.6	0.3	3.3	0.1	2.3	0.3	2.2	0.3
4	3.3	0.7	3.8	0.1	2.9	0.6	2.7	0.2
8	4.2	1.1	4.5	0.2	3.6	0.0	3.4	0.1
24	7.1	0.5	6.7	0.5	6.3	0.5	6.0	0.4
48	14.3	0.6	12.2	0.9	11.6	0.2	10.0	0.5
96	24.8	1.4	19.9	0.1	19.7	0.9	18.2	0.8
168	41.0	1.8	32.1	2.8	33.5	2.9	30.0	3.3
336	71.6	2.4	65.0	0.9	64.0	3.9	58.8	9.8

Panel c2: Si.)

Time [h]	blank-altered fibers + 0 µmol g^{-1} Fe ($\mu mol\ L^{-1}$)	SD	blank-altered fibers + 3 µmol g^{-1} Fe ($\mu mol\ L^{-1}$)	SD	blank-altered fibers + 30 µmol g^{-1} Fe ($\mu mol\ L^{-1}$)	SD	blank-altered fibers + 300 µmol g^{-1} Fe ($\mu mol\ L^{-1}$)	SD
0.5	2.4	1.4	2.9	0.3	2.3	1.4	1.2	0.2
1	0.9	0.2	2.0	0.1	3.1	0.2	2.5	0.1
4	3.0	0.4	2.0	0.8	3.1	0.6	3.8	2.1
8	2.1	0.8	3.4	0.3	5.4	0.0	3.0	0.2
24	5.1	0.6	5.5	0.1	6.7	0.5	5.1	0.8
48	8.4	0.5	9.7	1.3	10.7	0.5	8.3	0.8
96	12.9	0.0	9.9	0.1	15.3	0.4	9.7	1.2
168	19.1	1.8	14.9	2.0	20.0	0.9	15.0	0.7
336	29.5	0.0	27.7	0.2	32.0	2.4	25.2	4.6

SI-Table 4: *Residual H_2O_2 concentrations during H_2O_2 decomposition by pristine fibers, altered fibers and the MOPS buffer as a function of time. The initial H_2O_2 concentration was 3.34 g L^{-1}. (Data is plotted in Figure 4 in the main text; SD = standard deviation with n = 2).*

Panel a.)

Time	Pristine fibers		Blank-altered fibers		DFOB-altered fibers		MOPS buffer	
[h]	(g L^{-1})	SD	(g L^{-1})	SD	(g L^{-1})	SD	(g L^{-1})	SD
0.5	3.41	0.02	3.29	0.02	3.28	0.02	3.28	0.02
1	3.27	0.05	3.22	0.01	3.15	0.01	3.23	0.01
4	3.16	0.06	3.14	0.03	3.01	0.03	3.15	0.01
8	3.08	0.02	3.10	0.03	3.01	0.02	3.16	0.10
24	2.81	0.14	2.82	0.01	2.82	0.03	3.10	0.03
48	2.34	0.04	2.56	0.04	2.78	0.00	2.94	0.06
96	1.84	0.05	2.09	0.00	2.50	0.02	2.90	0.03
168	1.20	0.02	1.58	0.08	2.05	0.09	2.54	0.01
336	0.40	0.26	0.82	0.04	1.49	0.02	2.28	0.00

Panel b.)

Time	MOPS buffer + DFOB		Pristine fibers + DFOB		Blank-altered fibers + DFOB		DFOB-altered fibers + DFOB	
[h]	(g L^{-1})	SD	(g L^{-1})	SD	(g L^{-1})	SD	(g L^{-1})	SD
96	2.98	0.03	2.57	0.07	2.54	0.02	2.42	0.05
168	2.81	0.11	2.20	0.07	2.24	0.01	2.13	0.03
336	2.62	0.02	1.65	0.03	1.73	0.07	1.84	0.05

Panel c.)

Time [h]	DFOB-altered + 0 µmol g^{-1} Fe ($g\ L^{-1}$)	SD	DFOB-altered + 3 µmol g^{-1} Fe ($g\ L^{-1}$)	SD	DFOB-altered + 30 µmol g^{-1} Fe ($g\ L^{-1}$)	SD	DFOB-altered + 300 µmol g^{-1} Fe ($g\ L^{-1}$)	SD	MOPS buffer ($g\ L^{-1}$)	SD
0.5	3.32	0.05	3.40	0.01	3.28	0.05	3.27	0.02	3.28	0.02
1	3.12	0.09	3.20	0.06	3.21	0.00	3.13	0.04	3.23	0.01
4	3.02	0.00	3.20	0.01	3.00	0.05	2.97	0.02	3.15	0.01
8	3.04	0.11	3.19	0.00	3.06	0.01	2.97	0.00	3.16	0.10
24	2.86	0.04	3.03	0.00	2.82	0.02	2.68	0.03	3.10	0.03
48	2.73	0.05	2.82	0.08	2.54	0.00	2.31	0.01	2.94	0.06
96	2.44	0.01	2.52	0.07	2.30	0.03	1.80	0.06	2.90	0.03
168	2.00	0.03	1.98	0.07	1.72	0.01	1.25	0.00	2.54	0.01
336	1.51	0.01	1.36	0.05	1.05	0.07	0.58	0.01	2.28	0.00

Panle d.)

Time [h]	Blank-altered + 0 µmol g^{-1} Fe ($g\ L^{-1}$)	SD	Blank-altered + 3 µmol g^{-1} Fe ($g\ L^{-1}$)	SD	Blank-altered + 30 µmol g^{-1} Fe ($g\ L^{-1}$)	SD	Blank-altered + 300 µmol g^{-1} Fe ($g\ L^{-1}$)	SD	MOPS buffer ($g\ L^{-1}$)	SD
0.5	3.24	0.10	3.18	0.02	3.15	0.04	3.14	0.01	3.21	0.05
1	3.21	0.02	3.21	0.02	3.19	0.04	3.21	0.02	3.30	0.04
4	3.02	0.07	3.01	0.01	3.01	0.02	3.98	0.01	3.11	0.04
8	3.00	0.04	3.01	0.04	2.97	0.00	3.01	0.06	3.15	0.03
24	2.77	0.05	2.78	0.01	2.68	0.02	2.65	0.07	3.07	0.06
48	2.43	0.02	2.41	0.03	2.36	0.05	2.26	0.07	2.89	0.04
96	1.88	0.06	1.89	0.03	1.78	0.00	1.65	0.05	2.64	0.03
168	1.47	0.03	1.52	0.07	1.38	0.11	1.14	0.14	2.52	0.02
336	0.84	0.03	0.82	0.02	0.65	0.11	0.45	0.12	2.03	0.02

SI-Table 5: *HRFP of altered fibers relative to pristine fibers (i.e. 100%). (Data is potted in Figure 5 in the main text; SD = standard deviation with n = 4).*

Panel a.)

	DFOB-altered + 0 µmol g^{-1} Fe (0 µg Fe)	DFOB-altered + 3 µmol g^{-1} Fe (1.8 µg Fe)	DFOB-altered + 30 µmol g^{-1} Fe (18 µg Fe)	DFOB-altered + 300 µmol g^{-1} Fe (180 µg Fe)	3 mg ferrihydrite (1.8 mg Fe)
HRFP (%)	6.8	16.7	24.0	36.7	11.0
SD (%-point)	2.7	3.7	5.2	15.2	2.9

Panel b.)

	Blank-altered + 0 µmol g^{-1} Fe (0 µg Fe)	Blank-altered + 3 µmol g^{-1} Fe (1.8 µg Fe)	Blank-altered + 30 µmol g^{-1} Fe (18 µg Fe)	Blank-altered 300 µmol g^{-1} Fe (180 µg Fe)	3 mg ferrihydrite (1.8 mg Fe)
HRFP (%)	57.8	79.6	50.0	53.3	11.0
SD (%-point)	17.5	18.3	4.8	10.3	2.9

SI-Table 6: *Mobilized Mg and Si concentrations from 1 g L^{-1} pristine and blank altered fibers incubated in a 0.1 mol L^{-1} NaOH with addition of 3.34 g L^{-1} H_2O_2. The corresponding H_2O_2 decomposition rates can be found in Table 3 in the main text. (SD = standard deviation with n = 4).*

	Mg pristine fibers	SD	Mg blank altered fibers	SD	Si pristine fibers	SD	Si blank altered fibers	SD
[h]	(µmol L^{-1})		(µmol L^{-1})		(µmol L^{-1})		(µmol L^{-1})	
0.5	5.4	0.1	2.7	0.2	7.3	0.7	9.5	0.4
1	5.1	0.1	2.7	0.0	7.7	1.9	8.9	0.2
4	3.8	0.1	2.5	0.2	7.9	0.2	11.2	0.6
8	3.4	0.1	2.7	0.0	6.3	1.0	10.6	0.3
24	3.0	0.1	2.6	0.1	6.0	0.2	12.3	1.6
48	2.9	0.1	2.7	0.0	6.7	1.4	12.1	1.0
96	2.9	0.1	2.8	0.2	6.7	1.4	15.0	1.0
168	2.7	0.0	2.6	0.0	6.7	0.5	16.9	2.2
336	3.1	0.2	3.3	0.2	7.0	0.1	16.5	1.6

Addendum

Supporting Information to Chapter 3

"Presence, loss and recovery of redox cycling tetrahedral iron on chrysotile asbestos during dissolution"

Supporting information to the data material presented on page 78 to 98.

a1.) Blank

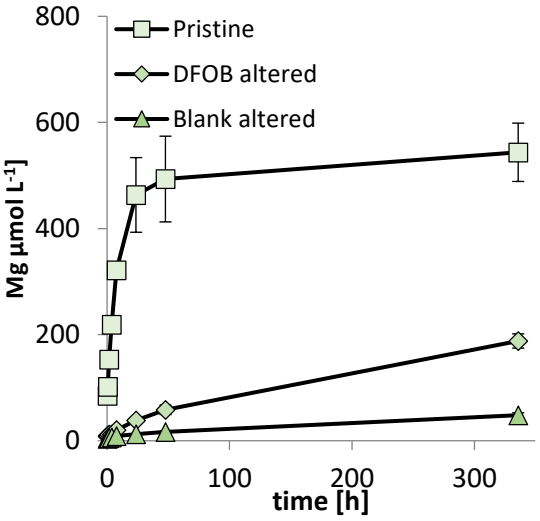

a2.) Ferr

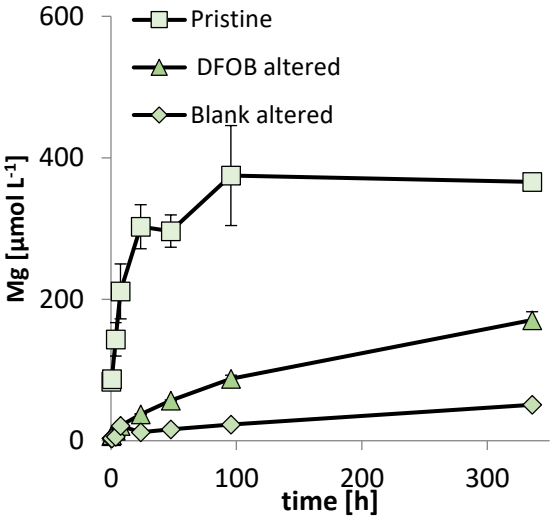

b1.) Blank

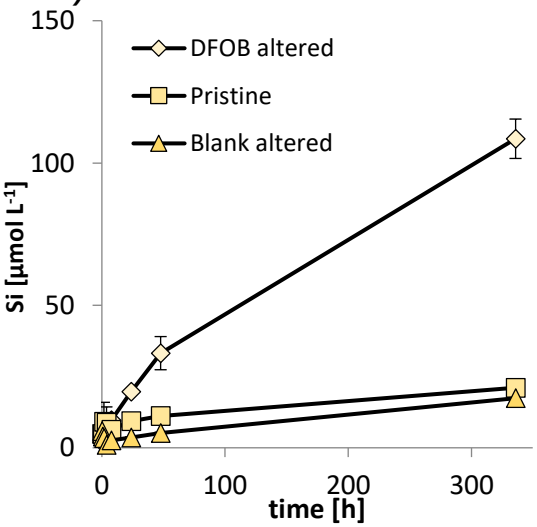

b2.) Ferr

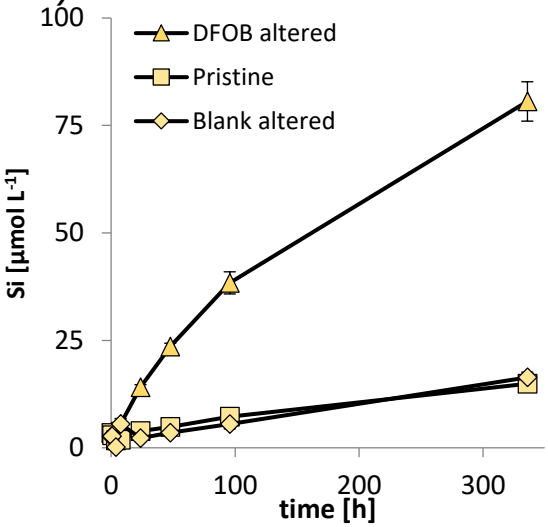

c1.) Blank

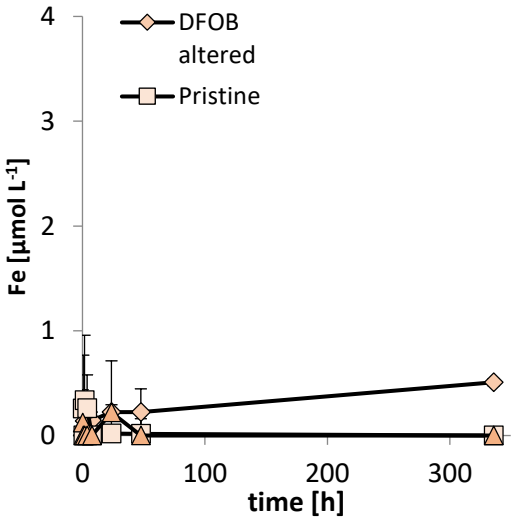

c2.) Ferr

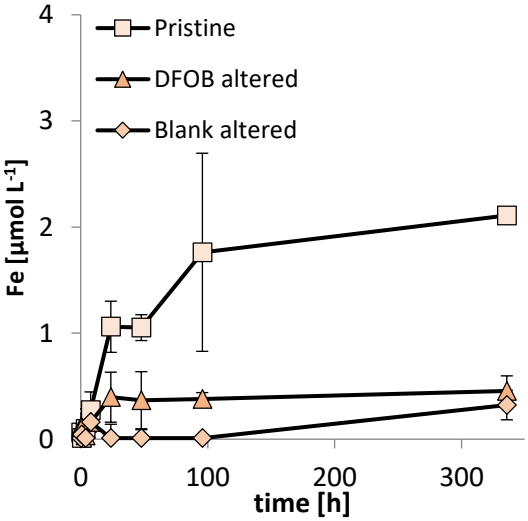

↑ ***SI-Figure 1.)*** *Anoxic incubation of pristine, blank and DFOB altered fibers in either pH 7.4 buffered blank or 1 mmol L^{-1} ferrozine solutions: Mobilized Mg (Panel a), Si (Panel b) and Fe (Panel c) concentrations from the blank treatment can be found in the subpanels 1, from the 1 mmol L^{-1} ferrozine solution in the subpanels 2. Incubation times were 0.5, 1, 2, 4, 8, 24, 48 and 336 h in the blank treatment and 0.5, 1, 4, 8, 24, 48, 96 and 336 h in the ferrozine treatment. Error bars indicate standard deviations (n = 2). The respective dataset to this figure can be found in SI-Figure 7.*

SI-Figure 2.) *Color of re-oxidized ascorbate altered fibers. While ascorbate altered fibers had a pale-pinkish color, the color of re-oxidized ascorbate altered fibers (in the right tube) was greyish to brownish. As a comparison, the blank altered fibers (left tube) with a brownish color were added.*

SI-Table 1: *Mg, Si and Fe concentrations in µmol L^{-1} mobilized during the pre-treatments of the differently altered fiber types used in the experiments and for EPR-measurements. All incubations lasted 336 h, unless specifically indicated. Values are means of two replicates only if round brackets with the standard deviation of these duplicates are added to the right of the respective concentrations.*

	Mg	Si	Fe
Blank fiber-alteration (all pH 7.4):			
Anoxic Blank/Ascorbate incubation (SI-Figure 1, Figure 2)	575	17.7	0.0
Anoxic Blank + Ascorbate incubation (Figure 2)	578	12.4	0.1
Anoxic Ferrozine incubation (SI-Figure 2)	655	15.5	0.0
Oxic blank and DFOB incubation (Figure 4)	578	12.4	0.1
Oxic H_2O_2 + DFOB incubation (Figure 5)	530	13.2	0.0
DFOB fiber-alteration (all pH 7.4):			
Anoxic Blank/Ascorbate incubation (SI-Figure 1, Figure 2)	671	107	32.3
Anoxic Blank + Ascorbate incubation (Figure 2)	698	70.0	34.1
Anoxic Ferrozine incubation (SI-Figure 2)	662 (82.6)	59.7 (19.2)	34.0 (1.8)
Oxic blank and DFOB incubation (Figure 4)	698	70.0	34.1
Oxic H_2O_2 + DFOB incubation (Figure 5)	604	80.9	28.5
Re-oxidized ascorbate altered fiber-alteration (all pH 7.4):			
Anoxic ascorbate incubation (Figure 3)	520 (18.3)	13.1 (0.3)	5.1 (0.0)
Oxidation (24 h) in blank solution + air bubbling (Figure 3)	41.4	21.0	0.0
EPR measurements on the HRFP of fibers:			
Blank alteration pristine fibers at pH 7.4 (Figure 6)	655	15.5	0.0
DFOB alteration pristine fibers at pH 7.4 (Figure 6)	662 (82.6)	59.7 (19.2)	34.0 (1.8)
Blank alteration pristine fibers at pH 3.0 (Figure 6)	1547	261	5.8
Blank alteration (pH 7.4) of pH 7.4 DFOB altered fibers (Figure 6)	151 (4.6)	67.4 (2)	0.2 (0.0)
Blank alteration (pH 3.0) of pH 7.4 DFOB altered fibers (Figure 6)	1606 (28.1)	484 (10.5)	5.7 (0.3)
Blank alteration (pH 3.0) of pH 3.0 blank altered fibers (Figure 6)	765	326	3.8

SI-Table 2: *Mg, Si and Fe concentrations in µmol L^{-1} mobilized from pristine, DFOB and blank altered fibers in anoxic pH 7.4 buffered 1 mmol L^{-1} ascorbate or 1 mmol L^{-1} ascorbate + ferrozine treatments. SD indicates standard deviation (n = 2)*

Mobilized Mg concentration, ascorbate incubation (Figure 2, Panel a1)

t[h]	Pristine	SD	Blank altered	SD	DFOB altered	SD
0.5	78.1	6.0	4.9	0.1	8.6	0.2
1	93.0	0.2	5.6	0.7	12.6	0.4
4	138	5.1	7.3	0.4	17.9	1.6
8	168	7.6	9.3	0.5	23.4	0.3
24	247	5.0	13.0	1.0	48.5	0.3
48	299	20.5	17.7	1.7	72.9	1.2
96	429	5.2	19.4	0.3	98.8	5.0
336	475	48.0	42.0	0.3	187	4.6

Mobilized Mg concentrations, ascorbate + ferrozine incubation (Figure 2, Panel a2)

t[h]	Pristine	SD	Blank altered	SD	DFOB altered	SD
0.5	82.4	6.8	6.1	1.6	10.2	2.2
1	90.2	3.3	5.7	0.1	10.9	0.4
4	134	9.1	9.4	0.1	16.3	4.6
8	162	2.6	12.9	0.5	27.6	2.1
24	277	19.2	23.7	2.5	54.3	2.1
48	334	22.7	38.2	2.4	77.8	5.4
96	483	45.7	59.5	3.2	113	5.7
336	600	0.0	132	2.0	270	3.4

Mobilized Si concentrations, ascorbate incubation (Figure 2, Panel b1)

t[h]	Pristine	SD	Blank altered	SD	DFOB altered	SD
0.5	5.9	0.2	5.9	1.3	5.9	0.2
1	6.4	0.3	5.9	0.2	8.5	0.1
4	5.8	0.7	5.6	0.5	9.3	0.1
8	7.8	1.5	6.8	0.3	13.4	0.3
24	7.3	1.0	7.7	0.0	28.9	0.4
48	8.2	0.3	9.3	0.3	44.5	1.2
96	12.3	0.3	12.7	0.9	54.6	5.2
336	15.8	1.8	17.3	0.0	110	3.7

Mobilized Si concentrations, ascorbate + ferrozine incubation (Figure 2, Panel b2)

t[h]	Pristine	SD	Blank altered	SD	DFOB altered	SD
0.5	2.3	1.1	0.4	0.0	0.6	0.2
1	4.0	0.2	0.0	1.5	2.4	0.5
4	4.8	1.5	1.1	0.0	5.1	1.9
8	6.8	0.1	2.0	0.0	12.2	3.2
24	17.5	0.1	9.4	1.5	33.0	1.4
48	21.8	0.2	21.1	1.4	50.4	2.9
96	29.8	2.6	34.5	4.2	76.1	5.4
336	59.2	0.0	83.8	1.5	189	3.4

Mobilized Fe concentrations, ascorbate incubation (Figure 2, Panel c1)

t[h]	Pristine	SD	Blank altered	SD	DFOB altered	SD
0.5	0.2	0.0	0.0	0.0	0.0	0.2
1	0.3	0.2	0.0	0.1	0.5	0.2
4	0.4	0.1	0.3	0.2	0.1	0.1
8	0.7	0.0	0.4	0.0	0.2	0.1
24	1.3	0.2	0.9	0.3	0.2	0.1
48	2.5	0.1	1.2	0.2	0.3	0.0
96	4.7	0.1	1.3	0.0	0.9	0.3
336	7.6	1.2	1.5	0.1	0.6	0.1

Mobilized Fe concentrations, ascorbate + ferrozine incubation (Figure 2, Panel c2)

t[h]	Pristine		Blank altered		DFOB altered	
0.5	0.5	0.1	0.0	0.1	0.0	0.1
1	0.6	0.3	0.0	0.0	0.0	0.0
4	3.1	0.3	1.7	0.2	0.0	0.0
8	5.7	0.7	3.1	0.1	0.0	0.0
24	11.2	0.9	8.0	2.1	0.0	0.2
48	14.4	0.8	12.9	2.4	0.0	0.0
96	22.0	1.7	16.1	0.9	0.5	0.1
336	29.5	0.0	23.5	1.4	3.5	0.0

SI-Table 3: *Mg, Si and Fe concentrations in µmol L^{-1} mobilized from re-oxidized ascorbate altered fibers in anoxic pH 7.4 buffered blank, 1 mmol L^{-1} ascorbate, 1 mmol L^{-1} ferrozine or 1 mmol L^{-1} ascorbate + ferrozine treatments. SD indicates standard deviation (n = 2).*

Blank incubation (Figure 3, Panel a)

t[h]	Mg	SD	Si	SD	Fe	SD
0.5	2.7	0.0	2.7	0.3	0.0	0.0
1	2.9	0.3	4.1	0.3	0.0	0.0
4	4.1	0.2	3.9	0.3	0.0	0.1
8	5.4	0.1	4.5	0.0	0.6	0.9
24	12.4	0.5	6.3	2.0	0.0	0.1
48	20.5	0.7	8.5	2.2	0.0	0.0
96	39.4	6.0	8.4	0.2	0.1	0.1
336	82.7	0.2	17.1	0.1	0.0	0.1

Ascorbate incubation (Figure 3, Panel b)

t[h]	Mg	SD	Si	SD	Fe	SD
0.5	3.3	0.4	3.6	3.4	1.2	1.4
1	3.4	0.5	3.7	0.6	0.5	0.7
4	4.3	0.4	3.5	1.1	0.7	0.5
8	4.9	0.5	2.4	0.8	1.1	0.3
24	10.1	0.0	7.0	0.0	1.2	0.1
48	19.2	1.0	7.1	0.0	1.9	0.1
96	31.4	0.9	9.3	0.0	2.7	0.0
336	84.2	5.0	16.1	Si	3.7	0.2

Ferrozine incubation (Figure 3, Panel c)

t[h]	Mg	SD	Si	SD	Fe	SD
0.5	4.0	0.1	4.0	8.0	0.4	1.4
1	4.2	0.3	4.4	1.6	0.1	0.0
4	5.1	0.5	3.7	0.9	0.1	0.0
8	5.7	0.0	5.1	0.4	0.0	0.1
24	11.7	3.1	7.8	0.1	0.1	0.2
48	19.6	2.0	6.6	0.1	0.1	0.3
96	33.5	5.9	8.9	1.0	0.4	0.0
336	73.3	12.7	16.5	1.2	1.7	0.2

Ascorbate + ferrozine incubation (Figure 3, Panel d)

t[h]	Mg	SD	Si	SD	Fe	SD
0.5	0.2	0.3	4.0	1.4	0.4	0.1
1	0.7	0.2	3.3	1.1	2.3	1.9
4	3.3	0.2	5.2	0.8	3.2	0.2
8	6.8	0.5	6.4	0.3	4.5	0.1
24	20.3	0.7	10.4	0.2	7.9	0.8
48	41.2	2.0	16.7	0.1	10.3	0.3
96	66.8	9.1	26.2	4.1	15.9	0.8
336	174	9.5	70.2	2.7	21.8	0.1

SI-Table 4: *Mg, Si and Fe concentrations in µmol L^{-1} mobilized from pristine, DFOB and blank altered fibers in oxic pH 7.4 buffered blank and 1 mmol L^{-1} DFOB treatments. SD indicates standard deviation (n = 2). Metal and Si concentrations mobilized from pristine fibers in 1 mmol L^{-1} DFOB treatments were taken from Walter et al. (2018a) [146].*

Blank incubation, Mobilized Mg and Si concentrations (Figure 4, Panel a)

t[h]	Mg: DFOB altered	SD	Mg: Blank altered	SD	Si: DFOB altered	SD	Si: Blank altered	SD
0.5	4.5	0.1	2.7	0.2	6.4	0.3	1.4	0.6
1	7.6	0.9	3.2	0.2	7.2	0.7	2.2	0.6
4	11.9	0.5	4.5	0.4	9.4	0.7	2.3	0.7
8	13.7	0.2	5.3	0.2	7.3	1.6	2.6	0.0
24	37.7	2.2	8.3	0.5	24.8	0.4	3.8	0.1
48	45.1	0.7	11.3	0.6	29.8	0.2	4.2	0.1
96	77.3	2.0	18.0	0.3	48.6	0.8	7.1	0.1
336	151	4.6	34.8	0.6	67.4	2.3	12.5	1.0

DFOB incubation, Mobilized Mg concentrations (Figure 4, Panel b1)

t[h]	Pristine	SD	Blank altered	SD	DFOB altered	SD
0.5	93.3	2.6	4.7	0.0	8.2	1.5
1	104	7.9	5.3	0.2	8.8	0.3
4	225	18.2	10.0	0.0	16.5	0.0
8	249	10.9	13.5	1.5	23.0	0.9
24	370	39.5	27.7	6.0	45.2	1.4
48	469	54.2	49.0	0.9	72.8	1.2
96	602	53.2	83.6	0.3	123	2.3
336	601	58.6	218	7.6	248	1.6

DFOB incubation, Mobilized Si concentrations (Figure 4, Panel b2)

t[h]	Pristine	SD	Blank altered	SD	DFOB altered	SD
0.5	0.0	0.4	1.3	1.5	2.5	0.2
1	0.0	0.3	0.0	0.0	0.0	0.3
4	5.4	1.2	0.7	0.2	4.3	0.0
8	8.3	1.0	3.3	1.4	8.4	0.8
24	17.7	2.0	12.3	3.1	25.6	0.4
48	26.2	0.5	26.8	0.6	44.8	0.2
96	39.9	3.2	50.5	2.0	80.8	2.2
336	62.9	7.7	145	4.9	171	1.5

DFOB incubation, Mobilized Fe concentrations (Figure 4, Panel b3)

t[h]	Pristine	SD	Blank altered	SD	DFOB altered	SD
0.5	4.1	0.3	0.8	0.1	0.0	0.1
1	5.7	0.4	1.4	0.2	0.0	0.2
4	13.7	1.2	3.5	0.1	0.0	0.1
8	15.1	1.5	4.8	0.5	0.0	0.4
24	22.6	2.4	7.8	0.1	0.3	0.2
48	27.5	3.8	10.7	0.6	0.8	0.3
96	32.4	4.1	14.0	0.2	1.8	1.1
336	29.3	0.2	22.6	1.2	4.2	0.4

SI-Table 5: *Mg, Si and Fe concentrations in µmol L^{-1} mobilized from pristine, blank and DFOB altered fibers in oxic pH 7.4 buffered blank, 3.34 g L^{-1} H_2O_2, 1 mmol L^{-1} DFOB and 3.34 g L^{-1} H_2O_2 + 1 mmol L^{-1} DFOB treatments. SD indicates standard deviation (n = 2). Metal and Si concentrations mobilized from pristine fibers in blank and 1 mmol L^{-1} DFOB treatments were taken from Walter et al. (2018a) [146], whereas data from all 3.34 g L^{-1} H_2O_2 treatments were taken from Walter et al. (2018b) [174]. Furthermore, the respective decomposition kinetics of all treatments involving H_2O_2 can be found in Walter et al. (2018b) [174].*

Mobilized Mg concentrations, 96 h of incubation (Figure 5, Panel a1)

	Blank	SD	H_2O_2	SD	DFOB	SD	DFOB + H_2O_2	SD
Pristine fibers	539	138	511	39.3	602	53.2	630	89.0
Blank altered fibers	18.0	0.3	32.9	1.4	83.6	0.3	125	0.9
DFOB altered fibers	77.3	2.0	95.9	4.7	72.8	1.2	155	3.9

Mobilized Mg concentrations, 336 h of incubation (Figure 5, Panel a2)

	Blank	SD	H_2O_2	SD	DFOB	SD	DFOB + H_2O_2	SD
Pristine fibers	585	105	602	18.9	601	58.6	983	13.8
Blank altered fibers	34.8	0.6	91.3	6.6	218	7.6	415	21.2
DFOB altered fibers	151	4.6	229	13.0	248	1.6	421	25.6

Mobilized Si concentrations, 96 h of incubation (Figure 5, Panel b1)

	Blank	SD	H_2O_2	SD	DFOB	SD	DFOB + H_2O_2	SD
Pristine fibers	15.9	1.2	13.2	1.0	50.9	3.2	64.3	2.3
Blank altered fibers	7.1	0.1	13.7	1.0	50.5	2.0	71.5	0.1
DFOB altered fibers	48.6	0.8	46.6	1.3	44.8	0.2	87.2	0.0

Mobilized Si concentrations, 336 h of incubation (Figure 5, Panel b2)

	Blank	SD	H_2O_2	SD	DFOB	SD	DFOB + H_2O_2	SD
Pristine fibers	15.4	0.7	22.5	1.3	73.9	7.7	212	1.1
Blank altered fibers	12.5	1.0	35.1	1.3	145	4.9	242	13.9
DFOB altered fibers	67.4	2.3	117	10.0	164	1.5	249	14.3

Mobilized Fe concentrations, 96 h of incubation (Figure 5, Panel c1)

	Blank	SD	H_2O_2	SD	DFOB	SD	DFOB + H_2O_2	SD
Pristine fibers	0.9	0.1	0.2	0.1	32.4	4.1	31.3	1.8
Blank altered fibers	0.0	0.0	0.1	0.1	10.7	0.6	20.4	0.2
DFOB altered fibers	0.0	0.1	0.6	0.2	0.8	0.3	3.4	0.3

Mobilized Fe concentrations, 336 h of incubation (Figure 5, Panel c2)

	Blank	SD	H_2O_2	SD	DFOB	SD	DFOB + H_2O_2	SD
Pristine fibers	0.1	0.0	0.1	0.1	29.3	0.2	40.8	1.4
Blank altered fibers	0.0	0.0	0.2	0.3	22.6	1.2	32.4	3.7
DFOB altered fibers	0.2	0.0	0.7	0.3	4.2	0.4	7.4	0.8

SI-Table 6: *Hydroxyl radical forming potentials (HRFPs) of DFOB altered fibers, DFOB altered fibers incubate in pH 7.4 and pH 3.0 blank solutions and pH 3.0 blank altered fibers and pH 3.0 blank altered fibers incubated in a pH 3.0 blank solution. The HRFPs represent the percentage relative to the HRFPs of pristine fibers measured on each measurement session. SD indicates standard deviation (n = 4).*

1st incubation: pH=7.4 DFOB; 2nd incubation pH 7.4 blank

Incubation	HRFP	SD
1st	8.8	2.5
2nd	12.8	1.7

1st incubation: pH=7.4 DFOB; 2nd incubation pH 3.0 blank

Incubation	HRFP	SD
1st	8.8	2.5
2nd	19.7	2.6

1st incubation: pH=3.0 blank; 2nd incubation pH 3.0 blank

Incubation	HRFP	SD
1st	30.2	3.3
2nd	21.6	4.1

SI-Table 7: *Mg, Si and Fe concentrations in µmol L^{-1} mobilized from pristine, DFOB and blank altered fibers in anoxic pH 7.4 buffered 1 mmol L^{-1} blank or 1 mmol L^{-1} ferrozine treatments. SD indicates standard deviation (n = 2).*

Mobilized Mg concentrations, blank incubation (SI-Figure 1, Panel a1)

t[h]	Pristine	SD	Blank altered	SD	DFOB altered	SD
0.5	84.6	0.9	4.0	0.6	8.1	0.8
1	102	2.5	4.4	0.1	9.7	1.7
2	153	10.7	5.5	0.4	11.6	1.5
4	219	9.8	6.2	0.5	11.8	0.3
8	321	7.0	8.6	1.5	20.3	0.0
24	463	70.3	12.4	0.2	38.2	0.3
48	493	80.8	16.7	1.7	58.3	8.9
336	544	55.0	48.2	4.4	188	13.4

Mobilized Mg concentrations, ferrozine incubation (SI-Figure 1, Panel a2)

t[h]	Pristine	SD	Blank altered	SD	DFOB altered	SD
0.5	83.5	9.4	3.3	0.5	6.8	1.3
1	87.2	0.8	3.6	0.4	8.1	0.7
4	143	23.6	5.7	0.1	14.2	1.2
8	211	38.8	20.9	0.3	20.9	0.1
24	303	31.1	12.2	0.4	37.5	0.4
48	296	22.8	16.1	0.5	56.8	0.8
96	375	70.7	22.9	1.8	87.5	5.1
336	366	7.0	50.8	1.3	171	11.7

Mobilized Si concentrations, blank incubation (SI-Figure 1, Panel b1)

t[h]	Pristine	SD	Blank altered	SD	DFOB altered	SD
0.5	4.9	1.4	5.9	1.6	2.0	1.0
1	4.8	1.5	4.0	0.8	4.7	0.7
2	9.1	6.9	3.3	0.3	6.8	3.6
4	8.8	5.6	1.0	0.6	4.6	1.0
8	6.3	0.9	2.6	0.1	9.7	0.7
24	9.4	0.2	3.7	0.2	19.7	0.4
48	11.2	1.6	5.2	0.3	33.2	5.8
336	21.1	1.9	17.4	2.2	109	6.9

Mobilized Si concentrations, ferrozine incubation (SI-Figure 1, Panel b2)

t[h]	Pristine	SD	Blank altered	SD	DFOB altered	SD
0.5	3.5	0.1	2.6	0.4	3.6	1.1
1	2.9	0.7	2.7	0.3	3.8	0.8
4	1.7	1.0	0.2	0.3	3.0	0.5
8	1.9	0.7	5.5	1.3	5.5	0.9
24	3.9	0.1	2.3	0.8	14.1	0.6
48	4.9	0.2	3.5	0.2	23.5	0.8
96	7.2	0.4	5.5	1.1	38.4	2.6
336	14.9	0.0	16.4	1.2	80.6	4.6

Mobilized Fe concentrations, blank incubation (SI-Figure 1, Panel c1)

t[h]	Pristine	SD	Blank altered	SD	DFOB altered	SD
0.5	0.3	0.1	0.1	0.3	0.0	0.0
1	0.0	0.0	0.0	0.1	0.3	0.5
2	0.3	0.6	0.0	0.1	0.1	0.1
4	0.3	0.3	0.0	0.1	0.0	0.0
8	0.0	0.1	0.0	0.0	0.1	0.1
24	0.0	0.0	0.2	0.5	0.2	0.1
48	0.0	0.1	0.0	0.2	0.2	0.2
336	0.0	0.1	0.0	0.0	0.5	0.0

Mobilized Fe concentrations, ferrozine incubation (SI-Figure 1, Panel c2)

t[h]	Pristine	SD	Blank altered	SD	DFOB altered	SD
0.5	0.1	0.1	0.0	0.2	0.1	0.1
1	0.0	0.1	0.0	0.0	0.1	0.2
4	0.1	0.0	0.0	0.1	0.0	0.1
8	0.3	0.2	0.2	0.1	0.2	0.1
24	1.1	0.2	0.0	0.1	0.4	0.2
48	1.1	0.1	0.0	0.1	0.4	0.3
96	1.8	0.9	0.0	0.0	0.4	0.1
336	2.1	0.1	0.3	0.1	0.5	0.1

Addendum

Supporting Information to Chapter 4

"Soil-pH and cement influence dissolution of, and radical formation by, chrysotile asbestos in soils"

Supporting information to the data material presented on page 99 to 117.

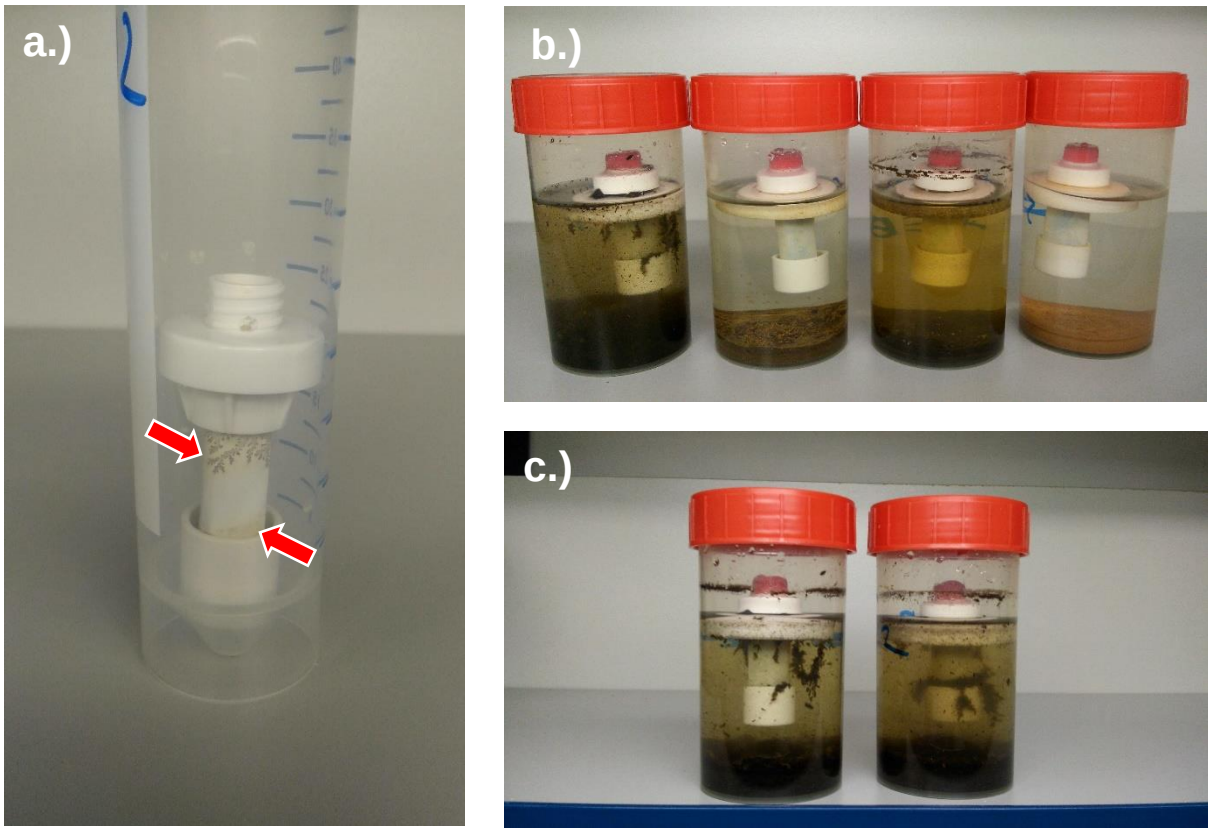

SI-Figure 1: *Fungal colonies in soil suspensions and on dried fiber-filled Float-A-Lyzers. Panel a.) Dried Float-A-Lyzer with signs of fungal growth on the outer membrane. The lower arrow points at a yellowish organic covering on the membrane, the upper arrow also points towards this organic covering, but also on dendritic metal crystals on the membrane, which looked similar to Mn-oxide dendrites. A fine whitish organic cover including whitish needles was furthermore observed on the outer membrane surface (not visible on this picture), Panel b.) Incubation of fibers in Schrems (left), Siebenlinden, Xeraco and Santomera (right) soil suspensions. Fungal colonies were observed in all soil suspensions apart from the Santomera treatment; Panel c.) Two samples of Schrems treatments. Fungal colonies attached to the Float-A-Lyzers, indicating that they used chrysotile for acquiring nutrients.*

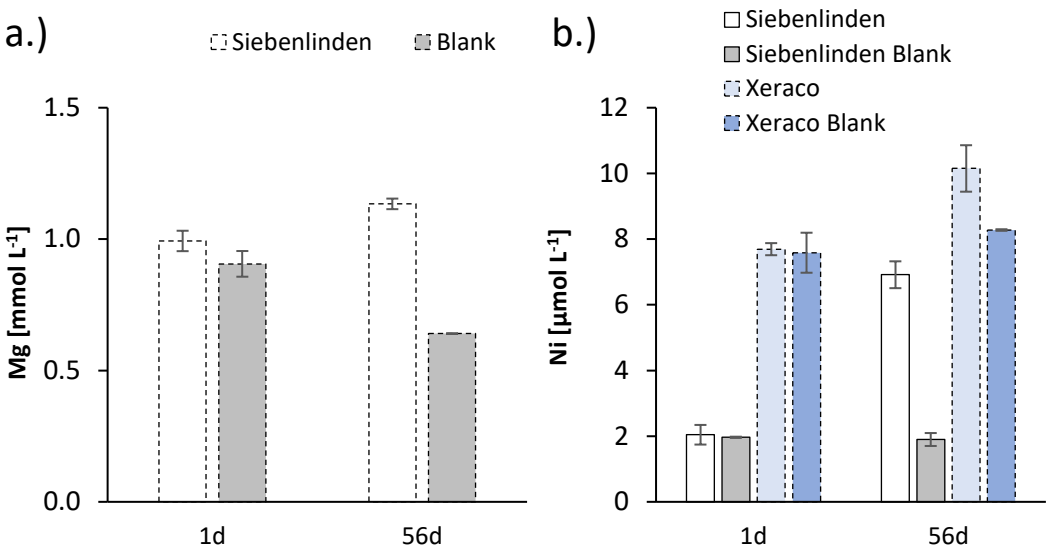

SI-Figure 2: *Mg and Ni concentrations extracted in nitric acid soil-extractions from aliquots of the Siebenlinden (Panel a) and Xeraco (Panel b) soils sampled from the soil suspensions. Ni in Xeraco soil was the only metal that was increased in the soil compartment of the two carbonaceous soil treatments of this study (Xeraco and Santomera). Error bars indicate standard deviations (n = 4). The respective dataset to this figure can be found in SI-Table 11.*

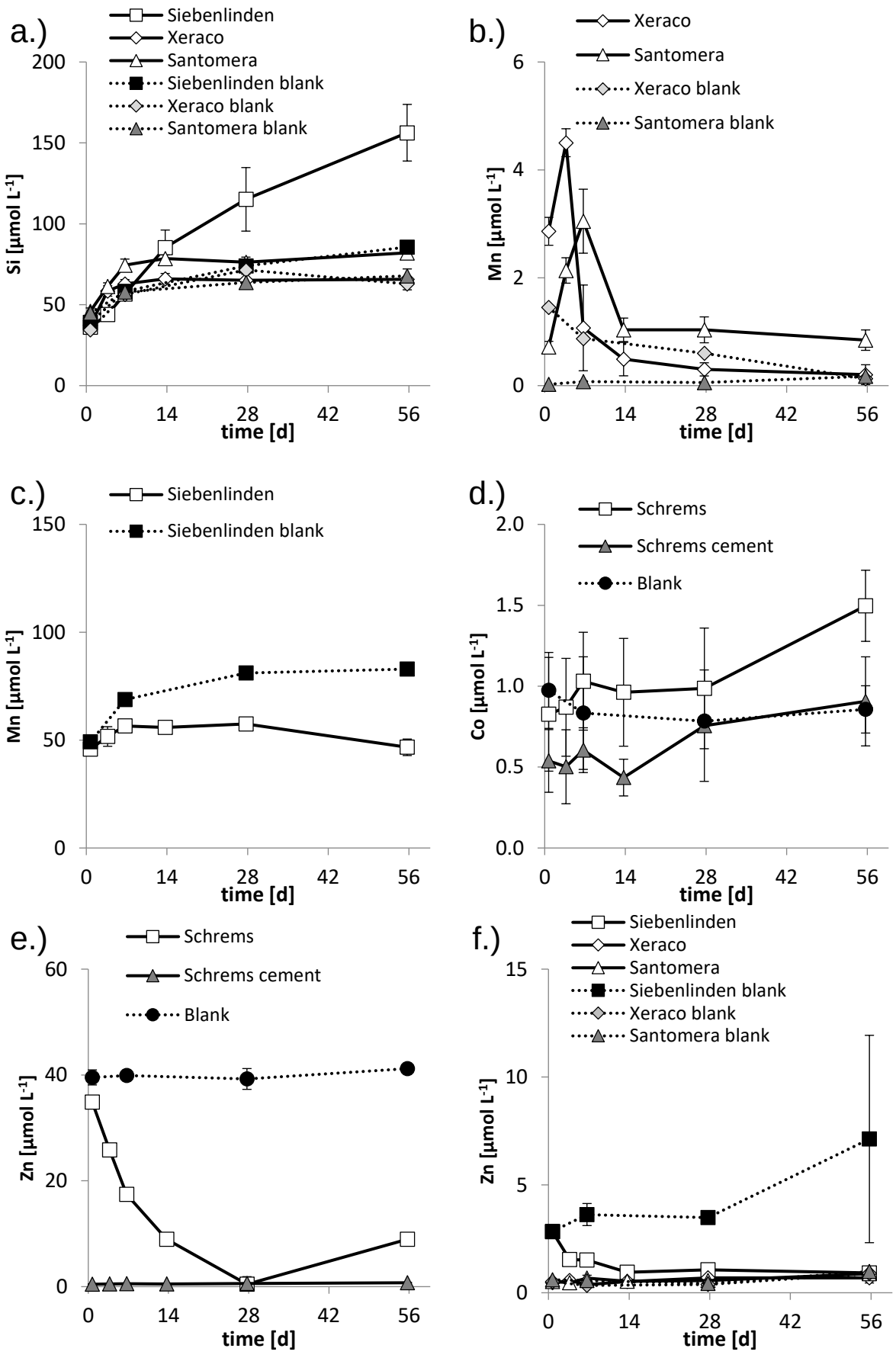
a.)
Siebenlinden
Xeraco
Santomera
Siebenlinden blank
Xeraco blank
Santomera blank
Si [µmol L-1]
time [d]
b.)
Xeraco
Santomera
Xeraco blank
Santomera blank
Mn [µmol L-1]
time [d]
c.)
Siebenlinden
Siebenlinden blank
Mn [µmol L-1]
time [d]
d.)
Schrems
Schrems cement
Blank
Co [µmol L-1]
time [d]
e.)
Schrems
Schrems cement
Blank
Zn [µmol L-1]
time [d]
f.)
Siebenlinden
Xeraco
Santomera
Siebenlinden blank
Xeraco blank
Santomera blank
Zn [µmol L-1]
time [d]

↑ ***Si-Figure 3:*** *Si (Panel a), Mn (Panel b and c), Co (Panel d) and Zn (Panel e and f) concentrations analyzed in soil solutions of Schrems, Siebenlinden, Xeraco, Santomera and cement-amended Schrems soils (at FSR 2 g L^{-1}). Incubation times were 1, 4, 7, 14, 28 and 56 days in Float-A-Lyzer treatments and 1, 7, 28 and 56 in blank treatments. Error bars indicate standard deviations (n = 4 in fiber samples and n = 2 in blanks). Mobilized Si concentrations in soil solutions were only elevated relative to blank concentrations in Siebenlinden (and Schrems) soils. Mn soil solution concentrations were clearly lower in Siebenlinden soil relative to their blank treatments, suggesting a partitioning of Mn out of the soil solution compartment. In Xeraco and Santomera soils, Mn contents however increased relative to the respective blanks at short incubation times, which was most likely fiber-related. Mobilized Co concentrations were only elevated in Schrems samples after 56 days of incubation relative to their blank treatments. This may eventually be accounted to the dissolution of the Co content of the fibers. Zn soil concentrations drastically decreased in Schrems treatments relative to Schrems blanks, the same was observed for Siebenlinden samples. Even though Zn accumulated at fiber surfaces in Schrems and Siebenlinden soils (SI-Figure 5), the reason for this considerable decrease in Schrems samples was not known. The respective dataset to this figure can be found in SI-Table 12.*

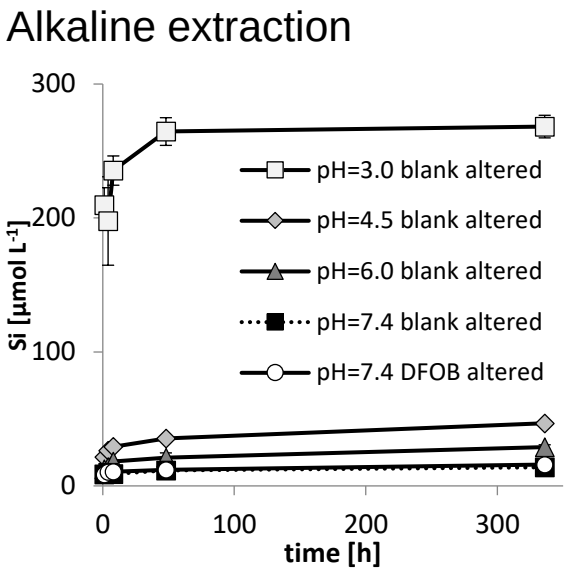

SI-Figure 4: *Si extracted with 0.1 mol L^{-1} NaOH from 1 g L^{-1} of preconditioned fibers: Pristine Shijiazhuang chrysotile asbestos was preconditioned for 336 h at a FSR 1 g L^{-1} at pH 3.0, 4.5, 6.0 and 7.4 in 1 g L^{-1} suspensions containing 50 mmol L^{-1} of PIPPS (1,4-piperazinedipropanesulfonic-acid, pH 3.0 and 4.5), MES (2-(N-morpholino)ethanesulfonic-acid, pH 6.0) and MOPS (3-(N-morpholino)propanesulfonic-acid, pH 7.4) buffer. The buffers maintained the pH within ± 0.3 pH units. Additionally, fibers were preconditioned in a pH 7.4 buffered solution containing 1 mmol L^{-1} of the siderophore DFOB (desferrioxamine B). After 336 h, fibers were sampled by vacuum filtration in Büchner funnels with 0.47 µm nylon membrane filters and rinsed with UPW. After vacuum drying, fibers were subjected to alkaline extraction for 1, 4, 8, 48 and 336 h. This experiment indicates that amorphous siliceous material only formed during fiber dissolution at pH 3.0. As fiber dissolution is stoichiometric at pH 4.5 (Walter et al. (2018a) [146]), the formation of amorphous siliceous material starts somewhere between pH 3.0 and 4.5. Not even the preconditioning of fibers with DFOB (and the consequent Si-labilization, [146]) induced the formation of extractable amorphous siliceous material.*

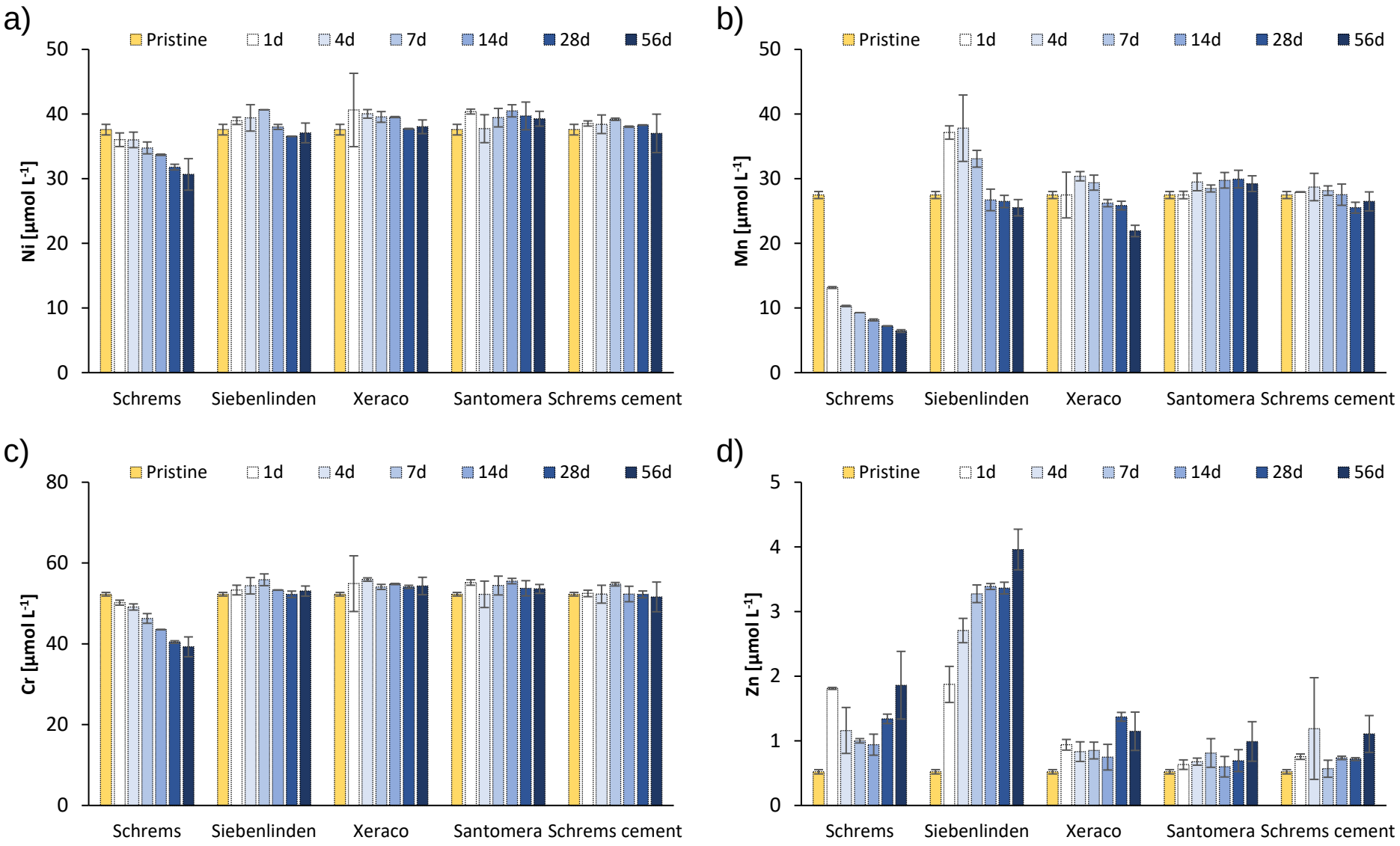
a)
Pristine
1d
4d
7d
14d
28d
56d
Ni [µmol L-1]
0
10
20
30
40
50
Schrems
Siebenlinden
Xeraco
Santomera
Schrems cement
b)
Mn [µmol L-1]
c)
Cr [µmol L-1]
0
20
40
60
80
d)
Zn [µmol L-1]
0
1
2
3
4
5

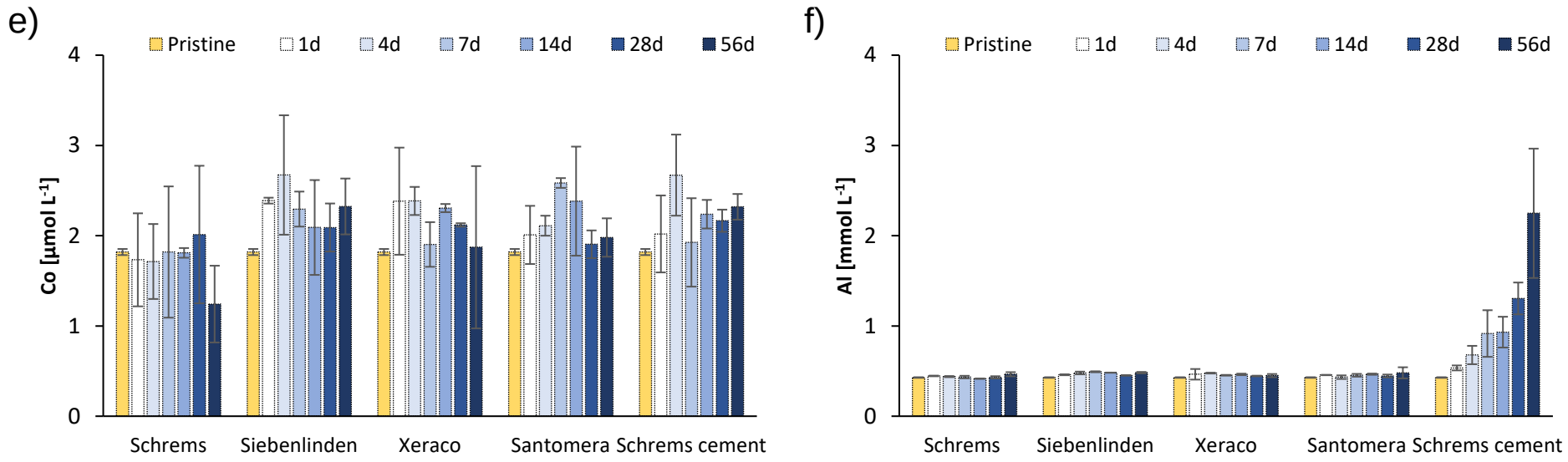

Si-Figure 5: *Ni (Panel a), Mn (Panel b), Cr (Panel c), Zn (Panel d), Co (Panel e) and Al (Panel f) concentrations analyzed in acid digestion of fiber-filled Float-A-Lyzers (FSR of 2 g L^{-1}) from all soil suspension. Incubation lasted for 1, 4, 7, 14, 28 and 56 days. Error bars indicate standard deviations (n = 2). Pristine fiber metal contents were taken from acid-digestions of pristine fibers (Ni, Mn, Cr, Al) or neutron activation analyses (Zn and Co, main text Table 1). Ni and Cr contents only consistently decreased in Schrems soil. The Co bulk only decreased after 56 days in Schrems soil, trends in other soils were unclear. Mn contents of fibers sharply decreased in Schrems soil and even increased in Siebenlinden soil at the first three sampling times. An increase was also recognized for Zn, whereby digested Zn concentrations were consistently higher in Schrems, Siebenlinden and Xeraco soils relative to the Zn contents of pristine fibers. However, Zn contamination in the acid digested Float-A-Lyzers may have partly caused this increase (SI-Table 3). Digested Al contents sharply increased in cement-amended Schrems soil over pristine fiber Al contents. The respective dataset to this figure can be found in SI-Table 14.*

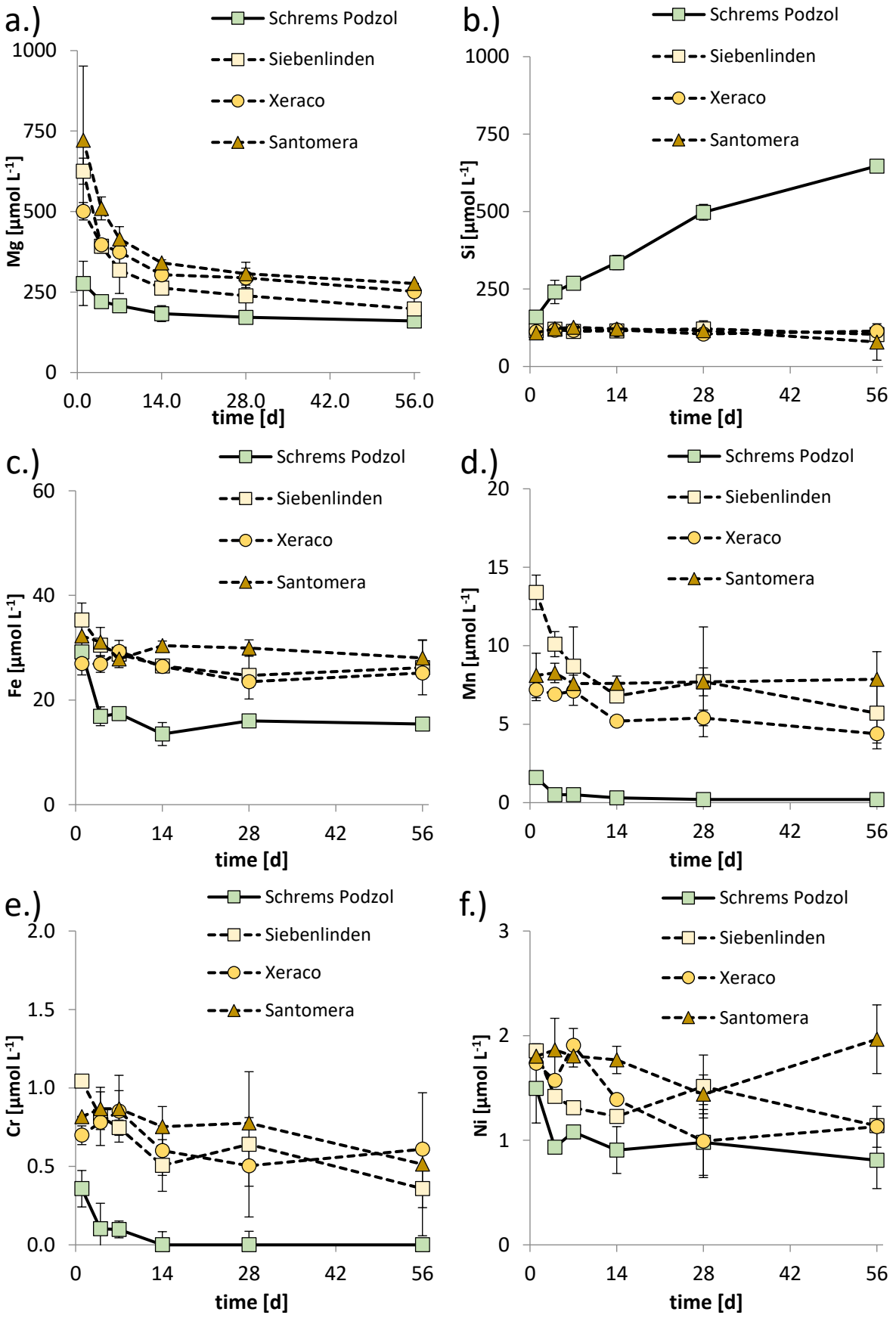
a.)
Schrems Podzol
Siebenlinden
Xeraco
Santomera
Mg [µmol L-1]
time [d]
b.)
Si [µmol L-1]
c.)
Fe [µmol L-1]
d.)
Mn [µmol L-1]
e.)
Cr [µmol L-1]
f.)
Ni [µmol L-1]

↑ ***SI-Figure 6:*** *Mg (Panel a), Si (Panel b), Fe (Panel c), Mn (Panel d) Cr (Panel e) and Ni (Panel f) concentrations mobilized after 336 h of incubation of 1 g L^{-1} of fibers sampled from soil suspensions in pH 7.4 extractions at a 1 mmol L^{-1} HEDTA concentration. The fibers were incubated for 1, 4, 7, 14, 28 and 56 d in Schrems, Siebenlinden, Xeraco and Santomera soil suspensions prior to the pH 7.4 extraction. Error bars indicate standard deviations (n = 2). In Schrems soil, the extracted metals were depleted to a higher extent than in other treatments, which is likely a consequence of the high dissolution rates of fibers in Schrems soil. However, Si concentrations were clearly elevated in Schrems soil, which was comparable to alkaline extraction results (SI-Table 6). This high extracted Si contents may have been caused by the dissolution of amorphous siliceous material that formed during fiber dissolution in Schrems soil. The respective dataset to this figure can be found in SI-Table 15.*

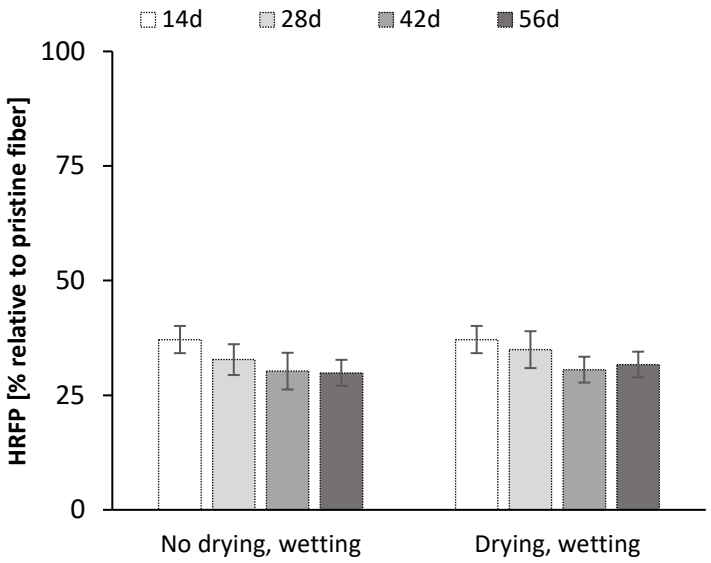

SI-Figure 7: *HRFP of fibers incubated for 2, 4, 6 or 8 weeks in MOPS buffered pH 7.4 solutions. After the incubation, the fibers were vacuum sampled and dried and stored in an evacuated desiccator until they were analyzed by EPR spin trapping. The fibers were either incubated for up to four consecutive intervals of 14 days, whereby the fibers were vacuum dried in between the incubations ("Drying/wetting cycles"), or they were incubated over the whole reaction time ("No drying/wetting cycles"). The HRFP of the fibers successively declined to approximately 30 %, a HRFP that was also observed fibers which were incubated in Siebenlinden, Xeraco and Santomera soils after ≈ 14 d of incubation, and in Schrems soil after 1 d of incubation. Whether fibers were biweekly dried and resuspended or not did not affect how the HRFP developed over time in this experiment. Data to the HRFPs and the Mg and Si concentrations that were mobilized during the fibers preconditioning can be found in SI-Table 16.*

SI-Table 1: *Bulk composition of the commercial cement used in the present study. Mean bulk conentrations of Ca, Mg, Si, Fe, Mn, Ni and Cr were determined in four replicates in fusion digestions (according to Walter et al. (2018a) [146]). Additionally, Fe, Ni, Cr, Zn and Co were analyzed by a NAA (n = 2). Values in round braces are standard deviations. Bulk concentrations of Ca and Si were high, but also had high standard deviations. This presumably may be explained by heterogeneities in the analyzed cement particle mixtures. Round braces indicate standard deviations.*

Bulk measurements of cement particles			
Bulk composition:		*Fusion digestion:*	*NAA:*
Ca	[g kg^{-1}]	134 (15.5)	
Mg	[mg kg^{-1}]	1828 (1.8)	
Si	[g kg^{-1}]	230 (33.0)	
Al	[g kg^{-1}]	33.9 (5,4)	
Na	[g kg^{-1}]	2.0 (1.4)	
K	[g kg^{-1}]	7.7 (5.1)	
Fe	[mg kg^{-1}]	13.8 (0.9)	16.8 (2.9)
Mn	[mg kg^{-1}]	182 (14.5)	
Ni	[mg kg^{-1}]	33.5 (2.1)	44.1 (8.1)
Cr	[mg kg^{-1}]	85.9 (11.3)	104 (15.6)
Zn	[mg kg^{-1}]		32.2 (4.3)
Co	[mg kg^{-1}]		3.7 (0.7)

SI-Table 2: *Efficiency to digest the metals and Si contained in pristine fibers (5 g L^{-1}) in a 1.4 mol L^{-1} HNO_3 for 336 h at 50°C, as performed with fiber-filled Float-A-Lyzers for the quantitative evaluation of metal dissolution of chrysotile in soil suspensions. Standard deviations can be found in the respective round braces (n = 2). Digested Fe contents were corrected for the magnetite content in Shijiazhuang chrysotile (Table 1 in the main text) in order to compare acid digested Fe concentrations with the bulk-Fe determined in fusion digestions. The digestion efficiency was expressed as a ratio of the means of concentrations measured in the acid digestions and their respective bulk concentrations determined either by fusion digestions ("Fusion") or neutron activation analyses ("NAA").*

Efficiency of metal digestion in a 1.4 mol L^{-1} HNO_3 for 336 h at 50°C									
Mean metal and Si concentration extracted in acid digestions of pristine fibers [g kg^{-1}]:						Mössbauer corrected			
Mg	**Si**	**Al**	**Cr**	**Mn**	**Fe**	**Fe**	**Ni**	**Zn**	**Co**
239.5 (1.9)	187.6 (3.3)	8.0 (0.5)	1.4 (0.0)	0.8 (0.0)	14.3 (0.2)	18.8	1.1 (0.0)	0.022 (0.0)	0.057 (0.0)
Bulk concentrations of pristine fibers [g kg^{-1}] (Table 1 in main text):									
Fusion	Fusion	Fusion	Fusion	Fusion	Fusion	Fusion	Fusion	NAA	NAA
Mg	**Si**	**Al**	**Cr**	**Mn**	**Fe**	**Fe**	**Ni**	**Zn**	**Co**
249.5 (6.8)	13.6 (0.1)	5.8 (0.0)	1.4 (0.1)	0.8 (0.1)	19.0 (1.4)	19.0 (1.4)	1.2 (0.1)	0.017 (1.1)	0.054 (1.0)
Ratio Means/Bulk [%]						Mössbauer corrected			
Mg	**Si**	**Al**	**Cr**	**Mn**	**Fe**	**Fe**	**Ni**	**Zn**	**Co**
96.0	7.2	72.3	98.5	98.0	75.3	99.2	90.4	131.8	106.3

SI-Table 3: *Metal and Si concentrations (in µmol L^{-1}) mobilized from empty Float-A-Lyzers in a 1.4 mol L^{-1} HNO_3 for 336 h at 50°C. The Float-A-Lyzers were incubated in all soil suspensions for 56 days and visually cleaned from soil particles with ultra-pure water. SD indicates standard deviations (n = 2). Metal concentration in the co-sampled soil solution were subtracted from the digested metal-contents (therefore negative values may be possible). The maximal extracted metal or Si concentration was ratioed with the total extracted metal or Si concentration from pristine fibers in acid digestions ("Maximal % of dissolved fiber bulk").*

		Mg	**Al**	**Si**	**Cr**	**Mn**	**Fe**	**Ni**	**Zn**	**Co**
Podzol	Mean	1.3	5.5	-4.4	0.5	0.0	-9.3	-0.5	1.4*	-0.3
	SD	1.1	6.2	0.2	0.1	0.0	0.8	0.3	0.0	0.1
Podzol cem	Mean	0.1	36.3*	1.4	0.8*	0.0	1.5	-0.4	0.7	0.7*
	SD	0.6	34.5	3.7	0.0	0.0	0.9	0.2	0.5	0.1
Siebenlinden	Mean	1.2	-0.5	1.6	0.5	0.5*	0.5	-0.7	0.3	0.2
	SD	0.2	5.3	0.4	0.1	0.1	0.2	0.5	0.2	0.3
Xeraco	Mean	3.2	7.8	1.9	0.6	0.1	1.3	-0.5	0.7	0.5
	SD	10.9	11.5	38.1	0.3	0.3	7.2	0.0	0.2	0.1
Santomera	Mean	10.7*	15.9	27.2*	0.3	0.2	5.1*	-0.8	0.7	-0.1
	SD	10.9	11.5	38.1	0.3	0.3	7.2	0.0	0.2	0.1
Maximal % of dissolved fiber bulk (marked with *]		0.1	8.4	2.8	1.5	1.8	1.0	0.0	204.3	36.2

SI-Table 4: *pH of the filtered soil solution of the soil suspensions in the presence or absence (blank) of fiber filled Float-A-Lyzers after the respective incubation times. Values represent the mean of two replicates, round braces indicate standard deviations. Abbreviations are Schrems podzol (POD), Schrems podzol with added cement (POD cem), Siebenlinden soil (SL), Xeraco soil (XER) and Santomera soil (SAN).*

t[d]	POD	POD cem	SL	XER	SAN
1	2.9 (0.0)	9.2 (0.0)	4.9 (0.1)	7.1 (0.0)	7.5 (0.0)
4	3.0 (0.0)	8.5 (1.4)	5.5 (0.1)	7.1 (0.0)	7.5 (0.0)
7	3.0 (0.0)	9.3 (0.7)	5.7 (0.2)	7.1 (0.1)	7.5 (0.0)
14	3.0 (0.0)	10.0 (0.5)	5.6 (0.1)	7.1 (0.0)	7.5 (0.0)
28	3.1 (0.1)	9.2 (0.5)	5.8 (0.0)	7.3 (0.0)	7.7 (0.1)
56	3.3 (0.0)	8.9 (0.1)	6.0 (0.0)	7.2 (0.0)	7.7 (0.0)
	POD Blank	**POD cem Blank**	**SL Blank**	**XER Blank**	**SAN Blank**
1	2.7 (0.0)	7.6 (0.9)	4.8 (0.1)	7.1 (0.1)	7.5 (0.0)
7	2.7 (0.0)	8.1 (0.1)	4.8 (0.0)	7.1 (0.0)	7.5 (0.0)
28	2.8 (0.0)	8.2 (0.6)	4.9 (0.1)	7.1 (0.0)	7.5 (0.0)
56	2.8 (0.0)	8.7 (0.0)	4.9 (0.1)	7.1 (0.0)	7.5 (0.0)

SI-Table 5: *Dissolution of Mg from fibers soil suspensions (data to main text Figure 1). Panel a.) Mass-balance of Mg in Schrems treatments. The values were recalculated to an equivalent concentration in soil solution for the conditions of the incubation experiment (SSR = 1:10 and FSR = 2 g L^{-1}). Values from fiber acid digests are the means of two replicates, values of the mobilized metal concentrations in nitric acid extracts and in soil solution are the means of four replicates. Standard deviations were summed (squared addition) for the three compartments; Panel b.) Mg concentrations from acid digestions of fibers from Siebenlinden, Xeraco, Santomera and cement-amended Schrems soils (FSR = 2 g L^{-1}). SD indicates standard deviations (n = 2); Panel c.) Mg concentrations measured in the soil solution of the same soil treatments as in Panel b (FSR = 2 g L^{-1}). SD indicates standard deviations (n = 4); Data with n.d. were not determined.*

Figure 1, Panel a.) Mobilized Mg-concentrations [mmol L^{-1}]

t[d]	Fibers (acid digest)	Soil solid phase	Soil solution	StDEV
Total	19.71	0.03	0.16	0.15
1d	18.90	0.15	1.09	0.27
4d	18.71	0.20	1.63	0.09
7d	18.36	0.23	1.89	0.48
14d	17.70	0.23	2.31	0.16
28d	16.76	0.41	2.87	0.41
56d	15.65	0.48	4.12	0.91

Figure 1, Panel b.) Acid-digested Mg-concentrations [mmol L^{-1}]

	Pristine	SD	1d	SD	4d	SD	7d	SD	14d	SD	28d	SD	56d	SD
Siebenlinden	19.71	0.15	19.71	0.15	20.44	0.62	19.98	0.14	20.74	0.41	19.60	0.02	18.77	0.58
Xeraco	19.71	0.15	19.71	2.59	20.60	0.50	20.58	0.13	20.11	0.29	20.82	0.26	19.72	0.91
Santomera	19.71	0.15	19.71	0.11	20.88	1.21	19.15	0.65	20.29	0.48	20.15	0.59	19.61	0.44
Schrems cement	19.71	0.15	20.16	0.38	20.10	0.18	20.39	0.60	20.07	0.15	20.15	0.48	19.81	0.83

Figure 1, Panel c.) Soil solution Mg-concentrations [mmol L^{-1}]

t[d]	Siebenlinden	SD	Xeraco	SD	Santomera	SD	Podsol cement	SD	Siebenlinden blank	SD	Xeraco blank	SD	Santomera blank	SD	Podsol blank	SD
1.0	0.58	0.01	1.59	0.04	1.11	0.02	0.03	0.01	0.40	0.00	1.51	0.06	1.01	0.01	0.16	0.00
4	0.94	0.06	1.97	0.05	1.37	0.03	0.07	0.08	n.d.	n.d.	n.d.	n.d.	n.d.	n.d.	n.d.	n.d.
7	1.07	0.03	2.04	0.03	1.50	0.02	0.03	0.03	0.43	0.01	1.57	0.03	1.05	0.01	0.16	0.01
14	1.29	0.07	2.08	0.09	1.69	0.05	0.01	0.00	n.d.	n.d.	n.d.	n.d.	n.d.	n.d.	n.d.	n.d.
28	1.34	0.04	2.06	0.04	1.65	0.04	0.01	0.00	0.43	0.00	1.63	0.11	1.04	0.02	0.16	0.01
56	1.62	0.04	2.22	0.06	1.79	0.05	0.01	0.00	0.43	0.00	1.66	0.00	1.07	0.00	0.16	0.00

SI-Table 6: *Dissolution of Si from fibers soil suspensions (data to main text Figure 2). Panel a.) Mg/Si-ratios of chrysotile incubated in soil suspension determined by fusion digestions (n = 2); Panel b.) Si concentrations mobilized in alkaline extractions (n = 2); Panel c.) Mass-balance of Si in Schrems treatments. Values from fiber acid digests and mobilized Si concentrations in alkaline extracts are the means of two replicates, values measured in the soil solution or soil solid phase are the means of four replicates. The values were recalculated to an equivalent concentration in soil solution for the conditions of the incubation experiment (SSR = 1:10 and FSR = 2 g* L^{-1}*). Standard deviations were summed (squared addition) for the three compartments; SD indicates standard deviation. Abbreviations are Schrems podzol amended with cement ("Pod cem"), Siebenlinden soil ("SL"), Xeraco soil ("Xer") and Santomera soil ("SAN"). Data with n.d. were not determined.*

Figure 2, Panel a.) Molar Mg/Si-ratios determined in fusion digestions

t[d]	Podzol	SD	Pod cem	SD	SL	SD	XER	SD	SAN	SD
1	1.45	0.00	1.52	0.00	1.51	0.00	1.52	0.01	1.51	0.03
4	1.42	0.01	n.d.	n.d.	n.d.	n.d.	n.d.	n.d.	n.d.	n.d.
7	1.40	0.00	n.d.	n.d.	n.d.	n.d.	n.d.	n.d.	n.d.	n.d.
14	1.38	0.01	n.d.	n.d.	n.d.	n.d.	n.d.	n.d.	n.d.	n.d.
28	1.35	0.00	n.d.	n.d.	n.d.	n.d.	n.d.	n.d.	n.d.	n.d.
56	1.28	0.00	1.53	0.02	1.45	0.01	1.44	0.02	1.45	0.01

Figure 2, Panel b.) Si-concentrations analyzed in alkaline extractions [µmol L^{-1}]

t[d]	Podzol	SD	Pod cem	SD	SL	SD	XER	SD	SAN	SD
1	35.3	8.8	10.4	1.1	10.2	0.4	9.7	0.7	9.3	0.8
4	78.0	7.0	14.0	0.4	11.3	1.4	9.8	1.1	9.7	0.8
7	89.3	0.0	11.7	1.5	10.7	0.1	11.9	0.2	11.0	0.3
14	218	11.8	14.2	0.0	13.3	2.1	14.3	2.3	12.7	1.1
28	455	82.4	16.0	0.3	13.1	1.8	15.1	1.1	12.2	0.3
56	660	12.1	14.1	2.0	12.5	0.7	15.1	1.2	12.4	1.6

Figure 3, Panel d.) Mobilized Si-concentrations [mmol L^{-1}]

t[d]	Fibers (acid digestion)	Alkaline extract	Soil solution	StDev
Total	13.36	0.00	0.00	0.24
1d	12.95	0.07	0.04	0.18
4d	13.05	0.16	0.18	0.06
7d	12.98	0.18	0.22	0.34
14d	12.42	0.44	0.48	0.11
28d	11.56	0.91	0.55	0.28
56d	10.94	1.32	0.78	0.71

SI-Table 7: *Mass-balance of Ni (Panel a), Cr (Panel b) and Mn (Panel c) in Schrems treatments (data to main text Figure 3). The values were recalculated to an equivalent concentration in soil solution for the conditions of the incubation experiment (SSR = 1:10 and FSR = 2 g L^{-1}). Values from fiber acid digests are the means of two replicates, values of the mobilized metal concentrations in nitric acid extracts and in soil solution are the means of four replicates. Standard deviations were summed (squared addition) for the three compartments*

Figure 1, Panel a.) Mobilized Ni concentrations [µmol L^{-1}]

t[d]	Fibers (acid digestion)	Soil nitric acid extract	Soil solution	StDEV
Total	37.6	1.0	1.9	0.9
1d	36.0	1.5	2.6	1.1
4d	36.0	2.0	3.4	1.2
7d	34.8	2.2	3.9	1.0
14d	33.7	2.1	4.0	0.3
28d	31.8	3.7	4.2	0.6
56d	30.7	4.8	4.3	2.5

Figure 3, Panel b.) Mobilized Cr concentrations [µmol L^{-1}]

t[d]	Fibers (acid digestion)	Soil nitric acid extract	Soil solution	StDEV
Total	52.3	0.0	0.6	0.5
1d	50.2	0.0	1.5	0.7
4d	49.1	0.2	1.9	0.8
7d	46.3	0.3	1.7	1.2
14d	43.5	0.3	1.6	0.3
28d	40.5	0.6	1.4	0.5
56d	39.3	0.9	1.3	2.5

Figure 1, Panel c.) Mobilized Mn concentrations [µmol L^{-1}]

t[d]	Fibers (acid digestion)	Soil nitric acid extract	Soil solution	StDEV
Total	27.5	3.4	12.1	1.1
1d	13.2	5.0	22.3	1.1
4d	10.3	4.9	25.6	0.6
7d	9.3	5.0	26.4	0.8
14d	8.1	4.0	26.1	0.8
28d	7.2	6.0	25.6	0.5
56d	6.4	6.2	25.6	0.7

SI-Table 8: *Hydroxyl radical forming potentials (HRFP, 100% ≙ HRFP of pristine fibers) of fibers that were incubated for 1, 4, 7, 14, 28 and 56 days in the respective soil suspensions (data to main text Figure 4). HRFPs are the means of four replicates. SD indicates standard deviations.*

	1d	SD	4d	SD	7d	SD	14d	SD	28d	SD	56d	SD
Schrems	23.7	4.4	24.8	4.8	30.0	8.0	27.6	5.7	29.3	6.0	39.1	8.0
Schrems cement	35.9	8.5	19.6	4.9	19.1	4.2	17.6	5.2	2.4	5.4	9.6	7.5
Siebenlinden	87.1	10.0	40.2	9.5	26.9	9.8	31.1	9.2	30.0	9.8	24.8	8.4
Xeraco	52.8	9.3	40.3	7.3	36.1	4.8	28.9	3.8	29.9	3.8	25.8	4.3
Santomera	69.2	12.8	63.2	21.0	39.4	5.9	33.4	3.9	29.6	5.3	27.7	6.7

SI-Table 9: *DOC (dissolved organic carbon) contents of the different soil suspensions at the start of the Float-A-Lyzer experiment (1d blank) and at the end (56d Float-A-Lyzer samples and blank). Values and standard deviations (in round braces) represent the mean of two (in blanks) or four (Float-A-Lyzer) replicates. Abbreviations are Schrems podzol amended with cement ("POD cem"), Siebenlinden soil ("SL"), Xeraco soil ("XER") and Santomera soil ("SAN").*

Analysis	**Time [d]**	**Treatment**						
				Schrems	**POD cem**	**SL**	**XER**	**SAN**
DOC	1	Blank	[mg L^{-1}]	265 (4.9)	187 (21.9)	10.4 (0.4)	41.5 (0.9)	1.7 (0.1)
DOC	56	Blank	[mg L^{-1}]	175 (6.7)	267 (9.5)	1.7 (0.4)	38.8 (0.2)	1.5 (0.1)
				Schrems	**POD cem**	**SL**	**XER**	**SAN**
DOC	56	Float	[mg L^{-1}]	139 (4.7)	472 (211)	13.4 (0.4)	36.5 (0.6)	1.9 (0.2)

SI-Table 10: *Extractable Mg contents from soils that were incubated for 1 and 56 days in blank suspensions (SSR 1:10) in nitric acid digestions. Values and standard deviations (in round braces) represent the mean of two replicates. Extractable Mg concentrations were low in Schrems and Siebenlinden soils, but very high in the carbonaceous Xeraco and Santomera soils. Data are presented in mmol L^{-1} to compare measured metal concentrations of nitric acid digestions with other data from this publication (also on a molar basis).*

		Schrems	Siebenlinden	Schrems cement	Xeraco	Santomera
HNO_3 Mg blank 1d	[mmol L^{-1}]	0.03 (0.0)	0.30 (0.01)	3.77 (0.20)	46.3 (0.0)	23.9 (2.3)
HNO_3 Mg blank 56d	[mmol L^{-1}]	0.03 (0.0)	0.19 (0.00)	5.60 (0.67)	49.7 (7.9)	22.7 (1.3)

SI-Table 11: *Mg and Ni concentrations analyzed in nitric acid extraction of soils from fiber and blank incubations that were incubated for 1 and 56 days. Mobilized metal concentrations are the means of four (fiber incubations) or two (blanks) replicates. SD indicates standard deviations. This table presents the data of SI-Figure 2.*

t[d]	Mg Siebenlinden	SD	Mg Siebenlinden blank	SD
1d	0.99	0.04	1.13	0.05
56d	0.91	0.02	0.64	0.00
t[d]	Ni Siebenlinden	SD	Ni Siebenlinden blank	SD
1d	2.04	0.30	1.96	0.02
56d	6.91	0.41	1.90	0.20
t[d]	Ni Xeraco	SD	Ni Xeraco blank	SD
1d	7.69	0.18	7.58	0.61
56d	10.15	0.71	8.28	0.02

SI-Table 12: *Metal concentrations measured in the soil solution of fiber incubations or blank samples after 1, 4, 7, 14, 28 and 56 days (fiber incubations), or 1, 7, 28 and 56 days (blank samples) of incubation (FSR of 2 g L^{-1}). Mobilized metal concentrations are the means of four (fiber incubations) or two (blank samples) replicates. SD indicates standard deviations. Abbreviations are Schrems podzol amended with cement ("Pod cem"), Siebenlinden soil ("SL"), Xeraco soil ("Xer") and Santomera soil ("SAN"), blank ("bl"). Data with n.d. were not determined. This table presents the data of SI-Figure 3.*

SI-Figure 3, Panel a.) Soil solution Mg concentrations [µmol L^{-1}]

t[d]	SL	SD	XER	SD	SAN	SD	SL bl	SD	XER bl	SD	SAN bl	SD
1	36.1	1.6	37.3	2.4	46.0	2.0	39.1	1.2	34.4	3.5	44.9	1.4
4	44.0	2.1	58.5	3.2	61.4	2.2	n.d.	n.d.	n.d.	n.d.	n.d.	n.d.
7	56.6	2.9	62.8	2.7	74.4	3.8	58.3	0.3	56.4	0.8	57.8	1.1
14	85.3	10.9	66.0	3.3	78.6	2.3	n.d.	n.d.	n.d.	n.d.	n.d.	n.d.
28	115	19.6	65.1	3.6	76.2	3.2	74.0	3.9	71.5	8.1	63.7	5.0
56	156	17.5	65.7	6.4	82.1	3.3	85.6	2.6	62.9	3.6	67.8	1.2

SI-Figure 3, Panel b.) Soil solution Mn concentrations [µmol L^{-1}]

t[d]	XER	SD	SAN	SD	XER bl	SD	SAN bl	SD
1	2.9	0.3	0.7	0.1	1.5	0.2	0.0	0.0
4	4.5	0.3	2.1	0.2	n.d.	n.d.	n.d.	n.d.
7	1.1	0.8	3.0	0.6	0.9	0.6	0.1	0.0
14	0.5	0.3	1.0	0.2	n.d.	n.d.	n.d.	n.d.
28	0.3	0.1	1.0	0.2	0.6	0.3	0.1	0.1
56	0.2	0.2	0.8	0.2	0.1	0.0	0.2	0.1

SI-Figure 3, Panel c.) Soil solution Mn concentrations [µmol L^{-1}]

t[d]	Siebenlinden	SD	Siebenlinden blank	SD
1	45.8	2.0	49.2	0.1
4	51.7	4.5	n.d.	n.d.
7	56.5	2.9	68.8	0.2
14	55.9	2.1	n.d.	n.d.
28	57.5	2.1	81.1	0.0
56	46.7	3.8	82.9	1.9

SI-Figure 3, Panel d.) Soil solution Co concentrations [µmol L^{-1}]

t[d]	Schrems	SD	Schrems cement	SD	Blank	SD
1.0	0.8	0.4	0.5	0.2	1.0	0.2
4	0.9	0.3	0.5	0.2	n.d.	n.d.
7	1.0	0.3	0.6	0.1	0.8	0.3
14	1.0	0.3	0.4	0.1	n.d.	n.d.
28	1.0	0.4	0.8	0.3	0.8	0.0
56	1.5	0.2	0.9	0.3	0.9	0.1

SI-Figure 3, Panel e.) Soil solution Zn concentrations [µmol L^{-1}]

t[d]	Schrems	SD	Schrems cement	SD	Blank	SD
1	34.8	1.1	0.5	0.1	39.5	1.4
4	25.8	0.6	0.5	0.1	n.d.	n.d.
7	17.4	1.1	0.5	0.1	39.9	0.8
14	9.0	0.8	0.5	0.1	n.d.	n.d.
28	0.5	1.4	0.6	0.1	39.2	2.0
56	8.9	0.6	0.7	0.1	41.2	0.7

SI-Figure 3, Panel f.) Soil solution Zn concentrations [µmol L^{-1}]

T[d]	SL	SD	XER	SD	SAN	SD	SL bl	SD	XER bl	SD	SAN bl	SD
1.0	2.8	0.0	0.5	0.1	0.5	0.1	2.8	0.0	0.5	0.1	0.6	0.1
4	1.5	0.3	0.6	0.1	0.5	0.1	n.d.	n.d.	n.d.	n.d.	n.d.	n.d.
7	1.5	0.2	0.4	0.1	0.7	0.1	3.6	0.5	0.3	0.0	0.6	0.3
14	0.9	0.1	0.5	0.2	0.5	0.2	n.d.	n.d.	n.d.	n.d.	n.d.	n.d.
28	1.1	0.2	0.7	0.1	0.6	0.3	3.5	0.2	0.4	0.0	0.4	0.1
56	0.9	0.1	0.7	0.2	0.9	0.3	7.1	4.8	0.9	0.3	1.0	0.3

SI-Table 13: *Si concentrations mobilized from 1 g L^{-1} fibers that were preconditioned for 336 h in pH 3.0, 4.5, 6.0 and 7.4 blank solutions and pH 7.4 1 mmol L^{-1} DFOB solutions in a 0.1 mol L^{-1} NaOH for 1, 4, 8, 48 and 336h (Panel c). SD indicates standard deviations (n = 2). This table presents the data of SI-Figure 4.*

t[d]	pH 3.0 blank altered	SD	pH 4.5 blank altered	SD	pH 6.0 blank altered	SD	pH 7.4 blank altered	SD	pH 7.4 DFOB altered	SD
1.0	210	13.1	21.5	2.1	12.6	0.2	8.6	0.5	8.5	0.9
4	198	33.0	26.4	1.8	14.1	2.0	9.7	0.7	10.3	0.9
8	235	10.9	29.3	0.1	18.3	1.1	8.8	0.4	10.6	1.2
48	265	10.3	35.5	0.5	21.1	3.5	11.5	0.9	12.1	0.3
336	268	8.4	46.8	0.1	29.0	1.7	13.9	1.2	15.9	0.2

SI-Table 14: *Metals measured in acid digestions of fiber-filled Float-A-Lyzer in a 1.4 mol L^{-1} HNO_3 for 336 h at 50°C (reported for a FSR of 2 g L^{-1}). Bulk metal data of pristine fibers were taken from fusion digestion or NAA results (main text Table 1). SD indicates standard deviations (n = 2). This table presents the data of SI-Figure 5.*

SI-Figure 5, Panel a.) Acid digested Ni concentrations [µmol L^{-1}] (Pristine concentrations taken from fusion digestion data)

	Pristine	SD	1d	SD	4d	SD	7d	SD	14d	SD	28d	SD	56d	SD
Schrems	37.6	0.8	36.0	1.1	36.0	1.2	34.8	0.9	33.7	0.1	31.8	0.4	30.7	2.4
Siebenlinden	37.6	0.8	39.0	0.6	39.4	2.0	40.7	0.0	38.0	0.4	36.5	0.0	37.1	1.5
Xeraco	37.6	0.8	40.6	5.7	40.0	0.7	39.6	0.8	39.5	0.1	37.7	0.1	38.0	1.1
Santomera	37.6	0.8	40.4	0.4	37.7	2.2	39.4	1.4	40.5	0.9	39.7	2.1	39.3	1.1
Schrems cement	37.6	0.8	38.5	0.4	38.4	1.4	39.2	0.2	38.0	0.1	38.3	0.0	37.0	3.0

SI-Figure 5, Panel b.) Acid digested Mn concentrations [µmol L^{-1}] (Pristine concentrations taken from fusion digestion data)

	Pristine	SD	1d	SD	4d	SD	7d	SD	14d	SD	28d	SD	56d	SD
Schrems	27.5	0.5	13.2	0.1	10.3	0.1	9.3	0.0	8.1	0.1	7.2	0.0	6.4	0.2
Siebenlinden	27.5	0.5	37.1	1.0	37.8	5.1	33.1	1.3	26.7	1.7	26.5	0.9	25.5	1.3
Xeraco	27.5	0.5	27.5	3.5	30.4	0.7	29.4	1.2	26.2	0.6	25.8	0.7	21.9	0.9
Santomera	27.5	0.5	27.5	0.6	29.5	1.4	28.5	0.5	29.8	1.2	29.9	1.4	29.2	1.2
Schrems cement	27.5	0.5	27.9	0.0	28.7	2.1	28.2	0.7	27.5	1.6	25.5	0.8	26.5	1.5

SI-Figure 5, Panel c.) Acid digested Cr concentrations [µmol L^{-1}] (Pristine concentrations taken from fusion digestion data)

	Pristine	SD	1d	SD	4d	SD	7d	SD	14d	SD	28d	SD	56d	SD
Schrems	52.3	0.4	50.2	0.6	49.1	0.8	46.3	1.2	43.5	0.0	40.5	0.3	39.3	2.5
Siebenlinden	52.3	0.4	53.3	1.2	54.4	2.0	55.9	1.5	53.3	0.0	52.2	0.8	53.1	1.2
Xeraco	52.3	0.4	54.9	6.9	55.9	0.4	54.1	0.6	54.8	0.1	54.1	0.4	54.3	2.2
Santomera	52.3	0.4	55.2	0.7	52.3	3.3	54.4	2.3	55.5	0.7	53.8	1.9	53.6	1.1
Schrems cement	52.3	0.4	52.5	0.8	52.3	2.2	54.8	0.4	52.3	1.9	52.2	0.8	51.6	3.7

SI-Figure 5, Panel d.) Acid digested Zn concentrations [µmol L^{-1}] (Pristine concentrations taken from NAA data)

	Pristine	SD	1d	SD	4d	SD	7d	SD	14d	SD	28d	SD	56d	SD
Schrems	0.5	0.0	1.8	0.0	1.2	0.4	1.0	0.0	0.9	0.2	1.3	0.1	1.9	0.5
Siebenlinden	0.5	0.0	1.9	0.3	2.7	0.2	3.3	0.1	3.4	0.0	3.4	0.1	4.0	0.3
Xeraco	0.5	0.0	0.9	0.1	0.8	0.2	0.8	0.1	0.7	0.2	1.4	0.1	1.1	0.3
Santomera	0.5	0.0	0.6	0.1	0.7	0.1	0.8	0.2	0.6	0.2	0.7	0.2	1.0	0.3
Schrems cement	0.5	0.0	0.8	0.0	1.2	0.8	0.6	0.1	0.7	0.0	0.7	0.0	1.1	0.3

SI-Figure 5, Panel e.) Acid digested Co concentrations [µmol L^{-1}] (Pristine concentrations taken from NAA data)

	Pristine	SD	1d	SD	4d	SD	7d	SD	14d	SD	28d	SD	56d	SD
Schrems	1.8	0.0	1.7	0.5	1.7	0.4	1.8	0.7	1.8	0.1	2.0	0.8	1.2	0.4
Siebenlinden	1.8	0.0	2.4	0.0	2.7	0.7	2.3	0.2	2.1	0.5	2.1	0.3	2.3	0.3
Xeraco	1.8	0.0	2.4	0.6	2.4	0.2	1.9	0.2	2.3	0.0	2.1	0.0	1.9	0.9
Santomera	1.8	0.0	2.0	0.3	2.1	0.1	2.6	0.1	2.4	0.6	1.9	0.2	2.0	0.2
Schrems cement	1.8	0.0	2.0	0.4	2.7	0.4	1.9	0.5	2.2	0.2	2.2	0.1	2.3	0.1

SI-Figure 5, Panel f.) Acid digested Al concentrations [mmol L^{-1}] (Pristine concentrations taken from fusion digestion data)

	Pristine	SD	1d	SD	4d	SD	7d	SD	14d	SD	28d	SD	56d	SD
Schrems	0.43	0.00	0.45	0.00	0.44	0.01	0.43	0.01	0.42	0.00	0.43	0.01	0.46	0.02
Siebenlinden	0.43	0.00	0.46	0.00	0.48	0.01	0.49	0.01	0.48	0.00	0.45	0.00	0.48	0.01
Xeraco	0.43	0.00	0.46	0.06	0.48	0.00	0.45	0.00	0.46	0.01	0.45	0.00	0.45	0.02
Santomera	0.43	0.00	0.46	0.00	0.43	0.02	0.45	0.02	0.47	0.01	0.45	0.02	0.48	0.06
Schrems cement	0.43	0.00	0.54	0.03	0.68	0.10	0.92	0.26	0.93	0.17	1.30	0.18	2.25	0.72

SI-Table 15: *Metal or Si concentrations mobilized in a pH 7.4 1 mmol L^{-1} HEDTA solution from 1 g L^{-1} fibers incubated for 1, 4, 7, 14, 28 and 56 days in the respective soil suspensions. SD indicates standard deviations (n = 2). This table presents the data of SI-Figure 6.*

SI-Figure 6, Panel a.) Mobilized Mg concentrations [µmol L^{-1}]

t[d]	Schrems	SD	Siebenlinde	SD	Xeraco	SD	Santomera	SD
1	277	68.7	625	40.5	501	27.1	722	230
4	220	6.4	392	21.5	397	11.4	510	35.7
7	208	0.0	318	72.4	375	12.3	415	37.7
14	183	24.8	263	3.9	304	6.5	341	9.1
28	172	2.4	238	72.9	294	30.2	307	35.4
56	160	1.6	198	53.2	252	0.0	276	0.0

SI-Figure 6, Panel b.) Mobilized Si concentrations [µmol L^{-1}]

t[d]	Schrems	SD	Siebenlinde	SD	Xeraco	SD	Santomera	SD
1	159	4.2	115	1.0	113	2.5	109	17.9
4	241	37.7	121	6.4	117	3.4	122	6.6
7	269	2.2	113	10.7	117	2.0	126	8.6
14	336	23.2	115	15.8	118	1.5	121	6.3
28	498	25.3	122	25.8	105	0.3	116	8.5
56	647	4.0	104	12.3	114	2.8	79	58.8

SI-Figure 6, Panel c.) Mobilized Fe concentrations [µmol L^{-1}]

t[d]	Schrems	SD	Siebenlinde	SD	Xeraco	SD	Santomera	SD
1	29.2	1.0	35.3	0.1	27.0	2.2	32.3	6.3
4	16.9	1.8	30.5	0.4	26.9	1.6	31.1	2.8
7	17.4	0.6	28.8	2.6	29.3	0.4	27.9	1.0
14	13.5	2.2	26.5	0.5	26.4	0.1	30.4	0.9
28	16.0	0.5	24.7	4.5	23.5	1.1	29.9	1.6
56	15.4	0.7	26.2	5.2	25.2	1.1	28.0	3.5

SI-Figure 6, Panel d.) Mobilized Mn concentrations [µmol L^{-1}]

t[d]	Schrems	SD	Siebenlinde	SD	Xeraco	SD	Santomera	SD
1	1.6	0.3	13.4	1.1	7.2	0.7	8.1	1.4
4	0.5	0.1	10.1	0.8	6.9	0.1	8.3	0.6
7	0.5	0.1	8.7	2.5	7.1	0.1	7.6	0.5
14	0.3	0.1	6.8	0.1	5.2	0.2	7.6	0.5
28	0.2	0.0	7.7	3.5	5.4	0.5	7.7	0.9
56	0.2	0.0	5.7	1.9	4.4	1.0	7.9	1.8

SI-Figure 6, Panel e.) Mobilized Cr concentrations [µmol L^{-1}]

t[d]	Schrems	SD	Siebenlinde	SD	Xeraco	SD	Santomera	SD
1	0.4	0.1	1.0	0.0	0.7	0.1	0.8	0.0
4	0.1	0.2	0.8	0.2	0.8	0.0	0.9	0.1
7	0.1	0.1	0.7	0.0	0.9	0.1	0.9	0.2
14	0.0	0.1	0.5	0.2	0.6	0.2	0.8	0.1
28	0.0	0.1	0.6	0.5	0.5	0.1	0.8	0.0
56	0.0	0.0	0.4	0.1	0.6	0.0	0.5	0.5

SI-Figure 6, Panel f.) Mobilized Ni concentrations [µmol L^{-1}]

t[d]	Schrems	SD	Siebenlinde	SD	Xeraco	SD	Santomera	SD
1	1.5	0.3	1.9	0.1	1.7	0.0	1.8	0.1
4	0.9	0.0	1.4	0.0	1.6	0.1	1.9	0.3
7	1.1	0.1	1.3	0.0	1.9	0.2	1.8	0.1
14	0.9	0.2	1.2	0.0	1.4	0.0	1.8	0.1
28	1.0	0.3	1.5	0.3	1.0	0.3	1.4	0.2
56	0.8	0.3	1.1	0.1	1.1	0.2	2.0	0.3

SI-Table 16: *Table a.) HRFP of fibers that were incubated for 2, 4, 6 or 8 weeks in pH 7.4 buffered solutions, either without interruptions or in consecutive drying wetting cycles of 2 weeks each. HRFP values are the means of four replicates; Table b.) Mg and Si concentrations (in µmol L^{-1}) mobilized during the preconditioning of the fibers that were analyzed in SI-Figure 7. Mobilized concentrations are the means of two replicates (apart from the 2 weeks incubation). SD indicates standard deviations.*

Table a.) HRFPs [%] of SI-Figure 7:

t[w]	Drying wetting cycles	SD	No drying wetting cycles	SD
2	37.1	3.0	37.1	3.0
4	34.9	4.0	32.8	3.4
6	30.6	2.8	30.3	4.0
8	31.7	2.8	29.9	2.8

Table b.) Mobilized Mg and Si concentrations during the preconditioning of the fibers used for the EPR spin trapping analyses in SI-Figure 7:

Time [w]	Treatment	Mg	SD	Si	SD
2	Both	549	no	14.4	no
4	No drying/wetting	53.1	1.1	20.1	0.5
	Drying/wetting	24.1	0.4	11.8	1.7
6	No drying/wetting	66.1	0.3	23.9	0.1
	Drying/wetting	21.7	0.6	11.8	0.6
8	No drying/wetting	77.1	2.4	27.9	1.8
	Drying/wetting	20.6	1.0	11.9	1.2

Addendum

Supporting Information to Chapter 5

"Weathering of chrysotile in a long-term microcosm experiment: The influence of soil type, plants and cement on dissolution kinetics and radical generation of asbestos in polluted soils"

Supporting information to the data material presented on page 118 to 136.

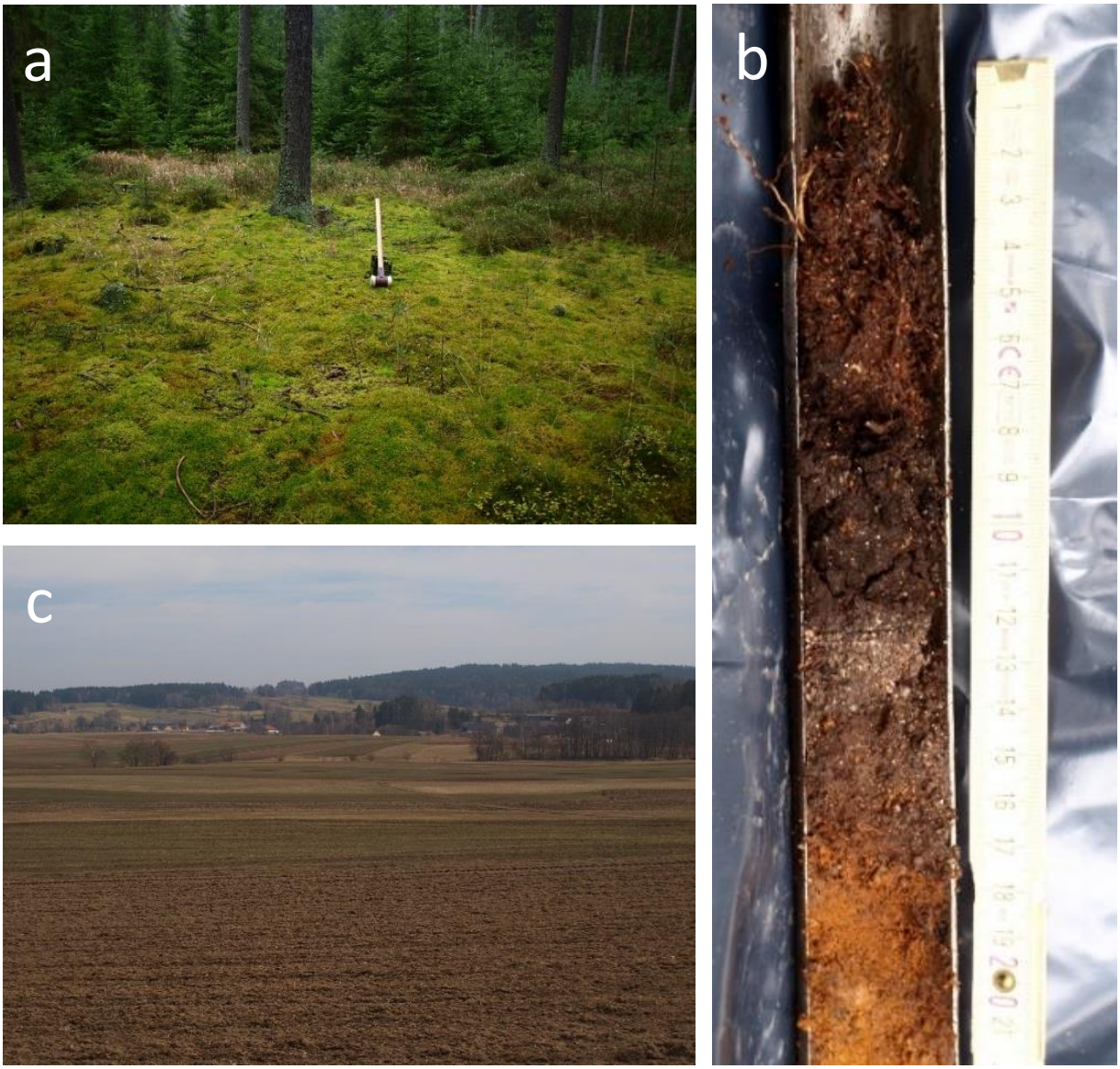

SI-Figure 1: *Sampling sites of the Schrems podzol and the agricultural Siebenlinden soil. Panel a.) Sampling site of the Schrems podzol in a coniferous forest in Lower Austria close to the village of Schrems; Panel b.) Typical sequence of podzolic horizons of the Schrems Podzol, the B horizon was sampled and used for experiments; Panel c.) Sampling site of the agricultural, mildly acidic Siebenlinden soil in Lower Austria, close to the village of Siebenlinden. Pictures of the sampling site of the Santomera soil can be found on the following website (September 2018):*

http://www.cebas.csic.es/general_english/field_cebas.html.

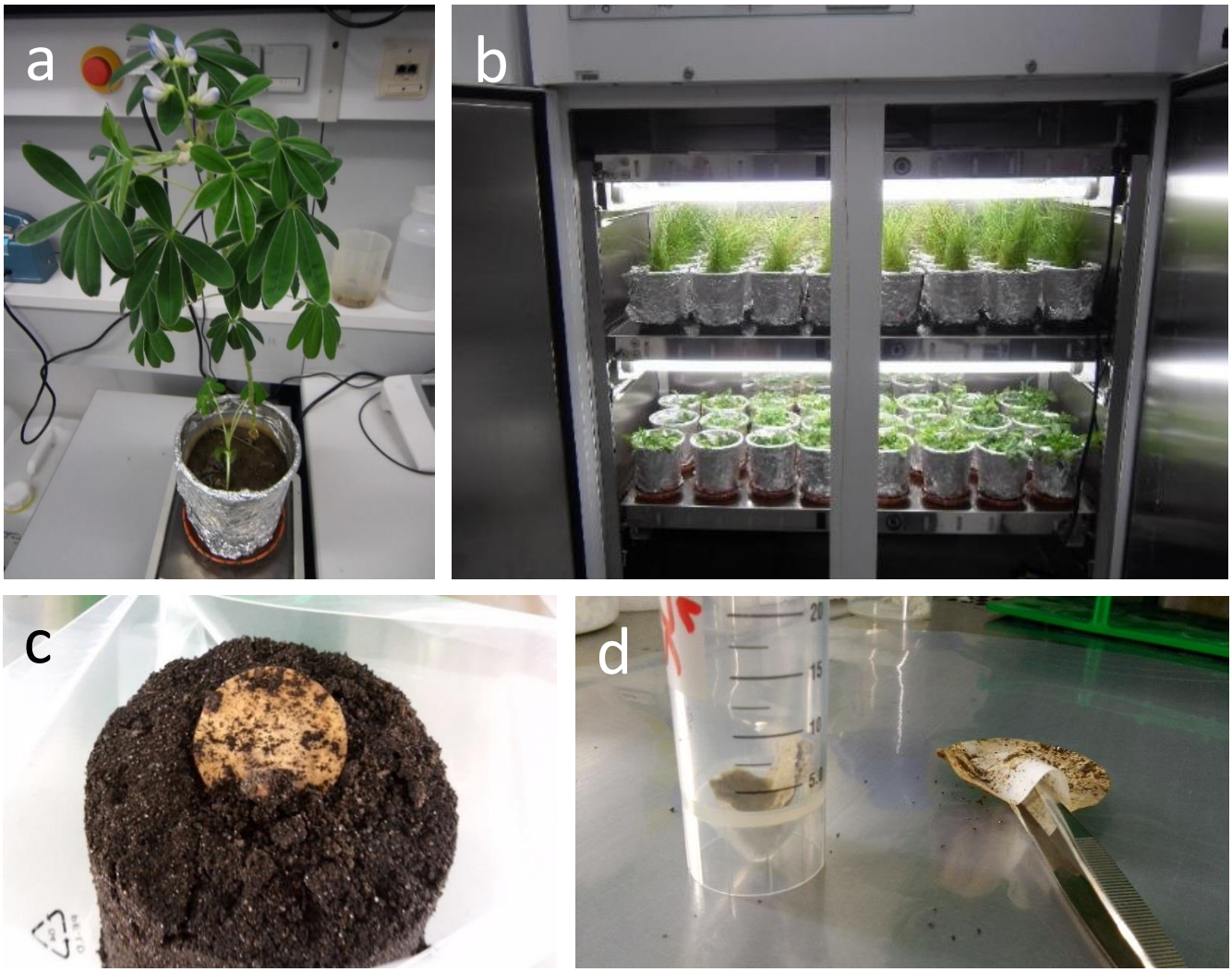

SI-Figure 2: *Long term microcosm experiment. Panel a.) White lupine in bloom during the first year of incubation; Panel b.) Fitotron growing champers with pao pratensis (top) and sorrel microcosms (bottom); Panel c.) Sampling a fiber bag incubated for one year in the acidic Schrems podzol on the bottom of a microcosm; Panel d.) Fiber sampling from a fiber bag incubated for one year in Siebenlinden soil.*

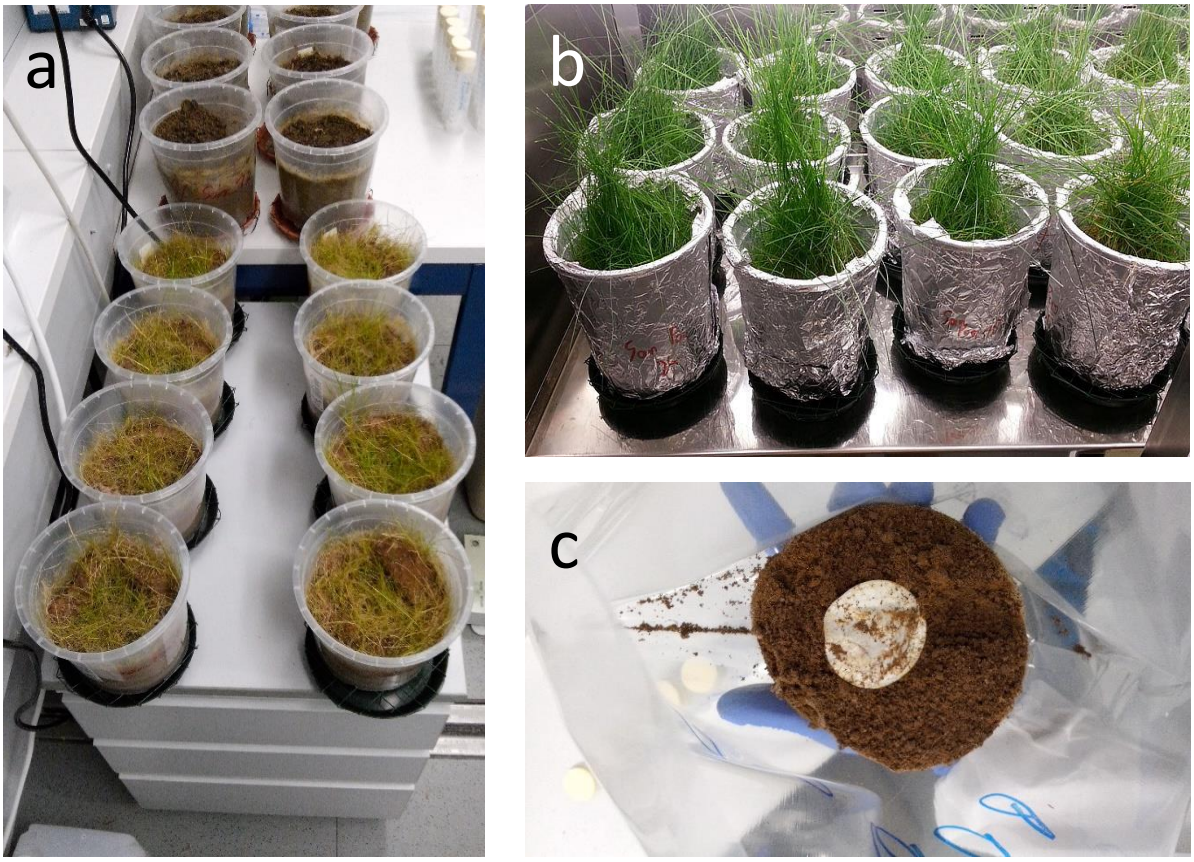

SI-Figure 3: *Kentucky bluegrass (poa pratensis cv Baron) becoming chlorotic. Panel a.) Chlorotic poa pratensis plants after 1.75 years of incubation; Panel b.) Poa pratensis plants at the beginning of the incubation, approximately 0.75 years after the start of the long-term microcosm experiment; Panel c.) A fiber incubation pot sampled from Santomera soil after 1.75 years of incubation, on which chlorotic poa pratensis plants grew.*

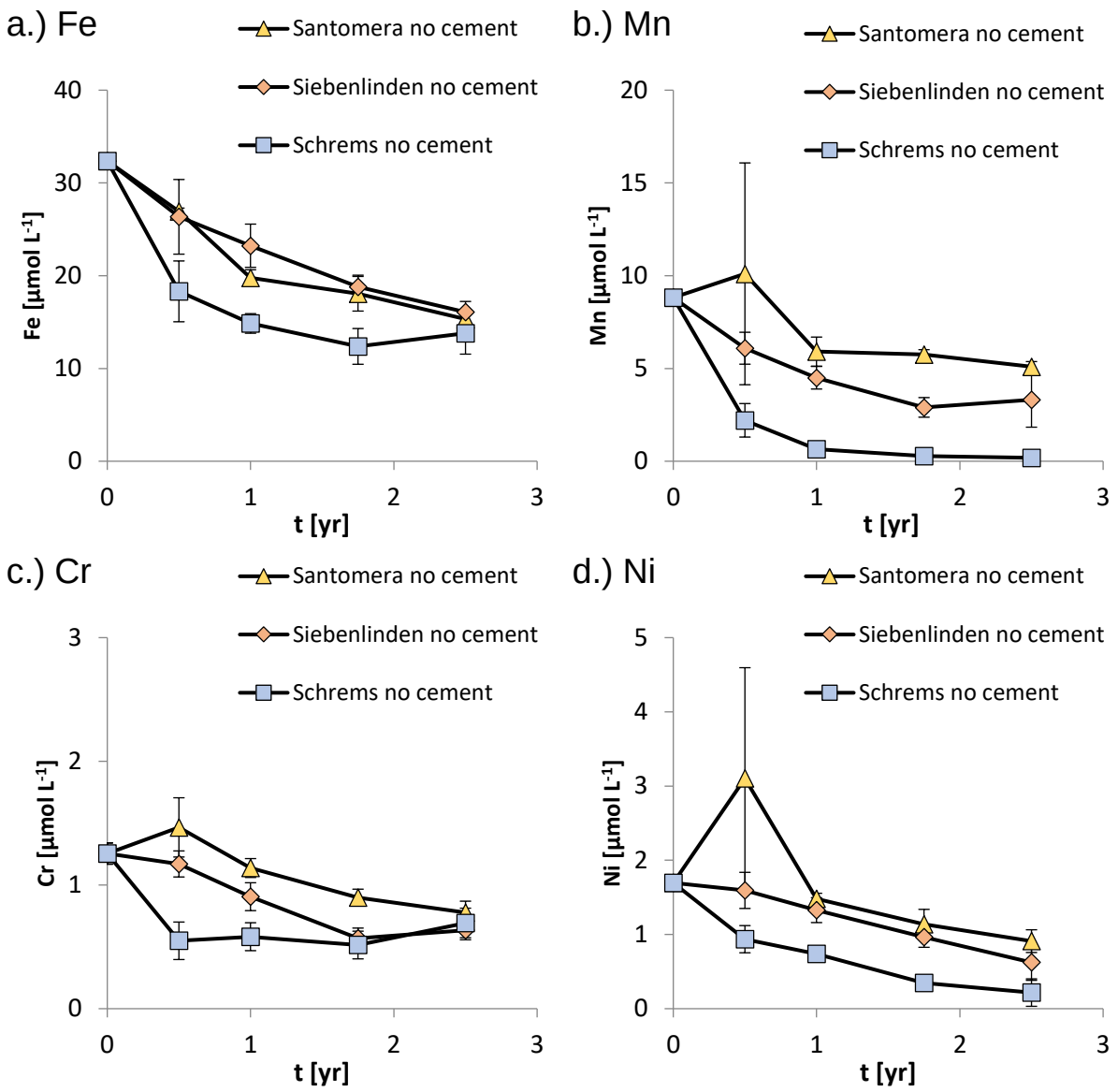

SI-Figure 4: *Extraction of Fe (Panel a), Mn (Panel b), Cr (Panel c) and Ni (Panel d) from the surfaces of fibers sampled in Schrems, Siebenlinden and Santomera no cement microcosms in pH 7.4 extractions. The metals were extracted from the fibers at pH 7.4 for 336 h in the presence of 1 mmol L^{-1} of the synthetic chelator HEDTA. Generally, lower metal contents were extracted from fibers of the Schrems microcosms, most probably because of the higher weathering potential of fibers in this soil relative to Siebenlinden and Santomera soil. Differences in extracted metals between Siebenlinden and Santomera treatments were small or not significant. Error bars indicate standard deviations (n = 4). Data to this Figure can be found in SI-Table 10.*

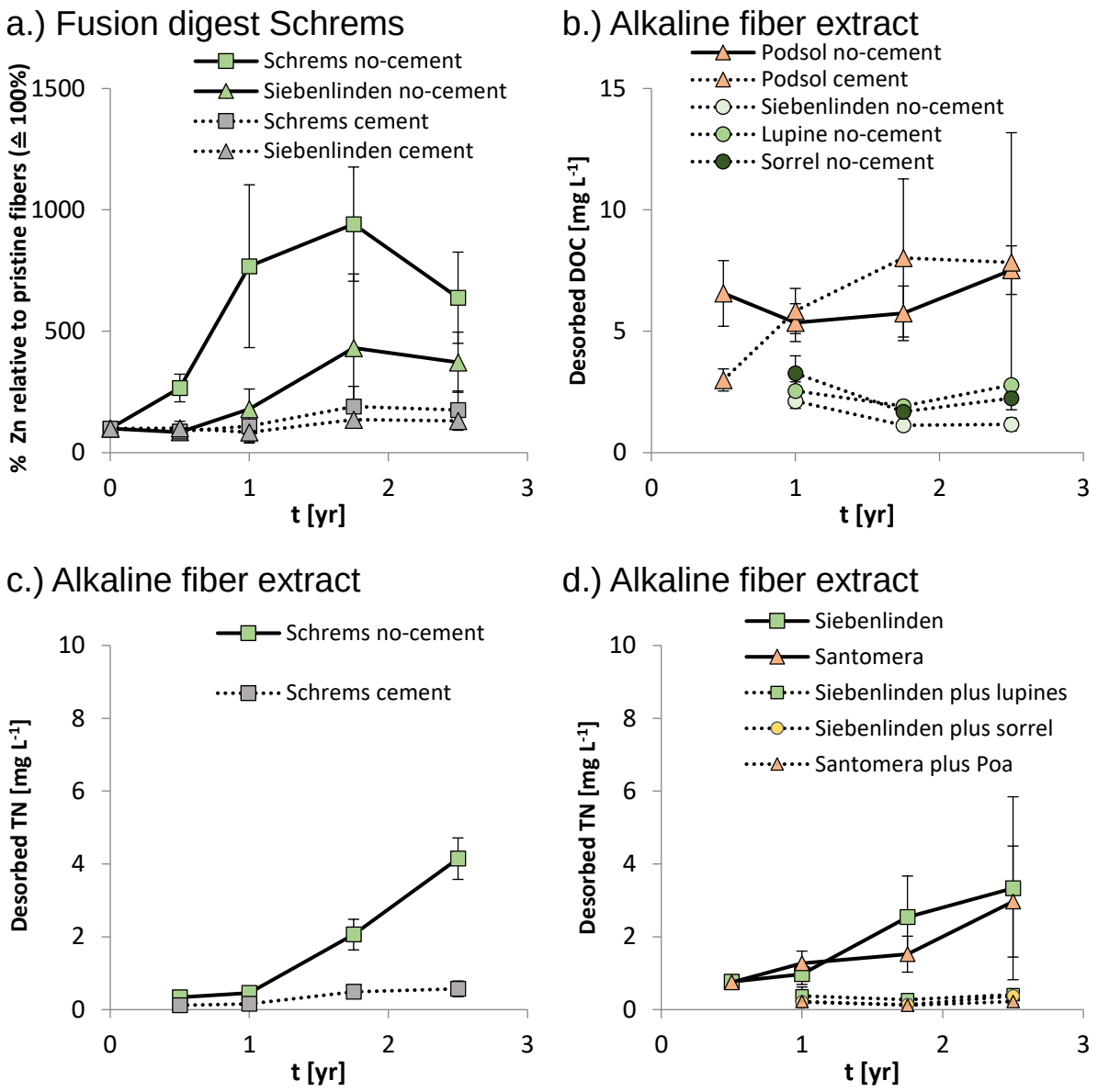

SI-Figure 5: *Accumulation of elements on chrysotile in soil microcosms. Panel a.) Accumulation of Zn on fibers in Schrems and Siebenlinden microcosms, determined in fusion digestions. Fibers from Schrems cement microcosms had a clearly decreased Zn content than fibers from no cement microcosms. In fibers from Santomera and planted microcosms, no clear increase of Zn was detected (data not shown); Panel b.) Desorbed DOC in Schrems microcosms was generally not influenced by cement. Desorbed DOC contents were higher from fibers of planted Siebenlinden microcosms than from unplanted ones; Panel c.) Desorbed TN from fibers of Schrems microcosms was inhibited by cement; Panel d.) Desorbed TN from fibers in Siebenlinden and Santomera microcosms was clearly decreased by all three tested plant species. Data to this figure can be found in SI-Table 11. Error bars indicate standard deviations (Panel a: n = 2; Panel b – d: n = 4).*

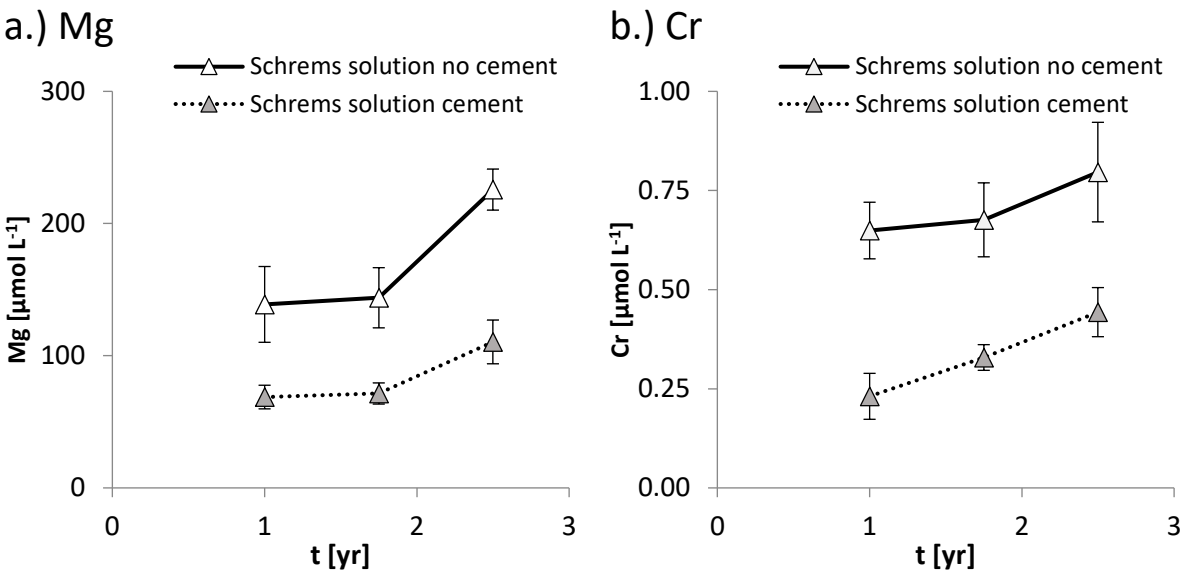

SI-Figure 6: *Soil solution Mg (Panel a) and Cr (Panel b) concentrations in Schrems no cement and Schrems cement microcosms. Due to the high dissolution rates of fibers in Schrems no cement microcosms, the soil solution was enriched in Mg, but also in Cr. This enrichment can furthermore be detected in nitric acid extractions of the respective soils (SI-Table 9). Data to this figure can be found in SI-Table 8. Error bars indicate standard deviations (n = 2).*

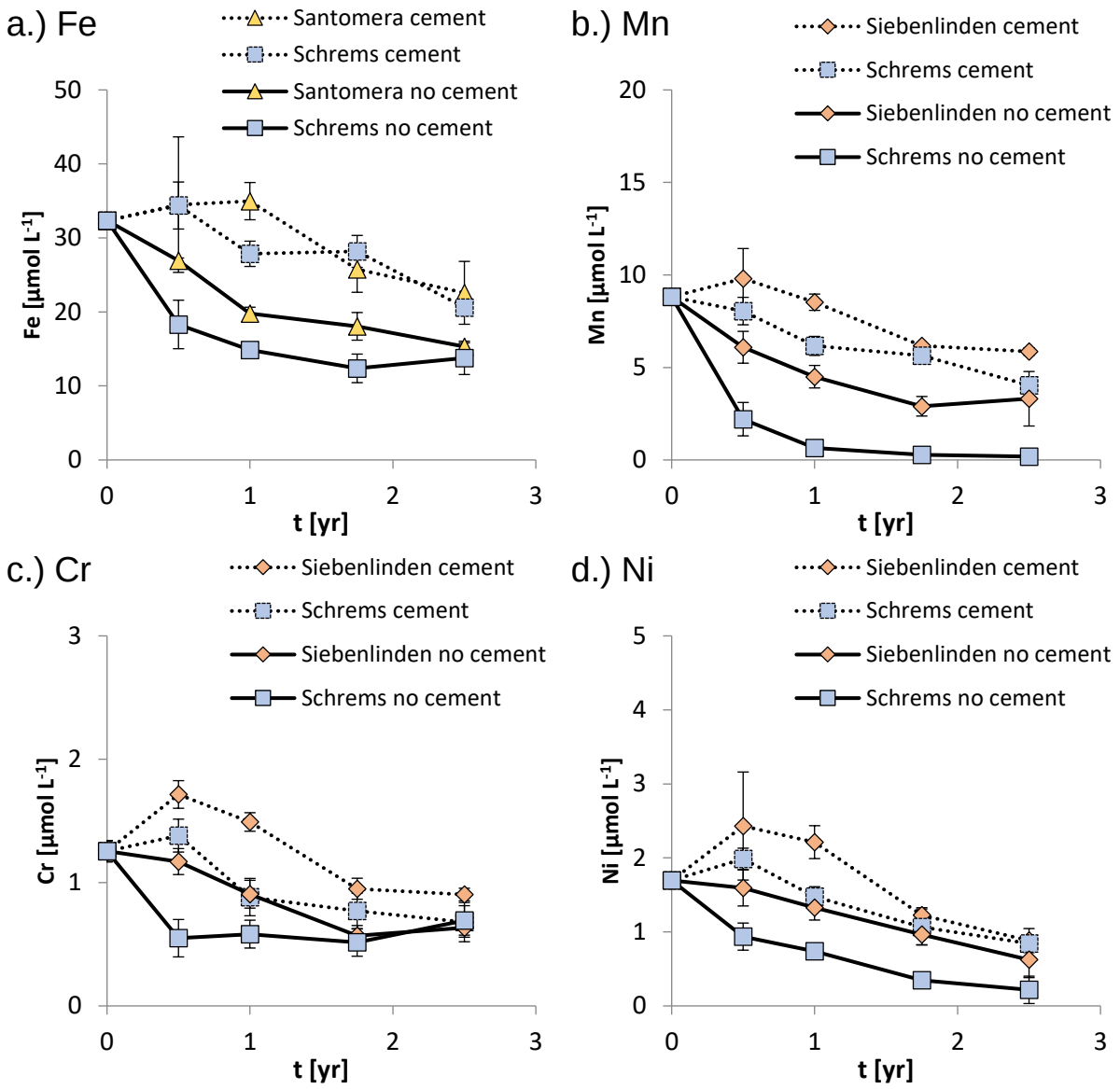

SI-Figure 7: *Extraction of Fe (Panel a), Mn (Panel b), Cr (Panel c) and Ni (Panel d) from the surfaces of fibers sampled in Schrems, Siebenlinden and Santomera no cement and cement microcosms in pH 7.4 extractions. The investigated metals were extracted from the fibers at pH 7.4 for 336 h in the presence of 1 mmol L^{-1} of the synthetic chelator HEDTA. Generally, lower metal contents were extracted from fibers of cement relative to no cement treatments, most probably because of the higher weathering potential of fibers in no cement treatments. Differences in extracted metals between cement and no cement treatments were generally highest in Schrems treatments. Error bars indicate standard deviations (n = 4). Data to this Figure can be found in SI-Table 10.*

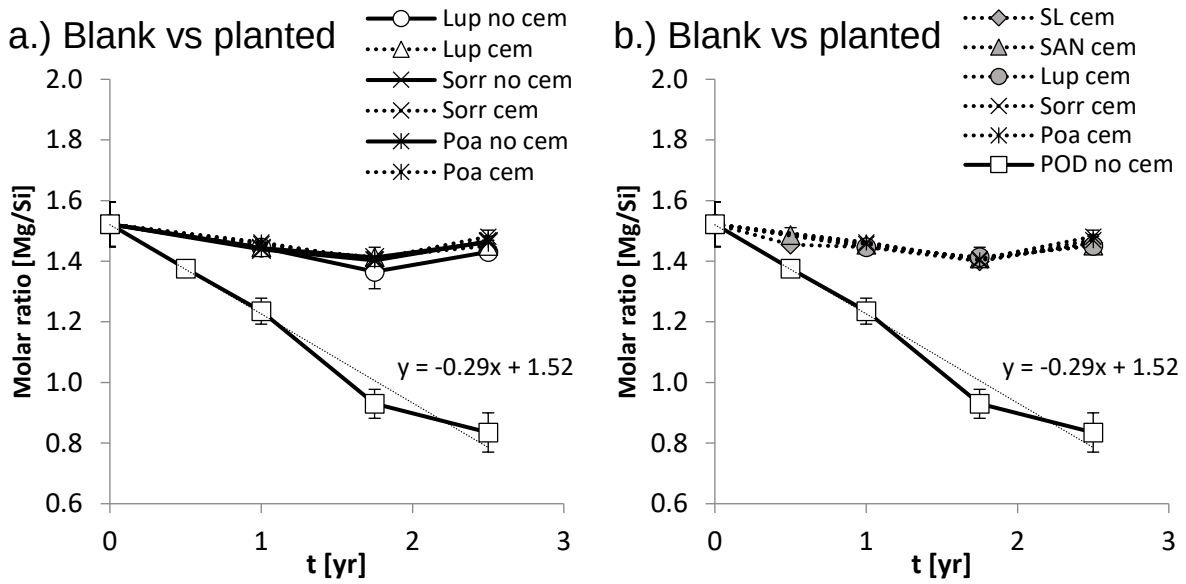

SI-Figure 8: *Molar Mg/Si ratios of fibers from planted Siebenlinden and Santomera no cement and cement treatments (Panel a), and from unplanted and planted Siebenlinden and Santomera cement microcosms (Panel b). The molar Mg/Si ratios from Schrems no cement microcosms were added as a reference. Both panels demonstrate that cement or plants did not change the molar Mg/Si ratios of fibers relative to the blank soil microcosms. Data to this figure can be found in SI-Table 1, 2 and 12. Error bars indicate standard deviations (n = 4).*

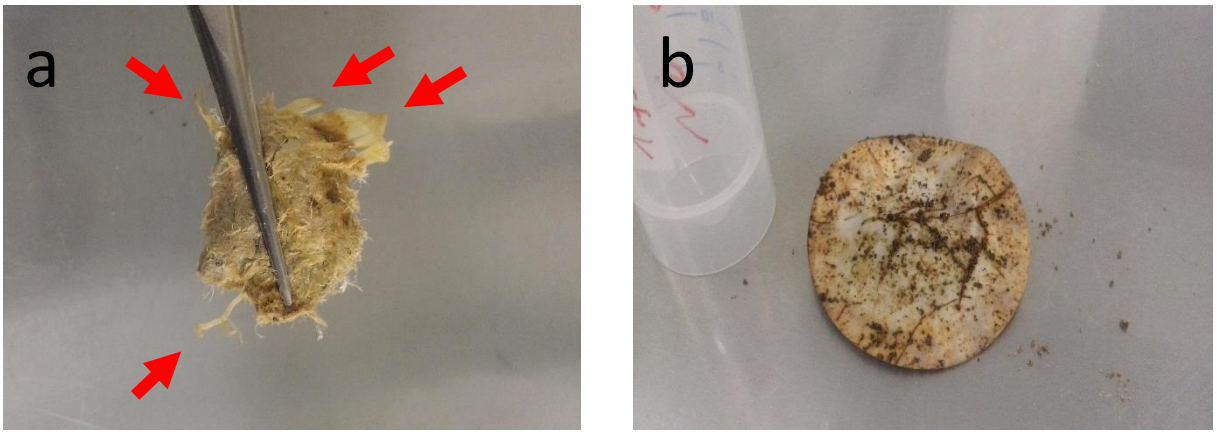

SI-Figure 9: *Signs of root growth in or on asbestos incubation bags in planted microcosms: In picture a, roots of the white lupine managed to penetrate one fiber bag replicate after 1.75 years of incubations. The roots (arrows) proliferated inside the fiber bag. In picture b, roots of the sorrel stuck on the fiber incubation bag (but did not penetrate it). Signs of root growth on fiber bags were also observed in Santomera poa pratensis microcosms (as e.g. seen in SI-Figure 3, Picture c)*

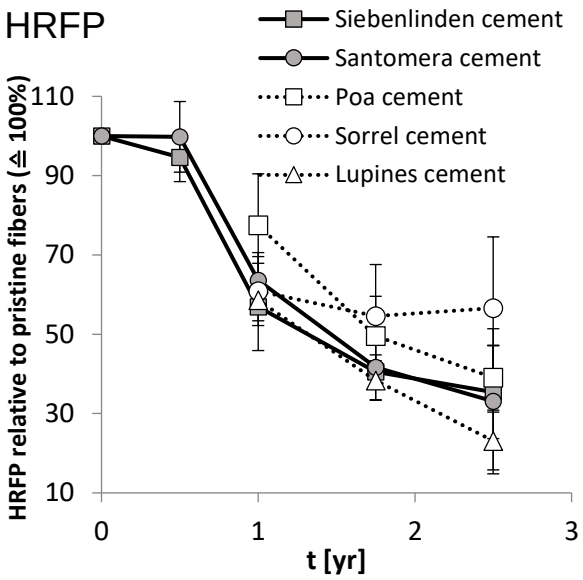

SI-Figure 10: *HRFPs of fibers sampled from unplanted and planted Siebenlinden and Santomera cement microcosms relative to the HRFP of pristine fibers (≙ 100%). The effect of plants on the HRFP of fibers in soil was inhibited by cement. Data to this figure can be found in SI-Table 2 and 13. Error bars indicate standard deviations (n = 8).*

SI-Table 1: *The effect of the soil type on dissolution of, and radical generation by, chrysotile fibers in soils. SD indicates standard deviations (Panel a – c: n = 4; Panel d: n = 8). This table presents the data of main text Figure 1.*

Figure 1a: Content of Mg, Si and Mn bulk of 100 mg digested fibers in % relative to the bulk of pristine fibers (≙ 100%)

Time [yr]	Mg	SD	Si	SD	Mn	SD
0	100	0	100	0	100	0
0.5	92.7	3.0	102	2.8	55.4	4.6
1	88.1	2.6	108	2.4	34.8	5.7
1.75	75.2	3.0	119	1.4	27.2	2.1
2.5	67.9	4.6	125	4.7	27.2	4.5

Figure 1b: Molar Mg/Si ratios of digested fibers from soil microcosm and pristine fibers (at 0 years of incubation)

Time [yr]	Schrems	SD	Siebenlinden	SD	Santomera	SD
0	1.52	0.07	1.52	0.07	1.52	0.07
0.5	1.38	0.01	1.45	0.02	1.45	0.01
1	1.24	0.04	1.45	0.01	1.46	0.01
1.75	0.93	0.05	1.39	0.01	1.39	0.01
2.5	0.84	0.06	1.45	0.01	1.44	0.02

Figure 1c: Alkaline extractable Si contents in mmol L^{-1} (Schrems) or µmol L^{-1} (Siebenlinden and Santomera)

Time [yr]	Schrems	SD	Siebenlinden	SD	Santomera	SD
0	0.0	0.0	6.0	0.0	6.0	0.0
0.5	0.2	0.1	11.6	1.4	11.8	0.7
1	1.1	0.5	14.9	1.6	13.5	0.6
1.75	2.6	0.3	3.5	1.2	2.6	1.2
2.5	3.4	0.7	16.0	3.1	12.4	1.1

Figure 1d: HRFPs in percent relative to the HRFP of pristine fibers (≙ 100%)

Time [yr]	Schrems	SD	Siebenlinden	SD	Santomera	SD
0	100	0	100	0	100	0
0.5	56.0	4.3	67.0	8.0	66.8	7.5
1	44.2	2.8	45.9	9.5	48.9	12.1
1.75	52.4	6.4	30.1	5.2	32.4	2.0
2.5	63.9	14.2	28.2	10.1	29.1	7.7

SI-Table 2: *The effect of cement on dissolution of, and radical generation by, chrysotile fibers in soils. Abbreviations are: POD (Schrems podzol), cem (cement), SL (Siebenlinden), SAN (Santomera), LUP (lupines), SORR (sorrel), POA (poa pratensis). SD indicates standard deviations (Panel a – b: n = 4; Panel c: n = 4 in nitric acid extractions and n = 2 in soil solution measurements; Panel d: n = 8). This table presents the data of main text Figure 2. Data with n.d. were not determined.*

Figure 2a: Mobilized Mg concentrations of fibers from Schrems, Siebenlinden and Santomera no cement and cement microcosm and pristine fibers (at 0 years of incubation) in pH 7.4 extractions

Time [yr]	Schrems no cement	SD	Schrems cement	SD	Siebenlinden no cement	SD	Siebenlinden cement	SD	Santomera no cement	SD	Santomera cement	SD
0	638	32.7	638	32.7	638	32.7	638	32.7	638	32.7	638	32.7
0.5	111	14.9	429	122	293	29.1	548	175	298	4.0	488	170
1	97.0	9.0	294	40.3	238	13.2	343	21.0	247	34.5	389	19.0
1.75	97.2	10.8	226	12.3	178	7.9	224	9.5	208	15.0	247	15.8
2.5	83.3	4.6	155	5.8	138	36.0	175	11.0	155	12.0	208	41.8

Figure 2b: Molar Mg/Si ratios of digested fibers from no cement and cement microcosms and pristine fibers (at 0 years of incubation)

Time [yr]	POD no cem	SD	POD cem	SD	SL no cem	SD	SL cem	SD	SAN no cem	SD	SAN cem	SD
0	1.52	0.07	1.52	0.07	1.52	0.07	1.52	0.07	1.52	0.07	1.52	0.07
0.5	1.38	0.01	1.46	0.02	1.45	0.02	1.46	0.01	1.45	0.01	1.49	0.02
1	1.24	0.04	1.45	0.01	1.45	0.01	1.45	0.00	1.46	0.01	1.46	0.01
1.75	0.93	0.05	1.40	0.00	1.39	0.01	1.40	0.02	1.39	0.01	1.41	0.01
2.5	0.84	0.06	1.45	0.01	1.45	0.01	1.46	0.03	1.44	0.02	1.45	0.02

Figure 2c: Extracted Mg concentrations (in µmol L^{-1}) in nitric acid extractions from soils of Schrems and Siebenlinden no cement and cement microcosms, and soil solution Mg concentrations in Schrems no cement and cement microcosms (in µmol L^{-1})

Time [yr]	Schrems soil no cement	SD	Schrems soil cement	SD	Siebenlinden soil no cement	SD	Siebenlinden soil cement	SD	Schrems solution no cement	SD	Schrems solution cement	SD
0	173	10.6	173	10.6	605	39.8	605	39.5	n.d.	n.d.	n.d.	n.d.
0.5	234	9.0	190	11.5	620	13.5	597	14.8	n.d.	n.d.	n.d.	n.d.
1	370	13.5	252	13.8	625	39.9	619	29.6	139	28.7	68.7	8.9
1.75	492	21.5	218	7.4	620	46.2	587	54.9	144	22.8	71.4	8.0
2.5	540	24.4	188	16.9	633	25.2	629	42.5	226	15.5	110	16.6

Figure 2d: HRFPs in % relative to the HRFP of pristine fibers (≙ 100%)

Time [yr]	0.5 yr cement	SD	0.5 yr no cement	SD	1 yr cement	SD	1 yr no cement	SD	1.75 yr cement	SD	1.75 yr no cement	SD	2.5 yr cement	SD	2.5 yr no cement	SD
Schrems	81.8	6.9	56.0	4.3	36.3	7.7	44.2	2.8	27.2	1.9	52.4	6.4	33.0	13.9	63.9	14.2
Siebenlinden	94.6	6.1	67.0	8.0	56.9	11.2	45.9	9.5	40.5	4.3	30.1	5.2	35.4	11.7	28.2	10.1
Santomera	99.8	8.9	66.8	7.5	63.6	6.8	48.9	12.1	41.7	8.2	32.4	2.0	33.1	18.3	29.1	7.7

SI-Table 3: *The effect of plants on dissolution of, and radical generation by, chrysotile fibers in soils. Abbreviations are: cem (cement), SL (Siebenlinden), SAN (Santomera), LUP (lupines), SORR (sorrel), POA (poa pratensis). In Panel a, the Schrems data were added as a reference. SD indicates standard deviations (Panel a & c: n = 4; Panel b: n = 2; Panel d: n = 8). This table presents the data of main text Figure 3. Data with n.d. were not determined.*

Figure 3a: Molar Mg/Si ratios of digested fibers from planted and unplanted microcosms and pristine fibers (at 0 years of incubation)

Time [yr]	Schrems	SD	SL bl	SD	SAN bl	SD	SL LUP	SD	SL SORR	SD	SAN POA	SD
0.0	1.52	0.07	1.52	0.07	1.52	0.07	1.52	0.07	1.52	0.07	1.52	0.07
1	1.38	0.01	1.45	0.02	1.45	0.01	n.d.	n.d.	n.d.	n.d.	n.d.	n.d.
1	1.24	0.04	1.45	0.01	1.46	0.01	1.45	0.01	1.44	0.01	1.44	0.01
2	0.93	0.05	1.39	0.01	1.39	0.01	1.37	0.06	1.40	0.01	1.41	0.01
3	0.84	0.06	1.45	0.01	1.44	0.02	1.43	0.01	1.47	0.02	1.46	0.01

Figure 3b: Soil solution contents of Mg (in mmol L^{-1}) and Fe (in µmol L^{-1}) in planted and unplanted microcosms

Time [yr]	Mg Siebenlinden bl	SD	Mg Santomera bl	SD	Mg Siebenlinden LUP	SD	Mg Siebenlinden SORR	SD	Mg Santomera POA	SD	Fe Siebenlinden SORR	SD
1.0	5.09	1.87	2.82	0.19	2.16	2.29	0.18	0.03	0.25	0.13	12.3	3.9
2	5.14	0.29	2.86	0.32	0.09	0.02	0.19	0.04	0.18	0.01	12.0	2.8
3	6.19	0.33	3.32	0.28	0.05	0.02	0.14	0.05	0.17	0.01	11.3	0.1

Figure 3c: Mobilized Mg concentrations (in µmol L^{-1}) from fibers of Siebenlinden and planted Siebenlinden microcosms in pH 7.4 extractions

Time [yr]	Siebenlinden	SD	Siebenlinden LUP	SD	Siebenlinden SORR	SD
0	638	32.7	n.d.	n.d.	n.d.	n.d.
0.5	293	29.1	n.d.	n.d.	n.d.	n.d.
1	238	13.2	222.7	15.2	189	14.7
1.75	178	7.9	72.6	6.7	139	6.3
2.5	138	36.0	39.2	4.3	141	47.7

Figure 3d: HRFPs in percent relative to the HRFP of pristine fibers (≙ 100%)

Time [yr]	Siebenlinden bl	SD	Santomera bl	SD	Siebenlinden SORR	SD	Siebenlinden POA	SD	Siebenlinden LUP	SD
0	100	0	100	0	n.d.	n.d.	n.d.	n.d.	n.d.	n.d.
0.5	67.0	8.0	66.8	7.5	n.d.	n.d.	n.d.	n.d.	n.d.	n.d.
1	45.9	9.5	48.9	12.1	37.7	2.8	36.7	4.0	46.3	7.4
1.75	30.1	5.2	32.4	2.0	32.0	3.2	30.7	3.0	28.1	6.3
2.5	28.2	10.1	29.1	7.7	24.8	7.0	24.9	7.1	22.2	7.3

SI-Table 4: *Selected results of the ANOVA analysis on the effect of soil type, cement and plants on chrysoitle dissolution in soils, on the HRFP of sampled fibers, and on soil solution properties (pH and DOC). Section a.) Effect of soil, cement and plants tested for all analyzed sampled times (blank treatments 0.5, 1, 1.75 and 2.5 yr; plant treatments 1, 1.75 and 2.5 yr); Section b.) Effect of plants analyzed for single sampling times. Abbreviations are: bl (blank), cem (cement), Siebenl (Siebenlinden), Lup (Lupines), Poa (Poa pratensis).*

Section a.) Effect of soil, cement and plants, no time steps:

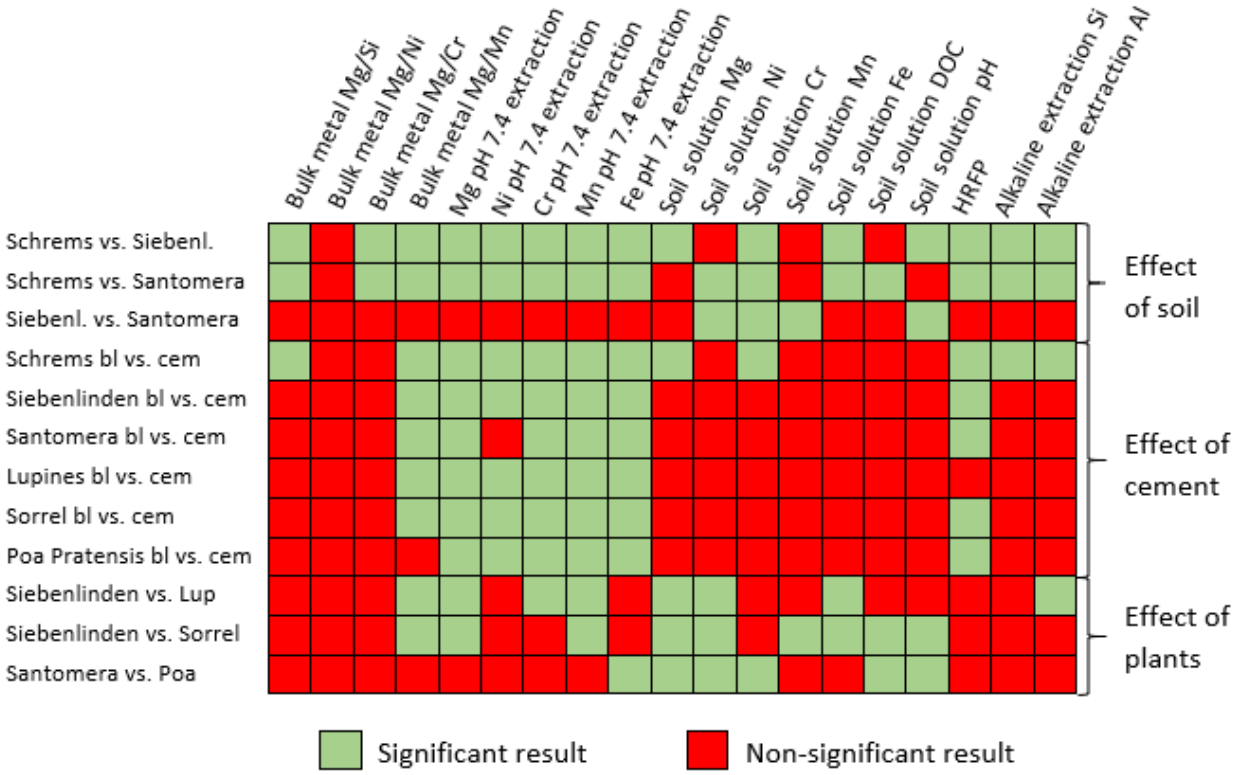

Section b.) Effect of plants, time steps:

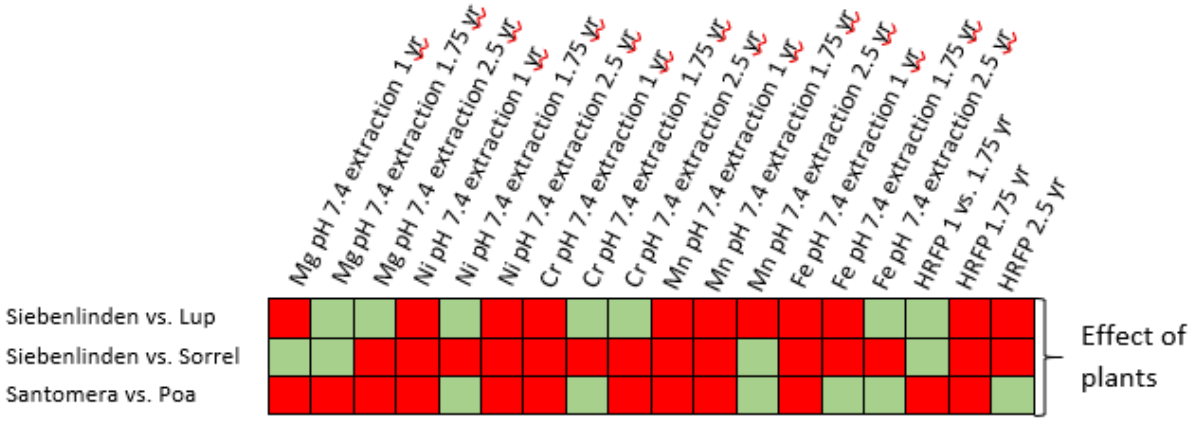

SI-Table 5: *% of Cr or Ni bulk of digested fibers from Schrems microcosms relative to pristine fibers (≙ 100%). Whereas bulk-Cr and bulk-Ni percentages of fibers in Schrems no cement microcosms decreased as a function of time, Cr and Ni bulk percentages of fibers from Schrems cement microcosms (and fibers from all other treatments, data not shown) followed no clear trend and remained approximately at 100 %. SD indicates standard deviations (n = 4).*

Table a: % of Cr bulk relative to pristine fibers (≙ 100%):

Time [yr]	No cement	SD	Cement	SD
0.5	96.1	1.9	97.6	2.1
1	95.4	3.5	96.7	4.1
1.75	83.8	7.2	99.4	3.2
2.5	81.9	7.1	97.2	4.0

Table b: % of Ni bulk relative to pristine fibers (≙ 100%):

Time [yr]	No cement	SD	Cement	SD
0.5	97.2	4.0	98.7	2.3
1	95.8	2.2	98.2	3.8
1.75	92.4	2.7	101	6.2
2.5	84.5	6.7	96.7	4.8

SI-Table 6: *% of Mn bulk of digested fibers from Schrems microcosms relative to pristine fibers (≙ 100%). Since Mn is only enriched in the outermost layers of Shijiazhuang chrysotile according to Walter et al. (2018d) [204], the decreasing Mn levels indicate that fiber dissolution only occurred to a clear extent in Schrems no cement microcosms. The high Mn bulk of fibers from all other microcosms relative to pristine fibers however indicates that fibers in these microcosms did not dissolve congruently. SD indicates standard deviations (n = 4). Data with n.d. were not determined.*

Table a: % of Mn bulk of digested fibers from no cement microcosms relative to pristine fibers (≙ 100%):

Time [yr]	Schrems	SD	SL	SD	SAN	SD	SL + LUP	SD	SL + SORR	SD	SAN + POA	SD
0.5	55.4	4.6	88.0	4.4	91.0	4.8	n.d.	n.d.	n.d.	n.d.	n.d.	n.d.
1	34.8	5.7	77.9	8.5	87.8	8.8	79.5	10.0	83.4	8.1	87.7	8.7
1.75	27.2	2.1	77.3	4.8	93.6	3.1	99.6	15.0	89.7	4.9	96.8	5.2
2.5	27.2	4.5	76.2	8.4	92.5	5.0	71.5	11.7	103	5.0	98.4	4.7

Table b: % of Mn bulk of digested fibers from cement microcosms relative to pristine fibers (≙ 100%):

Time [yr]	Schrems	SD	SL	SD	SAN	SD	SL + LUP	SD	SL + SORR	SD	SAN + POA	SD
0.5	97.9	3.4	98.9	3.8	97.0	5.3	n.d.	n.d.	n.d.	n.d.	n.d.	n.d.
1	95.1	9.3	97.7	9.0	97.2	9.7	95.1	9.1	96.8	8.6	91.8	8.3
1.75	94.3	4.2	99.0	3.7	104	3.2	95.3	6.0	98.6	4.8	99.0	5.6
2.5	90.5	4.1	103	9.0	97.9	5.9	90.1	10.7	115	5.4	106	8.4

SI-Table 7: *Alkaline extractable Al contents of fibers from Schrems no cement and Schrems cement microcosms. Apart from the Schrems no cement treatment, Al did in no other microcosm treatment increase (data not shown), comparable to fibers from Schrems cement microcosms. SD indicates standard deviations (n = 4). B.d. indicates data below the detection limit.*

Time [yr]	Schrems no-cement	SD	Schrems cement	SD
0	b.d.	b.d.	b.d.	b.d.
0.5	16.1	3.4	2.2	1.2
1	57.5	15.6	4.1	0.4
1.75	106	8.8	6.0	0.6
2.5	119	34.9	5.8	2.5

SI-Table 8: *Metal concentrations (DOC and TN in mmol L^{-1}, the others in µmol L^{-1}) in sampled soil solutions. Abbreviations are: cem (cement), SL (Siebenlinden), SAN (Santomera), LUP (lupines), SORR (sorrel), POA (poa pratensis). * indicates that at least one plant species decreased this element from the soil solution, □ indicates that at least one plant species increased this element in the soil solution, • indicates that this element accumulated in the soil solution of a no cement treatment relative to the soil solution of a cement treatment in at least one microcosm, ° indicates that this element accumulated on the surface of fibers of at least one microcosm. SD indicates standard deviations (n = 2). Data with n.d. were not determined.*

1 year	**DOC**□°	SD	**TN**	SD	**Na***	SD	**Mg***•	SD	**Al***	SD	**P**□	SD	**K***	SD	**Ca***	SD
Schrems no cem	63.5	3.6	n.d.	n.d.	94.4	3.6	139	28.7	334	30.1	59.0	2.7	459	18.5	144	8.9
Schrems cem	62.5	2.0	n.d.	n.d.	95.3	7.5	68.7	8.9	328	5.8	61.7	1.5	464	45.2	194	21.2
SL no cem	4.5	0.4	n.d.	n.d.	122	44.0	5871	2817	103	48.3	10.9	0.3	4967	2470	15565	7486
SL cem	5.5	0.8	n.d.	n.d.	114	2.4	4300	206	74.0	3.8	11.0	0.9	3508	165	11619	551
SAN	3.2	0.6	n.d.	n.d.	332	31.7	2854	320	20.4	5.4	3.5	0.4	462	54.8	14278	1441
SAN cem	3.4	0.2	n.d.	n.d.	352	2.7	2794	62.1	22.9	3.2	3.7	1.1	490	3.7	14503	667
SL + LUP no cem	6.3	1.1	n.d.	n.d.	98	39.9	1959	2532	111	71.1	15.6	1.4	1210	1391	5799	7410
SL + LUP cem	7.6	2.0	n.d.	n.d.	110	58.1	2353	3024	128	46.4	17.1	2.6	1783	2191	6742	8510
SL + SORR no cem	14.0	0.6	n.d.	n.d.	64.2	10.5	190	39.3	84.7	21.2	33.3	0.3	255	47.1	619	125
SL + SORR cem	15.2	0.5	n.d.	n.d.	73.6	6.2	174	10.3	83.4	7.1	37.1	4.3	291	97.5	605	4.0
SAN + POA no cem	15.1	0.1	n.d.	n.d.	146	66.9	178	95.2	3.3	2.6	6.3	1.7	27.7	16.3	880	467
SAN + POA cem	19.9	1.8	n.d.	n.d.	271	119	315	152	16.9	18.0	7.4	1.5	65.8	31.8	1666	809

1 year cont.	Ti□	SD	V*	SD	Cr□•	SD	Mn*	SD	Fe□	SD	Co	SD	Ni*	SD	Cu□	SD	Zn*○	SD
Schrems no cem	3.9	0.6	0.7	0.1	0.6	0.1	3.9	0.3	119	12.2	0.1	0.1	0.2	0.2	0.4	0.1	8.5	0.5
Schrems cem	3.8	0.1	0.7	0.1	0.2	0.1	3.6	0.3	120	6.3	0.1	0.0	0.1	0.0	0.4	0.2	8.6	1.4
SL no cem	b.d.	0.1	1.0	0.5	0.1	0.1	44.2	9.2	1.3	0.8	0.0	0.0	0.3	0.2	0.2	0.2	17.8	9.2
SL cem	b.d.	0.0	0.7	0.0	0.1	0.0	34.9	8.8	0.7	0.0	0.1	0.0	0.2	0.0	0.1	0.0	12.1	1.0
SAN	b.d.	0.0	0.6	0.0	0.4	0.0	0.4	0.2	1.0	0.7	0.1	0.1	0.0	0.0	0.2	0.0	0.9	0.7
SAN cem	b.d.	0.0	0.5	0.1	0.3	0.0	0.4	0.1	1.8	1.5	0.1	0.1	0.1	0.1	0.0	0.1	0.3	0.1
SL + LUP no cem	0.0	0.2	0.4	0.4	0.0	0.0	47.4	64.7	6.2	5.9	0.2	0.2	0.2	0.2	0.2	0.1	10.9	14.4
SL + LUP cem	0.0	0.2	0.5	0.5	0.0	0.0	46.8	62.6	6.4	6.2	0.2	0.1	0.1	0.2	0.1	0.2	9.5	11.8
SL + SORR no cem	0.5	0.3	0.2	0.0	0.0	0.0	1.8	0.6	13.4	6.3	0.1	0.0	0.0	0.0	0.3	0.1	1.6	0.8
SL + SORR cem	0.3	0.1	0.2	0.1	0.0	0.0	1.5	0.3	11.3	1.0	0.1	0.0	0.0	0.0	0.4	0.1	0.6	0.0
SAN + POA no cem	0.0	0.0	0.2	0.1	0.6	0.3	0.2	0.1	0.9	0.9	0.1	0.0	0.2	0.0	0.4	0.0	1.4	1.8
SAN + POA cem	0.2	0.2	0.3	0.2	0.9	0.1	0.2	0.2	4.1	4.1	0.2	0.1	0.3	0.1	0.8	0.3	1.1	0.7

1.75 years	DOC□○	SD	TN*○	SD	Na*	SD	Mg*•	SD	Al	SD	P□	SD	K*	SD	Ca*	SD
Schrems no cem	65.3	0.0	12.2	0.0	426	24.4	144	22.8	430	21.6	80.6	1.3	421	20.8	206	10.9
Schrems cem	67.8	0.7	12.0	0.8	444	27.2	71.4	8.0	431	12.9	77.7	3.0	438	10.3	287	32.8
SL no cem	2.3	0.2	32.0	0.2	612	8.4	5008	160	100	7.7	9.9	0.7	3407	62.1	14903	n.d
SL cem	3.0	0.1	34.5	2.7	768	41.4	5270	394	108	7.7	10.7	0.4	3580	156	n.d	n.d
SAN	1.9	0.2	30.2	5.3	1656	205	2706	402	8.8	1.8	1.9	0.6	328	43.8	13356	n.d
SAN cem	1.9	0.1	33.3	6.4	1970	18.9	3009	229	8.0	0.2	2.2	0.8	425	20.1	n.d	n.d
SL + LUP no cem	5.0	1.8	1.0	0.2	193	27.0	81.5	3.9	58.9	24.4	17.5	7.1	47.9	8.7	326	88.1
SL + LUP cem	6.0	3.7	1.5	0.4	246	40.9	106	35.1	56.6	33.8	17.0	11.1	82.7	22.8	528	225
SL + SORR no cem	15.6	3.0	1.0	0.1	408	21.2	153	8.2	117	23.9	51.2	4.9	159	25.8	716	29.0
SL + SORR cem	12.6	3.6	0.9	0.4	501	15.1	228	12.0	108	21.8	48.5	15.0	292	63.7	1002	44.6
SAN + POA no cem	8.3	5.4	0.6	0.1	550	0.7	176	10.6	5.5	2.8	6.7	1.3	30.6	1.8	1016	43.4
SAN + POA cem	7.1	3.5	0.8	0.2	672	28.7	186	13.8	6.8	4.1	6.1	1.2	42.6	11.6	1133	33.2

1.75 years cont.	**Ti**□	SD	**V***	SD	**Cr**□•	SD	**Mn***	SD	**Fe**□	SD	**Co**	SD	**Ni***	SD	**Cu**□	SD	**Zn***○	SD
Schrems no cem	4.9	0.3	0.3	0.0	0.7	0.1	3.7	0.3	147	5.1	0.4	0.0	0.3	0.1	0.5	0.2	8.2	0.5
Schrems cem	5.1	0.2	0.3	0.0	0.3	0.0	3.6	0.1	149	7.8	0.3	0.0	0.3	0.2	0.4	0.1	7.9	0.2
SL no cem	b.d.	0.0	0.5	0.0	0.1	0.0	39.7	6.1	0.8	0.1	0.2	0.0	0.3	0.1	b.d.	0.0	13.8	0.8
SL cem	b.d.	0.0	0.5	0.0	0.1	0.0	42.5	6.9	0.8	0.0	0.1	0.0	0.2	0.0	b.d.	0.0	14.6	0.9
SAN	b.d.	0.0	0.3	0.0	0.3	0.0	0.1	0.1	0.4	0.5	0.1	0.0	0.0	0.0	b.d.	0.0	0.2	0.1
SAN cem	b.d.	0.0	0.4	0.1	0.3	0.0	0.1	0.0	0.0	0.1	0.1	0.0	0.1	0.0	b.d.	0.0	0.4	0.0
SL + LUP no cem	0.4	0.3	0.1	0.0	0.1	0.1	2.8	0.0	15.8	11.4	0.2	0.1	0.0	0.0	0.1	0.1	0.7	0.3
SL + LUP cem	0.4	0.5	0.1	0.0	0.1	0.0	3.6	0.5	11.8	12.9	0.2	0.0	0.1	0.0	0.1	0.1	1.0	0.3
SL + SORR no cem	0.2	0.1	0.1	0.0	0.1	0.0	1.5	0.1	13.0	3.5	0.2	0.0	0.1	0.0	0.4	0.1	1.0	0.1
SL + SORR cem	0.2	0.0	0.1	0.0	0.1	0.0	1.7	0.6	11.1	2.9	0.1	0.0	0.1	0.0	0.4	0.1	1.3	0.3
SAN + POA no cem	0.0	0.0	0.1	0.0	1.0	0.4	0.1	0.0	1.4	0.8	0.1	0.0	0.1	0.0	0.4	0.0	0.3	0.1
SAN + POA cem	0.0	0.0	0.2	0.0	0.6	0.6	0.1	0.1	1.5	1.0	0.2	0.0	0.1	0.1	0.4	0.1	0.3	0.1

2.5 years	**DOC**□○	SD	**TN***○	SD	**Na***	SD	**Mg***•	SD	**Al***	SD	**P**□	SD	**K***	SD	**Ca***	SD
Schrems no cem	86.8	11.1	30.2	1.0	450	11.5	226	15.5	624	76.9	106	0.5	504	30.9	248	10.0
Schrems cem	91.1	13.1	34.3	4.1	508	30.4	110	16.6	612	109	101	12.1	561	51.1	477	97.7
SL no cem	3.5	0.1	100	3.6	767	15.3	6454	123	167	15.5	5.9	0.2	3539	82.7	18013	571
SL cem	4.0	0.6	95.4	2.2	840	16.5	5920	157	157	3.6	6.9	0.5	3398	55.6	17530	412
SAN	2.1	0.1	80.8	7.0	1672	82.8	3381	317	25.1	1.6	3.5	0.0	674	186	17489	1479
SAN cem	2.1	0.5	80.1	7.7	1827	167	3250	346	26.4	2.1	2.6	0.8	598	207	17503	1546
SL + LUP no cem	3.7	0.7	2.3	0.2	183	7.9	62.6	24.3	50.6	1.0	8.5	1.1	78.3	19.1	357	120
SL + LUP cem	7.5	1.4	1.7	0.4	209	69.1	40.0	5.5	108	11.9	13.4	2.0	69.2	26.8	219	36.6
SL + SORR no cem	15.9	3.1	2.5	0.3	461	79.6	144	74.8	100	8.0	23.1	4.4	300	15.1	643	258
SL + SORR cem	20.2	0.7	3.3	0.1	539	16.6	127	22.6	108	11.1	43.5	14.1	196	44.5	683	31.0
SAN + POA no cem	7.9	6.8	2.1	0.9	534	46.3	179	3.0	18.5	7.1	6.8	1.6	277	79.7	1005	70.4
SAN + POA cem	14.7	0.9	1.4	0.6	492	46.0	169	22.5	11.9	1.8	5.1	0.5	198	153	984	98.8

2.5 years cont.	**Ti**□	SD	**V***	SD	**Cr**□•	SD	**Mn***	SD	**Fe**□	SD	**Co**	SD	**Ni***	SD	**Cu**□	SD	**Zn***○	SD
Schrems no cem	16.7	2.7	0.8	0.0	0.8	0.1	4.3	0.1	228	31.6	0.1	0.1	0.5	0.0	0.4	0.0	9.7	0.1
Schrems cem	16.6	4.3	0.9	0.0	0.4	0.1	5.1	0.5	213	57.8	0.2	0.0	0.5	0.0	0.4	0.1	11.0	0.2
SL no cem	b.d.	0.0	2.6	0.0	0.2	0.1	77.6	16.6	1.7	0.3	0.2	0.1	0.4	0.0	b.d.	0.1	18.6	1.0
SL cem	b.d.	0.0	2.4	0.1	0.1	0.0	57.9	6.3	1.1	0.0	0.3	0.1	0.4	0.0	b.d.	0.0	16.9	0.1
SAN	b.d.	0.0	1.5	0.0	0.3	0.1	0.1	0.0	0.7	0.7	0.1	0.1	0.0	0.0	b.d.	0.0	0.4	0.2
SAN cem	b.d.	0.2	1.5	0.1	0.3	0.0	0.1	0.0	0.9	1.0	0.1	0.1	0.1	0.1	b.d.	0.2	0.4	0.2
SL + LUP no cem	1.3	0.1	0.0	0.0	0.0	0.0	2.6	0.9	13.6	1.6	0.2	0.1	0.1	0.0	0.1	0.0	0.9	0.2
SL + LUP cem	1.9	1.0	0.1	0.0	0.1	0.0	3.6	0.3	37.7	2.3	0.2	0.1	0.1	0.0	0.3	0.1	0.9	0.3
SL + SORR no cem	0.8	0.1	0.2	0.0	0.1	0.0	1.7	0.4	11.9	0.1	0.1	0.0	0.2	0.1	0.3	0.1	1.0	0.0
SL + SORR cem	0.2	0.0	0.6	0.4	0.2	0.2	2.2	0.9	10.6	1.0	0.2	0.2	0.1	0.1	0.0	0.1	1.4	0.2
SAN + POA no cem	0.1	0.1	0.3	0.2	1.3	0.0	0.2	0.1	4.1	1.7	0.4	0.2	0.2	0.1	0.3	0.3	0.4	0.1
SAN + POA cem	0.0	0.0	0.1	0.0	0.6	0.8	0.1	0.0	2.5	0.5	0.0	0.2	0.2	0.1	0.2	0.1	0.8	0.4

SI-Table 9: *Nitric acid extractable Ni and Cr concentrations (in µmol L^{-1}) of soils from Schrems no cement and Schrems cement microcosms. Extracted concentrations were in total significantly higher in no cement compared to cement microcosms. In Siebenlinden treatments however there was no significant difference (data not shown). SD indicates standard deviations (n = 4).*

Time [yr]	Ni Schrems no cement	SD	Ni Schrems cement	SD	Cr Schrems no cement	SD	Cr Schrems cement	SD
0	2.06	0.19	2.06	0.19	0.12	0.05	0.12	0.05
0.5	2.09	0.09	2.10	0.13	0.10	0.04	0.11	0.03
1	2.50	0.13	2.22	0.22	0.20	0.03	0.10	0.04
1.75	2.54	0.07	2.20	0.12	0.20	0.04	0.11	0.02
2.5	2.46	0.19	1.88	0.13	0.16	0.03	0.10	0.06

SI-Table 10: *Mobilized metal concentrations (in µmol L^{-1}) from fibers of the respective microcosms in pH 7.4 extractions. Abbreviations are: cem (cement), SL (Siebenlinden), SAN (Santomera), LUP (lupines), SORR (sorrel), POA (poa pratensis). * indicates that at least one plant species decreased this element from the surface of fibers of at least one microcosm, □ indicates that the addition of cement antagonized the mobilization of this element from the fiber surfaces in at least one microcosm. SD indicates standard deviations (n = 2).*

0.5 years	**Mg**□	SD	**Fe**□	SD	**Cr**□	SD	**Ni**□	SD	**Mn**□	SD
Schrems no cem	111	14.9	18.3	3.3	0.5	0.2	0.9	0.9	2.2	0.9
Schrems cem	429	122	34.4	3.2	1.4	0.1	2.0	0.3	8.0	0.7
SL no cem	293	29.1	26.3	4.0	1.2	0.1	1.6	0.3	6.1	0.9
SL cem	548	175	42.9	9.1	1.7	0.1	2.4	0.3	9.8	1.6
SAN	298	4.0	26.9	0.4	1.5	0.2	3.1	0.4	10.1	6.0
SAN cem	488	170	34.5	9.2	1.5	0.4	2.1	0.4	8.3	1.9

1 year	**Mg***□	SD	**Fe**□	SD	**Cr**□	SD	**Ni**□	SD	**Mn**□	SD
Schrems no cem	97.0	9.0	14.9	1.1	0.6	0.1	0.7	1.3	0.6	0.2
Schrems cem	294	40.3	27.9	1.7	0.9	0.2	1.5	0.4	6.2	0.5
SL no cem	238	13.2	23.2	2.3	0.9	0.1	1.3	0.3	4.5	0.6
SL cem	343	21.0	33.8	3.2	1.5	0.1	2.2	0.3	8.5	0.4
SAN	247	34.5	19.8	0.9	1.1	0.1	1.5	0.3	5.9	0.8
SAN cem	389	19.0	35.0	2.5	1.6	0.1	2.0	0.3	8.3	0.4
SL + LUP no cem	223	15.2	21.1	1.0	0.8	0.1	1.3	0.3	4.2	0.7
SL + LUP cem	337	52.0	30.4	6.3	1.4	0.2	1.8	0.2	7.0	1.4
SL + SORR no cem	189	14.7	20.4	0.9	0.7	0.1	1.3	0.4	4.7	0.3
SL + SORR cem	387	46.8	31.6	3.7	1.5	0.2	2.0	0.2	7.4	0.7
SAN + POA no cem	230	55.6	19.8	3.1	1.1	0.2	1.5	0.2	5.9	0.7
SAN + POA cem	454	13.1	33.7	2.7	1.6	0.1	2.0	0.2	8.1	0.6

1.75 years	**Mg***□	SD	**Fe***□	SD	**Cr***□	SD	**Ni***□	SD	**Mn***□	SD
Schrems no cem	97.2	10.8	12.4	1.9	0.5	0.1	0.3	0.0	0.3	0.1
Schrems cem	226	12.3	28.2	2.2	0.8	0.1	1.1	0.1	5.6	0.1
SL no cem	178	7.9	18.8	1.3	0.6	0.1	1.0	0.1	2.9	0.5
SL cem	224	9.5	23.0	2.5	1.0	0.1	1.2	0.2	6.2	0.8
SAN	208	15.0	18.1	1.9	0.9	0.1	1.1	0.2	5.7	0.3
SAN cem	247	15.8	25.7	3.1	1.1	0.1	1.3	0.1	6.4	0.5
SL + LUP no cem	72.6	8.5	16.3	4.7	0.2	0.1	0.6	0.2	3.5	1.6
SL + LUP cem	191	11.9	19.0	1.1	0.6	0.1	1.0	0.2	4.9	0.5
SL + SORR no cem	139	6.3	16.2	2.7	0.4	0.2	0.8	0.2	4.9	0.5
SL + SORR cem	304	8.2	31.4	1.0	0.9	0.4	1.7	0.5	9.1	4.0
SAN + POA no cem	150	25.0	12.2	1.0	0.5	0.2	0.7	0.2	4.6	0.5
SAN + POA cem	280	43.0	26.6	2.0	1.1	0.1	1.4	0.3	6.5	0.7

2.5 years	**Mg*□**	SD	**Fe*□**	SD	**Cr*□**	SD	**Ni□**	SD	**Mn*□**	SD
Schrems no cem	83.3	4.6	13.8	2.3	0.7	0.1	0.2	0.2	0.2	0.0
Schrems cem	155	5.8	20.6	1.0	0.7	0.2	0.8	0.1	4.0	0.4
SL no cem	138	36.0	16.1	1.1	0.6	0.1	0.6	0.2	3.3	1.5
SL cem	175	11.0	19.5	3.6	0.9	0.1	0.9	0.2	5.9	0.2
SAN	155	12.0	15.3	0.5	0.8	0.1	0.9	0.2	5.1	0.3
SAN cem	208	41.8	22.6	4.2	1.0	0.2	1.3	0.5	6.3	1.0
SL + LUP no cem	39.2	4.3	10.7	0.4	0.3	0.1	0.4	0.1	1.8	1.1
SL + LUP cem	148	16.7	17.0	2.5	0.7	0.1	0.8	0.1	4.0	0.6
SL + SORR no cem	141	47.7	16.6	3.0	0.6	0.3	0.8	0.3	5.3	0.7
SL + SORR cem	329	58.4	31.5	1.8	1.3	0.0	1.6	0.2	7.1	0.4
SAN + POA no cem	120	34.2	11.3	2.7	0.6	0.2	0.7	0.4	4.9	1.0
SAN + POA cem	236	26.8	23.6	1.6	1.1	0.2	1.6	0.6	6.5	0.4

SI-Table 11: *Zn, DOC and TN accumulation on fibers from Schrems no cement and cement microcosms, unplanted Siebenlinden no cement microcosms, and Siebenlinden no cement microcosms planted with lupines and sorrel. SD indicates standard deviations (n = 4). DOC adsorption on fibers from Santomera treatments was lower than all reported data (data not shown). This table presents the data from SI-Figure 5.*

Panel a: Zn accumulation on fibers from the respective microcosms in % determined by fusion digestions

Time [yr]	Schrems no-cement	SD	Schrems cement	SD	Siebenlinden no-cement	SD
0	100.0	0.0	100	0	100	0
0.5	266	56.9	87.7	21.9	84.5	20.6
1	768	335	110	64.9	180	82.3
1.75	941	235	190	83.1	432	305
2.5	638	188	176	78.0	373	124

Panel b: Desorbed DOC (in mg L^{-1}) from fibers of the respective microcosms in alkaline extractions

Time [yr]	Podzol no-cement	SD	Podzol cement	SD	Siebenlinden no-cement	SD	Lupine no-cement	SD	Sorrel no-cement	SD
0.5	6.6	1.4	3.0	0.5						
1	5.4	0.8	5.8	0.9	2.1	0.3	2.5	0.4	3.3	0.7
1.75	5.7	1.1	8.0	3.3	1.1	0.2	1.9	0.2	1.7	0.4
2.5	7.5	1.0	7.8	5.3	1.2	0.3	2.8	0.2	2.2	0.5

Panel c: Desorbed TN (in mg L^{-1}) from fibers of the respective microcosms in alkaline extractions

Time [yr]	Schrems no-cement	SD	Schrems cement	SD
0.5	0.3	0.1	0.1	0.1
1	0.5	0.1	0.2	0.0
1.75	2.1	0.4	0.5	0.2
2.5	4.1	0.6	0.6	0.2

Panel d: Desorbed TN (in mg L^{-1}) from fibers of the respective microcosms in alkaline extractions

Time [yr]	Siebenlinden	SD	Santomera	SD	Siebenlinden plus lupines	SD	Siebenlinden plus sorrel	SD	Santomera plus Poa	SD
0.5	0.8	0.2	0.7	0.0						
1	1.0	0.3	1.3	0.3	0.4	0.2	0.2	0.1	0.2	0.0
1.75	2.5	1.1	1.5	0.5	0.3	0.1	0.1	0.0	0.1	0.1
2.5	3.3	2.5	3.0	1.5	0.4	0.0	0.4	0.1	0.2	0.1

SI-Table 12: *Molar Mg/Si ratios of fibers from planted cement microcosms. The molar Mg/Si ratios of fibers from planted no cement microcosms can be found in SI-Table 3, the molar Mg/Si ratios of fibers from no cement and cement unplanted microcosms can be found in SI-Table 1 and 2. SD indicates standard deviations (n = 4). Data with n.d. were not determined. This table partly presents the data of SI-Figure 8.*

Time [yr]	SL + LUP cem	SD	SL + SORR cem	SD	SAN + POA cem	SD
0	1.52	0.07	1.52	0.07	1.52	0.07
0.5	n.d.	n.d.	n.d.	n.d.	n.d.	n.d.
1	1.45	0.03	1.46	0.01	1.46	0.01
1.75	1.41	0.02	1.41	0.02	1.40	0.01
2.5	1.45	0.00	1.48	0.00	1.47	0.00

SI-Table 13: *HRFPs of fibers from planted cement microcosms relative to the HRFP of pristine fibers (≙ 100%). The HRFPs of fibers from planted no cement microcosms can be found in SI-Table 3, the HRFPs from no cement and cement unplanted microcosms can be found in SI-Table 1 and 2. SD indicates standard deviations (n = 8). This table partly presents the data of SI-Figure 10.*

	1 year	SD	1.75 years	SD	2.5 years	SD
Siebenlinden + Lupines	58.6	5.2	38.3	4.9	23.1	7.3
Siebenlinden + Sorrel	60.9	8.7	54.6	12.8	56.6	18.0
Santomera + Poa pratensis	77.5	13.0	49.6	9.6	39.1	8.2